# Exploring the history of India-Eurasia collision and subsequent deformation in the Indus Basin, NW Indian Himalaya

by

Alka Tripathy

A Dissertation Presented in Partial Fulfillment
of the Requirements for the Degree
Doctor of Philosophy

Approved November 2011 by the
Graduate Supervisory Committee:

Kip Hodges, Chair
Steven Semken
Matthijs van Soest
Kelin Whipple
Philip Christensen

ARIZONA STATE UNIVERSITY

December 2011

ABSTRACT

Understanding the evolution of the Himalayan-Tibetan orogen is important because of its purported effects on global geodynamics, geochemistry and climate. It is surprising that the timing of initiation of this canonical collisional orogen is poorly constrained, with estimates ranging from Late Cretaceous to Early Oligocene. This study focuses on the Ladakh region in the northwestern Indian Himalaya, where early workers suggested that sedimentary deposits of the Indus Basin molasse sequence, located in the suture zone, preserve a record of the early evolution of orogenesis, including initial collision between India and Eurasia. Recent studies have challenged this interpretation, but resolution of the issue has been hampered by poor accessibility, paucity of robust depositional age constraints, and disputed provenance of many units in the succession.

To achieve a better understanding of the stratigraphy of the Indus Basin, multispectral remote sensing image analysis resulted in a new geologic map that is consistent with field observations and previously published datasets, but suggests a substantial revision and simplification of the commonly assumed stratigraphic architecture of the basin. This stratigraphic framework guided a series of new provenance studies, wherein detrital U-Pb geochronology, $^{40}Ar/^{39}Ar$ and (U-Th)/He thermochronology, and trace-element geochemistry not only discount the hypothesis that collision began in the Early Oligocene, but also demonstrate that both Indian and Eurasian detritus arrived in the basin prior to

deposition of the last marine limestone, constraining the age of collision to older than Early Eocene.

Detrital (U-Th)/He thermochronology further elucidates the thermal history of the basin. Thus, we constrain backthrusting, thought to be an important mechanism by which Miocene convergence was accommodated, to between 11-7 Ma.

Finally, an unprecedented conventional (U-Th)/He thermochronologic dataset was generated from a modern river sand to assess steady state assumptions of the source region. Using these data, the question of the minimum number of dates required for robust interpretation was critically evaluated. The application of a newly developed (U-Th)/He UV-laser-microprobe thermochronologic technique confirmed the results of the conventional dataset. This technique improves the practical utility of detrital mineral (U-Th)/He thermochronology, and will facilitate future studies of this type.

ACKNOWLEDGMENTS

The presentation of my dissertation, which represents the efforts of five years of my life, would have been neither enjoyable nor possible without the efforts of many faculty, post-docs, graduate students and other collaborators, as well as my family and friends. It would be impossible to name each person that has helped along the way, whether it was related to research or external distressing activities. However, I would be remiss in not trying to recognize at least a few of the people who were an integral part of this journey. First, I must thank my advisor, Kip Hodges, who provided the guidance I needed throughout the years, and always encouraged me to push my research and myself as much as possible. I must also thank three people who I consider mentors – Matthijs van Soest, Jo-Anne Wartho and Brian Monteleone – who not only taught me so much about my chosen field of study, but who were also supportive in every aspect of life as a graduate student (especially grilling/cooking/eating).

Doing fieldwork in the Himalaya requires careful planning, and is one of the most amazing experiences that I have had the pleasure of enjoying for three summers. I thank Talat Ahmad for his guidance regarding the geology of Ladakh, and C.P. Dorjay for assistance with field logistics, as well as Namgyal, Angdu, Kumar and Nima, who served as the most excellent drivers, cooks and field assistants. I must also acknowledge Joe Michalski, Peter Clift and Wendy Bohon for enjoying the spectacular geologic playground of Ladakh with me.

In the lab, many people assisted me in many ways, from training to troubleshooting, including Gwyn Gordon, Lynda Williams, Rick Hervig and Karl

Weiss as ASU, as well as George Gehrels and the LaserChron Facility at the University of Arizona. Christopher Edwards, Frances Cooper, Scott Dickenshied, and members of the JMARS and J-Earth team were key to helping me through the entirety of my second chapter. Byron Adams was my partner in Matlab coding and zircon dissolution, and without the help of the above-listed people and the members of Club NG, I am certain my dissertation would not have yielded the results that I present in the following pages. I also thank the remainder of my committee, Kelin Whiple, Phil Chirstensen and Steve Semken, for reach teaching me so much and guiding me along the way.

I would also like to acknowledge several sources of funding. I was awarded grants from the Lewis and Clark Foundation, the Graduate and Professional Student Associate at ASU, the Geological Society of America Student Research Grant Program, and Sigma Xi. These funds went toward my field and laboratory work. The National Science Foundation (NSF) funded the remainder of my research (awarded to Kip Hodges).

Finally, I would like to thank my parents, Kumud and Suman Tripathy, for their unfailing encouragement and support throughout my education, and my brother and sister, Raj and Anju, for providing much needed distractions every so often. And last, but not least, I must thank Tom Lang for keeping me sane and fed, and for putting up with me for the last three years of my dissertation. Without his help and support, Burfi and I would have been hungry and cranky pair. His presence has made this experience infinitely more enjoyable than it would have been otherwise.

TABLE OF CONTENTS

CHAPTER Page

CHAPTER Page

CHAPTER Page

5

CHAPTER Page

LIST OF TABLES

LIST OF FIGURES

Figure Page

# PREFACE

“The man who removes a mountain begins by carrying away small stones.”
—William Faulkner

# CHAPTER 1

# INTRODUCTION

## 1. Motivation

The rise of the Himalayan range and Tibetan plateau has created some of the most spectacular and complex landforms on Earth. As such, understanding the interrelationships between climate and orogenic processes has been the focus of modeling, with results implying that the rise of the Himalaya had a profound effect on regional and, likely, global climate patterns [*Raymo and Ruddiman*, 1992]. As the archetype for continental collision, the Himalayan-Tibetan orogenic system provides an active example by which to understand the evolution of ancient orogens, and the geodynamic effects that orogenic processes have on the surrounding region [*Rowley,* 1996].

Considering the importance of this system, it is surprising that the timing of collision between India and Eurasia that led to continental orogenesis is a highly disputed first-order boundary condition. Despite decades of research on this topic, estimates span a 35 million year range, from *ca.* 70 Ma to 35 Ma [e.g., *Yin and Harrison*, 2000; *Aitchison et al.*, 2007]. This unacceptably large range of possibilities was prime motivation for the research that led to this dissertation.

Over the years, a variety of methods have been used to assess the timing of collision. Commonly applied techniques such as paleomagnetism and biostratigraphy yield multiply interpretable and sometimes conflicting results. Compare, for example, the conclusions drawn by *Aitchison et al.* [2007] and *Najman et al.* [2010], wherein the same section was studied for biostratigraphic

markers, and interpretation of the data yielded estimates for collision of *ca.* 35 Ma versus 50 Ma. Cenozoic intermontane basins along the Indus-Tsangpo suture zone have garnered significant interest because the sediments they contain are thought to preserve a record of the earliest history of the orogen. Of particular interest are the sedimentary strata wherein both Indian- and Eurasian-derived detritus are identified; such "mixed provenance" is commonly cited as evidence of syn- or post-collisional deposition [e.g., *Wang et al.,* 2010]. However, the value of such studies for constraining the age of collision depends upon knowledge of depositional age and robust and unequivocal evidence of mixed-provenance for a given layer.

The advent of rapid data collection methods for detrital mineral geochronology [e.g., *Kosler et al.*, 2002] has facilitated provenance analysis within these basins, but the vast majority of published studies focused only upon detrital zircon U-Pb geochronology and zircon Hf isotopic constraints, which inherently biases the sampling toward zircon-bearing lithologies. Therefore, the thoughtful development and application of multiple methodologies for provenance studies is imperative to achieve a more comprehensive understanding of the early record of the orogen preserved in these basins.

The Indus Basin, located in the Ladakh region of northwestern India (Figure 1.1), is among the most studied of the Cenozoic intermontane basins of the Himalayan-Tibetan orogenic system because it is spectacularly exposed and lies in one of the few parts of the system that have remained continually accessible for geologic study over the past three decades (despite persistent

political tensions among China, India, and Pakistan). However, this basin is exposed in a very rugged, high-elevation landscape, with few trails and fewer roads. The rocks are complexly folded and faulted throughout the basin, and there is no undeformed "reference" stratigraphic section to enable quantitative reconstructions of the regional structure. Many stratigraphic units – most of which are conglomeratic with rare facing indicators – look alike, and have similar clast contents. The succession contains no known volcanic horizons and few age-diagnostic fossils. As a consequence, many fundamental questions remained regarding the basic stratigraphy and depositional ages of units within the Indus Basin at the start of my research. In the following chapters, a multi-faceted approach is presented that resolves (or at least clarifies) several of these questions. The stratigraphy was simplified based on careful remote sensing image analysis, and the resulting stratigraphy and geologic map were verified through fieldwork, compilation and addition of age constraints, and critical evaluation in the context of previous studies. The results subsequently guided provenance studies, which demonstrate that tectonic models for the orogenic system in which India-Eurasia collision is younger than to Early Eocene time (~53 Ma) are untenable.

One tool that is rarely used for the analysis of sedimentary basins – but which was particularly valuable for this project – was detrital mineral (zircon and apatite) (U-Th)/He thermochronology. Such studies can elucidate the thermal history of either the source area or depocenter, depending upon the degree to which the (U-Th)/He systematics have been reset subsequent to deposition. Both scenarios were encountered in the Indus Basin study. In some cases, unreset

grains were used to reveal the erosional and exhumation history of the source area. In others, reset to partially reset grains were used to constrain the timing of post-collisional deformation and basin inversion. To facilitate detrital (U-Th)/He studies for future researchers, the number of dates required for robust interpretation of the thermal histories of source regions was established, and those results were corroborated using data generated by a new (U-Th)/He thermochronologic technique – described here for the first time – that decreases sample bias and increases throughput.

A brief summary of each subsequent chapter is provided. Chapters 2-6 were prepared for publication in peer-reviewed journals, and as such, there is overlap in the background material.

**2. Outline of Chapters 2-6**

The Indus Basin sedimentary units have been variably mapped multiple times, but such efforts are limited by inaccessibility of most lithologic contacts due to rugged terrane, the deformation of the region caused by basin inversion, and the relative monotony of lithology. In Chapter 2, we examined these otherwise inaccessible contacts using Advanced Spaceborne Thermal Emission and Reflection Radiometer (ASTER) images, and mapped lithologic variations within the Indus Basin. Specifically, the visible imagery allowed for assessment of apparent color changes of the rocks, while masked thermal infrared data yielded information regarding lithologic variability. We used these images to generate a geologic map of the region that is not only internally consistent, but also consistent with external datasets, including a compilation of depositional age

constraints and sedimentary petrography. Furthermore, we simplified the stratigraphy such that discrete depocenters are now identifiable, each of which likely records different phases of collisional orogenesis.

In Chapter 3, we present new data for the Upper Oligocene (~30 Ma) Basgo Formation of NW India that are pertinent to the hypothesis that the collision initiated no earlier than the Eocene-Oligocene boundary (~34 Ma) [*Aitchison et al*., 2007]. The Basgo Formation, which represents a portion of the Indus molasse basin deposited along the Indus-Tsangpo suture zone, contains conglomerates with clasts of Eurasian plate rocks [*Garzanti and Van Haver,* 1988]. However, the distribution of U-Pb dates for detrital zircons in associated sandstones indicate an Indian plate source. This mixed provenance demonstrates a minimum Late Oligocene age (~30 Ma) for India-Eurasia collision in the NW Indian Himalaya. However, (U-Th)/He cooling dates for detrital zircons from the Basgo Formation range from 52.6 to 28.25 Ma, implying that their Indian plate source was emergent and eroding by the Early Eocene (~53 Ma) due to collision. Therefore, the hypothesis that collision commenced during Early Oligocene (~30 Ma) time is not supported by these data.

Most strata in the Indus Basin are poorly dated, and were likely deposited semi-continuously from Early Eocene to Miocene time. Whereas the majority of fine-grained detritus in these older units appears to preserve a distinct Transhimalayan (Eurasian) source, we present new geochemical and geochronological data that suggest a significantly varied provenance for the Indus Basin strata in Chapter 4. Specifically, detrital zircon U-Pb geochronology of

quartzite cobbles within conglomeratic beds of the oldest macrostratigraphic molasse unit demonstrates a potentially mixed source, which, on balance, appears most similar to Indian passive margin detrital zircon U-Pb age spectra. Trace element geochemistry of mafic pebbles, collected from conglomeratic horizons, appears to demonstrate derivation from the Shyok suture zone that is situated north of the Transhimalayan source area. However, several clasts are consistent with Indus-Tsanpgo suture zone ophiolites. This is interpreted as evidence for an Indian source area. Finally, $^{40}Ar/^{39}Ar$ thermochronology of detrital biotite from a sandstone unit intercalated with the last (late Ypresian, ~53 Ma) Indus Basin marine limestone is most consistent with an Indian plate source region. Therefore, the minimum age of India-Eurasia collision at this location is late Ypresian (Early Eocene, ~53 Ma).

Chapter 5 focuses on backthrusting, thought to play an important role within the Transhimalayan sector of the orogen in accommodating Cenozoic convergence between India and Eurasia. Backthrusts located near the Indus-Tsangpo suture zone have been postulated to represent a major structural system – the Great Counter Thrust system – that may persist many hundreds of kilometers along strike [*Yin*, 2006]. However, the ages of many structures grouped within the Great Counter Thrust system are not well constrained, complicating our understanding of the role of the system in Himalayan tectonics. In the Ladakh region of NW India, we used new apatite (U-Th)/He dates and published $^{40}Ar/^{39}Ar$ dates to constrain the timing of backthrusting to between 19 and 7 Ma. Importantly, zircon (U-Th)/He systematics were not fully reset during the

backthrusting event. Modeling of these results in light of the conditions of anchizonal metamorphism related to backthrusting provides a better estimate of the timing of metamorphism (11 to 7 Ma) and suggests a 3 to 3.5 my duration for the event. Comparison of this result with data from elsewhere along the suture suggests diachroneity in the timing of backthrusting structures along what is mapped as the Great Counter Thrust system.

In Chapter 6, I focus on detrital mineral thermochronology of modern sediments, which is a valuable tool for assessing catchment-wide exhumation rates [*Stock and Montgomery,* 1996]. However, this application is only acceptable for catchments that have achieved an erosional and thermal steady state. It is possible to assess the likelihood of steady-state conditions – as well as other necessary assumptions – through statistical comparisons of the distribution of thermochronologic dates in a detrital population to catchment hypsometry [*Ruhl and Hodges,* 2005]. This approach presumes that the thermochronologic dataset is representative of the overall distribution of bedrock dates in the catchment. Due to the time-intensive nature of conventional (U-Th)/He thermochronology, most previous studies of this kind have relied on data for a few tens of grains, even though conventional wisdom holds that a substantially larger number might be necessary for a robust characterization of the population of cooling ages in a sample. I explore the question of how many detrital grain dates are sufficient for such studies in a known non-steady–state setting by comparing subsamples of a large (U-Th)/He zircon dataset (n = 113) for a sediment sample that drains the Ladakh batholith, north of the Indus Basin. The results indicate that, even for a

basin with a complex thermal history, only ~ 35 grains may be sufficient to reveal that complexity and dissuade a researcher from inadvertently (and incorrectly) concluding that the catchment had achieved steady state. I also introduce the use of UV-laser microprobe (U-Th)/He thermochronology for detrital studies. The laser microprobe dataset yields comparable information about cooling age distributions and minimizes unwanted bias toward use of pristine, unabraded crystals, which are normally selected for conventional (U-Th)/He thermochronologic studies.

Chapter 7 provides a synthesis of the previous chapters, and focuses on designing future studies based upon the techniques and datasets presented and discussed in the preceding chapters.

The citations for chapters 2-6 are as indicated below:

Chapter 2: Tripathy, A. K., C. S. Edwards, K. V. Hodges, J.-A. Wartho, and F. J. Cooper (2011), Lithologic mapping of complexly deformed sedimentary strata using ASTER multispectral imagery: Implications for the evolution of Indus Basin depocenters, Ladakh, NW India, in preparation for submission to *Journal of Geophysical Research – Solid Earth*

Chapter 3: Tripathy, A. K., K. V. Hodges, M.C. van Soest, and T. Ahmad (2011), Pre-Oligocene emergence of the Indian passive margin and the timing of Indian-Eurasian collision, submitted to *Geology*

Chapter 4: Tripathy, A. K., K. V. Hodges, T. Ahmad, P. D. Clift, G. W. Gordon, and J.-A. Wartho (2011), Identifying mixed Indian-Eurasian provenance in the Indus Basin molasse sequence, northwestern Indian Himalaya: Implications for the timing of collision, in preparation for submission to *Chemical Geology*

Chapter 5: Tripathy, A. K., K. V. Hodges, M. C. van Soest, and T. Ahmad (2011), Timing of north-vergent deformation in Ladakh, northwestern India, and implications for the along-strike continuity for the Great Counter Thrust system, in preparation for submission to *Journal of the Geological Society of London*

Chapter 6: Tripathy, A. K., B. D. Monteleone, M. C. van Soest, and K. V. Hodges (2011), Robust detrital mineral (U-Th)/He thermochronology in non-steady-state settings, in preparation for submission to *Journal of Geophysical Research – Earth Surface*

**3. References**

Aitchison, J. C., J. R. Ali, and A. M. Davis (2007), When and where did India and Asia collide?, *J. Geophys. Res.*, *112*, B05423, doi: 10.1029/2006JB004706.

Garzanti, E., and T. Van Haver (1988), The Indus clastics: forearc basin sedimentation in the Ladakh Himalaya (India), *Sediment. Geol., 59*, 237-249.

Hodges K. V. (2000), Tectonics of the Himalaya and southern Tibet from two perspectives, *Geol. Soc. Am. Bull., 112*, 324-350.

Kosler, J., H. Fonneland, P. Sylvester, M. Tubrett, and R.-B. Pedersen (2002), U-Pb dating of detrital zircons for sediment provenance studies – comparison

of laser ablation ICPMS and SIMS techniques, *Chem. Geol., 182,* 605-618.

Najman, Y., E. Appel, M. Boudagher-Fadel, P. Bown, A. Carter, E. Garzanti, L. Godin, J. Han, U. Liebke, G. Oliver, R. Parrish, and G. Vezzoli (2010), Timing of India-Asia collision: Geological, biostratigrphic and palaeomagnetic constraints, *J. Geophys. Res.*, *115*, B12416, doi:10.1029/2010JB007673.

Raymo, M. E., and W. F. Ruddimann (1992), Tectonic forcing of late Cenozoic climate, *Nature, 359*, 117-122.

Rowley, D. B. (1996), Age of initiation of collision between India and Asia: A review of stratigraphic data, *Earth Planet. Sci. Lett., 145*, 1-13.

Ruhl, K. W., and K. V. Hodges (2005), The use of detrital mineral cooling ages to evaluate steady-state assumptions in active orogens: An example from the central Nepalese Himalaya, *Tectonics, 24,* TC4015.

Schlup, M., A. Carter, M. Cosco, and A. Steck (2003), Exhumation history of eastern Ladakh revealed by $^{40}Ar/^{39}Ar$ and fission-track ages: the Indus River – Tso Morari transect, NW Himalaya, *J. Geol. Soc.*, 160, 385-399.

Steck, A. (2003), Geology of the NW Indian Himalaya, *Eclogae Geol. Helv.*, 96, 147-196.

Stock, J. D. and D. R. Montgomery (1996), Estimating paleorelief from detrital mineral age ranges, *Basin Res.,* 8*,* 317-327.

Wang, J.-G., X.-M. Hu, F.-Y. Wu, and L. Jansa (2010), Provenance of the Liuqu Conglomerate in southern Tibet: A Paleogene erosional record of the Himalayan-Tibetan orogen, *Sediment. Geol., 231*, 74-84.

Yin, A. (2006), Cenozoic tectonic evolution of the Himalayan orogen as constrained by along-strike variation of structural geometry, exhumation history and foreland sedimentation, *Earth-Sci. Rev., 76*, 1-131.

Yin, A. and T. M. Harrison (2000), Geologic evolution of the Himalayan-Tibetan Orogen, *Ann. Rev. of Earth and Planet. Sci., 28,* 211-280.

## 4. Figure captions

Figure 1.1. Geologic map of the northwestern Himalaya, after *Hodges* [2000], *Schlup et al.* [2003], and *Steck* [2003]. Inset after *Sinclair and Jaffey* [2001]. The extent the Indus Basin studied in the following chapters is boxed and labeled. ITSZ – Indus-Tsangpo suture zone; GCT – Great Counter Thrust; KFZ – Karakoram fault zone; MBT – Main Boundary Thrust; MCT – Main Central Thrust; MFT – Main Front Thrust; SSZ – Shyok suture zone; STFS – South Tibetan fault system.

Figure 1.1.

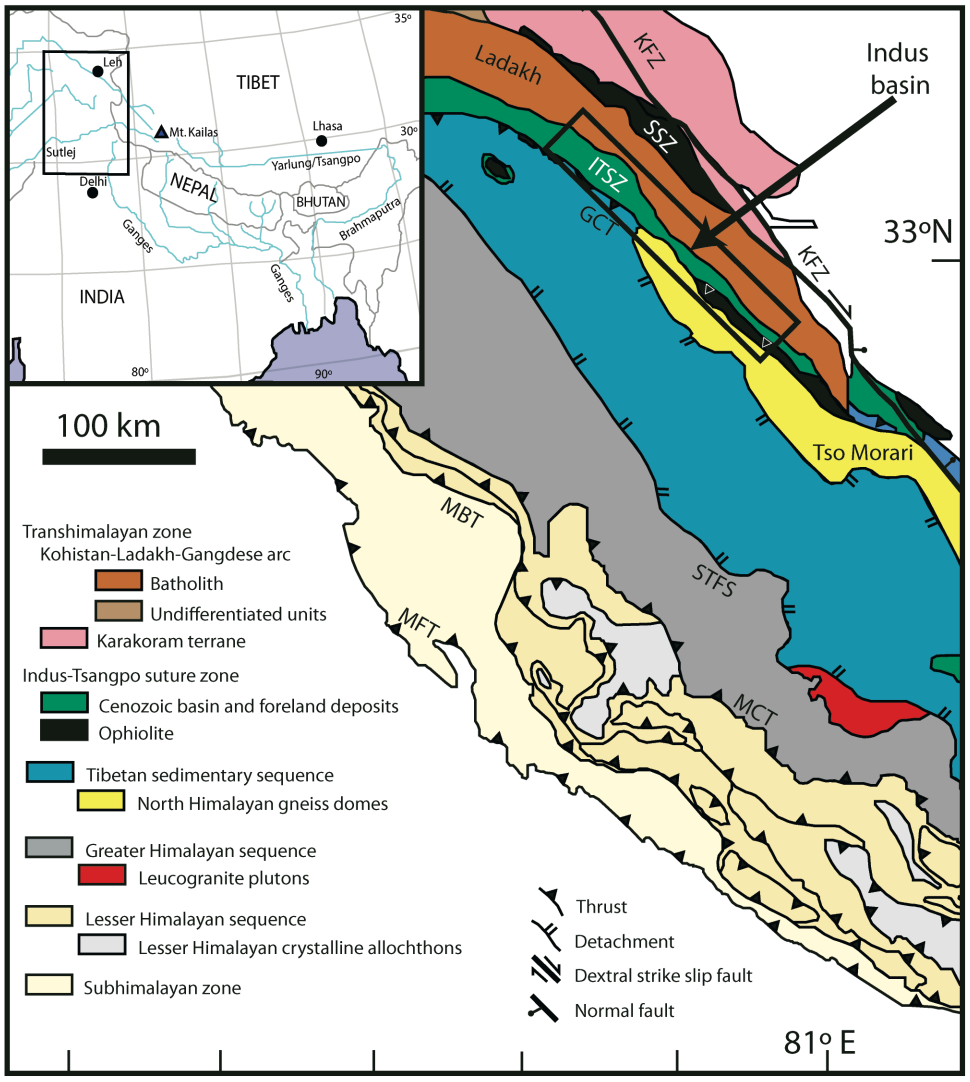
Ladakh
KFZ
Indus
basin
SSZ
ITSZ
GCT
33°N
KFZ
Tso Morari
MBT
STFS
MFT
MCT
81° E
100 km
TIBET
Leh
Mt. Kailas
Lhasa
Sutlej
Delhi
NEPAL
BHUTAN
Yarlung/Tsangpo
Ganges
Brahmaputra
INDIA
35°
30°
80°
90°
Transhimalayan zone
Kohistan-Ladakh-Gangdese arc
Batholith
Undifferentiated units
Karakoram terrane
Indus-Tsangpo suture zone
Cenozoic basin and foreland deposits
Ophiolite
Tibetan sedimentary sequence
North Himalayan gneiss domes
Greater Himalayan sequence
Leucogranite plutons
Lesser Himalayan sequence
Lesser Himalayan crystalline allochthons
Subhimalayan zone
Thrust
Detachment
Dextral strike slip fault
Normal fault

# CHAPTER 2

# LITHOLOGIC MAPPING OF COMPLEXLY DEFORMED SEDIMENTARY STRATA USING ASTER MULTISPECTRAL IMAGERY: IMPLICATIONS FOR THE EVOLUTION OF THE INDUS BASIN DEPOCENTERS, LADAKH, NW INDIA


## ABSTRACT

The Indus Basin, located in the northwestern Indian Himalaya, is of particular importance to understanding the history of the Himalayan-Tibetan orogen because it records the early Cenozoic history of the orogenic system that has since been eroded and modified by post-Oligocene deformation. Unfortunately, these strata have been variably mapped by previous workers because of the inaccessibility of most lithologic contacts due to rugged terrane, the deformation of the region caused by basin inversion, and the relative monotony of lithology. To examine these otherwise inaccessible contacts, we used Advanced Spaceborne Thermal Emission and Reflection Radiometer (ASTER) data to map the lithologic variation within the Indus Basin. Specifically, we used the visible-near infrared imagery to assess the apparent color changes of the rocks. We then applied several masks to the full dataset to generate images focused on lithologic variability using all wavelengths. We used these images to generate a regional-scale geologic map that is not only internally consistent, but also one that is permissible based on external datasets, including a compilation of depositional age constraints and sedimentary petrography. Furthermore, we demonstrate that the stratigraphy is far simpler than previous studies suggest,

which eliminates the need for complex changes between marine and terretiral depositional environments. This allows for identification of discrete depocenters within the terrestrial strata that likely record different aspects of collisional orogenesis, particularly the timing of collision and early erosional history of the orogen.

**1. Introduction**

Much of the modern tectonic architecture of the Himalaya was established over the past 20 million years [e.g., *Hodges*, 2000], and it should come as no surprise that our best understanding of the Himalayan orogenic processes pertain to that timeframe. However, the earliest stages of India-Eurasia collision appear to have begun at least thirty million years earlier [*Rowley,* 1996] and an increasing number of researchers are turning their attention to explorations of Eocene-Early Miocene (55-20 Ma) Himalayan tectonics. An important record of these early Himalayan tectonic events is preserved within the Indus-Tsangpo suture zone (ITSZ) of southern Tibet and adjacent regions of NW India [e.g., *Rowley*, 1996; *Searle et al.,* 1997; *Aitchison et al.*, 2002*; DeCelles et al*., 2011], wherein isolated sedimentary basins record the transition from the precollisional Andean-style subduction along the Eurasian margin to the dynamic steady state in which the orogen has persisted since Miocene time [*Hodges*, 2006]. The dating, correlation, and sedimentologic interpretation of stratigraphy in these basins are thus important for developing a rich understanding of the collisional processes. Unfortunately, because of the paucity of age-diagnostic fossils and tuffaceous horizons, age constraints remain poor in these strata. In the best-dated basins,

geochronologic evidence suggests Cretaceous (~65 Ma) or Oligocene to Miocene ages (~25-22 Ma) [*Wang et al.*, 2010; *DeCelles et al.*, 2011], but other basins have no known age constraints. Nevertheless, correlations have been attempted based upon lithologic similarities among basin fill deposits [e.g., *Aitchison et al.*, 2002], but these are speculative at best.

Even within a single basin, discrepancies exist among even the most detailed stratigraphic studies because: 1) the strata contain few obvious marker horizons; 2) many exposures occur in remote and inaccessible regions; 3) many exposures are highly deformed; and 4) complete undeformed sections that are optimal for stratigraphic characterization are rare. In this paper, we demonstrate how the analysis of high-resolution multispectral satellite imagery can be a tremendously useful tool that can provide a better understanding of the stratigraphy and depositional history of these basins.

We focused our study on the Indus Basin of Ladakh, India, which is one of the more extensive molasse basins in the ITSZ (Figure 2.1). Only a few transects across the basin are accessible by car or foot, and as a result, multiple published stratigraphic sections and geologic maps from this area are distinctively different (Figures 2.2 and 2.3). Instead of focusing on the more traditional outcrop-scale methods of correlating sedimentary units across >100 km that have been applied in numerous studies of this region, we used multispectral imagery, specifically Advanced Spaceborne Thermal Emission and Reflection Radiometer (ASTER) data, to create a comprehensive map of regional-scale lithologic variations in the Indus Basin. We substantiated the map not only with fieldwork, but also with a

comparison of predicted stratigraphic correlations and patterns of variation in sedimentary petrography and detrital mineral age populations across the region. This has yielded the most extensive regional-scale geolgic map in the Indus Basin that is not only interally consistent, but also consistent with published and additional depositional age constraints and sedimentary petrography. However, it is distinctively different from many previously published maps in that we resolve the issue of multiple transitions between marine and terrestrial depositional environments. Moreover, this map permits us to resolve discrete depostional systems across the region, such that we can discuss key locations for further study aimed at better constraining the timing of India-Eurasia collision and the early erosional history of the orogen.

**2. The Himalayan-Tibetan orogen**

Collision between India and Eurasia is commonly thought to have occurred during the Eocene along the ITSZ [e.g., *Najman et al.*, 2010]. Since the pioneering work of *Heim and Gansser* [1939] and *Le Fort* [1975], the Himalaya are frequently described in terms of six tectonostratigraphic packages (Figure 2.1).

The northernmost Eurasian component – the "Transhimalaya" – includes intrusive igneous units of the Mesozoic-early Cenozoic Kohistan-Ladakh-Gangdese system of batholiths and the country rocks into which they intrude. These units represent the remnants of an Andean-type continental arc developed along the southern margin of Eurasia prior to collision [*Honegger et al*., 1982].

The southernmost Indian components comprise four tectonostratigraphic packages – the Tibetan Sedimentary Sequence (TSS), the Greater Himalayan Sequence (GHS), the Lesser Himalayan Sequence (LHS), and the Subhimalaya, which all represent an orogenic wedge developed in Indian plate rocks during ongoing collisional orogenesis. The Neoproterozoic-Paleocene TSS preserves remnants of the precollisional Indian passive margin, and is bounded to the north by the Main Zanskar Backthrust (MZB) [*Searle,* 1986*; Yin,* 2006], and to the south by the South Tibetan fault system (STFS), an orogenic-scale normal fault system [*Burchfiel et al.,* 1992]. In the footwall of the STFS, the GHS consists of Proterozoic-Early Paleozoic metasedimentary rocks and magmatic rocks of both Miocene and Cambrian age [e.g., *Le Fort et al.,* 1987; *Miller et al.,* 2001]. The Miocene Main Central Thrust system (MCTS) separates the GHS from the structurally lower LHS, which comprises unmetamorphosed to lower amphibolite facies supracrustal rocks of Early Proterozoic to Miocene age [*DeCelles et al.,* 2001]. The LHS is bounded to the south by the Middle Miocene-Pliocene Main Boundary Thrust system (MBT), which separates it from the Middle Miocene to Pliocene rocks of the Subhimalaya [*DeCelles et al.,* 2001]. The Subhimalaya similarly overthrusts the modern-day foreland basin along the Pliocene-Holocene Main Frontal Thrust system [*Yeats et al.*, 1992].

The Indian and Eurasian elements of the Himalaya are separated by the ITSZ, which is a narrow, structurally complex region that includes disaggregated exposures of ophiolites, precollisional forearc basin strata, and the syn- to post-collisional Cenozoic intermontane molasse basins [*Gansser*, 1980]. Our research

focused on the Indus Basin, which is one of the larger, more accessible, and better exposed of these preserved molasse basins.

## 3. The Indus Basin

The Indus Basin, located in the Ladakh region of northwest India, is perhaps the most studied, yet least understood, of these intermontane basins. It has been recognized as potentially one of the most important of these successions for understanding the timing of collision [*Rowley,* 1996]. Preserved strata in the basin demonstrate the emergence and erosion of both sides of the orogen, with the majority of detritus interpreted as Eurasian [*Henderson et al.,* 2011], but some Indian-plate detritus sourced from the TSS, which contains evidence for the pre-Oligocene exhumation of the Indian passive margin (Chapter 3) [*Tripathy et al.,* in review].

### 3.1. Available datasets

The datasets available thus far include several transects through the steeply-dipping to near-vertical strata. The number of transects has increased due to relaxed military restrictions to disputed border regions, but the number of vehicle accessible transects has only increased from three to four. Thus, access to multiple transects in the field is still significantly limited.

Regarding age constraints, the biostratigraphy of the succession has been refined substantially since the pioneering work of *Garzanti and Van Haver* [1988] by *Bajpai et al.* [2004] and *Henderson et al.* [2010]. These findings have been supplemented with detrital mineral U-Pb geochronology and $^{40}Ar/^{39}Ar$ thermochronology [*Wu et al*., 2007; *Henderson et al.,* 2010, 2011; this study].

However, the lack of minerals suitable for $^{40}Ar/^{39}Ar$ thermochronology in all but the youngest strata restrict the utilization of this method. Moreover, when both chronometers are applied to the same sample, a significant difference between the youngest zircon U-Pb date versus the youngest muscovite $^{40}Ar/^{39}Ar$ date is often observed [*Henderson et al*., 2010], implying that the U-Pb data provide only a very loose constraint on the maximum depositional age.

The sedimentary petrography of the Indus Basin elucidates the change in provenance over time, which directly influences paleogeographic interpretations, yet, in some cases, different applications of this technique have led to inconsistent results [*Brookfield and Andrews-Speed,* 1984; *Henderson et al.,* 2010; 2011]. In particular, earlier studies suggest input from both Indian and Eurasian source regions, whereas more recent studies imply only Eurasian sources. Coupled with stratigraphic studies, these conflicting interpretations yield a variety of different suggestions for depositional environments (Figure 2.2). As a result, there is little consensus regarding both the depositional history of the Indus Basin rocks and the erosional history of the purported source regions.

The Zanskar Gorge section (Figures 2.3 and 2.4) is the most structurally complex transect through the Indus Basin, yet has become regarded as the "type section" for two reasons. First, it is the most easily accessible transect by road. Second, the Nummulitic Limestone, a rare yet important marker bed within the Indus Basin, is exposed here. In fact, the Nummulitic Limestone has only been described in detail here and in one other section, beneath the Spontang ophiolite some 40 km to the west [*Searle et al.,* 1997; *Green et al.,* 2008]. Though the

Zanskar Gorge has been the focus of several studies, the mapping through this section varies significantly from one published map to another. By way of illustration, we show the various map interpretations of the Zanskar Gorge by *Garzanti and Van Haver* [1988], *Clift et al.* [2002], and *Henderson et al*. [2010] in Figure 2.3. The differences highlight the variability of interpretation that is permitted by such complexly deformed, lithologically monotonous strata.

**3.2. Conflicting stratigraphic nomenclature in the Indus Basin**

In addition to variable maps, multiple interpretations of the stratigraphy and associated depositional environment have also been presented (Figure 2.2). These discrepancies reflect correlation challenges associated with laterally variable lithofacies within a single depositional system, a common characteristic of continental molasse basins. In light of the difficulty of following any single contact along strike because of the rugged terrain in this region, major differences in stratigraphic interpretations come as no surprise. The problem is exacerbated by the fact that early workers [e.g., *Brookfield and Andrews-Speed,* 1984] defined much of their stratigraphy along transects other than the Zanskar Gorge, and these original stratigraphic frameworks have been variably extrapolated in more recent studies. Different perspectives have resulted in confusing stratigraphic inconsistencies, such as the fact that the Tar Formation of *Garzanti and Van Haver* [1988] is very different in both definition and mapped location from the Tar Group of *Sinclair and Jaffey* [2001].

Below we demonstrate that remote sensing data, which permit a broader analysis of the stratigraphy than is possible from ground-based studies alone, are

suggestive of a relatively simple Indus Basin "macrostratigraphy" that can be interpolated between accessible transects and extrapolated beyond them.

### 3.3. ASTER-based stratigraphy

For clarity, we first provide our informal stratigraphy for the Indus Basin sedimentary rocks, and go on to demonstrate how it was built and verified throughout the remainder of this paper. We follow Figure 2.2, which is a comparison between our own stratigraphic framework and those derived from previously published studies. We did not extract stratigraphic sections directly from previous work, but rather, we examined each previously published map and associated field descriptions, and determined how each of these published units corresponds to our stratigraphic framework. As a consequence, not all previously published lithologic units are shown in Figure 2.2a because they do not correspond to any part of the Zanskar Gorge stratigraphy. We also include appropriate correlations to strata along the Leh-Manali road section to the east (Figures 2.2b, 2.4), which includes some, but not all, of the same stratigraphic units. Figure 2.2 also lists the interpreted depositional environments where explicitly stated by previous authors.

#### 3.3.1. Southern Zone: The Chilling Group

This unit comprises several complexly intermingled, yet mappable, lithologies that we group together for simplicity. Bounded to the south by the Main Zanskar Backthrust, the Chilling Group principally comprises elongate pods of ophiolite, ophiolitic mélange, coherent forearc strata, and limestone. Age

constraints are poor, but previous authors have described this section as Maastrichtian-Eocene (*ca.* 70-34 Ma) in age [e.g., *Searle et al.,* 1997].

### 3.3.2. Northern Zone: Ladakh batholith

North of the Indus Basin sedimentary strata lies the Ladakh batholith, onto which the Indus Group has been thrust. Comprised of calc-alkaline plutonic rocks, predominantly granite and granodiorite, U-Pb zircon ages, interpreted as crystallization ages, range from Early Cretaceous to Lutetian (*ca.* 48-40 Ma) [*Honegger et al,* 1982; *St. Onge et al*., 2010].

### 3.3.3. Tar Group

The Tar Group includes all marine strata exposed between the Chilling Group and the first continental clastic stratum of the Lower Indus Group. In general, the lithologies of the Tar Group include shales, sandstones and limestones, with black limestones dominating the upper parts of the unit. The top of the Tar Group comprises black fossiliferous limestones of the Sumda Formation as well as a Nummulitic Limestone that has been mapped explicitly by some research groups [e.g*., Searle et al.,* 1990; *Clift et al.,* 2002; *Henderson et al.,* 2010]. These carbonate units interfinger with overlying continental clastic rocks. Along the Leh-Manali road transect (Figure 2.4), the Tar Group forms the core of a syncline, upon which continentally derived strata lie, as observed by *Brookfield and Andrews-Speed* [1984].

The Tar Group can be subdivided into the Nindam forearc rocks [e.g., *Fuchs*, 1984; *Clift et al.*, 2002], the Ypresian (*ca.* 55-49 Ma) Jurutze Formation [*Henderson et al.,* 2010], and the upper Ypresian Sumda Formation and

Nummulitic Limestone [*Henderson et al.,* 2010]. As with the Chilling Group, there is little consensus regarding the most appropriate subdivisions, and our stratigraphy most closely follows that of *Sinclair and Jaffey* [2001]. In Figure 2.4, we do not subdivide the Tar Group because the nature of the contacts among many Tar Group units has not been studied in detail.

### 3.3.4. Lower Indus Group

We interpreted the Lower Indus Group as a combination of several units mapped separately by previous researchers, and subdivided it into two formations. The stratigraphically lowest of these, the Chogdo Formation, conformably overlies the Tar Group, and consists of cyclical packages of red shale and green sandstone. Conglomeratic horizons increase toward the top of the section such that the uppermost coarse-grained unit is the cobble-boulder conglomerate that is commonly referred to as the Choksti Conglomerate [*Henderson et al.*, 2010]. The Chogdo Formation is bounded to the north by a major backthrust structure that is potentially the Choksti Thrust of *Sinclair and Jaffey* [2001]. It is cut by at least one additional backthrust, which may account for the dramatic change in outcrop thickness in the Zanskar Gorge, as compared to easterly exposures. The depositional age for Chogdo rocks most likely ranges from upper Ypresian to Lutetian (*ca.* 50-40 Ma) [*Wu et al*., 2007; *Henderson et al.,* 2010]. From Figure 2.2, it is evident that our interpretation for the Chogdo Formation is the most significant departure that we make from the previous work in this region.

The second unit, the Stok Kangri Formation of *Fuchs* [1984] and *Brookfield and Andrews-Speed* [1984] (i.e., the Rong Formation of *Henderson et*

*al.* [2011]) is not continuous with the Chogdo Formation, but lies to the south of the Tar Group along the Leh-Manali road. In detail, subtle differences exist between the Stok Kangri Formation and the Chogdo Formation [*Henderson et al.*, 2011], but we nevertheless consider it likely that the Stok Kangri Formation is time correlative with parts of the Chogdo Formation. To the south, the Stok Kangri Formation overthrusts the Chilling Group, whereas to the north, the Stok Kangri Formation and the Tar Group have an angularly discordant contact relationship [*Henderson et al.*, 2011]. Because of significant snow cover in the ASTER imagery, we cannot characterize this formation in detail using remote sensing techniques. Instead, we discuss these strata in terms of geochronology, sedimentary petrography and contact relationships.

### 3.3.5. Upper Indus Group

The Upper Indus Group can be subdivided into three major sections, two of which are present in the Zanskar Gorge. The Choksti Formation, which is better exposed to the east of the Zanskar Gorge, is likely Middle Eocene (Lutetian, *ca.* 45 Ma) or younger in age [*Wu et al.*, 2007], and is in thrust contact with the underlying Lower Indus Group. Choksti rocks comprise mostly black shales and sandstones, with subordinate red and green shales and cobble conglomerates toward the top of the section. However, east of the Zanskar Gorge, this unit is significantly more conglomeratic.

The Hemis Formation, not exposed in the Zanskar Gorge section, is present along the Leh-Manali road transect. The type locality, at Hemis Gompa, preserves cyclical sandstone and conglomerate packages, with these

conglomerates containing abundant clasts derived from the Ladakh batholith. Its maximum age of deposition is Late Eocene (Priabonian, *ca.* 34 Ma; this study).

The Nimu Formation, which is mainly exposed in the Zanskar Gorge, comprises mostly black shales that contain plant remains, gray sandstones, and occasional cobble conglomerates. The Nimu Formation is separated from the Choksti Formation by an angular discordance, which we interpret as a fault. The Nimu Formation could be as old as Middle Eocene (*ca.* 41 Ma) at its base [*Wu et al*., 2007], but is clearly as young as Early Oligocene (Rupelian, *ca.* 30 Ma) toward the top of the section (this study).

### 3.3.6. Basgo Group

The Basgo Group includes both the Basgo Formation and the conformably overlying Temesgam Formation. The Basgo Formation is highly calcareous in comparison to the other molasse units, and contains distinct mustard colored sandstones. Ostracods are present in green-red calcareous shale and fine-grained sandstone sequences, and have been dated as Late Oligocene (*ca*. 28-23 Ma) [*Bajpai et al.,* 2004]. The conformably overlying Temesgam Formation, which is exposed north of the Zanskar Gorge, contains gray-yellow sandstones and blue-gray shales, with the occasional very fine-grained red horizon. In fault contact with the Nimu Formation, the Temesgam is as young as Miocene (*ca.* 19 Ma) toward the top of the section [*Henderson et al*., 2010]. The Basgo Group has been thrust over the Ladakh batholith, and the fault is exposed west of Likir.

## 4. Lithologic mapping with ASTER data

The stratigraphy described in the previous section was built differently from previous stratigraphies of the Indus Basin in that it represents mappable units that are easily distinguished using remote sensing data. Sensor systems on multispectral imaging satellites have advanced significantly over the last two decades, and the data products are commonly used to map mineral abundances in places such as the Moon and Mars, where few other means exist to quantitatively examine the geologic history. For Earth, there is a wealth of literature involving data from the Landsat program, active since 1972, such that remote sensing textbooks are written in the context of Landsat-based studies [e.g., *Sabins,* 1997].

The ASTER instrument, deployed in 1999 on the Terra satellite, offers improvement in the resolution of multispectral data for Earth, with 14 bands collected from three radiometers – the visible-near infrared (VNIR), short-wave infrared (SWIR) and thermal infrared (TIR) instruments (Table 2.1). These data are used to demonstrate changes in lithology and mineral abundances [e.g., *Rowan and Mars,* 2003; *Vaughan et al.*, 2005], and have been used in the Himalaya to map gneiss domes [*Watts et al.,* 2005], granite bodies in extremely variable topography [*Bertoldi et al*., 2011], and ophiolites along the ITSZ [*Corrie et al.,* 2010]. In this section, we first discuss processing methods used to create ASTER data products that maximize the information obtained from this multispectral dataset. We then use our resulting images to build the stratigraphic framework described above for the Indus Basin rocks. We discuss the general outline gleaned from the visible imagery (Figures 4 and 5a), describe the use of

TIR mapping of masked images to elucidate changes in mineralogy (Figure 2.5b), and perform principal component analysis (PCA) of the full dataset to highlight changes in both composition and structure (Figure 2.5c). At the end of this section, we corroborate our interpretations by comparing TIR spectra of different parts of the ASTER image to verify likeness of lithologies (Figures 2.6 and 2.7).

### 4.1. Processing ASTER data

#### 4.1.1. Data acquisition

We retrieved the ASTER Level 1B data products for scenes that minimize cloud and snow cover in order to reveal the maximum amount of surface, and, therefore, geology, as possible. Because we use SWIR data to identify and mask vegetation and ice/snow, we require data collected prior to April 2008 because high SWIR detector temperature has rendered recently collected ASTER SWIR data unusable. ASTER L1B data products are processed using *Davinci*, a free remote sensing image processing software developed at Arizona State University (http://davinci.asu.edu).

#### 4.1.2. Visible imagery

Because of the aridity and associated lack of vegetation of the Ladakh region, significant information can be acquired from only the visible imagery. These data formed the basis for our preliminary regional geologic map of the Indus Basin. We present in Figure 2.4 a mosaic of nine false color ASTER images (RGB images with VNIR bands 3, 2, and 1, respectively, where vegetation appears red due to the enhanced reflectivity in band 3) that show the lateral extent of the macrostratigraphic units described above, with further subdivisions of the

terrestrial Lower Indus, Upper Indus and Basgo Groups. The mosaic was created in Java Mission-planning and Analysis for Remote Sensing (JMARS) for Earth, which is an open-source Geographical Information System (GIS) system created at Arizona State University that is available to the general public (http://jmars.asu.edu). In Figure 5a, we focus on the scene that encompasses the Zanskar Gorge and surrounding areas because it allows comparison to the previously published maps depicted in Figure 2.3 and contains all major lithotectonic units, including those not exposed in the Zanskar Gorge transect.

### 4.1.3. Creating TIR decorrelation stretch images

An important application of TIR data is elucidating the mineralogy of the scene. In the rocks of the Indus Group, we utilized these data to differentiate not only between calcareous versus non-calcareous units, but also between various units that may have a different clast or matrix composition, which inherently implies a different source area than its neighboring rocks. We use TIR data to test our observations made from the visible imagery and further differentiate various strata. To visualize the variability in a given scene, we created a decorrelation stretch (DCS) image [*Gillespie et al.*, 1986], which is designed to highlight second- and third-order spectral variability in infrared data, rather than the first-order temperature differences that serve as a proxy for topography. To create this image, we follow the steps described below.

*Noise removal*

In order to exploit the full capability of the TIR bands from ASTER images, noise that is common to ASTER radiance data and infrared instruments in

general was removed using a specialized multi-wavelength line-to-line filter [*Nowicki and Christensen*, submitted].

*Masking*

Following the noise-removal process, we applied three data-exclusion masks that effectively remove unwanted pixels from the TIR data – pixels containing significant fractions of vegetation, snow, ice, water and clouds. The masking process plays an important role because it enhances the variability of pixels that are representative of the mineralogy of the exposed surface and not the spectral signature of the three excluded components.

To create these masks, all bands in each scene were first re-sampled to the same resolution as that of the 90m ASTER TIR data using a bilinear interpolation image-resampling algorithm. We masked vegetation, snow, ice, water, and clouds in different ways: 1) using the Normalized Difference Vegetation Index (NDVI) [*NASA Earth Observatory, earthobservatory.nasa.gov*] for vegetation; 2) snow, ice and water using the Normalized Difference Snow and Ice Index (NDSII) [*Xiao et al*., 2001]; and 3) clouds using the Cloud mask of *Cooper et al.* [in preparation], which uses ASTER band 1 to look for bright zones. For each of these masks, index values were carefully selected in order to maximize the elimination of pixels affected by any of these features.

*Temperature and Emissivity Separation*

The L1B data product provides information about the surface-emitted and solar-reflected radiance. However, in order to extract maximum information about spectral variability, the data must be converted to emissivity, which effectively

removes all temperature information from the scene, resulting in data that represent compositional variability [e.g., *Gillespie et al*., 1998]. No atmospheric correction was applied, as only relative differences in composition were of interest for the DCS image, and the paucity of clouds indicates a relatively uniform atmosphere.

*Creating the TIR Decorrelation Stretch Images*

To visualize compositional diversity in a radiance or emissivity image, a decorrelation stretch was applied to the masked scene, whereby the color differences found in three TIR bands were enhanced [see *Gillespie et al.,* 1986]. We use band combination 14-12-10 (or TIR 5-3-1) to maximize variability between different rock mineralogies. In this scheme, red pixels have high band 14 values, green pixels have high band 12 values, and blue pixels have high band 10 values. White areas have equal values in all three channels, whereas purple values are high in bands 14 and 10, green-blue are high in bands 12 and 10, and yellow pixels are high in bands 14 and 12.

To convert this to rock type/mineralogy, Figure 6, reproduced from *Ninomiya et al.* [2005]**,** shows the laboratory-determined emissivity spectra for common rock types with the ASTER TIR bands plotted at their appropriate wavelengths. Therefore, in a 14-12-10 image, a carbonate rock, which is strongly absorbing in band 14, will be strongly green-blue. A mafic rock does not have any strong absorption in these bands, and will be white. Felsic and quartz-rich rocks show strong absorptions at bands 12 and 10, and will show up as pink. However, quartz-rich rocks are not as strongly absorbing in band 10, and will therefore be

more purple than a felsic rock with less quartz, which will be more red. To further highlight these color differences, we performed a sampled stretch, whereby we applied the statistics of the region of interest to the entire scene, which enhanced the color variation for the mineralogies of interest (Figure 2.5b).

Care must be taken during interpretation of multiple scenes for which decorrelation stretches have been created because the color differences are specific to each individual scene, such that features of the same color in different scenes may be different lithologies. Therefore, we focus on the Zanskar Gorge scene and discuss the color changes from north to south within the stratigraphic framework of the visible imagery (Figure 2.5a), and lay out additional subdivisions that are apparent using only the TIR bands. Figure 2.5b is a sampled DCS of the Zanskar Gorge that shows our zones B1, B2 etc. that we use to highlight various features apparent in the image.

#### 4.1.4. Principal Component Analysis (PCA)

An additional use of multispectral data is PCA, which uses orthogonal data transformations to convert correlated variables into a set of components, or axes such that the first principle component has the maximum variance possible, and each subsequent component is both orthogonal to and has a decreasing amount of variance than the previous component [*Chavez and Kwarteng*, 1989]. In our analysis of the Zanskar Gorge region, all 14 bands were masked and collapsed into an 830x700x14 matrix, and 10 principle components were calculated, as any subsequent components were largely composed of random noise and eigenvalues that are several orders of magnitude lower than the first

several principle components. The first component was not useful because it highlighted any snow or ice that we were unable to fully mask. The tenth component shows the least variance and was also not useful. We focused only on features that were present in all intervening principle components images, and showed PCA component 5 (PCA5) because it maximizes the contrast of the persistent features, the most important of which are bounded by the yellow box (Figure 2.5c).

**4.2. ASTER image interpretation**

An examination of the different images in Figure 2.5 revealed patterns that permitted the classification of ten domains: the Chilling Formation to the south, the Ladakh batholith to the north, and eight distinctive domains within the Indus Basin sedimentary rocks. Each domain shows an overall NW-SE elongation parallel to the trace of the ITSZ, but not all are continuous throughout the study area. In some cases, domain boundaries truncate one another, suggestive of a fault relationship.

For each domain, we first describe the image analysis without any interpretation. All boundaries shown in Figure 2.5a are based solely upon color change in the VNIR bands that we inferred to imply change in lithology. In Figure 2.5b, we modified those boundaries when necessary, based upon the change in lithology that is directly represented by the color changes. Figure 2.5c corroborated several boundaries, and elucidated structural features that are not apparent in the previous two images.

Then, for each domain, we evaluated our image analysis in the context of fieldwork, which we supplemented in places with emissivity spectra extracted from atmospherically corrected emissivity data (Figure 2.7). This evaluation includes interpretation of the boundaries between each domain. Based on this discussion, we present our geologic map in Figure 2.8. The domain numbers correspond to those listed in Figures 2.4, 2.5a and 2.8, and we discuss them in numerical order. Zone numbers correspond to Figure 2.5b. Uninterpreted images for Figure 2.5 are available in Supplementary Material Appendix A.

#### 4.2.1. Domain 1 (zone B1)

*Description*

Domain 1, exposed near the village of Chilling, is distinctive in both the VNIR and TIR images because of the multitude of apparent lithologies. In Figure 2.5a, it includes lozenge-shaped black features, and elongated red and white units. The black features indicate mafic compositions when coupled with their white color in the TIR DCS image (zone B1, Figure 2.5b). The remaining lithologies are more felsic and/or quartz-rich, based upon their emissivity characteristics, which is illustrated by orange and pink colors in the TIR DCS image (Figure 2.5b). The southern boundary of Domain 1 is not apparent in Figure 2.5a, but shows up clearly in the TIR DCS image as a boundary between the green-blue carbonate-rich SW corner of the image versus the felsic units included within this Domain (Figure 2.5b). The northern boundary of Domain 1 is based upon Figure 2.5a, where the contact is a distinct color change from dark Domain 1 strata to significantly lighter Domain 2 rocks.

*Interpretation*

In the field, Domain 1 comprises multiple lithologies. The mafic pod exposed west of Chilling village is ophiolitic, and so we used this as a ground-truthed area with which to compare other mafic pods. In fact, the spectral signatures among the Chilling ophiolites and the other pods shown (zone B1) have similar slopes between ASTER bands and absorption features at each band, implying that they are similar mafic lithologies. The felsic strata surrounding these ophiolitic bodies have been described and interpreted in such varying detail by different authors [e.g., *Fuchs*, 1984; *Clift et al.*, 2002; *Henderson et al*., 2011] that we made no attempt to interpret the nature of these individual mappable units. Rather, the entirety of Domain 1 is considered a complex amalgam of lithologies that is likely correlative to ophiolites and ophiolitic mélange zones that are present along strike to both the east and west of this area [e.g., *Robertson and Dengan,* 1994]. Hereafter, we refer to Domain 1 as the Chilling Formation. As shown in Figure 2.8, we observe that the TSS to the south has been backthrust over the Chilling Formation, and must be the Main Zanskar Backthrust, as defined by *Searle et al*. [1997].

**4.2.2. Domain 2 (zones B2-B4, B6)**

*Description*

Domain 2 is clearly differentiated in the VNIR image (Figure 2.5a), and comprises all light colored strata in the central part of the Zanskar Gorge. However, based solely upon the VNIR image, further subdivision is not apparent. From the TIR DCS image, zone B2 comprises a multicolored unit, implying a

mixture of lithologies at a scale that is finer than the 90m resolution ASTER TIR data. In Figure 2.5b, a thin white layer, exposed to the east in a river valley, bounds zone B2 to the north. Upon further examination of Figure 2.5a, a thin dark layer is present that we interpreted as a sliver of mafic material located at the northern boundary of zone B2. However, we could not follow this boundary beyond the Zanskar Gorge region.

North of zone B2 lies zone B3, another multicolored unit. It contains fewer green-blue (carbonate) pixels, and more pink (felsic) pixels in the TIR DCS image than zone B2, and comprises the eastern continuation of Domain 2 (Figure 2.5b).

Zone B4 in Figure 2.5b is an enigmatic unit. In the VNIR image of Figure 2.5a, it corresponds to Domain 2 and bears no resemblance to the overlying Domain 3. However, in the TIR DCS image of Figure 2.5b, it is indistinguishable from Domain 3 because of the shared pink-red color, which implies a felsic lithology.

Finally, zone B6 in the far west of Figure 2.5b is a distinct blue-green carbonate layer that apparently caps the remainder of Domain 2 (zones B2-B4), and interfingers with the overlying Domain 3 (zone B5). Furthermore, pods of similar lithology to sonze B6 are fully enclosed within Domain 3.

*Interpretation*

Domain 2 is best discussed in the context of zones B2 through B6 of Figure 2.5b, although it excludes zone B5. Zone B2 comprises forearc strata commonly referred to as the Nindam Formation [e.g., *Clift et al.*, 2002] (Figure

2.2). Zone B3 is interpreted as the Jurutze Formation, which records a transition from marginal marine to distal turbidites [*Brookfield and Andrews-Speed*, 1984] (Figure 2.2). This is supported by the combination of carbonate and felsic lithologies indicated by the TIR DCS image.

Above the Jurutze Formation lies zone B4, which could belong to either Domain 2 or Domain 3. In Figure 2.7, we present emissivity spectra from both zone B4 and Domain 3, which demonstrates that they are similar to one another. However is possible that zone B5 of Domain 3, which topographically caps zone B4, has eroded, and subsequently covered, the entire slope with felsic detritus, thus obscuring the true spectral signature of zone B4. This hypothesis requires fieldwork for verification. Thus, we tentatively assign zone B4 to Domain 2 based upon Figure 2.5a.

Finally, zone B6 comprises limestones of the Sumda Formation and the Nummulitic Limestone, which are clearly exposed in the Zanskar Gorge as near-vertical limestone beds. Counter to the common interpretation that the Sumda Formation and Nummulitic limestone are separate and represent a complicated depositional history due to intervening terrestrial clastic strata with the marine sequence (Figure 2.2), they appear to be continuous with one another. This is supported by their emissivity spectra, which are equivalent (Figure 2.7). Furthermore, we interpreted the limestone pods that are fully enclosed within Domain 3 to be part of zone B6 as well, which implies that the boundary between Domains 2 and 3 is complexly deformed. One pod in particular is peculiar, in that it is an apparent dome of zone B6 that is cored by distinctly felsic pixels (Figures

2.5b and 2.8), and will be discussed during the interpretation of Domain 3. However, based upon our interpretation, all marine limestones of the Indus Basin are located stratigraphically below Domain 3, and are collectively referred to as the Tar Group.

### 4.2.3. Domain 3 (zones B5 and B7)

*Description*

Domain 3 contrasts sharply with its surrounding rock types in Figure 2.5a because its lithology is significantly redder in the VNIR image, and is generally distinctly pink-red (zone B5) in the TIR DCS image, implying significantly more felsic and/or quartz rich lithologies than the surrounding areas. There are two exceptions to this observation. One is the abovementioned limestone pods. The second is zone B7, which denotes the eastern continuation of Domain 3. It is not distinct in Figure 2.5b, and is a result of erosion of overlying carbonate strata of Domain 2 (zone B3) that mantles and obscures the characteristic TIR emissivity signature of Domain 3. This is apparent in Figure 2.5b, where large colluvial/alluvial features are clearly present. As such, Figure 2.5b is not useful for mapping the eastern extent of the boundary between Domains 2 and 3.

*Interpretation*

Domain 3 comprises the first appearance of continentally derived rocks in the Zanskar Gorge section, which we informally name the Chogdo Formation. Unlike many previous studies, we make no effort to further subdivide these strata. As a consequence, the Chogdo Formation combines the Chogdo Formation, Nurla Formation, Choksti Conglomerate and Red Shale Member of *Henderson et al*.

[2010]. It also includes the Gonmaru La and Artsa Formations of *Henderson et al.* [2011], exposed along the Leh-Manali road (Figure 2.2).

Where clearly exposed (Zanskar Gorge and Leh-Manali road transects, and near the village of Rumbak), the contact between the Chogdo Formation and the Tar Group (Sumda and Nummulitic limestones) is conformable, implying a transition between marine and deltaic depositional systems, as discussed by *Henderson et al*. [2010]. Along the Leh-Manali road, the Chogdo Formation forms the northern limb of the antiformal structure mentioned above.

Because of the isolated carbonate exposures within the Chogdo rocks located in and near the Zanskar Gorge, which is not characteristic of the rest of the unit, we infer complex folding of the Tar Group and the Chogdo Formation. Alternatively, the Chogdo Formation may contain minor carbonate lenses that are not present elsewhere. We infer the former to be more likely based upon the presence of fold axes observed along the Zanskar Gorge transect (Figure 2.8).

The most perplexing of these carbonate lenses is what appears to be a doubly plunging antiform along the Zanskar Gorge transect that is cored by rocks similar to the Chogdo Formation (Figures 2.5 and 2.8), as mentioned in the interpretation of Domain 2. We hypothesize that the core of this dome correlates to the pink pixels of zone B3, but recognize that an appropriate comparison of laboratory-derived spectra of hand samples from each area should be made in order to verify this suggestion.

Perhaps the most interesting observation regarding the Chogdo Formation is its relatively uninterrupted continuation between Chumathang and Rumback

that is apparent from Figure 2.4, spanning ~100 km. An interruption of the Chogdo Formation between Rumback and the Zanskar Gorge transect is only ~2 km long, and is located at the confluence of multiple rivers. As such, it is possible that the contact is simply obscured beneath alluvium. Because of its relative continuity over >120 km, the Chogdo Formation should be considered the most important marker bed within the Indus Basin.

#### 4.2.4. Domain 4

*Description*

In the ASTER image analyzed for the area immediately east of the Zanskar Gorge, there is significant snow cover that limits our capability to unambiguously identify and characterize units there. However, the image does show a clear transition from the light-colored Tar Group into darker rocks labeled as Domain 4 in Figure 2.5a.

*Interpretation*

Although obscured in the ASTER images of Figure 2.5, Domain 4 is well exposed along the Leh-Manali road, and has been mapped as the Stok Kangri Formation by *Brookfield and Andrews-Speed* [1984] and *Fuchs* [1984], as described in section 3.4.4.

Based on analysis of additional ASTER scenes, and corroborated by fieldwork, these rocks most likely represent the core of a large-scale synform exposed along this transect, as mapped by *Henderson et al*. [2011] (Figure 2.8). The southern contact, between the Stoki Kangri Formation and the Chilling Formation, is clearly a fault, originally mapped by *Fuchs* [1984]. We correlate

this fault with that which bounds the Chilling Formation in the Zanskar Gorge (Figure 2.8), which implies that the Stok Kangri Formation was not as laterally extensive as the Chogdo Formation. To the north, the Stok Kangri Formation forms the strata along the southern flank of the antiformal structure that is cored by the Tar Group along the Leh-Manali road. The contact is angularly discordant, but we could not differentiate whether this contact is faulted or depositional. However the simplest explanation is that the antiformal feature developed prior to deposition of the Stok Kangri Formation, thus explaining the angular discordance without the need for a fault.

#### 4.2.5. Domain 5 (zone B8)

*Description*

In Figure 2.5a, Domain 5, north of Domain 3, is distinctly lighter colored. Domain 5 is mostly exposed along the Leh-Manali road, where zone B8 comprises significantly more intermingled white and green-blue pixels than the surrounding felsic units, which implies more mixing of rock types (Figure 2.5b). Because these are sedimentary rocks, this likely denotes a more varied source region. In Figure 2.5c, the resolution of the PCA analysis of the ASTER data is sufficient to elucidate a major fold structure in Domain 5 that is not apparent in either the VNIR or TIR DCS images, and is highlighted by the yellow box.

*Interpretation*

The multicolored signature in the TIR DCS image (Figure 2.5b) of Domain 5 reflects that the majority of these strata comprise alternating pebble-cobble conglomerates and sandstones, with the conglomerates having a variety of

clast types. The southern contact of Domain 5 is a fault located between the Red Shale and Sandstone members of the Choksti Formation of *Henderson et al.* [2010] in the Zanskar Gorge, and an equivalent fault that separates the Artsa Formation from the Umlung Formation [*Henderson et al.,* 2011] along the Leh-Manali road transect. Because it includes the remainder of the Choksti Formation of *Henderson et al.* [2010], we informally named Domain 5 the Choksti Formation.

The Choksti Formation southern boundary fault can be traced along most of its length in Figure 2.5a, and west of the Zanskar Gorge its extent is inferred based upon an angular discordance apparent in the visible image (Figure 2.5a). This may be equivalent to the "Choksti Thrust" of *Sinclair and Jaffey* [2001].

The major fold present in the Choksti Formation (Figure 2.5c) is the only regional-scale fold structure that is distinctly apparent within strata north of the Chogdo Formation, although numerous km-scale tight folds are known to characterize much of the outcrop. Despite that degree of deformation, because we can discern a relatively simple macrostratigraphy, this implies that many of the large, tight folds visible in the field are actually intrafolial and do not repeat major stratigraphic units.

#### 4.2.6. Domain 6 (zone B9)

*Description*

Only present in the easternmost extent of this image, Domain 6 is nevertheless apparent not only as a color variation, but also as a change in strike

(Figure 2.5a). However, Domain 6 (zone B9) is not distinguishable from Domain 5 (zone B8) in the TIR DCS image (Figure 2.5b), implying similar source areas.

*Interpretation*

Exposed in the easternmost extent of Figure 2.5, Domain 6 is mapped strictly based upon an angular discordance in the visible imagery (Figure 2.5a). We trace this boundary to the Leh-Manali road, where we verified that it is a fault contact that has been mapped by *Henderson et al.* [2011], which separates their Umlung and Upshi Formations (Figures 2.2 and 2.8). Because these strata were originally named after their type locality near the Hemis Gompa, we name this unit the Hemis Formation. The northern contact of the Hemis Formation is inferred to be a fault, but is obscured beneath Indus River valley deposits except for a single exposure at Upshi, which is inaccessible due to military restrictions.

**4.2.7. Domain 7 (zone B10)**

*Description*

In Figure 5a, Domain 7 comprises all light colored strata north of Domains 3, 5 and 6. In the TIR DCS image, Domain 7 (zone B10) is more felsic than its surrounding units (Figure 2.5b), although much of its northern contact is obscured beneath the Indus River valley deposits (Figure 2.5a).

*Interpretation*

Exposed mostly in the Zanskar Gorge, Domain 7 correlates with the Lower Nimu Formation of *Henderson et al.,* [2010], and so we refer to it as the Nimu Formation. Its southern boundary with the Choksti Formation is observed as an angular discordance, but is not well exposed in the Zanskar Gorge, as

pointed out by *Henderson et al*. [2010]. We inferred that it is a fault contact based on age relationships that we will describe in subsequent sections. The northern contact of the Nimu Formation is exposed near Saspul, which we observed to be a fault contact (Figure 2.8). However, it is also mostly obscured beneath the alluvium of the Indus River valley.

### 4.2.8. Domain 8 (zone B11) and Domain 9 (zone B12)

*Domain 8 description*

Domain 8 lies north of the Indus River valley, and comprises light colored strata in the westernmost extent of Figure 2.5a. Both its southern and northern boundaries are apparent in Figure 2.5a as changes in color (southern boundary with Domain 9) and change in weathering pattern (northern boundary with Domain 10). In Figure 2.5b, the outcrop locations of Domain 8 (zone B11) are much more green than other parts of the image, which implies a carbonate-bearing lithology.

*Domain 9 description*

Domain 8 is south of and overlies Domain 9. Domain 9 is not significantly different in Figure 2.5a, although the contact is apparent upon close examination. However, in Figure 2.5b, zone B12 depicts significantly more orange strata than elsewhere, where these rocks outcrop, which implies a mixture between quartz-rich and carbonate lithologies at the sub-pixel scale.

*Interpretation of Domains 8 and 9*

We discuss these domains north of the Indus River and west of the Zanskar Gorge together because they form a single tectonostratigraphic package.

Domains 8 and 9 correspond to the Basgo and Temesgam Formations, respectively, as described by *Garzanti and Van Haver* [1988] and *Searle et al.* [1990]. We refer to them collectively as the Basgo Group.

They can be easily differentiated from the remainder of the Indus Basin rocks because of their distinctive alternating mustard and red colors at the outcrop scale, although the Basgo Group contains more green sandstones than the overlying Temesgam Formation. The contact between the Basgo and Temesgam Formations is conformable where observed in the field, but together, the Basgo Group comprises a single tilted package, over which the Nimu Formation has been thrust. The Basgo Group itself is emplaced over the Ladakh batholith by a north-directed backthrust.

**4.2.9. Domain 10 (zone B13-14)**

*Description*

In Figure 2.5a, Domain 10 clearly comprises rocks that are not sedimentary in nature, particularly due to the weathering pattern. In Figure 2.5b, this domain comprises significant mixing of various mineralogies (zone B13). However, all weathered material within catchments result in strongly red signatures in the TIR DCS image, which implies that these rocks are highly felsic compared to the surrounding lithologies (zone B14).

*Interpretation*

Domain 10 corresponds to the Ladakh batholith [*Honegger et al.,* 1982]. The boundary between the batholith and the Indus Basin sedimentary strata to the south is easily observed in the visible imagery because of the lack of layering in

the Ladakh batholith, as well as the dramatic change in weathering patterns between granites and granodiorites versus sandstones and shales (Figure 2.5a). Where the contact is observed, the Indus basin sedimentary strata are thrust northward over the Ladakh batholith (Figure 2.8), but the abundance of Ladakh batholith clasts in many of the Indus Group conglomerates suggests a primary unconformable relationship before thrust displacement.

## 5. Age constraints

In this section, we briefly summarize our muscovite $^{40}Ar/^{39}Ar$ thermochronology methods and data. We then synthesize all available age constraints from the Indus Basin, and place these data in the context of our units as defined by the ASTER image analysis.

### 5.1. Detrital muscovite $^{40}Ar/^{39}Ar$ thermochronology

#### 5.1.1. Methods

Three coarse-grained sandstone samples were analyzed for detrital muscovite $^{40}Ar/^{39}Ar$ thermochronology by the laser total fusion technique. Two samples, LM-K and LM-L, were collected from the Hemis Formation, and one sample, ZG-O, was collected from the Nimu Formation (Figure 2.8).

Muscovite grains were handpicked from the 120-250 μm aliquot and fast neutron irradiated at the McMaster University nuclear reactor, Hamilton, Ontario, Canada. Upon return, individual age standard and unknown grains were loaded into an aluminium palette and loaded into an ultra-high vacuum laser chamber. A 970 nm diode laser was employed to melt and degas each grain for 2 minutes with a 50 W 600 μm diameter beam.

The gases released by laser heating were first purified for 2 minutes using two SAES NP10 getter pumps, and then analyzed with a Nu Instruments *Noblesse* multi-collector mass spectrometer employing both a Faraday detector and an ion counting multiplier (depending on $^{40}Ar$ signal size). Faraday/ion counting detector intercalibration for $^{40}Ar$ was performed using the multiple aliquots air shots. Errors are quoted at the 2σ confidence level. For more a detailed description of our analytical methods, please see the Supplementary Material Appendix B.

### 5.1.2. Results

In Figure 2.9, the $^{40}Ar/^{39}Ar$ total fusion dates for each sample are plotted as probability density functions, which take into account the error associated with each measurement. We rejected any analysis with less than 90% radiogenic $^{40}Ar$ ($^{40}Ar^*$) yield, but still retain statistically robust datasets. Full data tables are reported in the Supplementary Material Appendix 3. Below, we discuss the results in the context of the stratigraphy.

## 5.2. Synthesis of age constraints in the Indus Basin

The ages of many of the macrostratigraphic units can be constrained by biostratigraphy [*Bajpai et al., 2004*; *Henderson et al.,* 2010] and isotope geochronology and thermochronology [*Wu et al.,* 2007; *Henderson et al.,* 2010, 2011; *Tripathy et al.,* in review (Chapter 3), this study]. We discuss these data in relative chronologic order, following our informal stratigraphic framework, listed in Figure 2.10. This description introduces the Lower and Upper Indus Groups, which are largely differentiated based upon their approximate depositional ages,

where the Lower Indus Group includes the Chogdo and Stok Kangri Formations, and the Upper Indus Group includes the Choksti, Hemis and Nimu Formations.

For the Upper Indus Group, detrital muscovite $^{40}Ar/^{39}Ar$ thermochronologic data not only provide information about the cooling history of the muscovite source region, but also provide a more robust maximum age of deposition than U-Pb dates because the Indus Basin rocks were not heated above 220°C [*Clift et al.,* 2002] after deposition, well below the bulk resetting temperature for the $^{40}Ar/^{39}Ar$ muscovite thermochronometer.

*Henderson et al.* [2010, 2011] presented many $^{40}Ar/^{39}Ar$ total fusion dates for detrital muscovites separated from several samples. These analyses have highly variable $^{40}Ar^*$ yields, some as low as 18%. Total fusion dating of materials by the $^{40}Ar/^{39}Ar$ method requires the correction of the total measured $^{40}Ar$ for atmospheric$^{40}Ar$. This correction has a much more significant effect on the calculated age when the $^{40}Ar^*$ yield is low, and thus dates characterized by $^{40}Ar^*$ yields higher than ca. 90% are more robust. In this paper, we present and interpret only those dates from *Henderson et al.* [2010, 2011] that fall into that category. As we show, the application of this criterion has a significant impact on the maximum age of deposition for many of their samples.

**5.2.1. Chilling Group**

Because of the disorderly nature of the various strata within this zone, the variety of maximum ages of deposition is not a surprise (Figure 2.10). We listed the age constrains by our estimation of stratigraphic level within this unit, but recognize that because of the complex contact relationships between various

lithologies, this is an approximation. The youngest lithology present in this zone (with a depositional age of <51.1 Ma, derived from U-Pb zircon data) appears in the Leh-Manali road section where *Henderson et al*. [2011] map it as their Lato Formation.

### 5.2.2. Tar Group

Detrital zircon U-Pb geochronologic samples in the Jurutze Formation of the Tar Group yield statistically indistinguishable maximum ages of deposition of 53.4±1.4 and 54.3±0.8 Ma for the Zanskar Gorge and Leh-Manali road transects, respectively [*Henderson, et al.,* 2010; 2011]. The ASTER imagery supports the conclusion of *Henderson et al.* [2011] that these are time-correlative parts of the same stratigraphic package.

In the Zanskar Gorge, a detrital zircon U-Pb geochronologic sample from the Nummulitic Limestone yields a maximum age of deposition of 52.5±0.7 Ma [*Henderson et al.,* 2010]. Additionally, *Henderson et al.* [2010] reported biostratigraphic ages of 54.9-51.0 Ma for their Sumda Formation, and 50.8-49.4 Ma for their Nummulitic Limestone. For the Sumda Formation, they report *Alveolina rotundata* (shallow benthic zone, SBZ8-9) in one sample, and *Nummulites atacicus* (SBZ8)*, N. planulatus* (SBZ10) and *Alveolina ellipsoidalis* (SBZ6) for another, which, together, are consistent with an Early Eocene age [*Serra-Kiel et al.,* 1998]. However *Henderson et al.* [2011] suggest that the fossil assemblage is largely reworked, and that the most likely depositional age is SBZ8 (Early Eocene). We consider it more likely that the youngest zone represented in this assemblage is closest to the depositional age of the unit. Therefore, the

depositional age should be that of SBZ10, or late Ypresian (*ca.* 50-48 Ma)**,** and we report this revised age range in Figure 2.10. For the Nummulitic Limestone, they report *Nummulites escheri* (SBZ11) and *Cuvillierina vanbellini*, which correspond to late Ypresian as well. We declined to assign numerical ages in Figure 2.10 because, as pointed out by *Gradstein et al.* [2004], shallow benthic zones are correlated such that there is room for subjective interpretation.

Based on our remote sensing analysis, we consider it likely that the Sumda Formation and the Nummulitic Limestone are not separate units, but rather different facies of the same unit. This correlation is permissible despite the biostratigraphic interpretations presented by Henderson and co-workers because the boundaries between shallow benthic zones are not constrained by Global Boundary Stratotype Section and Points, unlike the lower boundary of the Eocene [*Aubry et al.,* 2007]. Hence, we suggest that the entire Tar Group is Early Eocene (Ypresian, *ca.* 55-48 Ma).

### 5.2.3. Lower Indus Group

Detrital zircon U-Pb geochronologic samples from within the Chogdo Formation in the Zanskar Gorge yield maximum ages of deposition between 60±2 and 46.1±1.0 Ma [*Wu et al.,* 2007; *Henderson et al.,* 2010], which implies Paleocene-Middle Eocene depositional ages (Selandian-Lutetian, *ca.* 60-40 Ma). The Stok Kangri Formation has a maximum age of deposition of 48.4±1.4 Ma, and is therefore potentially time-correlative with at least the upper part of the Chogdo Formation that must be Lutetian or younger.

### 5.2.4. Choksti Formation of the Upper Indus Group

From the Upper Indus Group*, Wu et al.* [2007] present detrital U-Pb zircon data that yield a maximum age of deposition of 45±8 Ma (Lutetian). Although this youngest age has a significant error, the eight youngest grains cluster between 45-49 Ma, a range which we take as a robust estimate for the maximum age of deposition.

### 5.2.5. Hemis Formation of the Upper Indus Group

The Hemis Formation, exposed along the Leh-Manali Road transect, yields maximum ages of deposition from detrital muscovite $^{40}Ar/^{39}Ar$ thermochronology that range from 48.9±0.43 (sample LM-K) to 32.4±0.23 Ma (sample LM-L). While the oldest of these dates is permissive of some Hemis deposition as early as Ypresian time (*ca.* 50 Ma), we consider it most likely that the bulk of this unit was deposited between Late Eocene (Priabonian, <37 Ma) and Early Oligocene (Rupelian, >28 Ma) time (Figures 2.9 and 2.10).

### 5.2.6. Nimu Formation of the Upper Indus Group

For the Nimu Formation, the stratigraphically lowest sample has only been dated using detrital zircon U-Pb geochronology, and yields a maximum age of deposition of 41±0.6 Ma [*Wu et al.,* 2007]. The remaining samples constitute detrital muscovite $^{40}Ar/^{39}Ar$ dates, which provide a maximum age of deposition of 29.2±0.21 Ma (sample ZG-O). We infer a depositional age of Early Oligocene for most of this unit.

### 5.2.7. Basgo Group

To the west of the Zanskar Gorge, the Basgo Formation, originally interpreted as Maastrichtian (*ca.* 70-65 Ma) by *Garzanti and Van Hav*er [1988], has been revised to Late Oligocene (*ca.* 28-23 Ma) in age, based upon reexamination of ostracod fauna [*Bajpai et al.,* 2004]. A Late Oligocene age is supported by recently obtained detrital zircon (U-Th)/He thermochronologic data, which indicate an Early Oligocene (<29.63±1.13 Ma) maximum age of deposition (Figure 2.10) [*Tripathy et al*., submitted].

The base and top of the overlying Temesgam Formation yield detrital muscovite $^{40}Ar/^{39}Ar$ dates indicative of maximum depositional ages of 34.5±3.2 Ma and 19.1±1.0 Ma, respectively [*Henderson et al.,* 2010]. An additional constraint is that the Temesgam Formation must be younger than the underlying Late Oligocene Basgo Formation. Thus, we propose an Early Miocene age for the Temesgam Formation (*ca.* 19 Ma).

## 6. Provenance

Multiple studies employing a variety of methods have focused on the provenance of units within the Indus Basin. We present here a discussion of the currently available datasets related to provenance in the context of our new macrostratigraphic framework, focusing on both detrital mineral geochronology and the most recent petrographic work of *Henderson et al.* [2010, 2011].

In Figure 2.11, we replot the data of *Henderson et al.* [2010; 2011] using provenance discrimination diagrams based on quartz, feldspar and lithic compositions [*Dickinson and Suczek,* 1979], but do so in the context of our

stratigraphic framework for ease of comparison to the geochronologic and remote sensing data. We focus only on the sedimentary units of the Indus Basin.

### 6.1. Tar Group

The petrographic data of the Tar Group [*Henderson et al.,* 2010, 2011], which, based on our definition, includes all marine strata, tends to concentrate in the transitional arc field with outliers in both the undissected and dissected arc fields. This is reasonable for pre-collisional sands that have been sourced from an active arc that is in its incipient stage of unroofing. The detrital zircon U-Pb work presented in *Henderson et al.* [2010, 2011] corroborates this interpretation, as the data imply derivation from the Ladakh batholith, representing an active continental arc to the north.

### 6.2. Lower Indus Group

For the Chogdo Formation, the four petrographic samples [*Henderson et al.,* 2010, 2011] show an evolution from undisssected to dissected arc (Figure 2.11), such that the relative stratigraphic locations of the samples correlate with the degree of evidence of arc dissection. If this apparent evolution is real, the Chogdo Formation must be recording a significant portion of the syn- to post-collisional history of the Indus Basin sediments and associated source area. More sandstone petrography in these rocks is needed across the entire region to confirm this hypothesis.

Detrital zircon U-Pb data for the Chogdo and Stok Kangri Formations are very similar [*Henderson et al.,* 2010, 2011], and allow for our interpretation that the depositional ages for these units overlap. The provenance discrimination

diagram (Figure 2.11) suggests that the Stok Kangri Formation most likely correlates with the Chogdo Formation, further supporting our macrostratigraphic Lower Indus Group subdivision.

However, as noted by *Henderson et al.* [2011], the Stok Kangri Formation contains detrital muscovite whereas the Chogdo Formation does not. As a consequence, those researchers instead correlated the Stok Kangri Formation and their Umlung Formation (our Choksti Formation). Although their observation is significant, their preferred correlation is inconsistent with contact relationships expressed in the field. We regard the presence of muscovite in the Stok Kangri Formation as simply an indication of a variation in provenance.

### 6.3. Upper Indus Group

Samples from the Upper Indus Group plot within the dissected arc to basement uplift fields in Figure 2.11 [*Henderson et al*., 2010, 2011]. In particular, the lowermost Choksti Formation plots within the dissected arc field, whereas the younger, overlying Hemis Formation plots in both the dissected arc and basement uplift fields. The Nimu Formation plots in the basement uplift field, near the sample from the overlying Basgo Group (Temesgam Formation) [*Henderson et al*., 2010, 2011]. This evolution reflects an increased degree of dissection of the Ladakh arc over time, and is supported by the detrital zircon U-Pb data from *Wu et al*., [2007].

Probability density curves of our detrital muscovite $^{40}Ar/^{39}Ar$ samples demonstrate a distinct change in the source area over time (Figure 2.9). The base of the Hemis Formation (sample LM-K) contains detrital muscovite with

$^{40}Ar/^{39}Ar$ dates ranging from 49 to 87 Ma. In contrast, many muscovite dates from the upper part of the Hemis Formation are in the 35-40 Ma range (sample LM-L). A similar distribution of muscovite dates characterizes the Nimu Formation (sample ZG-O), implying that although the Hemis Formation may be older than the Nimu Formation, they may have had similar muscovite-bearing source areas. The difference in $^{40}Ar/^{39}Ar$ age distributions for the lower and upper parts of the Hemis Formation could suggest either completely different source areas, or, more likely, the progressive unroofing and exhumation of the muscovite-bearing source area.

**6.4. Basgo Group**

A single sample for the upper Temesgam Formation [*Henderson et al*., 2010, 2011] plots within the basement uplift field (Figure 2.11). Coupled with its Miocene $^{40}Ar/^{39}Ar$ muscovite maximum age of deposition (~19 Ma) [*Henderson et al*., 2010], these data support the interpretation that the Temesgam Formation is the youngest unit in the Indus Basin, and should, therefore, reflect the latter parts of the dissection of the Ladakh batholith.

However, the underlying Basgo Formation contains abundant evidence for mixed Indian-Asian provenance; the clasts in its conglomeratic horizons are clearly sourced from the Ladakh batholith [*Garzanti and Van Haver,* 1988], but the finer-grained sandstones in the sequence have detrital zircon U-Pb signatures indicative of derivation from the Tibetan Sedimentary sequence of the Indian plate [*Tripathy et al.,* in review; Chapter 3]. As the India-Eurasia collision continued into its Oligocene and Miocene phases (<33 Ma), the Indus Basin

recorded increasingly varied source areas. A wealth of information regarding the emergence of the north Indian margin during this process may be revealed in the course of future studies of Oligocene strata in the Indus Basin.

**7. Toward a simpler narrative of the history of the Indus Basin**

Our results resolve a significant paradox that arose from earlier studies regarding India-Eurasia collision as recorded in the Indus Basin. Traditionally, it was thought that the Tar Group recorded the latest stages of marine deposition and that the Indus Group recorded a transition to continental deposition in the Indus Basin [*Searle et al.,* 1990]. However, most recent papers [e.g., *Henderson et al*., 2010] place the unquestionably marine Nummulitic Limestone with the Lower Indus Group stratigraphy, requiring a foundering of the basin and at least a brief marine incursion. Our new stratigraphy eliminates the need for this incursion because the Nummulitic Limestone is placed entirely within the Tar Group succession and beneath all continentally derived molasse units in the Indus Basin.

We posit that multiple, discrete molassic units have been deposited since Eocene time into various depocenters within the Indus Basin. These different units/depocenters – the Lower Indus Group, the Choksti Formation, the Hemis Formation, the Nimu Formation, and the Basgo Group – record different parts of the history of the early evolution of the Himalayn-Tibetan orogen.

The Lower Indus Group is of particular importance because it likely contains the record of initiation of India-Eurasia collision, as well as the earliest history immediately after collision commenced. This is supported by the Early-Middle Eocene maximum ages of deposition for these strata, which imply that

these are the oldest terrestrial strata in the Indus Basin. The sandstone petrography of *Henderson et al.* [2010, 2011] further supports this interpretation because it hints at the potential for significant changes in the evolution of the source terrane after collision began.

In the Upper Indus Group, successively higher stratigraphic units record the progressive uplift and erosion of the Indian passive margin and the dissection of the Ladakh arc. The addition of muscovite, which is interpreted to be evidence of Indian-derived detritus [*Henderson et al.,* 2010], could represent evidence for diversification of the source area. However, it is unclear if all muscovite was, indeed, sourced from the Greater Himalayan sequence, as suggested by *Henderson et al.* [2010, 2011] because the specific source area for the 50-80 Ma muscovites is not known on the Indian margin. Muscovite is abundant within the Greater Himalayan sequence rocks, but those rocks only crop out today on the other side of the Himalayan range crest from the Indus Basin and all Greater Himalayan sequence muscovites yield Early Miocene or younger ages [*Clift et al*., 2008]. Hence, these rocks cannot be the source of the 50-80 Ma muscovites preserved in the Indus Basin. It is possible that the Indus Basin muscovite ages instead record Transhimalayan exhumation and erosion, and that today, there is very little of this muscovite-bearing part of the arc preserved. Thus, we interpret, these 50-80 Ma muscovite $^{40}Ar/^{39}Ar$ data to potentially reveal an important part of the history of the Eurasian plate that is no longer preserved. The units of the Upper Indus Group, which seem to record changes in provenance, should be the

focus of more detailed studies in the future to understand the potential co-evolution of these three depocenters.

Finally, the Basgo Group, which is known to contain coarse cobbles and boulders from the Ladakh batholith and fine-grained detritus from India [*Garzanti and Van Haver,* 1988; *Tripathy et al.,* submitted], should record the transition into the configuration of the orogen that has persisted from Miocene time to the present [*Hodges,* 2006].

*DeCelles et al*. [2011] suggested that Cenozoic intermontane basins of the ITSZ might have formed in an extensional, instead of contractional, environment. They examined the Kailas molasse basin east of our study area, and observed a fining upward sequence that resulted in a lacustrine sandwich, whereby after lacustrine environments existed and capped the intermontane basin lithologies, the depositional environment transitioned back to traditional intermontane basin red beds and sandstones. If any evidence of such an event exists in the Indus Basin rocks, it is likely to be found in either the Nimu Formation or the Temesgam Formation, both of which contain lacustrine sediments [*Searle et al.,* 1990]. The Upper Indus Group and Basgo Group should be the focus of studies that seek to understand the subsidence history of the Indus Basin, and the geodynamic implications of possible deposition in an extensional setting.

**8. Conclusions**

The Indus Basin contains Eocene to Miocene sedimentary rocks deposited during and after collision between India and Eurasia, and as such, records a wealth of information about the early evolution of the Himalayan-Tibetan

orogenic system. Although previous studies have been hampered by difficulties associated with accessing most exposures of the basin and tracing contacts along strike, we demonstrate that high-resolution multispectral ASTER imagery permits unit correlations between transects with high fidelity. Our result is a relatively simple macrostratigraphy of the Indus Basin that represents five discrete depocenters that young from south to north. The map and stratigraphy we present are simpler than earlier studies would suggest, yet they remain consistent with all existing chronostratigraphic and petrographic datasets. Finally, the simplifcation of the map units and stratigraphy allow for the eliminiation of complex changes in depositional history by placing all marine strata stratigraphically below the first appearnce of clastic, continentally-derived detritus.

**9. References**

Aitchison, J. C, A. M. Davis, Badengzhu, and H. Luo (2002), New constraints on the Indian-Asia collision: The lower Miocene Gangrinboche conglomerates, Yarlung Tsangpo suture zone, SE Tibet, *J. Asian Earth Sci., 21*, 253-265.

Aubry, M.-P., K. Ouda, C. Dupuis, W. A. Berggren, J. A. Van Couvering, and Members of the Working Group on the Paleocene/Eocene Boundary (2007), The Global Standard Stratotype-section and Point (GSSP) for the base of the Eocene Series in The Dababiya section (Egypt), *Episodes, 30,* 271-286.

Bajpai, S., R. C. Whatley, G. V. R. Prasad, and J. E. Whittaker (2004), An Oligocene non-marine ostracod fauna from the Basgo Formation (Ladakh Molasse), NW Himalaya, India, *J. Micropalaeontol., 23*, 3-9.

Bandfield, J. L., D. Rogers, M. D. Smith, and P. R. Christensen (2004), Atmospheric correction and surface spectral unit mapping using Thermal Emission Imaging System data, *J. Geophys. Res., 109*, 10.1029/2004JE002289.

Bertoldi, L., M. Massironi, Visona, R. Carosi, C. Montomoli, F. Gubert, G. Naletto, and M. G. Pelizzo (2011), Mapping the Buraburi granite in the Himalaya of Western Nepal: Remote sensing analysis in a collisional belt with vegetation cover and extreme variation of topography, *Remote Sens. Environ., 115*, 1129-1144.

Brookfield, M. E., and C. P. Andrews-Speed (1984), Sedimentology, petrography and tectonic significant of the shelf, flysch and molasse clastic deposits across the Indus suture zone, Ladakh NW India, *Sediment. Geol., 40*, 249-286.

Burchfiel, B. C., Z. Chen, K. V. Hodges, Y. Liu, L. H. Royden, C. Deng, and J. Xu (1992), The South Tibetan detachment system, Himalayan orogen: Extension contemporaneous with and parallel to shortening in a collisional mountain belt, *Spec. Pap. Geol. Soc. Am., 269,* 41 pp.

Chavez, P. S., and A. Y. Kwarteng (1989), Extractive spectral contrast in Landsat Thematic Mapper Image data using selective principal component analysis, *Photogramm. Eng. Remote Sens, 55,* 339-348.

Clift, P. D., N. Shimizu, G. Layne, and J. Blusztain (2001), Tracing patterns of unroofing in the Early Himalaya through microprobe Pb isotope analysis of detrital K-feldspars in the Indus Molasse, India, *Earth Planet. Sci. Lett., 188*, 475-491.

Clift, P. D., A. Carter, M. Krol, and E. Kirby (2002), Constraints on India-Eurasia collision in the Arabian Sea region taken from the Indus Group, Ladakh Himalaya, India, in *The Tectonic and Climatic Evolution of the Arabian Sea Region,* edited by P. D. Clift et al., *Geol. Soc. Spec. Publ., 195,* 97-116.

Clift, P. D., K. Hodges, D. Heslop, R. Hannigan, L. V. Hoang, and G. Calves (2008), Correlation of Himalayan exhumation rates and Asian monsoon intensity, *Nat. Geosci., 1*, doi:10.1038/ngeo1351.

Cooper, F. J., B. A. Adams, C. S. Edwards, and K. V. Hodges, Large-scale displacement on the South Tibetan fault system in the eastern Himalaya, *in preparation.*

Corrie, R. K., Y. Ninomiya, and J. C. Aitchison (2010), Applying Advanced Spaceborne Thermal Emission and Reflection Radiometer (ASTER) spectra indices for geological mapping and mineral identification on the Tibetan plateau, *Int. Arch. Photogramm., Remote Sens. Spat. Information Sci., XXXVIII*, 464-469.

DeCelles, P. G., D. M. Robinson, J. Quade, T. P. Ojha, C. N. Garzione, P. Copeland, and B. N. Upreti (2001), Stratigraphy, structure, and tectonic evolution of the Himalayan fold-thrust belt in western Nepal, *Tectonics, 20*, 487-509.

DeCelles, P. G., P. Kapp, J. Quade, and G. E. Gehrels (2011), Oligocene-Miocene Kailas basin, southwestern Tibet: Record of postcollisional upper-plate extension in the Indus-Yarlung suture zone, *Geol. Soc. Am. Bull., 123*, 1337-1362.

Dickinson, W. R., and C. A. Suczek (1979), Plate tectonics and sandstone compositions*, AAPG Bull., 63*, 2164-2182.

Fuchs, G. (1984), Note on the geology of the Markha-Nimaling Area in Ladakh (India), *Jahrb. Geol. Bundesanst., 127*, 5-12.

Gansser, A. (1980), The significance of the Himalayan suture zone, *Tectonophysics, 62*, 37-52.

Garzanti, E., and T. Van Haver (1988), The Indus clastics: forearc basin sedimentation in the Ladakh Himalaya (India), *Sediment. Geol., 59*, 237-249.

Gillespie, A. R., A. B. Kahle, and R. E. Walker (1986), Color enhancement of highly correlated images. I. Decorrelation and HSI contrast stretches, *Remote Sens. the Environ., 20*, 209-235.

Gillespie, A., S. Rokugawa, T. Matsunaga, J. S. Cothern, S. Hook, and A. B. Kahle (1998), A temperature and emissivity separation algorithm for Advanced Spaceborne Thermal Emission and Reflection Radiometer (ASTER) images, *IEEE Trans. Geosci. Remote Sens., 36*, 1113-1126.

Gradstein, F. M., J. G. Ogg, and A. G. Smith (2004), *A Geologic Time Scale,* 588 pp., Cambridge Univ. Press, Cambridge, U. K.

Green, O. R., M. P. Searle, R. I. Corfield, and R. M. Corfield (2008), Cretaceous-Tertiary carbonate platform evolution an the age of the India-Asia collision along the Ladakh Himalaya (Northwest India), *J. Geol., 116*, 331-353.

Heim, A., and A. Gansser (1939), Central Himalaya – Geological observations of Swiss expedition, 1936, *Mem. Soc. Helv. Sci. Nat., 73*, 1-245.

Henderson, A. L., Y. Najman, R. Parrish, M. BouDagher-Fadel, D. Barford, E. Garzanti, and S. Ando (2010), Geology of the Cenozoic Indus Basin sedimentary rocks: paleoenvironmental interpretation of sedimentation from the western Himalaya during the early phases of India-Eurasia collision, *Tectonics, 29,* TC6015, doi:10.1029/2009TC002651.

Henderson, A. L., Y. Najman, R. Parrish, D. F. Mark, and G. L. Foster (2011), Constraints to the timing of India-Eurasia collision; a re-evaluation of evidence from the Indus Basin sedimentary rocks of the Indus-Tsangpo Suture Zone, Ladakh, India, *Earth-Sci. Rev., 106*, 265-292.

Hodges K. V. (2000), Tectonics of the Himalaya and southern Tibet from two perspectives, *Geol. Soc. Am. Bull., 112*, 324-350.

Hodges, K. V. (2006), A synthesis of the Channel Flow–Extrusion hypothesis as developed for the Himalayan-Tibetan orogenic system, in *Chanel Flow, Ductile Extrusion and Exhumation in Continental Collision Zones,* edited by R. D. Law et al., *Geol. Soc Spec. Publ., 268*, 71-90.

Honegger, K., V. Dietrich, W. Frank, A. Gansser, M. Thöni, and V. Trommsdorf (1982), Magmatism and metamorphism in the Ladakh Himalayas (the Indus-Tsangpo suture zone), *Earth Planet. Sci. Lett., 60*, 253-292.

Le Fort, P. (1975), Himalayas: The collided range. Present knowledge of the continental arc, *Am. J. Sci., 275-1*, 1-44.

Le Fort, P., M. Cuney, C. Ceniel, C. France-Lanord, S. M. F. Sheppard, B. N. Upreti, and P. Vidal (1987), Crustal generation of the Himalayan leucogranites, *Tectonophysics, 134*, 39-57.

Miller, C., M. Thöni, W. Frank, B. Grasemann, U. Klötzli, P. Guntli, and E. Draganits (2001), The early Paleozoic magmatic event in the Northwest Himalaya, India: source, tectonic setting and age of emplacement, *Geol. Mag., 138*, 237-251.

Najman, Y., E. Appel, M. Boudagher-Fadel, P. Bown, A. Carter, E. Garzanti, L. Godin, J. Han, U. Liebke, G. Oliver, R. Parrish, and G. Vezzoli (2010), Timing of India-Asia collision, Geological, biostratigrphic and palaeomagnetic constraints, *J. Geophys. Res, 115*, B12416, doi:10.1029/2010JB007673.

NASA Earth Observatory site, accessed March 2011, Measuring Vegetation (NDVI & EVI),http://earthobservatory.nasa.gov/Features/Measuring Vegetation/measuringvegetation_2.php.

Ninomiya, Y., B. Fu, and T. J. Cudahy (2005), Detecting lithology with Advanced Spaceborne Thermal Emission and Reflection Radiometer (ASTER) multispectral thermal infrared "radiance-at-sensor" data, *Remote Sens. Environ., 99,* 127-139.

Nowicki, K. J., and P. R. Christensen (2011), Removal of Line- and Row-Correlated Noise in THEMIS Multi-Spectral Infrared Data, *submitted to Mars.*

Robertson, A. and P. Degnan (1994), The Dras arc Complex: lithofacies and reconstruction of a Late Cretaceous oceanic volcanic arc in the Indus Suture Zone, Ladakh Himalaya, *Sediment. Geol., 92*, 117-145.

Rowan, L. C., and J. C. Mars (2003), Lithological mapping in the Mountain Pass, California area using Advanced Spaceborne Thermal Emission and Reflection Radiometer (ASTER) data, *Remote Sens. Environ., 84*, 350-366.

Rowley, D.B. (1996), Age of initiation of collision between India and Asia: A review of stratigraphic data, *Earth Planet. Sci. Lett., 145*, 1-13.

Sabins, F. F. (1997), *Remote Sensing, Principles and Interpretation*, 512 pp., Waveland Press, Inc.

Schlup, M., A. Carter, M. Cosco, and A. Steck (2003), Exhumation history of eastern Ladakh revealed by $^{40}Ar/^{39}Ar$ and fission-track ages: the Indus River – Tso Morari transect, NW Himalaya, *J. Geol. Soc.*, 160, 385-399.

Searle, M. (1986), Structural evolution and sequence of thrusting in the High Himalayan Tibetan-Tethys and Indus suture zones of Zanskar and Ladakh, Western Himalaya, *J. Struct. Geol., 8*, 923-936.

Searle, M. P., K. T. Pickering, and D. J. W. Cooper (1990), Restoration and evolution of the intermontane Indus molasse basin, Ladakh Himalaya, India, *Tectonophysics, 174*, 301-314.

Searle, M., R. I. Corfield, B. Stephenson, and K. McCarron (1997), Structures of the North Indian continental margin in the Ladakh Zanskar Himalayas: implications for the timing of the obduction of the Spontang ophiolite, India-Asia collision and deformational events in the Himalaya, *Geol. Mag., 134,* 297-316.

Serra-Kiel, J., L. Hottinger, E. Caus, K. Drobne, C. Ferrandez, A. K. Jauhri, G. Less, R. Pavlovec, J. Pignatti, J. N. Samso, H. Schaub, E. Sirel, A. Strougo, Y. Tambareau, J. Tosquella, and E. Zakrevskaya (1998), Larger

foraminiferal biostratigraphy of the Tethyan Paleocene and Eocene, *Bull. Soc. Geol. Fr., 169*, 281-299.

Sinclair, H. D. and N. Jaffey (2001), Sedimentation of the Indus Group, Ladakh, northern India: implications for the timing of initiation of the palaeo-Indus River, *J. Geol. Soc., 158*, 151-162.

Steck, A. (2003), Geology of the NW Indian Himalaya, *Eclogae Geol. Helv.*, 96, 147-196.

St.-Onge, M. R., N. Rayner, and M. P. Searle (2010), Zircon age determinations of the Ladakh batholith at Chumathang (Northwest India): Implications for the age of the India-Asia collision in the Ladakh Himalaya, *Tectonophysics, 495*, 171-183.

Tripathy, A. K., K. V. Hodges, M. C van Soest, and T. Ahmad (2011), Pre-Oligocene emergence of the Indian passive margin and the timing of Indian-Eurasian collision, *submitted to Geology.*

Vaughan, R. G., S. J. Hook, W. M. Calvin and J. V. Taranik (2005), Surface mineral mapping at Steamboat Springs, Nevada with multi-watelength Thermal Infrared Images, *Remote Sens. Environ., 99.,* 140-158.

Wang, J.-G., X.-M. Hu, F.-Y. Wu, and L. Jansa (2010), Provenance of the Liuqu Conglomerate in southern Tibet: A Paleogene erosional record of the Himalayan-Tibetan orogen, *Sediment. Geol., 231*, 74-84.

Watts, D. R., and N. B. Harris (2005), Mapping granite and gneiss in domes along the North Himalayan antiform with ASTER SWIR band ratios, *Geol. Soc. Am. Bull., 117*, 879-886.

Wu, F.-Y., P. D. Clift, and J.-H. Yang (2007), Zircon Hf isotopic constraints on the sources of the Indus Molasse, Ladakh Himalaya, India, *Tectonics, 26*, TC2014, doi:10.1029/2006TC002051.

Xiao, X., Z. Shen, and X. Qin (2001), Assessing the potential of VEGETATION sensor data for mapping snow and ice cover: a Normalized Difference Snow and Ice Index, *Int. J. Remote Sens., 22*, 2479–2487.

Yeats, R. S., T. Nakata, A. Farah, M. Fort, M. A. Mirza, M. R. Pandey, and R. S. Stein (1992), The Himalayan frontal fault system, *Ann. Tectonicae, 6*, 85-98.

Yin, A. (2006), Cenozoic tectonic evolution of the Himalayan orogen as constrained by along-strike variation of structural geometry, exhumation history and foreland sedimentation, *Earth-Sci. Rev., 76*, 1-131.

**10. Figure captions**

Figure 2.1. Geologic map of the northwestern Himalaya, after *Hodges* [2000], *Schlup et al.* [2003], and *Steck* [2003]. Inset after *Sinclair and Jaffey* [2001]. The extent of Figure 4 is boxed and labeled. ITSZ – Indus-Tsangpo suture zone; GCT – Great Counter Thrust; KFZ – Karakoram fault zone; MBT – Main Boundary Thrust; MCT – Main Central Thrust; MFT – Main Front Thrust; SSZ – Shyok suture zone; STFS – South Tibetan fault system.

Figure 2.2. Comparison of proposed stratigraphy for Indus Basin sedimentary rocks, as determined in (a) Zanskar Gorge region, and (b) the Leh-Manali road transect, by careful examination of each authors' map and associated rock descriptions. Both (a) and (b) are scaled the same, and correlate to one another as well.

Figure 2.3. Published maps of the same extent of the northern part of the Zanskar Gorge, shown to highlight the variability of published maps. (a) *Garzanti and Van Haver* [1988]. (b) *Clift et al.* [2002]. (c) *Henderson et al.* [2010].

Figure 2.4. Mosaic of false color visible-near infrared images (3-2-1 in RGB), with lithotectonic boundaries drawn and labeled in white. The red box denotes the

location of Figure 2.5. The two black boxes bound the Zanskar Gorge transect to the west and the Leh-Manali road transect to the east.

Figure 2.5. (a) Boundaries discerned from false color visible-near infrared imagery (bands 3-2-1), where all white lines are drawn based upon color changes that are inferred to represent changes in lithology. Black dash-dot lines denote the Indus (NW-SE) and Zanskar Rivers (N-S). Numbers are described in the text as Domains 1-10, and follow those in Figure 2.4. The Tibetan Sedimentary sequence (TSS) is labeled for clarity. (b) Sampled DCS of TIR bands 14-12-10. White lines were transferred directly from Figure 2.5a, and subsequently modified when necessary, as described in the text. Various locations of interest, labeled numerically, are described in the text as zones B1-B14, etc. (c) PCA 5 image, with contacts shown in red instead of white for enhanced visibility. The yellow box highlights an important fold structure in Domain 5 of Figure 2.5a.

Figure 2.6. TIR laboratory emissivity spectra for common rock types, with ASTER channels labeled at appropriate wavelengths. After *Ninomiya et al.* [2005].

Figure 2.7. Emissivity spectra extracted from atmospherically corrected emissivity data that demonstrate the similarity between various sectors of the Zanskar Gorge region.

Figure 2.8. Geologic map of the Indus-Tsangpo suture zone in the eastern Ladakh region of northwestern India. Except for the units that bound the Indus Basin sedimentary rocks (Chilling Formation and Ladakh batholith), lithotectonic units young with increasing number. Contacts are drawn based upon ASTER image analysis and interpreted based on fieldwork and basic structural requirements, and are dashed where appropriate. This regional-scale map is very similar to the earliest maps produced from this region [*Brookfield and Andrews-Speed*, 1984].

Figure 2.9. Probability density plots of the three detrital muscovite $^{40}Ar/^{39}Ar$ thermochronologic samples, plotted using in-house Matlab software.

Figure 2.10. Full informal stratigraphy as determined in this study, with all possible quantitative age constraints listed. Detrital zircon data include U-Pb geochronology and (U-Th)/He thermochronology (italicized date), and detrital $^{40}Ar/^{39}Ar$ muscovite data include only dates that contained >90% $^{40}Ar^{*}$ and less than 10% error (1σ level). We report the youngest date for all detrital samples, which provides a maximum age of deposition for the sample.

Figure 2.11. Ternary diagram that depicts the proportion of quartz (Q), feldspar (F) and lithics (L). Data plotted from *Henderson et al.* [2010, 2011]. Each point represents a single sample. These data show the evolution toward increased arc dissection as marine sedimentation gave way to continental molasse depositional systems.

Table 2.1. ASTER instrument characteristics

| Radiometer | Spatial resolution | ASTER Band Number | Center Wavelength (μm) |
|---|---|---|---|
| VNIR | 15 m/px | 1 | 0.556 |
| | | 2 | 0.661 |
| | | 3 | 0.807 |
| SWIR | 30 m/px | 4 | 1.66 |
| | | 5 | 2.17 |
| | | 6 | 2.21 |
| | | 7 | 2.27 |
| | | 8 | 1.34 |
| | | 9 | 2.40 |
| TIR | 90 m/px | 10 | 8.29 |
| | | 11 | 8.63 |
| | | 12 | 9.08 |
| | | 13 | 10.7 |
| | | 14 | 11.3 |

Figure 2.1

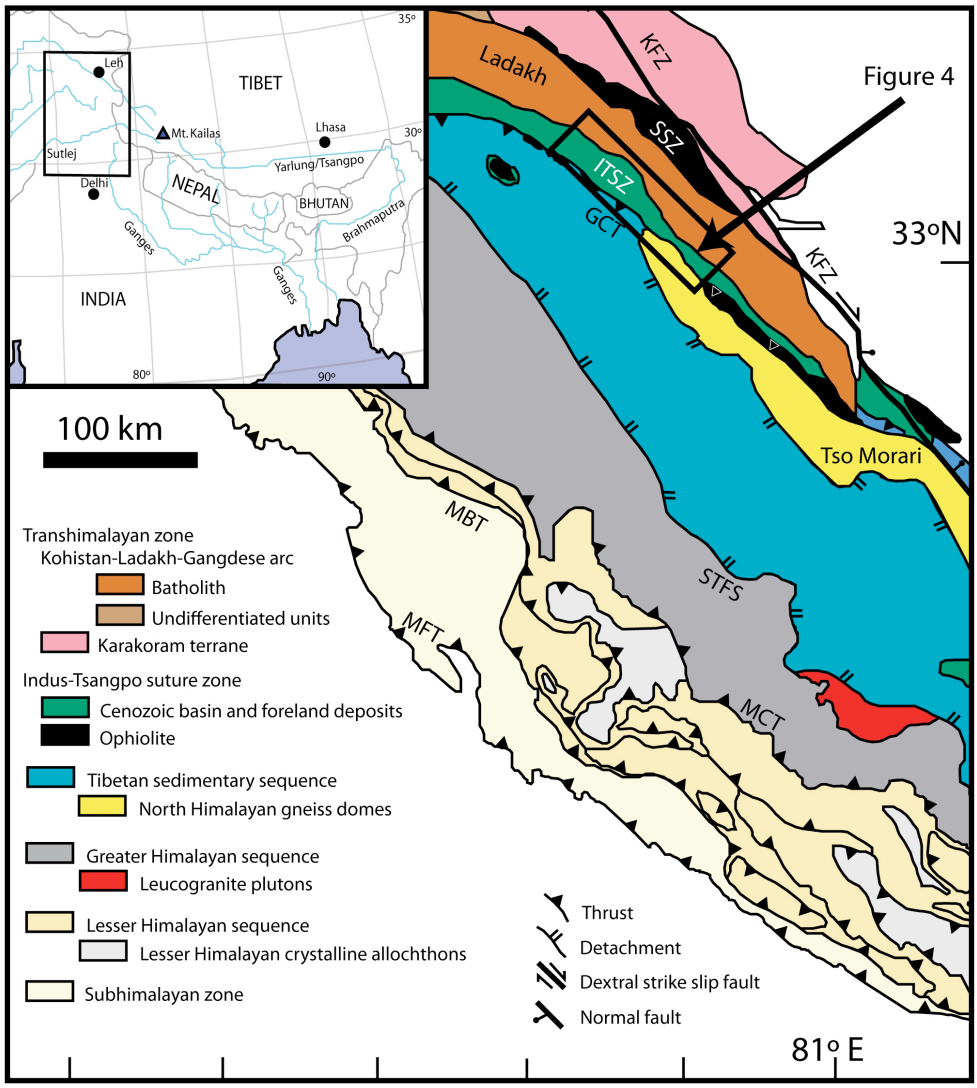
Ladakh
KFZ
SSZ
ITSZ
GCT
Figure 4
33°N
Tso Morari
MBT
STFS
MFT
MCT
100 km
Transhimalayan zone
Kohistan-Ladakh-Gangdese arc
Batholith
Undifferentiated units
Karakoram terrane
Indus-Tsangpo suture zone
Cenozoic basin and foreland deposits
Ophiolite
Tibetan sedimentary sequence
North Himalayan gneiss domes
Greater Himalayan sequence
Leucogranite plutons
Lesser Himalayan sequence
Lesser Himalayan crystalline allochthons
Subhimalayan zone
Thrust
Detachment
Dextral strike slip fault
Normal fault
81° E
TIBET
INDIA
NEPAL
BHUTAN
Leh
Mt. Kailas
Lhasa
Sutlej
Delhi
Yarlung/Tsangpo
Ganges
Brahmaputra
35°
30°
80°
90°

Figure 2.2a

| A | This study | Henderson et al. (2010) | Sinclair & Jaffey (2001) | Clift et al. (2001, 2002) | Searle et al. (1990) | Garzanti & Van Haver (1988) | Fuchs (1984) |
|---|---|---|---|---|---|---|---|
| Basgo Group | Temesgam | Upper Nimu<br>river and flood deposits | Nimu<br>slope and delta | Nimu | Choksti<br>alluvial to subaqueous mass flow | Nimu<br>lacustrine | |
| | Basgo | | | | | | |
| Upper Indus Group | Nimu | Lower Nimu<br>axial river channel | | | | | |
| | Choksti | Choksti Formation alluvial: Upper Sandstone / Middle Sandstone / Red Shale | Hemis<br>fluvial channels/ floodplain | | | | Multicolored Molasse |
| Lower Indus Group | Chogdo | Choksti Formation alluvial: Basal Conglomerate | Choksti<br>alluvial | Choksti<br>alluvial | | Choksti | |
| | | Nurla<br>fluvial delta | Nurla<br>fluvial channels/floodplains | Nurla<br>braided alluvial to lacustrine | Nurla<br>lacustrine | Nurla<br>braided river | |
| | | | | | | Hemis<br>alluvial | |
| | | Nummulitic limestone<br>back reef with deltaic input | Nummulitic limestone<br>inner carbonate ramp | Nummulitic limestone | Nummulitic limestone<br>marine | Gonmaru La<br>distal alluvial | |
| | | Chogdo<br>fluvial delta | Chogdo<br>fluvial channels/ floodplain | Chogdo<br>alluvial | Chogdo<br>ephemeral stream/ lacustrine | Urucha Marl<br>bioclastic tempesites/deltaic | |
| Tar Group | Sumda and Nummulitic Limestone | Sumda<br>shallow marine | Sumda<br>carbonate ramp | Jurutze<br>shallow water carbonate sedimentation | Sumda<br>shallow marine | Nummulitic Limestone<br>shallow water neritic, invaded by fan or delta | |
| | Jurutze | Jurutze<br>outer shelf/slope | Jurutze<br>outer shelf/slope | | Jurutze<br>marine sediments | Sumda Gompa<br>shallow water carbonates - deltaic environment | Jurutze<br>flysch |
| | Nindam | | Nindam<br>forearc | Nindam<br>forearc | | | Nindam<br>forearc |

Figure 2.2b

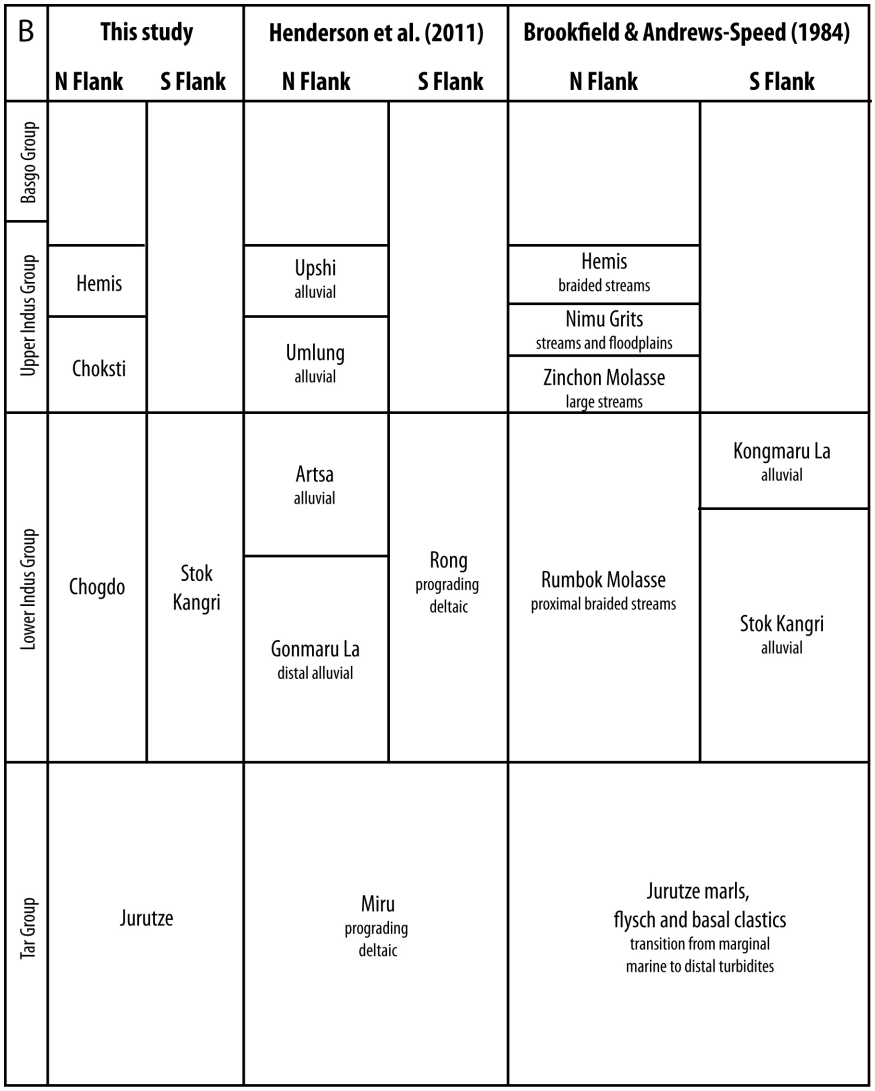
B
This study
N Flank
S Flank
Henderson et al. (2011)
N Flank
S Flank
Brookfield & Andrews-Speed (1984)
N Flank
S Flank
Basgo Group
Upper Indus Group
Hemis
Choksti
Upshi
alluvial
Umlung
alluvial
Hemis
braided streams
Nimu Grits
streams and floodplains
Zinchon Molasse
large streams
Lower Indus Group
Chogdo
Stok Kangri
Artsa
alluvial
Gonmaru La
distal alluvial
Rong
prograding deltaic
Rumbok Molasse
proximal braided streams
Kongmaru La
alluvial
Stok Kangri
alluvial
Tar Group
Jurutze
Miru
prograding deltaic
Jurutze marls,
flysch and basal clastics
transition from marginal marine to distal turbidites

Figure 2.3.

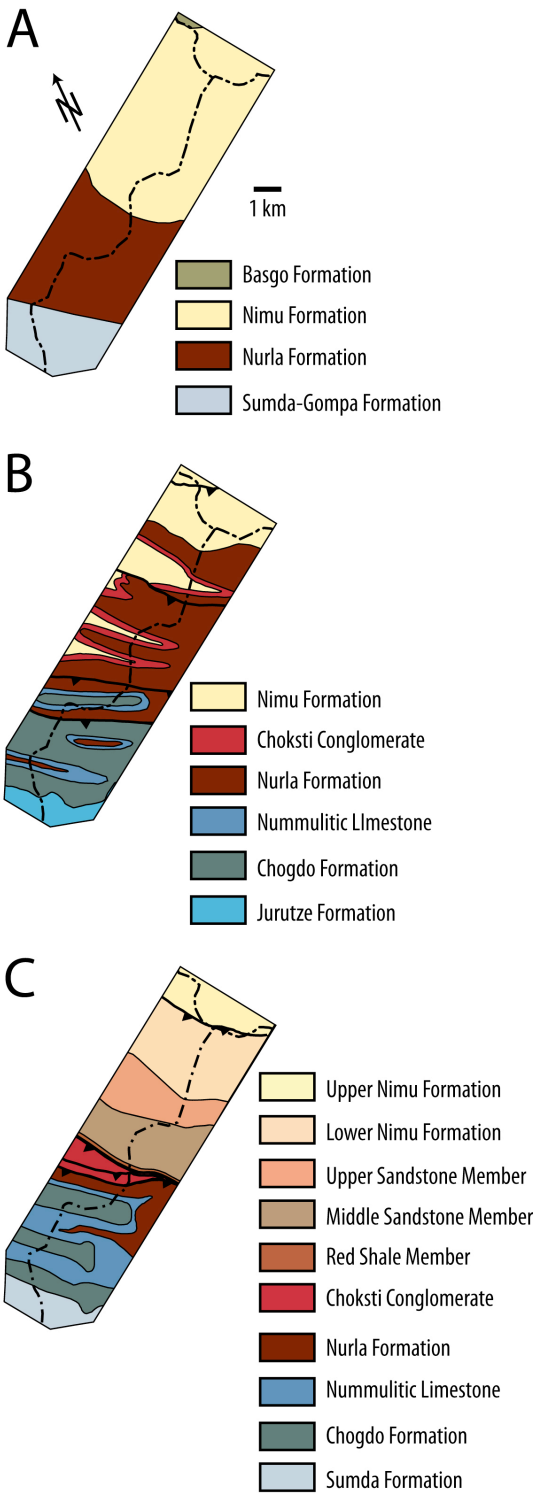
A
N
1 km
Basgo Formation
Nimu Formation
Nurla Formation
Sumda-Gompa Formation
B
Nimu Formation
Choksti Conglomerate
Nurla Formation
Nummulitic LImestone
Chogdo Formation
Jurutze Formation
C
Upper Nimu Formation
Lower Nimu Formation
Upper Sandstone Member
Middle Sandstone Member
Red Shale Member
Choksti Conglomerate
Nurla Formation
Nummulitic Limestone
Chogdo Formation
Sumda Formation

Figure 2.4.

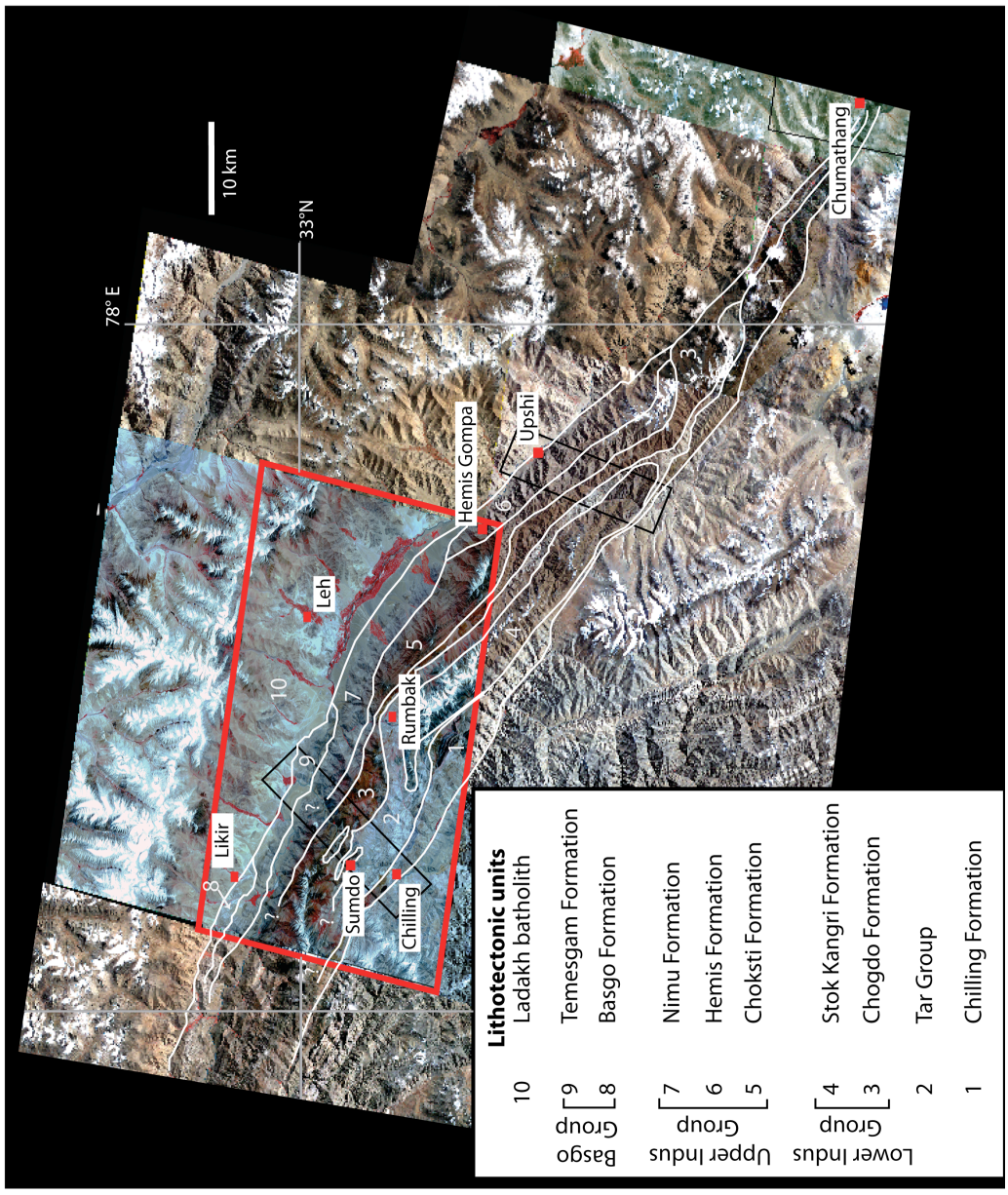
78° E
33°N
10 km
Likir
Leh
Sumdo
Chilling
Rumbak
Hemis Gompa
Upshi
Chumathang
Lithotectonic units
10 Ladakh batholith
Basgo Group
9 Temesgam Formation
8 Basgo Formation
Upper Indus Group
7 Nimu Formation
6 Hemis Formation
5 Choksti Formation
Lower Indus Group
4 Stok Kangri Formation
3 Chogdo Formation
2 Tar Group
1 Chilling Formation

Figure 2.5.

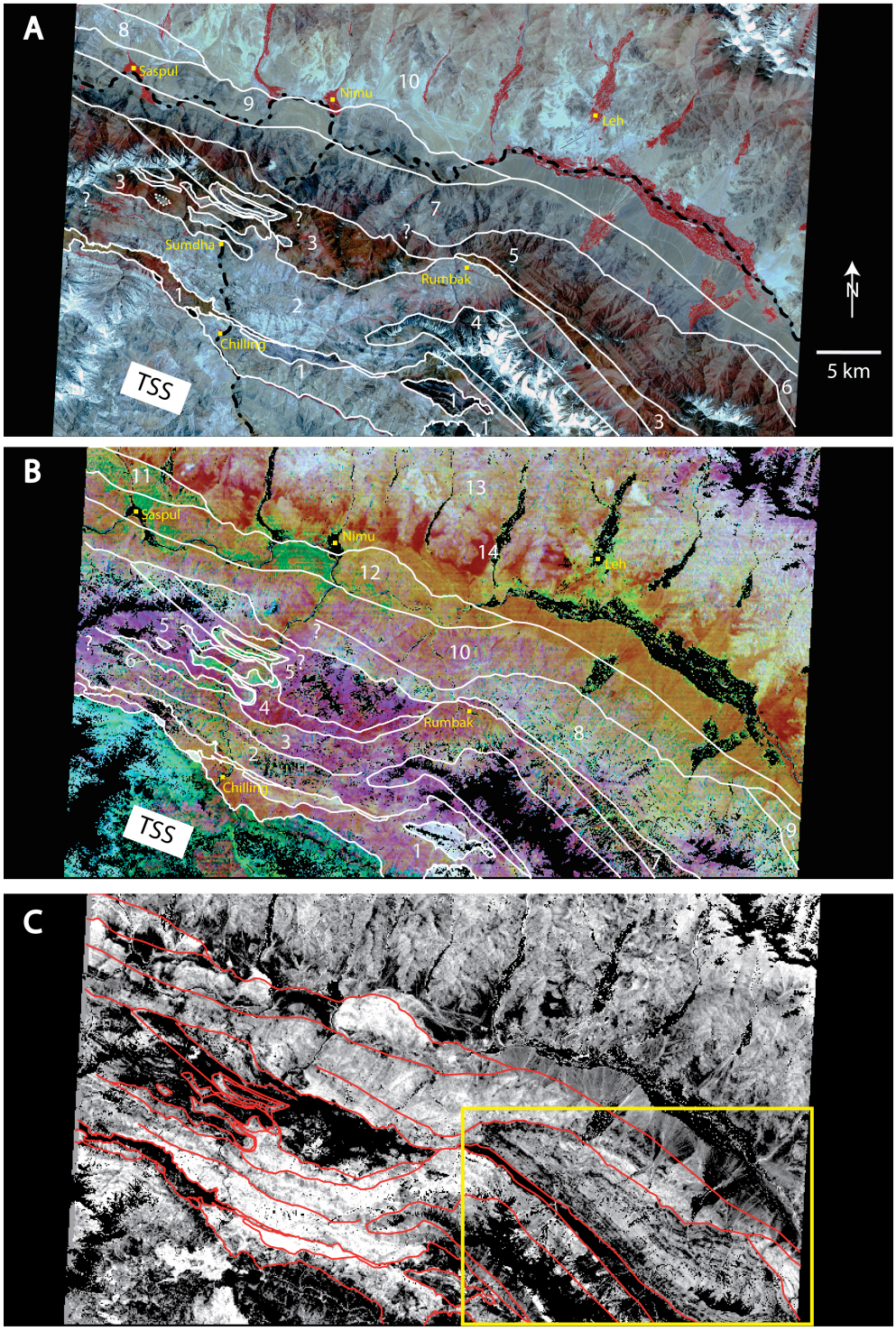
A
Saspul
Nimu
Leh
Sumdha
Rumbak
Chilling
TSS
N
5 km
B
Saspul
Nimu
Leh
Rumbak
Chilling
TSS
C

Figure 2.6.

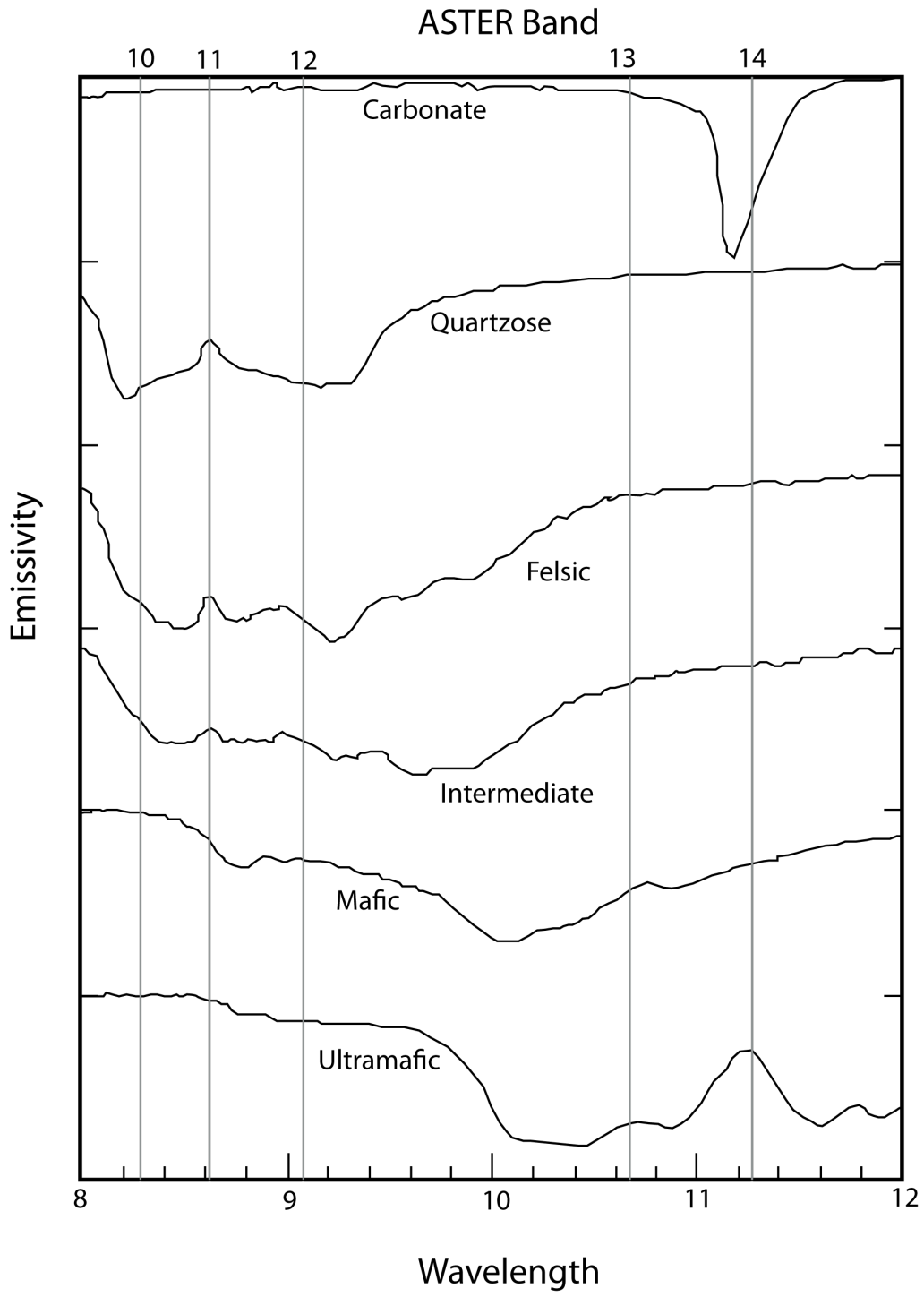
ASTER Band
10
11
12
13
14
Carbonate
Quartzose
Felsic
Intermediate
Mafic
Ultramafic
Emissivity
8
9
10
11
12
Wavelength

Figure 2.7.

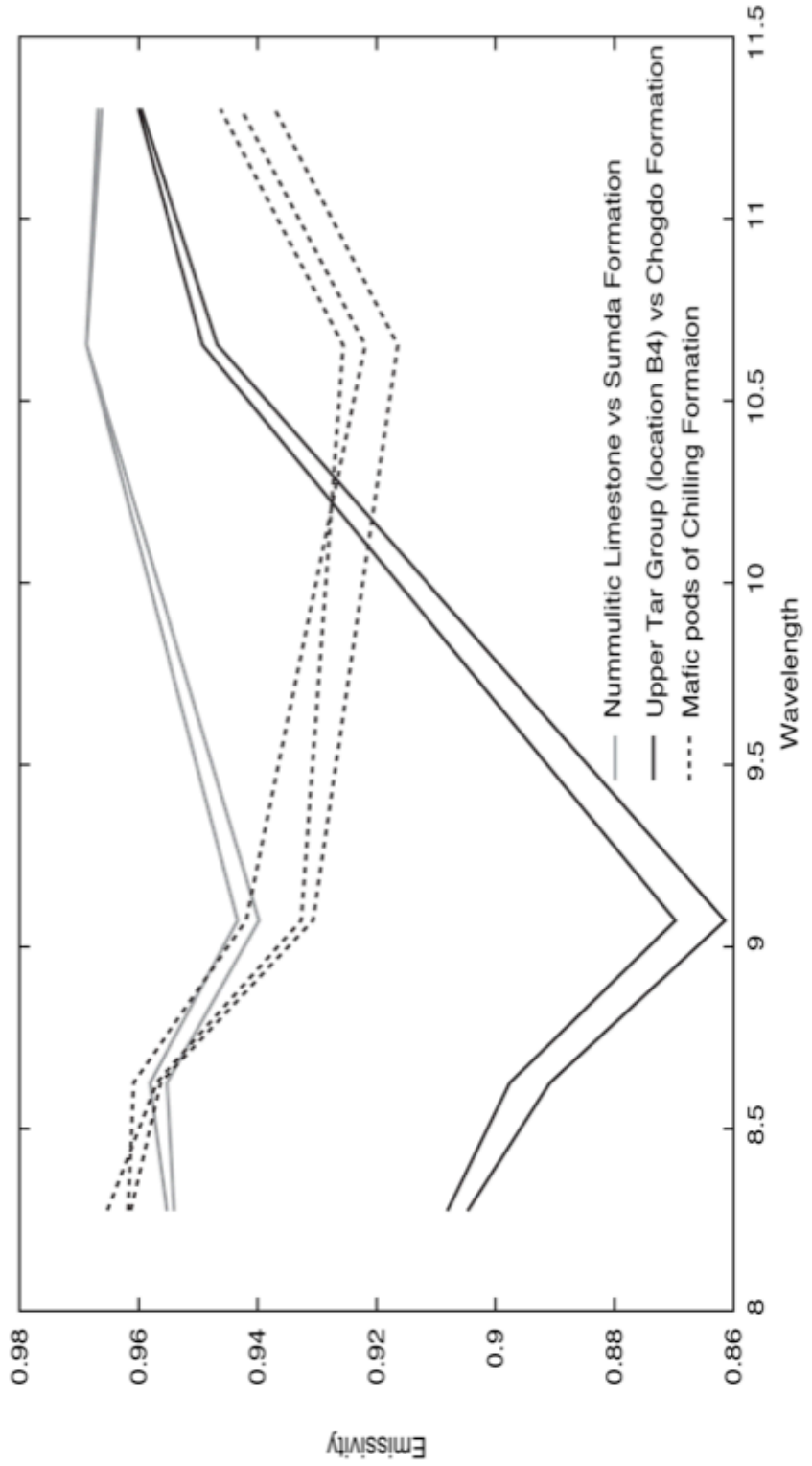
Emissivity
0.98
0.96
0.94
0.92
0.9
0.88
0.86
8
8.5
9
9.5
10
10.5
11
11.5
Wavelength
Nummulitic Limestone vs Sumda Formation
Upper Tar Group (location B4) vs Chogdo Formation
Mafic pods of Chilling Formation

Figure 2.8.

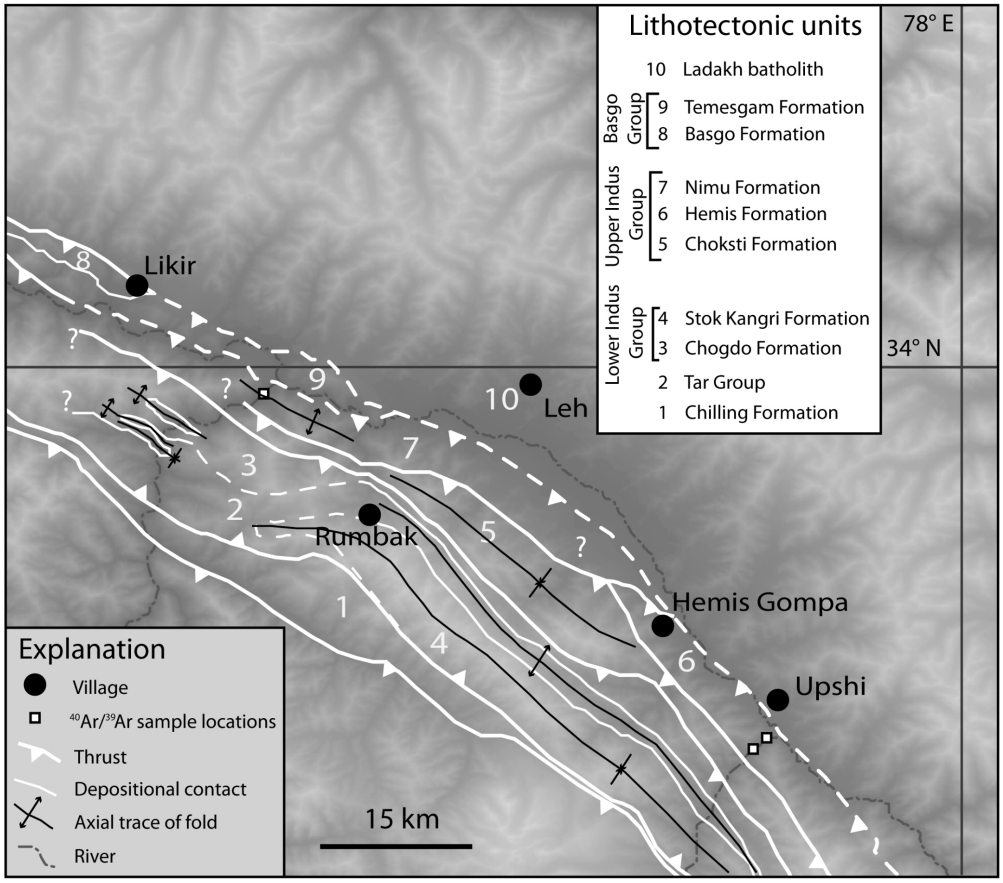
Lithotectonic units
10 Ladakh batholith
Basgo Group
9 Temesgam Formation
8 Basgo Formation
Upper Indus Group
7 Nimu Formation
6 Hemis Formation
5 Choksti Formation
Lower Indus Group
4 Stok Kangri Formation
3 Chogdo Formation
2 Tar Group
1 Chilling Formation
78° E
34° N
Likir
Leh
Rumbak
Hemis Gompa
Upshi
Explanation
Village
40Ar/39Ar sample locations
Thrust
Depositional contact
Axial trace of fold
River
15 km

Figure 2.9.

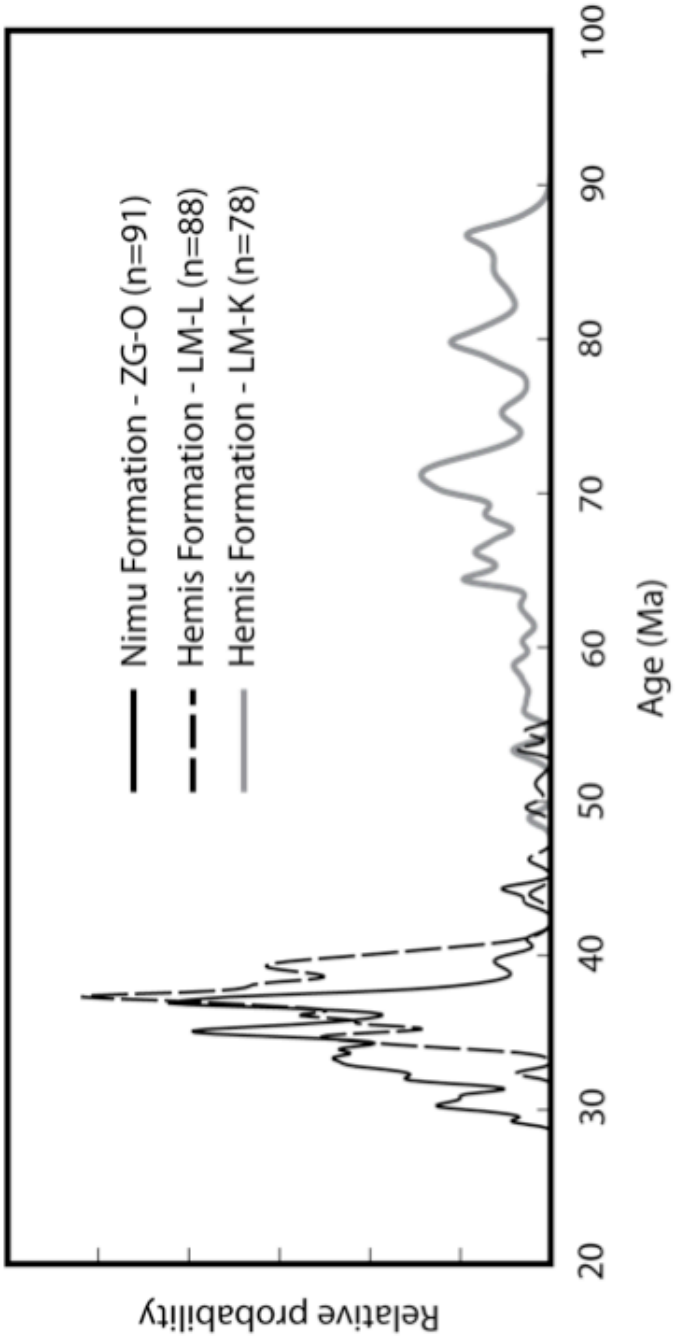
Nimu Formation - ZG-O (n=91)
Hemis Formation - LM-L (n=88)
Hemis Formation - LM-K (n=78)
Relative probability
Age (Ma)
20
30
40
50
60
70
80
90
100

Figure 2.10.

| | Stratigraphic Unit | Biostratigraphy | Detrital zircon | Detrital muscovite | Source |
|---|---|---|---|---|---|
| Basgo Group | Temesgam | | < 41.3 Ma | < 19.1 Ma<br>< 34.5 Ma | *Henderson et al.* (2010)<br>*Henderson et al.* (2010) |
| | Basgo | 28.4-23.03 Ma | *< 29.6 Ma* | | *Tripathy et al.* (submitted)<br>*Bajpai et al.* (2004) |
| Upper Indus Group | Nimu | | < 41.1 Ma | <38 Ma<br>< 29.2 Ma | *Henderson et al.* (2010)<br>*This study*<br>*Wu et al.* (2007) |
| | Hemis | | | < 34.7 Ma<br>< 33 Ma<br>< 50 Ma<br>< 37.6 Ma | *Henderson et al.* (2011)<br>*This study*<br>*This study*<br>*Henderson et al.* (2011) |
| | Choksti | | < 45 Ma | | *Wu et al.* (2007) |
| Lower Indus Group | Stok Kangri *south limb* | | < 48.4 Ma | | *Henderson et al.* (2011) |
| | Chogdo *north limb* | | < 46.1 Ma<br>< 51.1 Ma<br>< 50.8 Ma<br>< 52 Ma<br>< 60 Ma | | *Henderson et al.* (2010)<br>*Henderson et al.* (2010)<br>*Henderson et al.* (2010)<br>*Wu et al.* (2007)<br>*Wu et al.* (2007) |
| Tar Group | Sumda and Nummulitic Limestone | late Ypresian<br>late Ypresian | < 52.5 Ma | | *Henderson et al.* (2010)<br>*Henderson et al.* (2010)<br>*Henderson et al.* (2010) |
| | Jurutze | | < 53.4 Ma<br>< 54.3 Ma | | *Henderson et al.* (2010)<br>*Henderson et al.* (2011) |
| | Nindam | | | | |
| Chilling Formation | *Undifferentiated* | | < 62.8 Ma<br>< 51.1Ma<br>< 159.2 Ma | < 67.2Ma | *Henderson et al.* (2011)<br>*Henderson et al.* (2011)<br>*Henderson et al.* (2011) |

Figure 2.11.

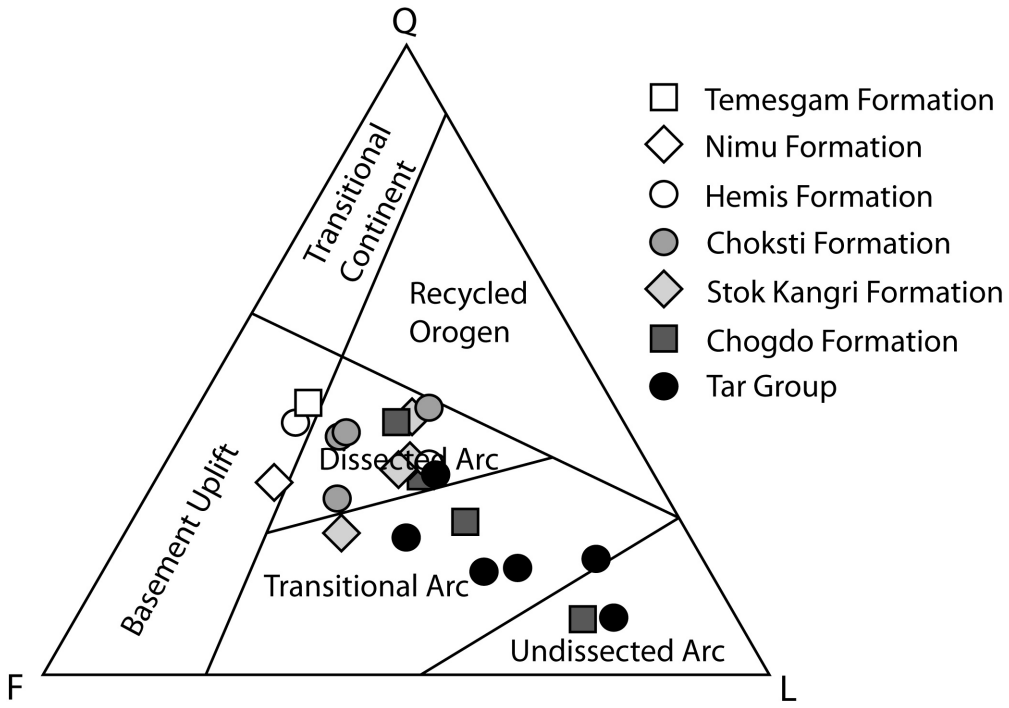
Q
F
L
Transitional Continent
Recycled Orogen
Basement Uplift
Dissected Arc
Transitional Arc
Undissected Arc
Temesgam Formation
Nimu Formation
Hemis Formation
Choksti Formation
Stok Kangri Formation
Chogdo Formation
Tar Group

CHAPTER 3

# PRE-OLIGOCENE EMERGENCE OF THE INDIAN PASSIVE MARGIN AND THE TIMING OF INDIAN-EURASIAN COLLISION


## ABSTRACT

Precise knowledge of the timing of Indo-Eurasian collision is prerequisite for understanding the subsequent evolution of the Himalayan-Tibetan orogenic system, yet the topic remains controversial despite decades of research. We present new data for the Upper Oligocene Basgo Formation of NW India that are pertinent to one proposal – that the collision initiated no earlier than the Eocene-Oligocene boundary. The Basgo Formation, which represents a portion of the Indus molasse basin deposited along the Indus-Tsangpo suture zone, contains conglomerates with clasts of Eurasian plate rocks. However, the distribution of U-Pb dates for detrital zircons in associated sandstones indicate an Indian plate source. This mixed provenance demonstrates a minimum Late Oligocene age for India-Eurasia collision in the NW Indian Himalaya. (U-Th)/He cooling dates for detrital zircons from the Basgo Formation range from 52.6 to 28.25 Ma, however, implying that their Indian plate source was likey emergent and eroding by Early Eocene due to collision.


## 1. Introduction

The collision between India and Eurasia, which resulted in the demise of Neothethys, was a profound geodynamic event that, beyond building the Himalayan-Tibetan orogenic system, has affected regional – and possibly global –

climate patterns [e.g., *Raymo and Ruddiman*, 1992]. However, the timing of this event remains controversial despite years of research on the topic, with popular estimates ranging from Late Cretaceous to Early Oligocene [e.g., *Yin and Harrison*, 2000; *Aitchison et al*., 2007].

Proponents of a Late Cretaceous collision are most strongly persuaded by paleomagnetic data of Lhasa block rocks [*Chen et al*., 2010], paleontologic evidence that demonstrates exchange of terrestrial fauna during the Maastrichtian [*Jaeger et al*., 1989], and emplacement of ophiolites atop the Indian passive margin in the Latest Cretaceous [*Searle et al*., 1997]. However, other researchers [e.g., *Aitchison et al*., 2007] interpret several observations to imply an Early Oligocene collision; an apparent decrease in northward motion of India at 20 Ma [*Acton*, 1999]; Late Oligocene to Early Miocene molasse-type conglomerates along the Indus-Tsangpo suture zone (ITSZ) [*Aitchison et al*., 2002; *DeCelles et al*., 2011]; Oligocene to Miocene uplift and unroofing of the Transhimalayan batholiths [e.g., *Kirstein et al*., 2009]; and Late Oligocene-Miocene movement along the major Himalayan fault systems [e.g., *Hodges*, 2000 and references therein]. In particular, proponents of young collision point to the relatively small amount of pre-Oligocene orogen-derived clastic detritus in the Himalayan foreland as further evidence of limited pre-Oligocene shortening [*Aitchison et al*., 2007]. Nevertheless, the most frequently cited age interval for collision among geoscientists working in the orogen, *ca.* 50-55 Ma, is based on several lines of reasoning. Most notable are the coincidence of an apparent decrease in Indian ridge spreading rates [*Patriat and Achache*, 1984], an apparent decrease in the

rate of northward motion of India [*Klootwijk et al*., 1992; *Acton*, 1999], and the timing of ultrahigh–pressure subduction-related, metamorphism of the leading Indian margin [*Leech et al*., 2005]. Some observations that have significant implications regarding the timing of collision remain controversial; compare, for example, the *Aitchison et al*. [2007] and *Najman et al*. [2010] interpretations of the paleolatitude of India at 55 Ma as derived from paleomagnetic data, and the arguments for the timing of final marine deposition between India and Asia in the vicinity of the ITSZ by *Wang et al*. [2002] and *Zhu et al*. [2005].

Direct evidence of the timing of India-Eurasia collision is potentially preserved in sediments of Eocene-Miocene intermontane basins – located near the ITSZ – which were deposited during much of the interval over which collision might have occurred [*Rowley*, 1996]. Because most of these basins contain an abundance of coarse clastic fill with few fossils or volcanogenic layers in all but the youngest strata [e.g., *DeCelles et al*., 2011], the ages of many important units are not well known, thus contributing to the uncertainty.

In this paper, we explore the provenance of one of the best-dated parts of one of these intermontane basin sequences, the Upper Oligocene Basgo Formation of the Indus Basin in NW India [*Bajpai et al*., 2004]. Although this unit lies in direct depositional contact on Eurasian plate rocks and its more conglomeratic horizons contain clasts derived from the Eurasian plate, we present detrital zircon U-Pb dates that show, unequivocally, that most of the detritus in finer-grained Basgo clastic strata was derived from the Indian plate. Moreover, based on detrital zircon (U-Th)/He thermochronology of the sandstones, it

appears that the Indian plate provenance region for these zircons experienced early Tertiary exhumation well before Basgo deposition. Collectively, these data suggest that India-Eurasia collision drove the emergence of the pre-collisional Indian passive margin by Early Eocene time.

**2. Cenozoic intermontane basins of the ITSZ**

The ITSZ extends along the Yarlung-Tsangpo River to the east and the Indus River to the west, and comprises ophiolitic material, forearc basin deposits, and intermontane basin clastic strata. The molassic intermontane basins along the Yarlung Tsangpo River are relatively isolated from one another, and are represented, from east to west, by rocks mapped as the Luobosa, Dazhuqu, Liuqu, Qiuwu, and Kailas Formations (Figure 3a). These basins share many lithologic similarities, particularly among conglomerate facies, which has spurred correlation across several hundred kilometers [*Aitchison et al*., 2002]. However, the ages of similar lithologic units in different basins are relatively poorly known, making these correlations speculative at best. The Luobosa Formation outcrops for approximately 100 km east of Zedong and contains fossils of Oligocene-Miocene age [*Aitchison et al*., 2002]. The Dazhuqu Formation, located southwest of Lhasa near Renbung, can be traced eastward to Daga, and has not been dated. The Liuqu Conglomerates, located south of Xigaze, must be no older than Middle or Late Eocene based upon U-Pb detrital zircon dates [*Wang et al*., 2010]. Just north of the Liuqu conglomerates are rocks similar to the Dazhuqu Formation that have been referred to as the Qiuwu and Qianbulin Formations [*Aitchison et al*., 2002; *Wang et al*., 2010]. Based on palynology, *Li et al*. [2010] regard the

Qianbulin Formation as Cretaceous, whereas the overlying Qiuwu Formation is thought to be Eocene to Miocene. One of the best-known molassic depocenters in southern Tibet is the Kailas Basin in the area surrounding the mountain of the same name. Recently obtained U-Pb dates for interstratified volcanic units confirm a Miocene age for the Kailas Formation [*DeCelles et al*., 2011].

The largest and most thoroughly studied of the ITSZ molassic depocenters lies along the Indus River valley in the Ladakh region of NW India and is referred to as the Indus Basin [e.g., *Garzanti and van Haver*, 1988; *Henderson et al*., 2010]. An important cross section through the Indus Basin stratigraphy is spectacularly exposed in the Zanskar Gorge (34°07'N, 77°13'E). Here clastic sedimentary rocks of the Lower Indus Group conformably overlie limestones of the Tar Group that are 54.9-49.4 Ma, based on their fossil assemblages [*Henderson et al*., 2010]. Younger strata in the gorge, referred to as the Upper Indus Group in this paper and separated from the Lower Indus Group by a fault, have Oligocene maximum ages of deposition [*Henderson et al*., 2010].

The work presented here focuses on the youngest units of the Indus Basin that outcrop to the west of the Zanskar Gorge. The Basgo Formation unconformably overlies the Cretaceous-Paleogene Ladakh batholith [*Garzanti and Van Haver*, 1988], and is in conformable contact with the overlying Temesgam Formation, the youngest rocks of the Indus Basin. This section is separated from the Upper Indus Group by another fault (Figure 1b).

The Basgo Formation contains a well-studied faunal assemblage of Upper Oligocene *ostracoda* [*Bajpai et al*., 2004]. Although units of this age should be

present in the canonical Zanskar Gorge section of the Indus Group, no lithologies similar to the Basgo sequence occur there in what could be a time-correlative stratigraphic position. The paucity of age-diagnostic fossils in the Zanskar Gorge section, as well as the existence of faults with unknown throw, make it difficult to know precisely how the Basgo and Temesgam Formations correlate with the Upper and Lower Indus Group, so we prefer to consider the Indus Group and the Basgo/Temesgam succession as distinctive packages within the Indus Basin.

## 3. Establishing provenance of the Basgo Formation

In order to explore this enigmatic section of the Indus Basin, we first use U-Pb detrital zircon geochronology to evaluate the provenance of the Basgo Formation. A wealth of such data exists for the Indus Basin strata exposed in the Zanskar Gorge [*Wu et al*., 2007; *Henderson et al*., 2010]. This provides a simple means by which to compare the Basgo Formation provenance with the provenance of other, better-studied Indus Basin units.

### 3.1. U-Pb Methods

Sandstone samples of the Basgo Formation were collected from several locations in and around a paleontological sampling locality of *Bajpai et al*. [2004], and are listed in terms of relative stratigraphic height. Lowest is sample ST-B, collected for its proximity to the contact with the Ladakh batholith and its distinctive yellow color. Next, 0.9 km to the east, sample TR-B was collected from the most ostracod-rich section of *Bajpai et al*. [2004; location TR2]. The stratigraphically equivalent sample TR-D was collected 0.4 km to the southeast, and the final sample, TR-E, is 100 m away from, and above sample TR-D.

The samples were crushed and sieved, and zircon grains were separated using standard magnetic and gravimetric techniques. U-Pb detrital zircon dates for samples TR-D and TR-E were obtained using laser-ablation multicollector-inductively coupled plasma-mass spectrometry (LA-MC-ICPMS) at the University of Arizona Laserchron facility, with procedures detailed in *Gehrels et al*. [2008], and those specific to our analytical session in the Supplementary Material Appendix D.

**3.2. U-Pb Results**

Detrital zircon U-Pb dates from both Basgo samples are similar, displaying dates ranging from ~3400-90 Ma (Figure 3.2a). Probability density curves from both samples are calculated and plotted using in house software at Arizona State University (Figure 3.2a; Supplementary Material Appendix E), and for comparison, we plot zircon U-Pb dates from the potential source areas from both the north and the south. For the northern Eurasian source, we plot bedrock and detrital U-Pb zircon dates from the Transhimalayan arcs (Kohistan-Ladakh-Gangdese), the Karakoram, and the Lhasa and Qiantang blocks, whereas for the southern Indian source, we plot the most proximal detrital samples collected from Cambrian-Ordovician rocks within the Tibetan sedimentary series (TSS; Figure 3.2a). The two Basgo samples have major modes highlighted by gray bands at *ca.* 2500, 950, and 540-520 and 90 Ma. The Cretaceous mode is almost certainly indicative of a Eurasian source, but accounts for only 4 of 183 grains, or ~2% of the dataset. The Cambrian mode may be indicative of either an Indian or Eurasian source, but the older modes are required to be Indian in origin. Overall, the Basgo

sandstone spectra are consistent with a very high proportion of zircons having been derived from Indian sources, particularly the TSS (Figure 3.2a).

In the classic section of the Indus Group in the nearby Zanskar Gorge, detrital U-Pb zircon data yield mostly Cretaceous-Paleogene dates; by comparing these results with the spectra of U-Pb zircon dates for possible sediment sources, *Wu et al*. [2007] and *Henderson et al*. [2010] inferred that the Indus Group sandstones derived almost exclusively from Eurasia. The Zanskar Gorge spectrum contrasts strongly with those of the Basgo Formation, implying that the two juxtaposed sedimentary successions had significantly different source areas, further supporting our interpretation that the Basgo Formation had a significantly different source region that is almost certainly the Indian plate.

**4. Exhumation of the zircon source region**

Zircon (U-Th)/He (hereafter referred to as ZHe) dates record cooling below the nominal bulk closure temperature of 180°C [*Reiners et al*., 2004], and provide information for both the maximum age of deposition of the Basgo Formation and the exhumation of the source region as determined from the detrital zircon U-Pb geochronology.

**4.1. ZHe Methods**

ZHe dates from all samples were obtained in the Noble Gas, Geochronology and Geochemistry Laboratory at Arizona State University using conventional techniques, detailed in *van Soest et al*. [2011]. Age ranges are plotted in Figure 3.1c and a probability density curve for all the data (n=20) is

plotted in Figure 3.3. Analytical results are listed in the Supplementary Material Appendix F.

### 4.2. ZHe Results

The ZHe dates range from 52.6±1.7 to 28.52±0.96 Ma (2σ), providing information about the low-temperature history of the two potential source areas. Based on the detrital zircon U-Pb results described above, we infer that the majority of these grains were derived from TSS rocks that were exposed and eroding prior to or during Late Oligocene Basgo deposition. This inference is supported by youngest ZHe dates that indicate Early Oligocene cooling. Notably, 70% of the zircons yield (U-Th)/He cooling dates of Eocene age.

## 5. Implications

Clasts within more conglomeratic units [*Garzanti and van Haver*, 1988; *Bajpai et al*., 2004], as well as the Cretaceous mode of detrital zircons in the sandstones, indicate that the Basgo Formation contains sediments from Eurasia, but the detrital zircon U-Pb data presented here suggest that the major source for finer-grained Basgo detritus was India – specifically the TSS. The mixed India-Eurasia provenance of the Basgo Formation strongly implies post-collisional deposition as suggested by *Aitchison et al*. [2007]. Moreover, the timing of Basgo deposition, best constrained as Late Oligocene by the paleontological data, is supported by the youngest ZHe dates.

However, it is clear from the ZHe dataset that the provenance region did not experience a single phase of rapid and uniform erosion in Late Oligocene time because most zircons passed through their closure temperature ranges tens of

millions of years earlier. This implies that erosional exhumation and cooling of much of the source region was related to an older deformational event. The majority of the Basgo ZHe cooling ages are Eocene, corresponding to the timing ascribed by many researchers to the onset of India-Eurasia collision. The simplest explanation of our detrital zircon U-Pb and ZHe datasets is that the Tibetan sedimentary sequence in this region had been incorporated into the Himalayan-Tibetan orogenic system by Eocene time and was actively eroding as a consequence.

Although we can neither rule out a pre-Eocene timing for collision, nor definitively say that the Eocene exhumation event along the northern Indian margin did not predate the final stages of collision, our data are collectively consistent with the large body of evidence that favors India-Eurasia collision at *ca.* 55-50 Ma in the western Himalayan-Tibetan orogenic system [e.g., *Rowley*, 1996]. Understanding whether the timing of collision is consistent or variable to the east will require further studies of the kind described here in other Cenozoic intermontane basins along the ITSZ.

## 6. References

Acton, G. D., 1999, Apparent polar wander of India since the Cretaceous with implications for regional tectonics and true polar wander, in *The Indian subcontinent and Gondwana: A paleomagnetic and rock magnetic perspective,* edited by T. Radhakrishna et al., *geol. Soc. India Mem., 44,* 129-175.

Aitchison, J. C, A. M. Davis, Badengzhu, and H. Luo (2002), New constraints on the Indian-Asia collision: The lower Miocene Gangrinboche

conglomerates, Yarlung Tsangpo suture zone, SE Tibet, *J. Asian Earth Sci., 21*, 253-265.

Aitchison, J. C., J. R. Ali, and A. M. Davis (2007), When and where did India and Asia collide?, *J. Geophys. Res.*, *112*, B05423, doi: 10.1029/2006JB004706.

Bajpai, S., R. C. Whatley, G. V. R. Prasad, and J. E. Whittaker (2004), An Oligocene non-marine ostracod fauna from the Basgo Formation (Ladakh Molasse), NW Himalaya, India, *J. Micropalaeontol., 23*, 3-9.

Chen, J., B. Huang, and L. Sun (2010), New constraints to the onset of the India-Asia collision: paleomagnetic reconnaissance on the Linzizong Group in the Lhasa Block, China, *Tectonophysics, 489*, 189-209.

DeCelles, P. G., P. Kapp, J. Quade, and G. E. Gehrels (2011), Oligocene-Miocene Kailas basin, southwestern Tibet: Record of postcollisional upper-plate extension in the Indus-Yarlung suture zone, *Geol. Soc. Am. Bull., 123*, 1337-1362.

Garzanti, E., and T. Van Haver (1988), The Indus clastics: forearc basin sedimentation in the Ladakh Himalaya (India), *Sediment. Geol., 59*, 237-249.

Gehrels, G. E., V. Valencia, and J. Ruiz (2008), Enhanced precision, accuracy, efficiency and spatial resolution of U-Pb ages by laser ablation-multicollector-inductively coupled plasma-mass spectrometry*, Geochem., Geophys., Geosyst., 9*, Q03017, doi:10.1029/2007GC001805.

Henderson, A. L., Y. Najman, R. Parrish, M. BouDagher-Fadel, D. Barford, E. Garzanti, and S. Ando (2010), Geology of the Cenozoic Indus Basin sedimentary rocks: paleoenvironmental interpretation of sedimentation from the western Himalaya during the early phases of India-Eurasia collision, *Tectonics, 29,* TC6015, doi:10.1029/2009TC002651.

Hodges K. V. (2000), Tectonics of the Himalaya and southern Tibet from two perspectives, *Geol. Soc. Am. Bull., 112*, 324-350.

Jaeger J.-J., V. Courtillot, and P. Tapponnier (1989), Paleontological view of the ages of the Deccan Traps, the Cretaceous/Tertiary boundary and the India-Asia collision, *Geology, 17*, 316-319.

Kirstein, L. A., J. P. T. Foeken, P. Van der Beek, F. M. Stuart, and R. J. Phillips (2009), Cenozoic unroofing history of the Ladakh Batholith, western

Himalaya, constrained by thermochronology and numerical modeling, *J. Geol. Soc., 166*, 667-678.

Klootwijk, C. T., J. S. Gee, J. W. Pierce, G. M. Smith, and P. L. McFadden (1992), An early India-Asia contact; paleomagnetic constraints from Ninetyeast Ridge, ODP Leg 121, *Geology, 20*, 395-398.

Leech, M. L., S. Singh, A. K. Jain, S. L. Klemperer, and R. M. Manickavasagam (2005), The onset of India-Asia continental collision: Early, steep subduction required by the timing of UHP metamorphism in the western Himalaya, *Earth Planet. Sci. Lett., 234*, 83-97.

Li, J.-G., Z.-Y. Guo, D. J Batten, H.-W. Cai, and Y.-Y. Zhang (2010), Palynological stratigraphy of Late Cretaceous and Cenozoic collision related conglomerates at Qiabulin, Xigaze, Xizang (Tibet) and its bearing on palaeoenvironmenta development, *J. Asian Earth Sci., 28*, 86-95.

Myrow, P. M., N. C. Hughes, J. W. Goodge, C. M. Fanning, I. S. Williams, S. Peng, O. N. Bhargava, S. K. Parcha, and K. R. Pogue (2010), Extraordinary transport and mixing of sediment across Himalayan central Gondwana during the Cambrian-Ordovician, *Geol. Soc. Am. Bull.*, 122, 1660-1670.

Najman, Y., E. Appel, M. Boudagher-Fadel, P. Bown, A. Carter, E. Garzanti, L. Godin, J. Han, U. Liebke, G. Oliver, R. Parrish, and G. Vezzoli (2010), Timing of India-Asia collision, Geological, biostratigrphic and palaeomagnetic constraints, *J. Geophys. Res, 115*, B12416, doi:10.1029/2010JB007673.

Patriat, P., and J. Achache (1984), India-Eurasia collision chronology has implications for crustal shortening and driving mechanism of plates, *Nature, 311*, p. 615-621.

Raymo, M. E., and W. F. Ruddimann (1992), Tectonic forcing of late Cenozoic climate, *Nature, 359*, 117-122.

Reiners, P. W., T. L. Spell, S. Nicolescu, and K. A. Zanetti (2004), Zircon (U-Th)/He thermochronometry: He diffusion and comparisons with $^{40}Ar/^{39}Ar$ dating, *Geochim. Cosmochim. Acta, 68*, 1857-1887, doi: 10.1016/j.gca.2003.10.021.

Rowley, D.B. (1996), Age of initiation of collision between India and Asia: A review of stratigraphic data, *Earth Planet. Sci. Lett., 145*, 1-13.

Searle, M. (1986), Structural evolution and sequence of thrusting in the High Himalayan Tibetan-Tethys and Indus suture zones of Zanskar and Ladakh, Western Himalaya, *J. Struct. Geol., 8*, 923-936.

Searle, M., R. I. Corfield, B. Stephenson, and K. McCarron (1997), Structures of the North Indian continental margin in the Ladakh Zanskar Himalayas: implications for the timing of the obduction of the Spontang ophiolite, India-Asia collision and deformational events in the Himalaya, *Geol. Mag., 134,* 297-316.

Sinclair, H. D. and N. Jaffey (2001), Sedimentation of the Indus Group, Ladakh, northern India: implications for the timing of initiation of the palaeo-Indus River, *J. Geol. Soc., 158*, 151-162.

St.-Onge, M. R., N. Rayner, and M. P. Searle (2010), Zircon age determinations of the Ladakh batholith at Chumathang (Northwest India): Implications for the age of the India-Asia collision in the Ladakh Himalaya, *Tectonophysics, 495*, 171-183.

Van Soest, M. C., K. V Hodges, J.-A. Wartho, M. B Biren, B. D. Monteleone, J. Ramezani, J. G. Spray, and L. M. Thompson (2011), (U-Th)/He dating of terrestrial impact structures: the Manicouagan example, *Geochem., Geophys., Geosyst., 12*, Q0AA16, doi:10.29/2010GC003465.

Wang, C. S., X. H. Li, X. M. Hu, and L. F. Jansa (2002), Latest marine horizon north of Qomolangma (Mt Everest): Implications for closure of Tethys seaway and collisional tectonic, *Terra Nova, 14*, 114-120.

Wang, J.-G., X.-M. Hu, F.-Y. Wu, and L. Jansa (2010), Provenance of the Liuqu Conglomerate in southern Tibet: A Paleogene erosional record of the Himalayan-Tibetan orogen, *Sediment. Geol., 231*, 74-84.

Wu, F.-Y., P. D. Clift, and J.-H. Yang (2007), Zircon Hf isotopic constraints on the sources of the Indus Molasse, Ladakh Himalaya, India, *Tectonics, 26*, TC2014, doi:10.1029/2006TC002051.

Yin, A. and T. M. Harrison (2000), Geologic evolution of the Himalayan-Tibetan Orogen, *Ann. Rev. of Earth and Planet. Sci., 28,* 211-280.

Yin, A., T. M. Harrison, M. A. Murphy, M. Grove, S. Nie, F. J. Ryerson, X. F. Wang, and Z. L. Chen (1999), Tertiary deformational history of southeastern and southwestern Tibet during the Indo-Asian collision, *Geol. Soc. Am. Bull. 111*, 1644-1664.

Zhu, B., W. S. F. Kidd, D. B. Rowley, B. S. Currie, and N. Shafique (2005), Age of initiation of the India-Asia collision in the east-central Himalaya, *J. Geol., 113*, 265-285.

**7. Figure captions**

Figure 3.1. (a) GTOPO30 shaded relief map overlain with ASTER DEM, with Cretaceous-Miocene intermontane basins shown in black [from *Searle,* 1986*; Yin et al*., 1999; *Aitchison et al.,* 2002; *Li et al.,* 2010; *Wang et al;* 2010]. (b) Geologic map of ITSZ to the west of Leh. (c) Geologic map of area around Likir showing sample locations and ZHe age ranges. Filled circles depict geographic locations, whereas filled squares depict samples from this study.

Figure 3.2. (a) Stacked probability density curves, from bottom to top, of Indian detrital U-Pb data (*Myrow et al.* [2011] samples KU-2, Thango, PV and Batal), Basgo samples TRD and TRE from this study, and Eurasian U-Pb bedrock and detrital data (see Supplementary Material Appendix G for complete listing of sources for Eurasian data). Gray bands signify important modes common to the Basgo samples. (b) Compilation of detrital U-Pb data from classic Indus Group section in the Zanskar Gorge [*Wu et al.,* 2007; *Henderson et al*., 2010]. Curve is plotted at a different scale than those in (a), but x-axis is the same.

Figure 3.3. Probability density curve of all ZHe data from this study.

Figure 3.1.

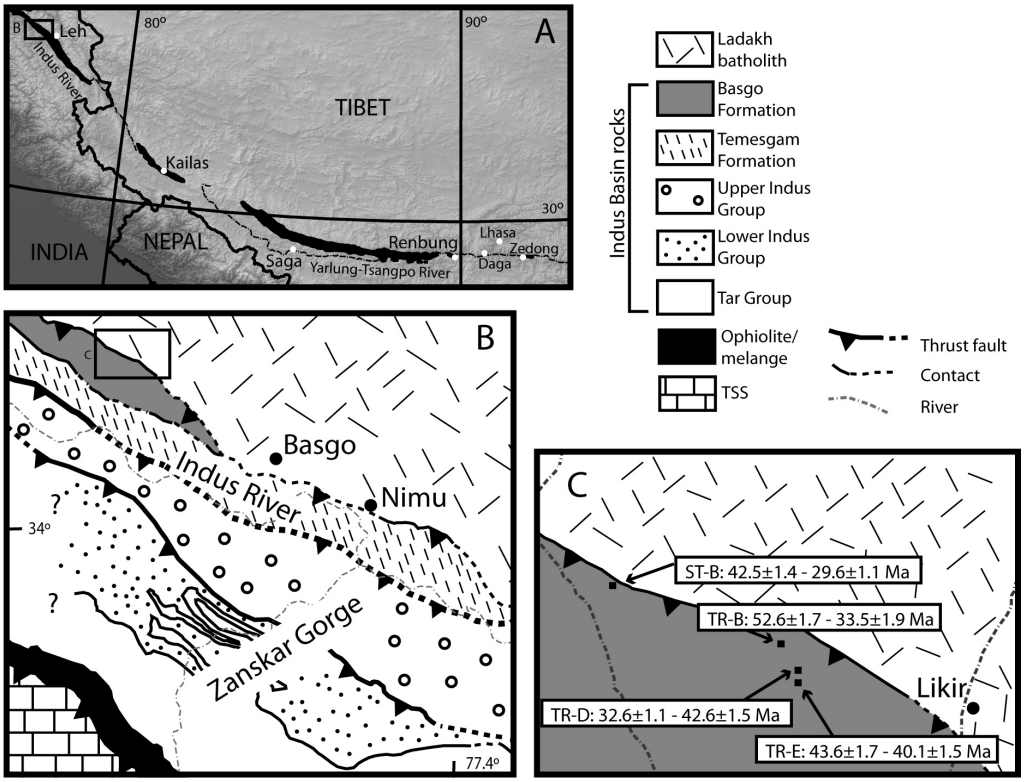
A
B
Leh
Indus River
80°
90°
TIBET
Kailas
30°
INDIA
NEPAL
Saga
Yarlung-Tsangpo River
Renbung
Lhasa
Zedong
Daga
B
C
Basgo
Nimu
Indus River
34°
?
?
Zanskar Gorge
77.4°
Ladakh batholith
Basgo Formation
Temesgam Formation
Upper Indus Group
Lower Indus Group
Tar Group
Indus Basin rocks
Ophiolite/ melange
TSS
Thrust fault
Contact
River
C
ST-B: 42.5±1.4 - 29.6±1.1 Ma
TR-B: 52.6±1.7 - 33.5±1.9 Ma
TR-D: 32.6±1.1 - 42.6±1.5 Ma
TR-E: 43.6±1.7 - 40.1±1.5 Ma
Likir

Figure 3.2.

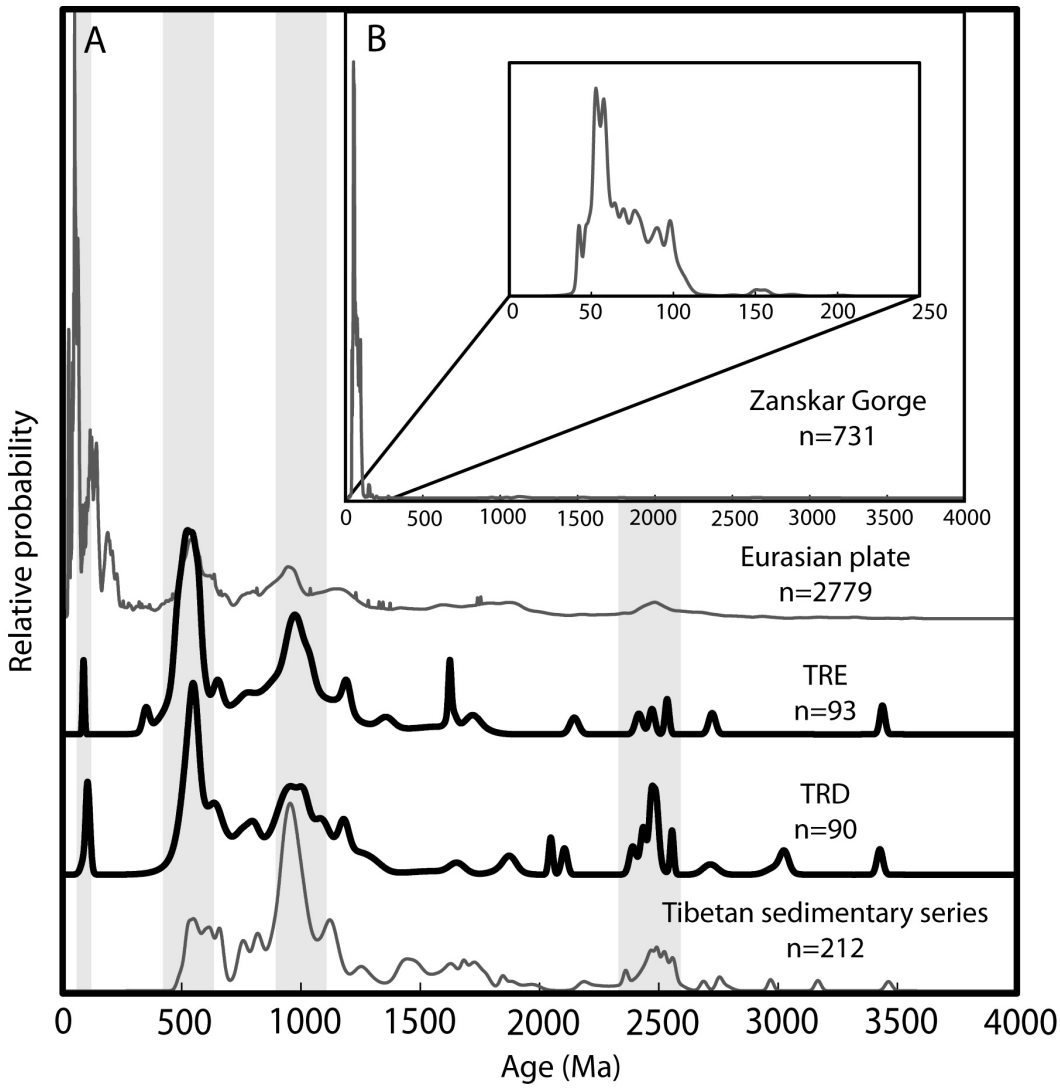
A
B
Relative probability
Zanskar Gorge
n=731
Eurasian plate
n=2779
TRE
n=93
TRD
n=90
Tibetan sedimentary series
n=212
0
500
1000
1500
2000
2500
3000
3500
4000
Age (Ma)
0
50
100
150
200
250

Figure 3.3.

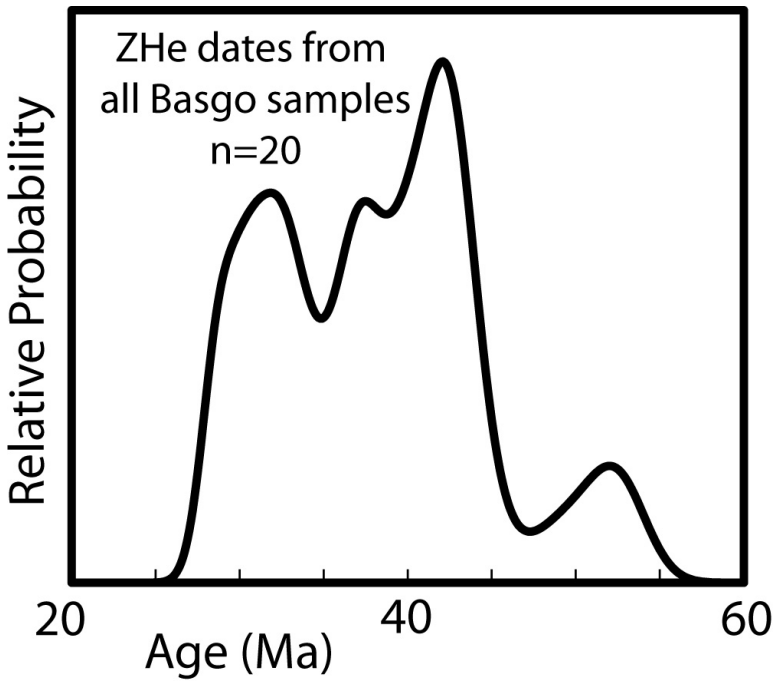
ZHe dates from
all Basgo samples
n=20
Relative Probability
20
40
60
Age (Ma)

# CHAPTER 4

# IDENTIFYING MIXED INDIAN-EURASIAN PROVENANCE IN THE INDUS BASIN MOLASSE SEQUENCE, NORTHWESTERN INDIAN HIMALAYA: IMPLICATIONS FOR THE TIMING OF COLLISON


## ABSTRACT

Cenozoic intermontane basins in southern Tibet preserve a record of the early stages of the India-Eurasia collisional event that initiated the Himalayan-Tibetan orogenic system. Of particular interest for establishing the age of collision are strata wherein both Indian- and Eurasian-derived detritus are identified.

We present a multifaceted isotopic and trace element geochemical study of Early Eocene-Miocene sediments of the Indus Basin of the Ladakh region in the northwestern Indian Himalaya. Based on previously published detrital zircon U-Pb geochronological studies, the majority of fine-grained detritus in these older units appears to indicate a distinctive Eurasian source. However, we present new data that suggests a more varied provenance for the Indus Basin strata. The distribution of detrital zircon U-Pb dates from quartzite cobbles within conglomeratic beds of the oldest molasse unit are comparable to those found in Indian passive margin units. Trace element geochemistry of mafic pebbles from throughout the older Indus Basin molasse units appear to demonstrate derivation from the Shyok suture zone, situated north of the local Eurasian source area. However, several clasts are geochemically similar to ophiolitic material found within the Indus-Tsanpgo suture zone separating India and Eurasia, implying sourcing from fragments of the Neo-Tethys Ocean basin caught up in the suture

or obducted onto the Indian passive margin prior to collision. $^{40}Ar/^{39}Ar$ cooling dates for detrital biotite from a sandstone unit intercalated with an upper Ypresian marine limestone (the youngest marine unit in the Indus Basin) are more consistent with an Indian plate source region than a Eurasian provenance. These results collectively point to an Early Eocene minimum age for India-Eurasia collision in this sector of the orogenic system.

**1. Introduction**

Sedimentary basins often record the erosional history of both active orogenic systems and ancient ones that have long-since eroded away. By focusing on detrital geochemical studies of such areas, this history can be reconstructed, particularly by application of detrital geochemical techniques that preserve different characteristics of sediment sources.

Geochemical studies of the units in intermontane sedimentary basins found near the Indus-Tsangpo suture zone (ITSZ) – a feature that marks the locus of the collision between India and Eurasia that led to development of the Himalayan-Tibetan orogenic system [*Hodges,* 2000] – provide an opportunity to better constrain the timing of India-Eurasia collision. Surprisingly, the timing of this important event remains controversial despite years of study. Some researchers, favor Late Cretaceous collision based on paleontological evidence for the exchange of terrestrial fauna during the Maastrichtian (*ca.* 70-65 Ma) [*Jaeger et al.,* 1989], and on provenance analysis of Cretaceous strata in Tibet that implies derivation of sediment from both sides of the suture zone [*Cai et al.,* 2011]. Proponents of Early Oligocene (*ca.* 34 Ma) collision cite paleomagnetic studies

that place India significantly south of Eurasia during Eocene time (*ca.* 55-34 Ma), and sedimentologic studies that imply only a minor contribution of pre-Oligocene orogen-derived clastic detritus to the Himalayan foreland [*Aitchison et al.,* 2007]. The most commonly referenced estimate for the timing of collision, between *ca.* 55-50 Ma, is largely based upon the coincidence of an apparent decrease in Indian ridge spreading rates [*Patriat and Achache,* 1984], an apparent decrease in the rate of northward motion of India [*Klootwijk et al.,* 1992; *Acton,* 1999], the timing of ultrahigh–pressure subduction-related metamorphism of the leading Indian margin [*Leech et al.,* 2005], and the age of the last marine sedimentary units [*Rowley,* 1996].

We addressed this controversy through geochemical studies of the detritus in one of the most accessible and best preserved of these intermontane depocenters, the Indus Basin of the northwestern Indian Himalaya (Figure 4.1). Although abundantly folded and faulted, its basic stratigraphy is relatively simple [*Tripathy et al.,* in prep.; Chapter 2] thus providing an ideal location at which to examine the provenance of the coarse clastic strata with the goal of determining the commencement of combined Indian–Eurasian sedimentation, and by inference, the collision of the Indian and Eurasian plates. We applied three geochemical techniques to various Indus Basin sedimentary units: detrital zircon U-Pb geochronology of quartzite cobbles; trace element geochemistry of mafic clasts; and detrital biotite $^{40}Ar/^{39}Ar$ thermochronology of sandstones. Armed with these results, we explored possible source areas, identified the oldest stratigraphic level at which mixed provenance can be demonstrated, and established the

minimum age of collision in this sector of the orogenic system as late Ypresian (Early Eocene, *ca*. 52-48 Ma), thereby confirming the conclusion of *Green et al.* [2008].

**2. General architecture of the Himalayan-Tibetan orogenic system**

The Himalayan-Tibetan orogenic system formed as a result of the closure of the Neo-Tethys Ocean and subsequent collision between India and Eurasia, the location of which is marked by the ITSZ [*Gansser*, 1980].

Immediately north of the ITSZ, intrusive igneous rocks of the Kohistan-Ladakh-Gangdese (KLG) batholith complex and associated volcanic units [*Honegger et al.,* 1982] likely represent an Andean-type arc built upon the southern margin of Eurasia prior to collision. These arcs form the southern margin of the Lhasa block, which includes much of the country rock [*Dewey et al.,* 1988]. In the Ladakh region, a belt of oceanic sediments and ophiolitic remnants (the Shyok suture zone, or SSZ [*Dunlap and Wysoczanski*, 2002], separates Ladakh batholith from another arc terrain to the northwest, the Karakoram block. Most researchers working in the region assign an Early Cretaceous age to this suturing event and regard final collision of the Indian and Eurasian continents as a younger phenomenon [e.g., *Treloar et al.,* 1989]. However, *Bouilhol et al.* [2011] have suggested that suture zone rocks that are typically mapped in the Ladakh region as ITSZ actually comprise an older suture between the Ladakh island arc complex within Neo-Tethys and India, whereas the SSZ represents a Middle-Late Eocene-aged (*ca.* 45-35 Ma) zone of collision between Eurasia and an amalgamated India-Ladakh mass to the south.

South of the ITSZ, the Indian plate elements of the orogen comprise the traditionally discussed tectonostratigraphic units of the Himalaya, which include, from north to south, the Tibetan Sedimentary Sequence (TSS), the Greater Himalayan Sequence (GHS), the Lesser Himalayan Sequence (LHS), and the Subhimalaya. All of these are separated by major north-dipping fault systems. The TSS comprises Neoproterozoic-Paleocene remnants of the precollisional Indian passive margin [*DeCelles et al.,* 2001], and is separated from the ITSZ by a north-vergent backthrust system that *Yin* [2006] defines as the Great Counter thrust along the length of the orogen. The southern boundary of the TSS, the South Tibetan fault system (STFS), is north-dipping normal fault system [*Burchfiel et al.,* 1992], which carries Proterozoic-Miocene metasedimentary and intrusive rocks of the GHS in its footwall [e.g., *Le Fort et al.,* 1987; *Miller et al.,* 2001]. The subjacent Miocene Main Central thrust system (MCTS) separates the GHS from unmetamorphosed to lower amphibolite facies, Early Proterozoic to Miocene supracrustal rocks of the Lesser Himalayan sequence. Those units are bounded to the south by the Middle Miocene-Pliocene Main Boundary thrust system (MBTS) [*DeCelles et al.,* 2001]. The LHS overthrusts Middle Miocene to Pliocene foreland basin sediments of the Subhimalaya [*Burbank et al.,* 1996; *DeCelles et al.,* 2001], which similarly overthrust the modern-day foreland basin along the Pliocene-Holocene Main Frontal thrust system [*Yeats et al.,* 1992]. Together, these tectonostratigraphic units represent an orogenic wedge that developed in the northern margin of the Indian plate during India-Eurasia collision.

## 3. Cenozoic intermontane basins of the ITSZ

The ITSZ itself is a narrow, structurally complex region that includes disaggregated exposures of ophiolites, precollisional forearc basin strata, and a series of syn- to post-collisional Cenozoic intermontane basins that frequently contain post-collisional molassic sedimentary deposits (Figure 4.1) [*Gansser*, 1980].

Molasse deposits in these basins have been mapped, from east to west, as the Luobosa, Dazhuqu, Liuqu, Qiuwu, Kailas and Indus Formations. Several of these basins have been correlated across several hundred kilometers because of lithologic similarities, particularly among conglomerate facies [*Aitchison et al.,* 2002]. However, age constraints of the purportedly correlative strata are poorly known in several of these regions, rendering such conclusions speculative.

### 3.1. Tibetan molasse basins

The easternmost Luobusa Formation can be traced approximately 100 km east of Zedong, terminating near the eastern syntaxis of the Himalaya. It comprises cobble- and boulder-conglomerates with clasts derived from all nearby tectonostratigraphic blocks [*Aitchison et al.,* 2002; *Yin et al.,* 1999]. Based upon the mixed provenance argument, the minimum age of collision (Oligocene-Miocene) is approximated by the depositional age of the oldest strata containing detritus from both sides of the orogenic system [*Badengzhu*, 1981].

The Dazhuqu Formation, located southwest of Lhasa near Renbung, can be traced eastward to Daga, and is dominated by coarse clastic rocks of mixed provenance [*Aitchison et al.,* 2002]. Unfortunately, it has not been studied in

detail, so any correlation made with similar sections along the ITSZ should be considered tentative.

The Liuqu conglomerates, exposed in the area south of Xigaze, record derivation from both the Indian and Eurasian plates based upon combined U-Pb dates and Hf-isotopic characteristics of zircon [*Wang et al.,* 2010] The minimum age of collision, interpreted as Middle to Late Eocene (*ca.* 48-34 Ma), is estimated from the maximum age of deposition determined by detrital U-Pb zircon geochronology and arguments regarding the uplift of one of its source areas. *Wang et al.* [2010] interpret these strata to record a Middle Eocene minimum age of collision.

North of the Liuqu conglomerates lie rocks that are superficially similar to the Dazhuqu Formation; they have been variably referred to as the Qianbulin Formation [*Wang et al.,* 2010] and the Qiuwu Formation [*Aitchison et al.,* 2002]. Using palynology, *Li et al.* [2010] have identified the Qianbulin Formation as Cretaceous, and have argued that the overlying Qiuwu rocks represent an overlying Eocene to Miocene fining upward sequence.

The Kailas Formation, among the best studied of the Tibetan molasse basins, comprises both fluvial and lacustrine deposits, with only the uppermost strata demonstrating mixed provenance [*DeCelles et al.,* 2011]. Dating of detrital and igneous zircons by U-Pb geochronology suggests that most of the Kailas Formation was deposited between 26-24 Ma [*DeCelles et al.,* 2011]. Therefore, these strata yield an Oligocene minimum age of collision, based upon evidence for mixed provenance. A*itchison et al.* [2002] correlated Kailas Formation strata

with deposits to the west that lie along the Indus River, which are collectively referred to the Indus Basin deposits.

### 3.2. The Indus Basin

The Indus Basin, located in the Ladakh region of northwest India, is potentially one of the most important of the Cenozoic intermontane basins for understanding the timing of collision [*Rowley,* 1996]. Sedimentary rocks within the Indus Basin span at least the Early Eocene to Early Miocene (*ca.* 55-19 Ma), and record a transition from marine to terrestrial deposition. We follow the nomenclature of *Tripathy et al.* [in prep.; Chapter 2], in which the Indus Basin was informally subdivided into four macrostratigraphic units (Figure 4.2). We briefly summarize each unit in terms of its stratigraphy, age, and provenance as determined from previous studies focused along the Zanskar Gorge and Leh-Manali road transects through the Indus Basin succession (Figure 4.3).

#### 3.2.1. Tar Group

The Tar Group includes marine strata within the Indus Basin: shales, sandstones and limestones, with black limestones dominating the upper parts of the unit. The Tar Group can be broadly subdivided into the Nindam forearc rocks [e.g., *Fuchs*, 1984; *Clift et al.*, 2002], the Ypresian (*ca.* 55-49 Ma) Jurutze Formation [*Henderson et al.,* 2010], and the upper Ypresian (*ca.* 50 Ma) Sumda Formation and Nummulitic Limestone [*Henderson et al.,* 2010]. Although originally mapped as separate units, *Tripathy et al.* [in prep.; Chapter 3] demonstrated that, in the Zanskar Gorge, the Sumda Formation and Nummulitic Limestone are likely temporally and spatially correlative. Along the Leh-Manali

road transect (Figure 4.3), the Tar Group forms the core of an antiform, upon which continentally derived strata lie both to the north and south, as observed by *Brookfield and Andrews-Speed* [1984].

*Henderson et al.* [2010, 2011] presented detrital zircon U-Pb geochronology data from three Tar Group samples. Collected from the Jurutze Formation and the Sumda Formation/Nummulitic Limestone, their dataset implies derivation of material predominantly from the Kohistan-Ladakh-Gangdese arcs (hereafter referred to as the KLG arc system).

### 3.2.2. Lower Indus Group

The Lower Indus Group conformably overlies the Tar Group in the Zanskar Gorge transect, and flanks either side of the Tar Group antiform exposed along the Leh-Manali road transect. In the Zanskar Gorge, and on the northern flank of the anticlinorium, the Lower Indus Group is refered to as the Chogdo Formation, which consists of cyclical packages of red shale and green sandstone. In general, the Chogdo Formation coarsens upwards such that the uppermost conglomerate unit is the Choksti Conglomerate of *Henderson et al.* [2010]. It is truncated by a major backthrust structure in both transects. The depositional age for the Chogdo Formation ranges from late Ypresian to Lutetian (*ca*. 52-45 Ma) (Figure 4.2).

The southern flank of the antiform comprises the Stok Kangri Formation of *Fuchs* [1984] and *Brookfield and Andrews-Speed* [1984]. Although the Chogdo and Stok Kangri Formations are not physically continuous, we nevertheless

consider it likely that the Stok Kangri Formation is time-correlative with parts of the Chogdo Formation (Figure 4.2).

Multiple detrital zircon U-Pb geochronologic studies have focused on Lower Indus Group strata, and yield superficially similar results, although the maximum age of deposition and location of major modes vary among different samples [*Wu et al.,* 2007; *Henderson et al.,* 2010; 2011]. The U-Pb geochronologic data, as well as Hf isotopic data from two samples studied by *Wu et al.* [2007] imply a KLG arc source.

The Stok Kangri Formation contains muscovite, which has been interpreted to imply an Indian source area [*Henderson et al*., 2011]. If this interpretation is correct, then the Stok Kangri Formation records the first mixed Indian and Eurasian provenance, and could be interpreted to indicate a minimum age of collision of early Lutetian (*ca.* 48 Ma). However, muscovite is not strictly an Indian plate-derived mineral in this region [*Singh et al*., 2007] and may not be a robust indicator of Indian provenance.

### 3.2.3. Upper Indus Group

The Upper Indus Group can be subdivided into three major units. The Choksti Formation, which is well exposed east of the Zanskar Gorge, is likely Middle Eocene (Lutetian) or younger in age (<45 Ma) [*Wu et al.*, 2007], and is in thrust contact with the underlying Lower Indus Group. Choksti Formation rocks comprise mostly black shales and sandstones, with subordinate red and green shales and cobble conglomerates towards the top of the section. However, east of the Zanskar Gorge, this unit is significantly more conglomeratic. The Hemis

Formation, present along the Leh-Manali road transect, preserves cyclical sandstone and conglomerate packages, with the conglomerates containing abundant clasts derived from the Ladakh batholith [*Tripathy et al.,* in prep.; Chapter 2]. Its maximum age of deposition is Late Eocene (Priabonian, *ca.* 34 Ma; *Tripathy et al.,* [in prep.; Chapter 2]). The Nimu Formation, which is mainly exposed in the Zanskar Gorge, comprises mostly black shales that preserve plant remains, gray sandstones, and occasional cobble conglomerates. The upper parts of the section are as young as Early Oligocene (*ca.* 30 Ma) [*Tripathy et al.,* in prep.; Chapter 2].

*Wu et al.* [2007] presented detrital zircon U-Pb geochronologic data from both the Choksti and Nimu Formations, and the dates again indicate derivation from the KLG arc sources. However, the Hf isotopic signature of the sample collected from the Nimu Formation more closely matches the Lhasa block, implying that additional parts of Eurasia were eroding into the Indus Basin. Furthermore, all three units contain detrital muscovites, which could (but does not necessarily) imply an Indian source [*Henderson et al.,* 2010].

### 3.2.4. Basgo Group

The Basgo Group includes both the Basgo Formation and the conformably overlying Temesgam Formation. The Basgo Formation is distinct from the other Indus Basin strata because of its mustard colored sandstones, highly calcareous sandstones and shales, and the presence of ostracods within it that have been dated as Late Oligocene (*ca.* 28-23 Ma) [*Bajpai et al.,* 2004]. The conformably overlying Temesgam Formation, which is exposed north of the Zanskar Gorge,

contains gray-yellow sandstones and blue-gray shales, with the occasional red shale horizon. In fault contact with the Nimu Formation, the Temesgam is as young as Miocene (*ca.* 19 Ma) toward the top of the section [*Henderson et al*., 2010]. The Basgo Group has been thrust over the Ladakh batholith.

The Basgo Formation contains cobbles and boulders in conglomeratic horizons that are sourced directly from the Ladakh batholith, thus providing clear evidence of the KLG arc source [*Garzanti and Van Haver,* 1988]. However, detrital zircon U-Pb geochronologic data from sandstones indicate a drastically different source area than the remainder of the Indus Basin rocks, with age distributions matching the TSS of the Indian plate [*Tripathy et al.,* in review; Chapter 3]. Therefore, the Basgo Formation provides ample evidence for a mixed Indian-Eurasian provenance, and implies a minimum Early Oligocene age of collision. Moreover, the Basgo Formation is the only part of the Indus Basin that unequivocally demonstrates mixed provenance in the literature.

**4. Detrital zircon U-Pb geochronology of quartzite clasts**

We have taken a unique approach to seeking distinctly Indian plate detritus by focusing on the conglomerate clasts, which likely came from a more proximal source area than the finer-grained sands that are usually studied. In particular, we hypothesize that quartzite clasts from the Stok Kangri Formation of the Lower Indus Group were derived from the TSS, and contain a similar detrital zircon U-Pb geochronologic signature to the sandstones that are presently exposed to the south of the Indus Basin [*Myrow et al.,* 2010].

### 4.1. Methods and results

To test this hypothesis, we collected multiple cobble-sized quartzite clasts from two conglomerate beds (Figure 4.2). For each sample locality, we combined all the clasts together to ensure sufficient numbers of zircon for dating. Thus, for each conglomerate bed, if there existed multiple quartzite source areas, we would be unable to deconvolve the mixed signal without *a priori* knowledge of the source area.

Zircon crystals were extracted from crushed samples by traditional gravimetric and magnetic susceptibility methods designed to concentrate heavy minerals. A large split of zircon grains was incorporated into a 1" epoxy mount together with fragments of University of Arizona Sri Lanka standard zircon [*Gehrels et al.*, 2008]. The mounts were polished, imaged photographically, examined with a cathodoluminescence detector at the Arizona State University LeRoy Eyring Center for Solid State Science using a JEOL 840 scanning electron microscope, and cleaned prior to isotopic analysis.

U-Pb geochronology was conducted by laser ablation multicollector inductively coupled plasma mass spectrometry (LA-MC-ICPMS) at the Arizona LaserChron Center [*Gehrels et al.,* 2006, 2008]. The procedure generally follows that of *Gehrels et al.* [2011], but we provide details for our specific analytical session. Zircons were ablated with a New Wave UP193HE Excimer laser using a spot diameter of 30 μm and pit depths of ~15 μm. The ablated material was carried in helium into the plasma source of a *Nu* HR ICPMS for simultaneous measurement of U, Th, and Pb isotopes. All measurements were made in static

mode, using Faraday detectors with $3x10^{11}$ ohm resistors for $^{238}U$, $^{232}Th$, $^{208}Pb$, $^{207}Pb$, $^{206}Pb$, and discrete dynode ion counters for $^{204}Pb$ and $^{202}Hg$. Ion yields were ~0.8 mV per ppm. Each analysis consisted of one 15-second integration on the isotope peaks with the laser off (for backgrounds), 15 one-second integrations with the laser firing, and a 30-second delay to purge the previous sample and prepare for the next analysis.

For each analysis, the errors in determining $^{206}Pb/^{238}U$ and $^{206}Pb/^{204}Pb$ generally resulted in measurement errors of ~1-2% (at $2\sigma$ level) in the $^{206}Pb/^{238}U$ age. The errors in measurement of $^{206}Pb/^{207}Pb$ and $^{206}Pb/^{204}Pb$ generally also resulted in ~1-2% (at $2\sigma$ level) uncertainties in age for grains that are >1.0 Ga, but were substantially larger for younger grains due to the low intensity of the $^{207}Pb$ signal. For most analyses, the crossover in precision of $^{206}Pb/^{238}U$ and $^{206}Pb/^{207}Pb$ ages occurred at ~1.0 Ga.

$^{204}Hg$ interference with $^{204}Pb$ was accounted for by measurement of $^{202}Hg$ during laser ablation and subtraction of $^{204}Hg$ according to the natural $^{202}Hg/^{204}Hg$ ratio of 4.35. This Hg correction was not significant for most analyses because Hg backgrounds were low (typically ~150 cps at mass 204). Common Pb correction was accomplished using the Hg-corrected $^{204}Pb$ and assuming an initial Pb composition from *Stacey and Kramers* [1975], with uncertainties of 1.5 for $^{206}Pb/^{204}Pb$ and 0.3 for $^{207}Pb/^{204}Pb$.

Inter-element fractionation of Pb/U was generally ~5%, whereas apparent fractionation of Pb isotopes was generally <0.2%. In-run analyses of fragments of a large Sri Lanka zircon crystal (generally every fifth measurement) with a known

U-Pb age of 563.5 ± 3.2 Ma (2σ error; *Gehrels et al.,* [2008]) were used to correct for this fractionation. The uncertainty resulting from the calibration correction was generally 1-2% (2σ) for both $^{206}Pb/^{207}Pb$ and $^{206}Pb/^{238}U$ ages. Concentrations of U and Th were calibrated relative to the same zircon standard, which contains ~518 ppm of U and 68 ppm Th [*Gehrels et al.,* 2008].

The U-Pb analytical data are reported in Supplementary Material Appendix H. Uncertainties shown in these tables are at the 2σ level, and include only the analytical errors. Analyses that were >20% discordant (by comparison of $^{206}Pb/^{238}U$ and $^{206}Pb/^{207}Pb$ ages) or >5% reverse discordant were not considered further [*Gehrels et al*., 2011].

The resulting interpreted ages are shown in relative age-probability diagrams using a Matlab program written at Arizona State University. These probability density curves show the summation of each age and its associated Gaussian uncertainty (for analytical errors only) as a single curve. The area under each curve is normalized to 1 according to the number of constituent analyses. The ordinates for the curves plotted in Figure 4.4 have the same scale, such that the relative peak heights of different curves have significance.

## 4.2. Provenance interpretation

### 4.2.1. Potential source areas

To facilitate comparison, we plot zircon U-Pb dates from potential source areas on either side of the ITSZ as stacked probability density curves (Figure 4.4), with explicit focus upon published detrital zircon U-Pb geochronologic data from pre-Tertiary sandstones. For the northern Eurasian source area, we consider data

from sandstones on the Lhasa block, as presented by *Gehrels et al.* [2011]. For the Indian southern source area, we focus only on sandstones from the TSS and upper parts of the LHS that span sample locations from Bhutan to Pakistan, which *Geherls et al*. [2011] interpret as equivalent and, as a consequence, combine. We restrict the comparison to the adjacent local Lhasa block and TSS-type source areas because it is unlikely that the cobbles were derived from beyond central Tibet. Furthermore, we only plot pre-Cenozoic source area datasets. The three Cenozoic dates in this dataset (sample 09-AT-LM-Z, Supplementary Material Appendix H) likely represent sandstone matrix from the outer edges of the cobbles that was not completely removed during sample preparation. As such, we exclude these three dates from the probability density curve in Figure 4 for a more accurate comparison between the hypothesized source areas for the cobbles themselves.

Four major modes are apparent in the TSS dataset from *Gehrels et al.* [2011] (gray bands in Figure 4.4). Mode 1 is centered at approximately 150 Ma. Mode 2 comprises a broad peak between 450-550 Ma. Mode 3 is centered at approximately 900 Ma, and Mode 4 is located at 2500 Ma. Data exist between major modes, but are not abundant, except for a very broad scatter of dates between 1500-2000 Ma.

When compared to the Lhasa block age spectrum (Figure 4.4), the TSS modes 1 and 4 are interpreted as diagnostic of an Indian source, as these modes are not observed in the Eurasian Lhasa block age spectrum. Modes 2 and 3 broadly overlap with both Indian and Lhasa block spectra and are therefore non-

diagnostic for either source terrane. However, in the Lhasa block age spectra, there is an apparent age peak between 1000-1200 Ma which is far less pronounced in the TSS spectrum (Figure 4.4). Although this mode cannot be considered diagnostic, it is suggestive of derivation from the Lhasa block.

### 4.2.2. Comparison of detritus with bedrock sources

The U-Pb zircon age distribution of sample 09-AT-LM-Z (Figures 4.3 and 4.4) contains five major modes. A distinct Cretaceous mode broadly overlaps Mode 1 of the TSS spectrum. Although less prominent, two modes are present in the Triassic and middle Paleozoic. Neither is particularly distinctive in the reference Lhasa block or TSS spectra. The final two modes – one similar to Mode 2 and a more diffuse peak between 800 and 1300 Ma –could match either reference spectrum and are thus not diagnostic. Although the spectrum for this sample superficially resembles the TSS age spectrum, it is possible that this sample contains a mix of cobbles derived from either potential source. Based on the presence of diagnostic Mode 1 zircon dates, we infer that at least some of the cobbles were sourced from the Indian Plate.

Sample 09-AT-LM-Y (Figure 4.3) has a different age spectrum than 09-AT-LM-Z, and presents six major modes and multiple minor modes (Figure 4.4). The most prominent mode is Triassic in age, and this corresponds to a similar mode in 09-AT-LM-Z, but U-Pb zircon ages in this range are not common in either the TSS or Lhasa block reference spectra. A second major mode comprises the same Cambrian mode found in all other age spectra. Between 1100-1300 Ma the next mode is encountered, which most closely corresponds to the Lhasa block

age spectrum, but is not diagnostic because zircons of this age are also present in the TSS age spectrum. We consider the peaks between 1500-2000 Ma as a diffuse scattering of dates that comprise the fourth mode of this sample's age spectrum; this range is not specific to either source area. A distinct peak at 2500 Ma corresponds to Mode 4 of the TSS age spectrum. Another mode, between 2700-2800 Ma is, again, not diagnostic of either source area. Therefore, although this age spectrum is distinct from the previous sample, we interpret it similarly. Most modes are not specific to either potential source area, implying that either could have contributed clasts, but the presence of Mode 4, which is diagnostic of a TSS source, suggests that at least some of these cobbles were sourced from the Indian plate. Therefore, we interpret these data to imply a mixed Indian-Eurasian source, particularly when coupled with published U-Pb detrital zircon geochronology from sandstones that imply a Eurasian provenance [*Henderson et al.,* 2011].

**5. Trace element geochemistry of mafic clasts**

By comparing the trace element geochemistry of the ophiolites of the ITSZ and SSZ, *Ahmad et al.* [2008] was able to demonstrate that these mafic rocks can be distinguished from one another based upon their chondrite-normalized rare earth element (REE) diagrams, primitive mantle-normalized multi-element patterns, and discrimination diagrams for the least mobile elements. Thus, the trace element geochemical signatures for individual mafic clasts collected from conglomerates throughout the Indus Group should provide further insights regarding clast provenance.

Ophiolitic rocks within the ITSZ are representative of the Neo-Tethys ocean basin that separated India and Eurasia prior to collision. Farther to the east, in southern Tibet, large tracts of ophiolitic material mark the trace of the ITSZ [*Gansser*, 1980]. In northwestern India, the ITSZ is mostly a tectonic mélange with relatively minor metabasaltic components [e.g., *Honegger et al*., 1982]. True ophiolites in northwestern India, such as the Spontang ophiolite, exposed not far from the study area, were obducted onto the North Indian continental margin prior to the final stages of collision [*Searle et al.,* 1997]. As a consequence, we interpret the derivation of clasts from an "ITSZ ophiolite" as likely indicative of derivation from the Indian Plate, though we cannot rule out derivation from the suture zone itself. Ophiolitic rocks with SSZ characteristics most likely derive from the SSZ itself, which was either internal to the Eurasian plate during Indus Basin sedimentation or external such that it marked a later collision zone between Eurasia and an amalgamated Ladakh-India block, following the recent interpretation of *Bouilhol et al*. [2011].

**5.1. Methods and results**

We collected a minimum of four mafic clasts per sample from four conglomeratic horizons in the Lower and Upper Indus Group exposed in the Zanskar Gorge (Figures 4.2 and 4.3), yielding a total of 26 mafic clasts. Each clast was individually powdered using a ceramic ball mill to minimize trace metal contamination.

Approximately 50 mg of powder was weighed per sample and digested in concentrated HF and $HNO_3$ on a hotplate for 12 hours. The solutions were dried

and concentrated HCl was added. The mixture was heated for 12 hours to digest any fluoride salts. The solutions were subsequently dried, and the remainders were dissolved in 0.32 M $HNO_3$ for analysis by quadrupole ICP-MS. To control the quality of our procedure, we processed blanks and two U.S. Geological Survey (USGS) basalt reference samples – BCR-2 (Columbia River Basalt) and BIR-1 (Icelandic Basalt) – alongside the unknowns. These standards were chosen for both their lithology and reference values of elements of interest.

The measurement of selected major, minor and trace elements was performed on a Thermo *X-series* quadrupole mass spectrometer in the W. M. Keck Foundation Laboratory for Environmental Biogeochemistry at Arizona State University. For minor and trace elements, we used a dilution factor of ~1:1,000, and ~1:25,000 for the major elements. Calibration and optimization of the instrument was done using a series of internal standards to create a set of calibration curves for the analyzed elements at levels of ~650 ppb, ~100 ppb, ~25 ppb, ~5 ppb, ~1 ppb, ~500 ppt, ~100 ppt and ~50 ppt. After initial calibration, one of these calibration solutions was run after approximately five unknowns to monitor reproducibility, which was generally around 10%, but could be as high as 15% for elements that were difficult to measure, such as phosphorous. During analysis, a Ge-In-Bi internal standard was simultaneously introduced with sample solutions to monitor plasma suppression throughout the course of the run, which explains some of the variability in the repeated measurements of the calibration curve solutions.

The analytical software package corrected for the system blank and applied the calibration curve before producing "raw" data in concentration form. These data were then corrected for process blanks, and the exact dilution factor was applied to each sample. Analyses less than the limit of detection (LOD) for each element, reported in Table 4.1, were discarded. Accuracy was checked using external standards BCR-2 and BIR-1, and both accuracy and reproducibility are reported in Table 4.1. We regard the accuracy with which we can measure these external standards as the most robust estimation of error associated with these analyses, particularly because the analytical imprecision associated with each measurement is generally much smaller, sometimes less than 1% (1σ), when compared to reproducibility of the standards, which can be as high as 20%. The final concentrations are presented in Table 4.1.

## 5.2. Provenance interpretation

### 5.2.1. Potential source areas

Because this study focuses on individual mafic pebbles that have undergone a relative complex thermal history since their initial formation, we focused on REE patterns, which are distinctive to each potential source area in the Ladakh region [*Ahmad et al*., 2008].

*Rolland et al.* [2000; 2002] divided the SSZ in this region into western and eastern domains, based upon geochemical characteristics and subsequent interpretation. The Western Ladakh domain was further subdivided into Northern and Southern groups, which are differentiable based upon differences in Nb depletion. However, as shown in Figure 4.5, the average chondrite-normalized

REE patterns for all Northern Group (curve A) and Southern Group (curve B) samples are similar in that they both demonstrate enrichment in LREE, a flat heavy REE (HREE) pattern, and no Eu anomaly (Figure 4.5). Rolland and co-workers [2000; 2002] interpret these data as evidence of a back-arc basin tectonic setting. In contrast, the Eastern Ladakh domain preserves basalts that are more enriched in LREE relative to HREE than their western counterparts, and have marked negative Eu anomalies (Figure 4.5). Rolland et al. [2000; 2002] interpreted these data, coupled with additional geochemical evidence, as characteristic of a mature volcanic arc that is unrelated to a back-arc basin setting. We refer to REE patterns that have a negative slope and Eu anomaly as Type 1 (Eastern Ladakh type), and those that have a negative slope but lack a Eu anomaly as Type 2 (Western Ladakh type).

For the ITSZ of the Ladakh region, *Ahmad et al.* [2008] presented data from the Nidar complex. Both plutonic and volcanic rocks have nearly flat to slightly depleted REE patterns, and show a distinct positive Eu anomaly in some cases. Coupled with additional geochemical information, they interpreted this complex as containing mafic rocks of an intraoceanic subduction environment. The average chondrite-normalized REE curve for the data presented therein is plotted on Figure 4.5, and is distinctive, particularly because of its positive slope. We refer to these as Type 3 REE patterns.

### 5.2.2. Comparison of detritus with bedrock sources

Based on the chondrite-normalized REE patterns of the mafic clasts from the four samples analyzed in this study, we are able to divide the dataset based

upon REE pattern type (Figure 4.6), as defined above. The vast majority of the clasts resemble SSZ ophiolites from both the eastern (Type 1) and western (Type 2) domains, while three clasts preserve the Type 3 REE pattern characteristic of the ITSZ (Figure 4.6), which could imply a mixed provenance. We explored this further with the use of a discrimination diagram, where we plot primitive mantle-normalized La versus the primitive mantle-normalized Yb/La ratio. Such diagrams are often used to demonstrate the degree of partial melting, and in part, expresses the steepness of the REE pattern (Figue 4.7).

As expected, most of the clasts that showed Type 1 and Type 2 patterns plot within the field drawn from the Eastern and Western Ladakh datasets [*Rolland et al.,* 2000; 2002], with the exception of five clast analyses that are immediately adjacent to and above this field. All but one of the three analyses that were characterized as having Type 3 REE patterns indicative of an ITSZ source plot within the Nidar complex field. This supports our subdivision based on chondrite normalized REE patterns, and suggests that the majority of these clasts were derived from the SSZ, but a select few clasts are of Neo-Tethyan affinity. All conglomerate horizons examined in this study contain clasts that preserve varying REE types, such that no stratigraphic correlation can be made with our dataset. Thus, we interpret these data to represent mixed provenance with an SSZ source and an ITSZ source.

**6. Detrital biotite $^{40}Ar/^{39}Ar$ thermochronology**

Our final dataset includes detrital biotite $^{40}Ar/^{39}Ar$ dates from a sample (08-AT-ZG-A) collected from one of several sandstone horizons intercalated with

the last marine limestone of the Tar Group (Figures 4.2 and 4.3), which is late Ypresian (*ca.* 52-48 Ma) in age [*Henderson et al.,* 2010]. Biotite is a common rock-forming mineral in the Ladakh batholith today. We originally hypothesized that if these grains were derived from the batholith they would record the earliest part of its cooling history. However, if an Indian provenance can be demonstrated, this would be the lowermost (and best dated) unit within the Indus Basin to contain Indian detritus.

**6.1. Methods and results**

Here, we describe the procedure of the Arizona State University Noble Gas, Geochronology and Geochemistry Laboratories ($NG^3L$) in detail. Biotite grains were handpicked from the 250-100 μm aliquot, cleaned in acetone, methanol, and deionised water, and individually wrapped in aluminium foil packets. For the irradiation package, sample packets were regularly interspersed with packets of biotite age standard HD-B1 (24.18 ± 0.09 Ma, *Schwarz and Trieloff,* [2007]) to monitor the neutron flux gradient, along with natural and synthetic salts to determine interfering nuclear production ratios. The small aluminium disks into which the packets were loaded were then stacked and secured together to make up the irradiation package, which was then Cd shielded and irradiated for 5 hours at a near-core position (5C) within the McMaster University nuclear reactor, Hamilton, Ontario, Canada.

Upon return, individual age standard and unknown sample grains were loaded into a 61 mm diameter aluminium palette containing a series of 2 x 2 x 2 mm holes. The palette and a glass coverslip were loaded into an ultra-high

vacuum 4.5" laser chamber with a Kovar glass viewport and baked at 120°C for one day and then pumped at ultrahigh vacuum for one day to remove adsorbed atmospheric argon from the samples and chamber walls.

To degas and melt each grain, a 60 W IPG Photonics infrared (970 nm) diode laser, with computer-controlled Photon Machines optics and X-Y-Z stages linked to a Newport controller, was fired such that two minutes of lasing with a 50 W, 0.6 mm diameter beam was sufficient to ensure total fusion of each grain. The gases released by laser heating were purified for an additional two minutes using two SAES NP10 getter pumps (one at 400°C and one at room temperature) to remove all active gases. The remaining gases were equilibrated into a high sensitivity multi-collector mass spectrometer (Nu Instruments *Noblesse*), containing a Nier-type source operated at 400 mA. The Ar isotopes were measured using a 1 x $10^{11}$-Ohm Faraday detector or an ETP ion counting multiplier, depending upon the $^{40}$Ar signal size. Detector intercalibration for $^{40}$Ar was performed using multiple air shots. Laser heating, X-Y stage movement, automated valve operation, and data acquisition was automated and computer controlled using the *Mass Spec* software program. Errors throughout this paper are quoted at the 2σ confidence level. $^{40}$Ar/$^{39}$Ar ages were calculated using the decay constant, branching ratio, and atmospheric $^{40}$Ar/$^{36}$Ar ratio recommended by *Steiger and Jäger* [1977]. J-values and errors are noted in data tables of the supplementary materials.

Total system blanks during the experiments were estimated as 1.80 x $10^{-16}$, 1.22 x $10^{-18}$, 9.12 x $10^{-20}$, 1.95 x $10^{-19}$, and 3.85 x $10^{-20}$ moles STP (standard

temperature and pressure) for $^{40}Ar$, $^{39}Ar$, $^{38}Ar$, $^{37}Ar$, and $^{36}Ar$, respectively. The sensitivities of the Faraday and ion counting detectors were 8.2314 x $10^{-13}$ moles/V and 1.4633 x $10^{-20}$ moles/cps, respectively. Unknown analyses were corrected for mass spectrometer discrimination using air shots. Measured $^{40}Ar/^{36}Ar$ air ratios varied from 296.39± 2.18 to 306.80±1.87 (1σ errors) during the unknown analyses. Nuclear interference correction factors were as follows: $^{40}Ar/^{39}Ar_K$ = 0.027945, $^{36}Ar/^{38}Ar_{Cl}$ = 316, Ca/K = 1.92234, and Cl/K = 0.16863.

We interpreted no data for experiments yielding less than 90% $^{40}Ar^*$ or having $^{40}Ar^*$ signals less than ten times the level of the $^{40}Ar$ blank. The remaining data for sample 08-AT-ZG-A are listed in the Supplementary Material Appendix I. On a relative probability density plot (Figure 4.8), these data exhibit a prominent mode at ~550 Ma with small secondary mode at ~475 Ma. Overall, the data include a range of $^{40}Ar/^{39}Ar$ detrital biotite cooling ages between 480.5 ± 5.4 to 608.0 ± 12 Ma.

**6.2. Provenance interpretation**

The prominent ~ 550 Ma mode in the $^{40}Ar/^{39}Ar$ data is highly significant. The U-Pb crystallization ages for various plutons in the Ladakh arc are exclusively Mesozoic or Cenozoic [e.g., *Honegger et al.,* 1982; *St. Onge et al.,* 2010]. K-Ar and $^{40}Ar/^{39}Ar$ biotite dates from the Ladakh arc are Lower-Middle Eocene, and there is no indication that they harbor significant amounts of non-radiogenic ("excess") $^{40}Ar$ that might result in our obtaining impossibly old $^{40}Ar/^{39}Ar$ total fusion dates for grains derived from the batholith [*Honegger et al*., 1982; *Clift et al*., 2002]. It is essentially impossible for the biotites in sample 08-

AT-ZG-A to represent a Ladakh batholith source. We are aware of no reports of ~ 550 Ma $^{40}Ar/^{39}Ar$ biotite dates from other parts of the Lhasa block, as the only confirmed Cambrian-Ordovician location is the non-biotite-bearing rhyolite terrane in the Xainza area [*Ji et al*., 2009]. Most $^{40}Ar/^{39}Ar$ biotite dates from the Himalayan realm, particularly from the Greater Himalayan sequence where metamorphic biotite is common, have Miocene or younger cooling ages.

However, some Proterozoic-Cambrian $^{40}Ar/^{39}Ar$ muscovite cooling ages have been obtained from the Lesser Himalayan sequence and Bengal Basin [*Wobus et al.,* 2003; *Najman et al.,* 2008]. The Bengal Basin dataset is especially interesting: *Najman et al.* [2008] presented detrital muscovite $^{40}Ar/^{39}Ar$ thermochronologic dates from the Paleocene to Early Eocene Tura and Sylhet Formations, which both contain a single major mode in the probability density curves that is centered at *ca.* 500 Ma. Because the depositional ages of these strata overlap the most likely depositional age of sample 08-AT-ZG-A, we posit that Cambrian to Ordovician detritus was likely common in the early stages of the initiation of collision. Thus, this detritus was synchronously shed both southward into the Bengal Basin and northward into intermontane depocenters such as the Indus Basin. If this hypothesis is correct, the sample 08-AT-ZG-A biotite dataset implies that the stratigraphically highest unit of the Tar Group contains detritus from the Indian plate. When considered in light of detrital zircon U-Pb dates for this part of the section that strongly indicate derivation from the Eurasian Lhasa block [*Henderson et al.*, 2010], our data suggest that the upper Tar Group records a mixed Indian and Eurasian provenance, such that both the Indian and Eurasian

plates were proximal to and eroding into the Indus Basin during upper Tar Group deposition.

**7. Synthesis and conclusions**

Despite the suggestion by *Henderson et al,* [2010] that only parts of the younger Indus Basin stratigraphy contain detritus derived from the Indian Plate (Upper Indus Group), we present multiple lines of geochemical evidence that suggest a mixed provenance throughout the depositional history of the Indus Basin. The U-Pb detrital zircon geochronology of quartzite clasts suggests a dominantly Indian source area, though some contribution from Eurasian sandstones is plausible. Trace element geochemistry suggests a predominately northerly source of mafic clasts from the Shyok suture zone. Following the conventional interpretation of an Early Cretaceous age for the Shyok suture, this implies that the mafic clasts in the Indus Basin predominately had a Eurasian source. However, if the interpretation of *Bouilhol et al.* [2011] regarding the significance of the SSZ is correct, our trace element geochemical results imply deposition of the Indus Basin succession after that younger collisional event, with material sourced from north of the Ladakh arc. This would imply an as yet unidentified unconformity between the late Ypresian upper Tar Group and the Lower Indus Group, which is generally observed to be a depositional contact. Detrital biotite $^{40}Ar/^{39}Ar$ dates from the sandstones intercalated with the late Ypresian marine limestones in the Tar Group of the Indus Basin are not consistent with dates from previously analyzed bedrock samples from the Ladakh batholith

or Lhasa block. Comparison with other datasets from the Indian realm of the orogenic system reveals potential sources there.

Collectively, the evidence supports an interpretation of the Indus Basin detrital record as containing a mixed Indian-Eurasian provenance throughout its depositional history. We conclude that collision in this region is no younger than late Early Eocene (*ca.* 52-48 Ma), and that the recent hypothesis that collision could be as young as Early Oligocene in this region, put forth by *Aitchison et al*. [2007] is unlikely to be correct. Moreover, we recommend that for other intermontane basins within the Indus suture zone, such studies as the one presented herein, where specfic clasts are chosen for study based upon their most likely source region, should be carried out to resolve this conflict regarding the timing of collision.

## 8. References


Acton, G. D., 1999, Apparent polar wander of India since the Cretaceous with implications for regional tectonics and true polar wander, in *The Indian subcontinent and Gondwana: A paleomagnetic and rock magnetic perspective,* edited by T. Radhakrishna et al., *geol. Soc. India Mem., 44,* 129-175.

Ahmad, T., T. Tanaka, H. K. Sachan, Y. Asahara, R. Islam, and P. P. Khanna (2008), Geochemical and isotopic constraints on the age and origin of the Nidar Ophiolitic Complex, Ladakh, India: Implications for the Neo-Tethyan subduction along the Indus suture zone, *Tectonophysics, 451*, 206-224.

Aitchison, J. C, A. M. Davis, Badengzhu, and H. Luo (2002), New constraints on the Indian-Asia collision: The lower Miocene Gangrinboche conglomerates, Yarlung Tsangpo suture zone, SE Tibet, *J. Asian Earth Sci., 21*, 253-265.

Aitchison, J. C., J. R. Ali, and A. M. Davis (2007), When and where did India and Asia collide?, *J. Geophys. Res.*, *112*, B05423, doi: 10.1029/2006JB004706.

Badengzhu (1981), (Compiler) Xizang Autonomous Region Sangri–Jiacha Regional Geology Reconnaissance Map 1:50,000, *Xizang Geol. Survey Geol. Team #2, Lhasa.*

Bajpai, S., R. C. Whatley, G. V. R. Prasad, and J. E. Whittaker (2004), An Oligocene non-marine ostracod fauna from the Basgo Formation (Ladakh Molasse), NW Himalaya, India, *J. Micropalaeontol., 23*, 3-9.

Bohon, W., K. Hodges, and J. R. Arrowsmith (2011), Refining estimates of Quaternary slip on the Karakoram fault system, Ladakh, northwest India, *submitted to Geology.*

Brookfield, M. E., and C. P. Andrews-Speed (1984), Sedimentology, petrography and tectonic significant of the shelf, flysch and molasse clastic deposits across the Indus suture zone, Ladakh NW India, *Sediment. Geol., 40*, 249-286.

Bouilhol, P., O. Jagoutz, F. O. Dudas, and J. M. Hanchar (2011), Dating the India-Eurasia collision through arc magmatic records, *Geophys. Res. Abstr., 13*, Abstract 1662.

Burbank, D. W., J. Leland, E. Fielding, R. S. Anderson, N. Brozovic, M. R. Reid, and C. Duncan (1996), Bedrock incision, rock uplift and threshold hillslopes in the northwestern Himalayas, *Nature, 379*, 505-510.

Burchfiel, B. C., Z. Chen, K. V. Hodges, Y. Liu, L. H. Royden, C. Deng, and J. Xu (1992), The South Tibetan detachment system, Himalayan orogen: Extension contemporaneous with and parallel to shortening in a collisional mountain belt, *Spec. Pap. Geol. Soc. Am., 269,* 41 pp.

Cai, F., L. Ding, and Y. Yue (2011), Provenance analysis of upper Cretaceous strata in the Tethys Himalaya, southern Tibet: Implications for timing of India-Asia collision, *Earth Planet. Sci. Lett., 305,* 195-206.

Clift, P. D., A. Carter, M. Krol, and E. Kirby (2002), Constraints on India-Eurasia collision in the Arabian Sea region taken from the Indus Group, Ladakh Himalaya, India, in *The Tectonic and Climatic Evolution of the Arabian Sea Region,* edited by P. D. Clift et al., *Geol. Soc. Spec. Publ., 195,* 97-116.

DeCelles, P. G., D. M. Robinson, J. Quade, T. P. Ojha, C. N. Garzione, P. Copeland, and B. N. Upreti (2001), Stratigraphy, structure, and tectonic evolution of the Himalayan fold-thrust belt in western Nepal, *Tectonics, 20*, 487-509.

DeCelles, P. G., P. Kapp, J. Quade, and G.E. Gehrels (2011), Oligocene-Miocene Kailas basin, southwestern Tibet: Record of postcollisional upper-plate extension in the Indus-Yarlung suture zone, *Geol. Soc. Am. Bull., 123*, 1337-1362.

Dewey, J. F. (1988), Extensional collapse of orogens, *Tectonics, 7,* 1123-1139.

Dunlap, W. J. and R. Wysoczanski (2002), Thermal evidence for early Cretaceous metamorphism in the Shyok suture zone and age of the Khardung volcanic rocks, Ladakh, India, *J. Asian Earth Sci., 20,* 481-490.

Fuchs, G. (1984), Note on the geology of the Markha-Nimaling Area in Ladakh (India), *Jahrb. Geol. Bundesanst., 127*, 5-12.

Gansser, A. (1980), The significance of the Himalayan suture zone, *Tectonophysics, 62*, 37-52.

Garzanti, E., and T. Van Haver (1988), The Indus clastics: forearc basin sedimentation in the Ladakh Himalaya (India), *Sediment. Geol., 59*, 237-249.

Gehrels, G. E., V. Valencia, and A. Pullen (2006), Detrital zircon geochronology by Laser-Ablation Multicolector ICPMS at the Arizona LaserChron Center, in *Geochronology: Emerging Opportunities, Paleontological Society Short Course, October 21, 2006, Philadelphia, PA,* edited by T. Olszewski et al., *Paleontol. Soc. Pap., I2,* 1-10.

Gehrels, G. E., V. Valencia, and J. Ruiz (2008), Enhanced precision, accuracy, efficiency and spatial resolution of U-Pb ages by laser ablation-multicollector-inductively coupled plasma-mass spectrometry, *Geochem., Geophys., Geosyst., 9*, Q03017, doi:10.1029/2007GC001805.

Gehrels, G. E., P. Kapp, P. DeCelles, A. Pullen, R. Blakely, A. Weislgel, L. Ding, J. Guynn, A. Marin, N. McQuarrie, and A. Yin (2011), Detrital zircon geochronology of pre-Tertiary strata in the Tibetan-Himalayan orogen, *Tectonic, 30*, TC5016, doi:10.1029/2011TC002868.

Green, O. R., M. P. Searle, R. I. Corfield, and R. M. Corfield (2008), Cretaceous-Tertiary carbonate platform evolution an the age of the India-Asia

collision along the Ladakh Himalaya (Northwest India), *J. Geol., 116*, 331-353.

Henderson, A. L., Y. Najman, R. Parrish, M. BouDagher-Fadel, D. Barford, E. Garzanti, and S. Ando (2010), Geology of the Cenozoic Indus Basin sedimentary rocks: paleoenvironmental interpretation of sedimentation from the western Himalaya during the early phases of India-Eurasia collision, *Tectonics, 29,* TC6015, doi:10.1029/2009TC002651.

Henderson, A. L., Y. Najman, R. Parrish, D. F. Mark, and G. L. Foster (2011), Constraints to the timing of India-Eurasia collision; a re-evaluation of evidence from the Indus Basin sedimentary rocks of the Indus-Tsangpo Suture Zone, Ladakh, India, *Earth-Sci. Rev., 106*, 265-292.

Hodges K. V. (2000), Tectonics of the Himalaya and southern Tibet from two perspectives, *Geol. Soc. Am. Bull., 112*, 324-350.

Honegger, K., V. Dietrich, W. Frank, A. Gansser, M. Thöni, and V. Trommsdorf (1982), Magmatism and metamorphism in the Ladakh Himalayas (the Indus-Tsangpo suture zone), *Earth Planet. Sci. Lett., 60*, 253-292.

Jaeger J.-J., V. Courtillot, and P. Tapponnier (1989), Paleontological view of the ages of the Deccan Traps, the Cretaceous/Tertiary boundary, and the India-Asia collision, *Geology, 17*, 316-319.

Ji, W. H., S. J. Chen, Z. M. Zhao, R. S. Li, S. P. He, and C. Wang (2009) Discovery of the Cambrian volcanic rocks in the Xainza area, Gangdese orogenic belt, Tibet, China, and its significance, *Geol. Bull. China, 28,* 1350-1354.

Klootwijk, C. T., J. S. Gee, J. W. Pierce, G. M. Smith, and P. L. McFadden (1992), An early India-Asia contact; paleomagnetic constraints from Ninetyeast Ridge, ODP Leg 121, *Geology, 20*, 395-398.

Leech, M. L., S. Singh, A. K. Jain, S. L. Klemperer, and R. M. Manickavasagam (2005), The onset of India-Asia continental collision: Early, steep subduction required by the timing of UHP metamorphism in the western Himalaya, *Earth Planet. Sci. Lett., 234*, 83-97.

Le Fort, P., M. Cuney, C. Ceniel, C. France-Lanord, S. M. F. Sheppard, B. N. Upreti, and P. Vidal (1987), Crustal generation of the Himalayan leucogranites, *Tectonophysics, 134*, 39-57.

Li, J.-G., Z.-Y. Guo, D. J. Batten, H.-W. Cai, and Y.-Y. Zhang (2010), Palynological stratigraphy of Late Cretaceous and Cenozoic collision

related conglomerates at Qiabulin, Xigaze, Xizang (Tibet) and its bearing on palaeoenvironmenta development, *J. Asian Earth Sci., 28*, 86-95.

Miller, C., M. Thöni, W. Frank, B. Grasemann, U. Klötzli, P. Guntli, and E. Draganits (2001), The early Paleozoic magmatic event in the Northwest Himalaya, India: source, tectonic setting and age of emplacement, *Geol. Mag., 138*, 237-251.

Myrow, P. M., N. C. Hughes, J. W. Goodge, C. M. Fanning, I. S. Williams, S. Peng, O. N. Bhargava, S. K. Parcha, and K. R. Pogue (2010), Extraordinary transport and mixing of sediment across Himalayan central Gondwana during the Cambrian-Ordovician, *Geol. Soc. Am. Bull., 122*, 1660-1670.

Najman, Y., M. Bickle, M. BouDagher-Fadel, A. Carter, E. Garzanti, M. Paul, J. Wijbrans, E. Willett, G. Oliver, R. Parrish, S. H. Akhter, R. Allen, S. Ando, E. Chisty, L. Reisberg, and G. Vezzoli (2008), The Paleogene record of Himalayan erosion: Bengal Basin, Bangladesh, *Earth Planet. Sci. Lett., 273*, 1-14.

Patriat, P., and J. Achache (1984), India-Eurasia collision chronology has implications for crustal shortening and driving mechanism of plates, *Nature, 311*, 615-621.

Rolland, Y., A. Pecher, and C. Picard (2000), Middle Cretaceous back-arc formation and arc evolution along the Asian margin: the Shyok Suture Zone in northern Ladakh (NW Himalaya), *Tectonophysics, 325*, 145-173.

Rolland, Y., C. Picard, A. Pecher, H. Lapierre, D. Bosch, and F. Keller (2002), The Cretaceous Ladakh arc of NW Himalaya – slab melting and melt-mantle interaction during fast northward drift of Indian Plate, *Chem. Geol., 182*, 139-178.

Rowley, D.B. (1996), Age of initiation of collision between India and Asia: A review of stratigraphic data, *Earth Planet. Sci. Lett., 145*, 1-13.

Searle, M. (1986), Structural evolution and sequence of thrusting in the High Himalayan Tibetan-Tethys and Indus suture zones of Zanskar and Ladakh, Western Himalaya, *J. Struct. Geol., 8*, 923-936.

Searle, M., R. I. Corfield, B. Stephenson, and K. McCarron (1997), Structures of the North Indian continental margin in the Ladakh Zanskar Himalayas: implications for the timing of the obduction of the Spontang ophiolite, India-Asia collision and deformational events in the Himalaya, *Geol. Mag., 134,* 297-316.

Singh, S., R. Kumar, M. E. Barley, and A. K. Jain (2007), SHRIMP U-Pb ages and depth of emplacement of Ladakh batholith, Eastern Ladakh, India, *J. Asian Earth Sci., 30,* 490-503.

Stacey, J. S., and J. D. Kramers (1975), Approximation of terrestrial lead isotope evolution by a two stage model, *Earth Planet. Sci. Lett., 26,* 207-221, doi:10.1016/002-821X(75)90088-6.

St.-Onge, M. R., N. Rayner, and M. P. Searle (2010), Zircon age determinations of the Ladakh batholith at Chumathang (Northwest India): Implications for the age of the India-Asia collision in the Ladakh Himalaya, *Tectonophysics, 495*, 171-183.

Steiger, R. H. and E. Jäger (1977), Subcommission on geochronology: Convention on the use of decay constants in geo- and cosmochronology, *Earth Planet. Sci. Lett., 36*, 21-23.

Sun, S.-S. and W. F. McDonough (1989), Chemical and Isotopic Systematics of oceanic basalts: implications for Mantle Composition and Processes, in *Magmatism in the Ocean Basings,* edited by A. D. Saunders et al., *Geol. Soc. Spec. Publ., 42,* 313-345.

Swartz, W. H. and M. Trieloff (2007), Intercalibration of $^{40}$Ar-$^{39}$Ar age standards NL-25, HB3gr hornblende, GA1550, SB-3, HD-B1 biotite and BMus/2 muscovite, *Chem. Geol. 242*, 218-231.

Treloar, P. J., D. C. Rex, P. G. Guise, M. P. Coward, M. P. Searle, B. F. Windley, M. G. Peterson, M. Q. Jan, and I. W. Luff (1989), K-Ar and Ar-Ar geochronology of the Himalayan collision in NW Pakistan: constraints on the timing of suturing, deformation, metamorphism and uplift, *Tectonics, 8*, 881-909.

Tripathy, A. K., K. V. Hodges, M. C. van Soest, and T. Ahmad (2011), Pre-Oligocene emergence of the Indian passive margin and the timing of Indian-Eurasian collision, *submitted to Geology.*

Tripathy, A. K., C. S. Edwards, K. V. Hodges, J.-A. Wartho, and F. J. Cooper, Lithologic mapping of complexly deformed sedimentary strata using ASTER multispectral imagery: Implications for the evolution of Indus Basin depocenters, Ladakh, NW India, *in preparation.*

Wang, J.-G., X.-M. Hu, F.-Y. Wu, and L. Jansa (2010), Provenance of the Liuqu Conglomerate in southern Tibet: A Paleogene erosional record of the Himalayan-Tibetan orogen, *Sediment. Geol., 231*, 74-84.

Wobus, C. W., K. V. Hodges, and K. X. Whipple (2003), Has focused denudation sustained active thrusting at the Himalayan topographic front?, *Geology, 31*, 861-864

Wu, F.-Y., P. D. Clift, and J.-H. Yang (2007), Zircon Hf isotopic constraints on the sources of the Indus Molasse, Ladakh Himalaya, India, *Tectonics, 26*, TC2014, doi:10.1029/2006TC002051.

Yeats, R. S., T. Nakata, A. Farah, M. Fort, M. A. Mirza, M. R. Pandey, and R. S. Stein (1992), The Himalayan frontal fault system, *Ann. Tectonicae, 6*, 85-98.

Yin, A., T. M. Harrison, M. A. Murphy, M. Grove, S. Nie, F. J. Ryerson, X. F. Wang, and Z. L. Chen (1999), Tertiary deformational history of southeastern and southwestern Tibet during the Indo-Asian collision, *Geol. Soc. Am. Bull., 111*, 1644-1664.

## 9. Figure captions

Figure 4.1. Shaded relief map derived from GTOPO30 (30m/pixel DEM) overlain with ASTER DEM (15m/pixel), with Cretaceous-Miocene intermontane basins shown in black from *Searle* [1986], *Yin et al.* [1999], *Aitchison et al.* [2002], *Li et al.,* [2010], *Wang et al.,* [2010], and major Himalayan fault systems as white lines from *Hodges* [2000] and *Yin et al.,* [1999]. GCTS – Great Counter Thrust system, MBTS – Main Boundary Thrust system, MCTS – Main Central Thrust System, MFTS – Main Frontal Thrust system, and STFS - South Tibetan Fault system. Major Himalayan lithotectonic units labeled in Nepal (from *Hodges* [2000]). GHS – Greater Himalayan Sequence, LHS – Lesser Himalayan sequence, SH – Subhimalaya, and TSS – Tibetan Sedimentary Sequence. White box around Leh shows the extent of Figure 4.3.

Figure 4.2. Summary of stratigraphy and age constraints of the Indus Basin, from *Tripathy et al.* [in preparation]. Sample locations for the current study are listed in their approximate stratigraphic location, and the final interpration of provenance, based on data presented herein, as well as other lines of evidence, are shown for ease of correlation to approximate stratigraphic age. TEG – trace element geochemistry, UPb – U-Pb zircon geochronology, bt – biotite $^{40}Ar/^{39}Ar$ thermochronology.

Figure 4.3. Simplified geologic map of the Ladakh region. Strata between the Tibetan Sedimentary Series (TSS) and the Ladakh batholith comprise the ITSZ, and are drawn from *Tripathy et al.* [in prep]. The northern boundary of the Ladakh batholith, Karakoram Fault zone (KFZ) and exposures of SSZ strata after *Bohon et al.* [submitted]. The Zanskar Gorge transect is marked by samples labeled "ZG", and the Leh-Manali road transect is marked by samples labeled "LM."

Figure 4.4. Stacked probability density curves, from bottom to top, of Indian plate TSS detrital U-Pb data (compiled by *Gehrels et al.* [2011]), Indus Basin samples 09-AT-LM-Z and 09-AT-LM-Y from this study, and Eurasian plate Lhasa block detrital sandstone samples (compiled by *Gehrels et al.* [2011]). The gray bands highlight major modes, which are labeled above, in the detrital zircon U-Pb signature of the TSS. The arrow points to the broad peak at *ca.* 1200 Ma in the Lhasa block age spectrum.

Figure 4.5. REE patterns, normalized to chondrites [*Sun and McDonough,* 1989], of published data, averaged based upon location. The Western Ladakh SSZ curves (Type 2) comprise all ophiolitic material analyzed from the Northern Group (A) and Southern Group (B) of the SSZ rocks exposed in western Ladakh [*Rolland et al.,* 2000; 2002]. The Eastern Ladakh SSZ curve comprises ophiolitic material analyzed from the SSZ exposed just north of Leh [*Rolland et al.,* 2000; 2002]. The ITSZ curve comprises data from the Nidar complex [*Ahmad et al.,* 2008].

Figure 4.6. Chondrite normalized REE patterns [*Sun and McDonough,* 1989], of the data presented herein. The gray curves are the averages from previous studies, as shown in Figure 4.5. We subdivide by type, as assigned in the text. (a) Type 1 diagram, which most closely matches the Eastern Ladakh SSZ because of the enrichment in LREEs and negative Eu-anomaly. (b) Type 2 diagram, which most closes matches the Western Ladakh SSZ because of LREE enrichment but either positive or no Eu anomaly. (c) Type 3, which most closely matches ITSZ Nidar complex samples because of the slight depletion of LREEs.

Figure 4.7. $[La/Yb]_N$ versus $[La]_N$ diagram, ratios normalized to the primitive mantle of *Sun and McDonough* [1989]. We plot data from *Rolland et al.* [2000; 2002] and *Ahmad et al.* [2008] as colored fields based upon where the majority of their data lie, with their outliers plotted for in gray for completeness. Our data are

presented as black symbols based upon Type, as defined in the text and in Figure 4.6.

Figure 4.8. Probability density curve of all detrital biotite $^{40}Ar/^{39}Ar$ data from sample 08-AT-ZG-A.

Table 4.1. Whole rock geochemistry of mafic clasts.

| Sample | ZGC6 | ZGC9 | ZGD3 | ZGD5 | ZGE3 | ZGE4 | ZGF1 | ZGF3 | ZGC1 | ZGC2 | ZGC3 |
|---|---|---|---|---|---|---|---|---|---|---|---|
| (ppm) | | | | | | | | | | | |
| P | 453.52 | 805.8 | 602 | 77.0 | 934 | 286.3 | 329.0 | 600 | 103.4 | 519 | 513 |
| K | 20900 | 19400 | 8000 | 1646.1 | 28900 | 1129 | 4448 | 10100 | 2497 | 7200 | 6000 |
| Sc | 34.36 | 47.00 | 7.20 | 1.559 | 34.45 | 34.27 | 19.92 | 39.73 | 18.924 | 51.59 | 37.39 |
| Ti | 8850 | 6616 | 2125 | 683.8 | 4418 | 3653 | 2773 | 4840 | 1032.5 | 4138 | 3974 |
| Rb | 83640 | 78380 | 39940 | 8750 | 115000 | 4003 | 18670 | 43210 | 9716 | 30140 | 24090 |
| Sr | 121.15 | 77.91 | 177.0 | 47.25 | 215.1 | 106.2 | 594.0 | 520.4 | 29.651 | 308.5 | 351.9 |
| Y | 9.629 | 22.323 | 23.329 | 21.19 | 16.82 | 16.878 | 19.47 | 27.40 | 3.105 | 18.67 | 18.43 |
| Zr | 23.12 | 13.378 | 43.74 | 12.444 | 7.688 | 40.9 | 56.9 | 47.28 | 2.0 | 14.03 | 24.7 |
| Nb | 1.100 | 2.2942 | 1.998 | 2.156 | 1.932 | 1.117 | 3.351 | 3.725 | - | - | - |
| Ba | 383.3 | 306.0 | 154.5 | 51.71 | 809 | 65.96 | 127.7 | 299.5 | 50.05 | 132.56 | 111.11 |
| La | 3.491 | 8.66 | 6.236 | 12.91 | 17.78 | 4.785 | 10.90 | 14.20 | 1.541 | 10.96 | 11.791 |
| Ce | 8.90 | 19.877 | 15.83 | 24.78 | 37.26 | 12.63 | 22.49 | 29.93 | 3.215 | 23.04 | 23.075 |
| Pr | 1.283 | 2.802 | 2.3091 | 2.770 | 4.72 | 1.668 | 2.680 | 4.003 | 0.408 | 2.986 | 2.975 |
| Nd | 6.601 | 13.44 | 11.27 | 10.352 | 20.07 | 7.86 | 11.301 | 17.931 | 1.82 | 13.36 | 13.196 |
| Sm | 1.890 | 3.726 | 3.19 | 1.907 | 4.43 | 2.269 | 2.706 | 4.677 | 0.451 | 3.35 | 3.344 |
| Eu | 0.874 | 1.290 | 0.892 | 0.342 | 1.327 | 0.528 | 0.772 | 1.521 | 0.107 | 0.988 | 0.949 |
| Gd | 2.068 | 4.159 | 3.37 | 1.702 | 3.949 | 2.614 | 2.87 | 5.15 | 0.483 | 3.47 | 3.55 |
| Tb | 0.3114 | 0.669 | 0.579 | 0.2126 | 0.580 | 0.4672 | 0.451 | 0.839 | 0.0821 | 0.527 | 0.5044 |
| Ho | 0.402 | 0.880 | 0.7895 | 0.2109 | 0.680 | 0.701 | 0.599 | 1.128 | 0.1131 | 0.671 | 0.632 |
| Er | 1.151 | 2.485 | 2.375 | 0.6093 | 1.968 | 2.181 | 1.806 | 3.302 | 0.346 | 1.971 | 1.861 |
| Tm | 0.1513 | 0.3285 | 0.340 | 0.0820 | 0.2725 | 0.3159 | 0.260 | 0.457 | 0.0513 | 0.2742 | 0.2581 |
| Yb | 0.986 | 2.103 | 2.35 | 0.563 | 1.818 | 2.43 | 1.789 | 2.95 | 0.342 | 1.842 | 1.782 |
| Lu | 0.1322 | 0.2919 | 0.3738 | 0.07811 | 0.2654 | 0.3111 | 0.2708 | 0.4412 | 0.0464 | 0.2656 | 0.2583 |
| Pb | 9.01 | 4.650 | 4.552 | 22.53 | 9.44 | 2.06 | 9.37 | 9.76 | 4.020 | 9.92 | 11.53 |

Table 4.1. *Continued*

| Sample | ZGC4 | ZGC5 | ZGC7 | ZGC10 | ZGC11 | ZGD1 | ZGD4 | ZGD9 | ZGE1 |
|---|---|---|---|---|---|---|---|---|---|
| (ppm) | | | | | | | | | |
| P | 323.2 | 564 | 291.3 | 718.0 | 566 | 348 | 416.4 | 717 | 496.4 |
| K | 26901 | 13100 | 12300 | 15025 | 10100 | 13700 | 915.5 | 1536 | 36500 |
| Sc | 48.74 | 37.02 | 4.981 | 53.50 | 20.77 | 14.89 | 2.709 | 19.45 | 47.00 |
| Ti | 5326 | 4589 | 1636 | 6980 | 4265 | 3301 | 216.22 | 4732 | 6475 |
| Rb | 107190 | 53590 | 45640 | 58080 | 35470 | 74000 | 7600 | 7480 | 137000 |
| Sr | 82.12 | 105.63 | 123.40 | 23.57 | 381.1 | 165.5 | 400.8 | 73.47 | 22.993 |
| Y | 14.811 | 20.237 | 13.760 | 20.637 | 35.837 | 28.11 | 20.831 | 30.58 | 17.44 |
| Zr | 5.85 | 26.45 | 9.063 | 13.7 | 107.38 | 116.3 | 8.8 | 108.3 | 39.91 |
| Nb | - | - | - | - | - | - | - | - | - |
| Ba | 572.0 | 186.7 | 223.1 | 288.4 | 227.5 | 162.2 | 15.60 | 48.78 | 724.5 |
| La | 2.30 | 7.78 | 13.32 | 3.258 | 26.71 | 20.15 | 10.21 | 11.94 | 0.981 |
| Ce | 6.481 | 16.35 | 27.18 | 8.45 | 53.36 | 41.11 | 16.13 | 24.55 | 4.943 |
| Pr | 0.999 | 2.208 | 2.856 | 1.333 | 6.363 | 4.974 | 2.568 | 3.314 | 0.855 |
| Nd | 5.296 | 10.373 | 10.258 | 6.858 | 25.85 | 20.620 | 11.67 | 14.98 | 4.580 |
| Sm | 1.832 | 2.778 | 2.106 | 2.333 | 5.837 | 4.778 | 3.05 | 3.974 | 1.824 |
| Eu | 0.6623 | 1.0004 | 0.576 | 0.4248 | 1.495 | 1.630 | 0.532 | 1.087 | 0.6182 |
| Gd | 2.34 | 3.21 | 2.042 | 3.01 | 6.41 | 4.96 | 3.88 | 4.53 | 2.13 |
| Tb | 0.407 | 0.480 | 0.2926 | 0.5567 | 0.919 | 0.7286 | 0.529 | 0.688 | 0.417 |
| Ho | 0.6109 | 0.6316 | 0.350 | 0.918 | 1.169 | 0.9573 | 0.565 | 0.932 | 0.659 |
| Er | 1.843 | 1.799 | 1.035 | 2.881 | 3.483 | 2.910 | 1.450 | 2.830 | 2.061 |
| Tm | 0.2612 | 0.2423 | 0.1477 | 0.437 | 0.477 | 0.4170 | 0.1699 | 0.3985 | 0.300 |
| Yb | 1.763 | 1.573 | 1.016 | 3.21 | 3.49 | 3.07 | 1.019 | 2.88 | 2.000 |
| Lu | 0.261 | 0.2119 | 0.1435 | 0.453 | 0.458 | 0.432 | 0.1386 | 0.4045 | 0.2631 |
| Pb | 6.528 | 6.031 | 6.501 | 3.199 | 16.83 | 13.60 | 8.25 | 9.15 | 2.436 |

Table 4.1. *Continued*

| | | | | | | | | BIR-1 | | BCR-2 | |
|---|---|---|---|---|---|---|---|---|---|---|---|
| Sample | ZGE2 | ZGE5 | ZGE6 | ZGE7 | ZGE8 | ZGF2 | LOD | Rep. (%)[1] | Acc (%)[1] | Rep. (%)[1] | Acc (%) [1] |
| (ppm) | | | | | | | | | | | |
| P | 558.6 | 259.6 | 408 | 272.60 | 215.8 | 351.0 | 10.332 | 96.0 | 80.0 | 89.0 | 95.0 |
| K | 5400 | 1505 | 373 | 569.3 | 2239 | 14100 | 2.670 | - | - | 98 | 96 |
| Sc | 21.00 | 24.39 | 45.48 | 6.49 | 5.032 | 34.70 | 0.072 | 99.4 | 97 | 99.9 | 95 |
| Ti | 3806 | 2934 | 5811 | 1949 | 1489 | 4576 | 0.546 | 97 | 90 | 90 | 100 |
| Rb | 15377 | 3854 | 1619 | 1101 | 9360 | 61710 | 6.180 | - | - | 99.6 | 91 |
| Sr | 154.96 | 155.0 | 647 | 116.6 | 104.69 | 251 | 0.006 | 98 | 90 | 94 | 95 |
| Y | 13.381 | 14.46 | 26.85 | 39.07 | 27.626 | 20.72 | 0.006 | 98 | 88 | 99 | 94 |
| Zr | 85.65 | 24.48 | 28.6 | 18.79 | 17.7 | 31.01 | 0.024 | 99 | 82 | 97 | 94 |
| Nb | - | - | - | - | - | - | 3.360 | - | 88 | - | - |
| Ba | 128.5 | 67.00 | 14.11 | 43.29 | 62.3 | 415 | 0.012 | 99 | 83 | 95 | 93 |
| La | 13.1 | 3.218 | 7.27 | 21.507 | 15.58 | 7.52 | 0.666 | 97 | 95 | 99.8 | 97 |
| Ce | 16.22 | 8.243 | 16.81 | 49.28 | 38.75 | 17.31 | 0.000 | 99.5 | 98 | 99.9 | 98 |
| Pr | 1.970 | 1.150 | 2.148 | 6.04 | 4.877 | 2.193 | 0.432 | - | - | 99 | 93 |
| Nd | 8.249 | 5.706 | 10.24 | 23.95 | 20.18 | 10.19 | 1.692 | 99.3 | 97 | 99 | 92 |
| Sm | 1.705 | 1.722 | 2.91 | 5.65 | 4.4527 | 2.83 | 1.380 | 93 | 93 | 99.5 | 93 |
| Eu | 0.4000 | 0.499 | 0.960 | 0.597 | 0.558 | 0.961 | 0.552 | 99.5 | 98 | 98 | 93 |
| Gd | 1.811 | 2.20 | 3.83 | 5.36 | 4.25 | 3.17 | 0.000 | 98 | 100 | 98 | 91 |
| Tb | 0.2892 | 0.3607 | 0.593 | 0.9009 | 0.6011 | 0.5313 | 0.132 | - | - | 98 | 97 |
| Ho | 0.417 | 0.5175 | 0.833 | 1.1473 | 0.7260 | 0.731 | 0.282 | - | - | 99.5 | 98 |
| Er | 1.233 | 1.5652 | 2.475 | 3.506 | 2.177 | 2.155 | 0.462 | - | - | - | - |
| Tm | 0.1668 | 0.2204 | 0.343 | 0.5086 | 0.308 | 0.2985 | 0.258 | - | - | 99.9 | 90 |
| Yb | 1.084 | 1.512 | 2.27 | 3.56 | 2.078 | 2.006 | 0.498 | 98 | 98 | 99 | 99 |
| Lu | 0.1500 | 0.2228 | 0.335 | 0.455 | 0.2889 | 0.2708 | 0.276 | 96 | 100 | 98 | 90 |
| Pb | 1.322 | 2.598 | 16.91 | 3.70 | 2.562 | 4.92 | 4.170 | 99 | 96 | 93 | 94 |

[1]Rep - % reproducibility from replicate analyses, Acc - % accuracy from replicate analyses

Figure 4.1.

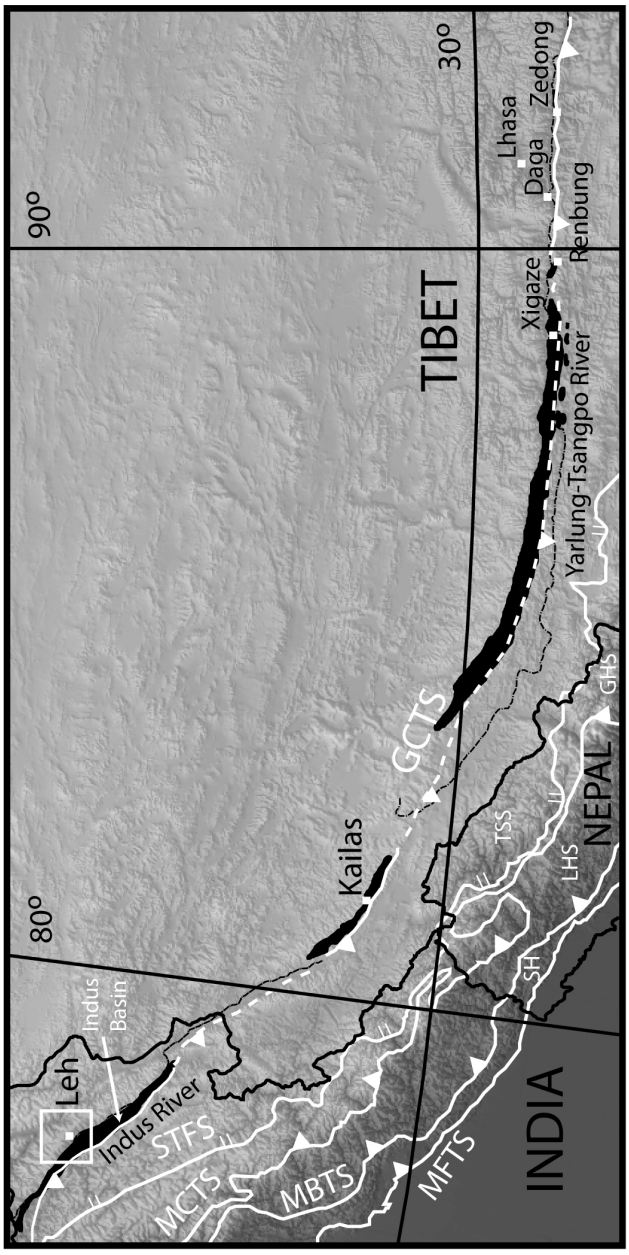
80°
90°
30°
TIBET
INDIA
NEPAL
Leh
Indus Basin
Indus River
Kailas
Lhasa
Daga
Zedong
Renbung
Xigaze
Yarlung-Tsangpo River
GCTS
STFS
MCTS
MBTS
MFTS
TSS
LHS
SH
GHS

Figure 4.2.

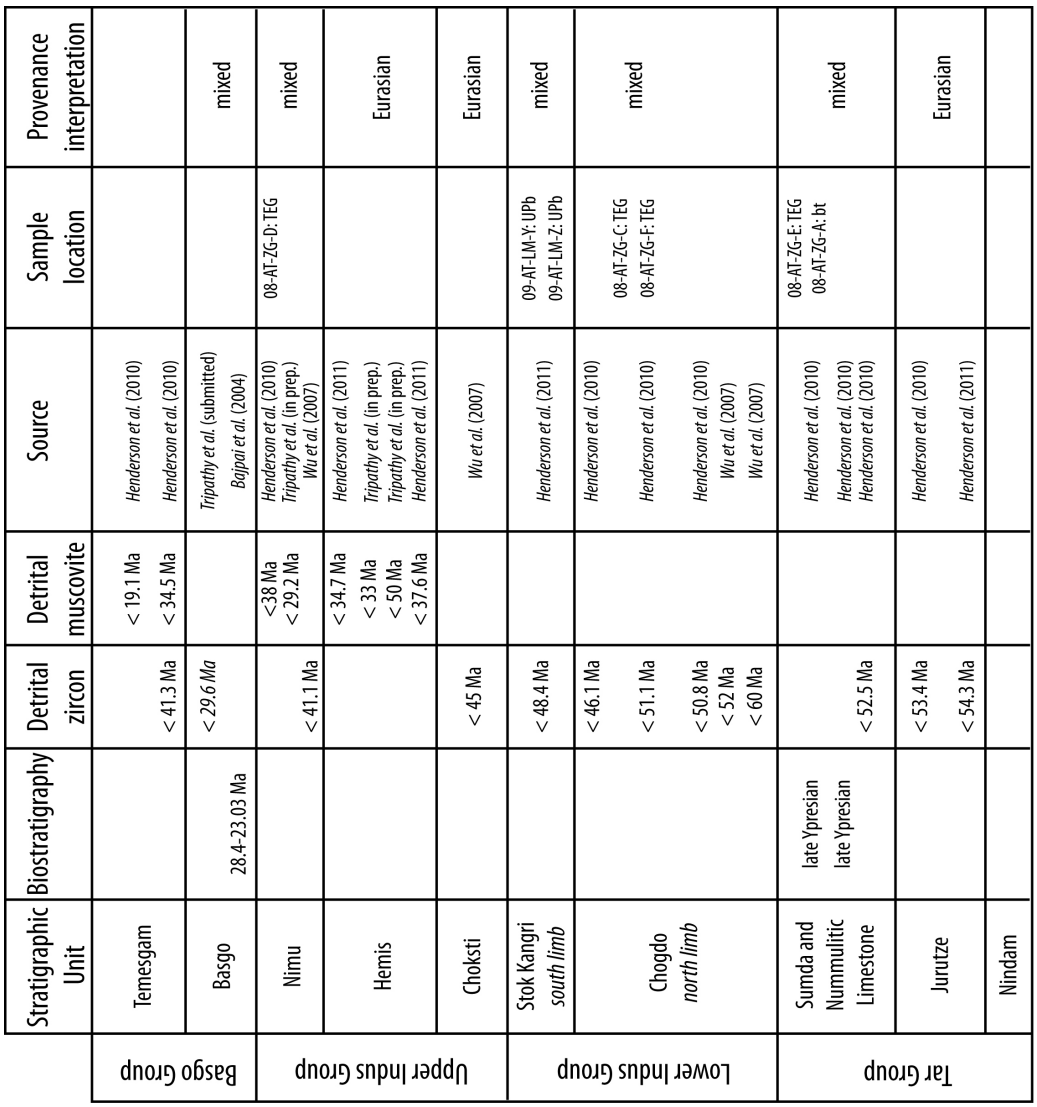

| | Stratigraphic Unit | Biostratigraphy | Detrital zircon | Detrital muscovite | Source | Sample location | Provenance interpretation |
|---|---|---|---|---|---|---|---|
| Basgo Group | Temesgam | | < 41.3 Ma | < 19.1 Ma<br>< 34.5 Ma | *Henderson et al.* (2010)<br>*Henderson et al.* (2010) | | |
| | Basgo | 28.4-23.03 Ma | *< 29.6 Ma* | | *Tripathy et al.* (submitted)<br>*Bajpai et al.* (2004) | | mixed |
| Upper Indus Group | Nimu | | < 41.1 Ma | <38 Ma<br>< 29.2 Ma | *Henderson et al.* (2010)<br>*Tripathy et al.* (in prep.)<br>*Wu et al.* (2007) | 08-AT-ZG-D: TEG | mixed |
| | Hemis | | | < 34.7 Ma<br>< 33 Ma<br>< 50 Ma<br>< 37.6 Ma | *Henderson et al.* (2011)<br>*Tripathy et al.* (in prep.)<br>*Tripathy et al.* (in prep.)<br>*Henderson et al.* (2011) | | Eurasian |
| | Choksti | | < 45 Ma | | *Wu et al.* (2007) | | Eurasian |
| Lower Indus Group | Stok Kangri<br>*south limb* | | < 48.4 Ma | | *Henderson et al.* (2011) | 09-AT-LM-Y: UPb<br>09-AT-LM-Z: UPb | mixed |
| | Chogdo<br>*north limb* | | < 46.1 Ma<br>< 51.1 Ma<br>< 50.8 Ma<br>< 52 Ma<br>< 60 Ma | | *Henderson et al.* (2010)<br>*Henderson et al.* (2010)<br>*Henderson et al.* (2010)<br>*Wu et al.* (2007)<br>*Wu et al.* (2007) | 08-AT-ZG-C: TEG<br>08-AT-ZG-F: TEG | mixed |
| Tar Group | Sumda and Nummulitic Limestone | late Ypresian<br>late Ypresian | < 52.5 Ma | | *Henderson et al.* (2010)<br>*Henderson et al.* (2010)<br>*Henderson et al.* (2010) | 08-AT-ZG-E: TEG<br>08-AT-ZG-A: bt | mixed |
| | Jurutze | | < 53.4 Ma<br>< 54.3 Ma | | *Henderson et al.* (2010)<br>*Henderson et al.* (2011) | | Eurasian |
| | Nindam | | | | | | |

Figure 4.3.

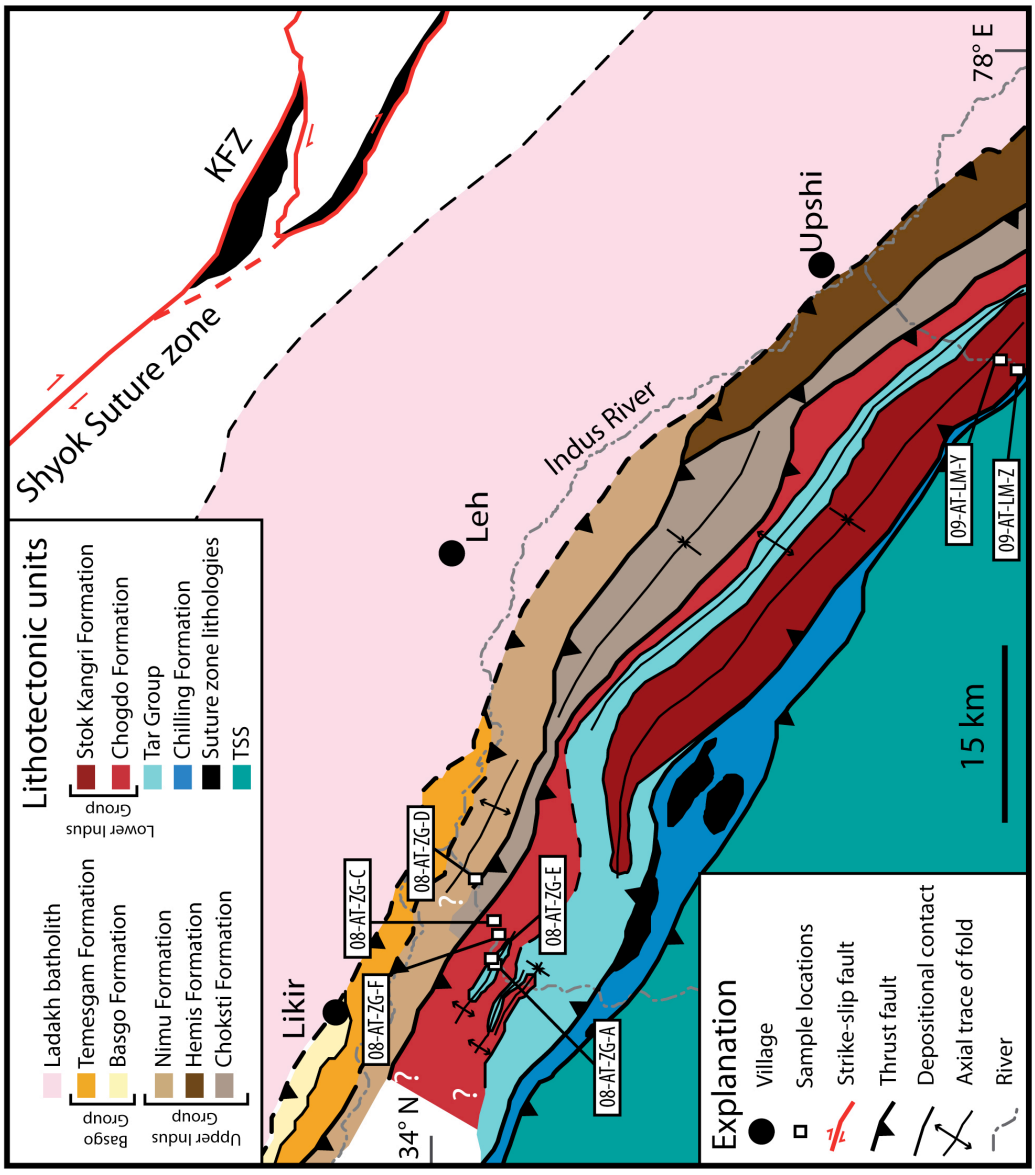
Lithotectonic units
Ladakh batholith
Temesgam Formation
Basgo Formation
Basgo Group
Stok Kangri Formation
Chogdo Formation
Lower Indus Group
Nimu Formation
Hemis Formation
Choksti Formation
Upper Indus Group
Tar Group
Chilling Formation
Suture zone lithologies
TSS
Shyok Suture zone
KFZ
Likir
Leh
Upshi
Indus River
34° N
78° E
08-AT-ZG-C
08-AT-ZG-F
08-AT-ZG-D
08-AT-ZG-E
08-AT-ZG-A
09-AT-LM-Y
09-AT-LM-Z
15 km
Explanation
Village
Sample locations
Strike-slip fault
Thrust fault
Depositional contact
Axial trace of fold
River

Figure 4.4.

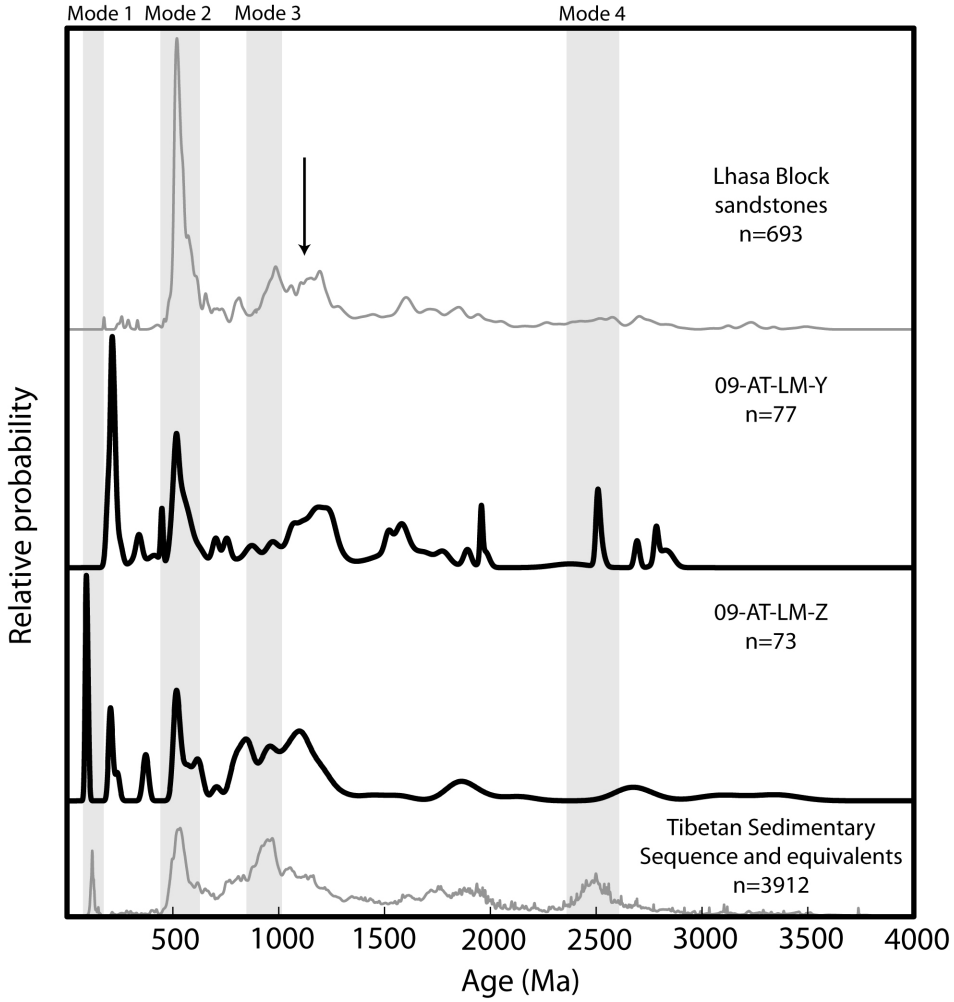
Mode 1
Mode 2
Mode 3
Mode 4
Lhasa Block
sandstones
n=693
09-AT-LM-Y
n=77
09-AT-LM-Z
n=73
Tibetan Sedimentary
Sequence and equivalents
n=3912
Relative probability
500
1000
1500
2000
2500
3000
3500
4000
Age (Ma)

Figure 4.5.

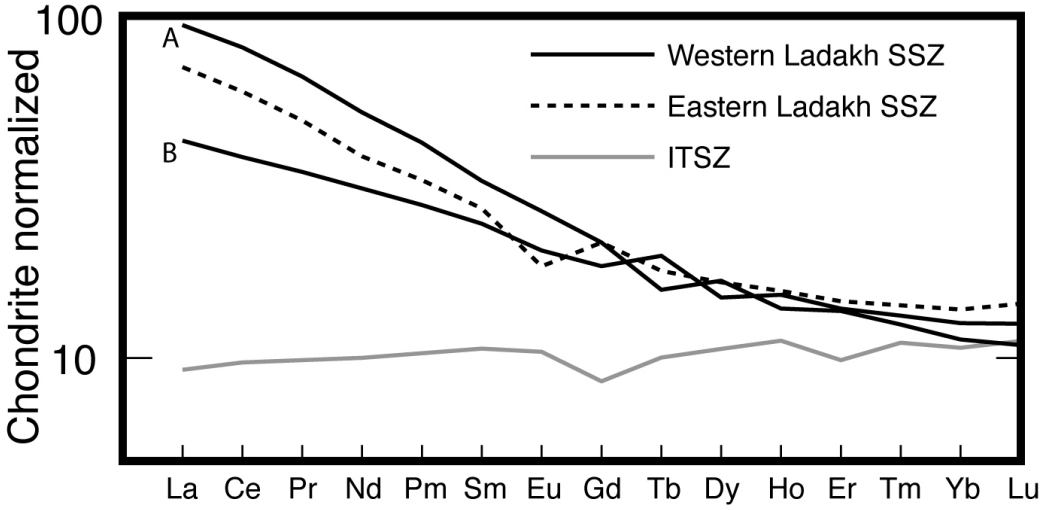
100
10
Chondrite normalized
A
B
Western Ladakh SSZ
Eastern Ladakh SSZ
ITSZ
La
Ce
Pr
Nd
Pm
Sm
Eu
Gd
Tb
Dy
Ho
Er
Tm
Yb
Lu

Figure 4.6.

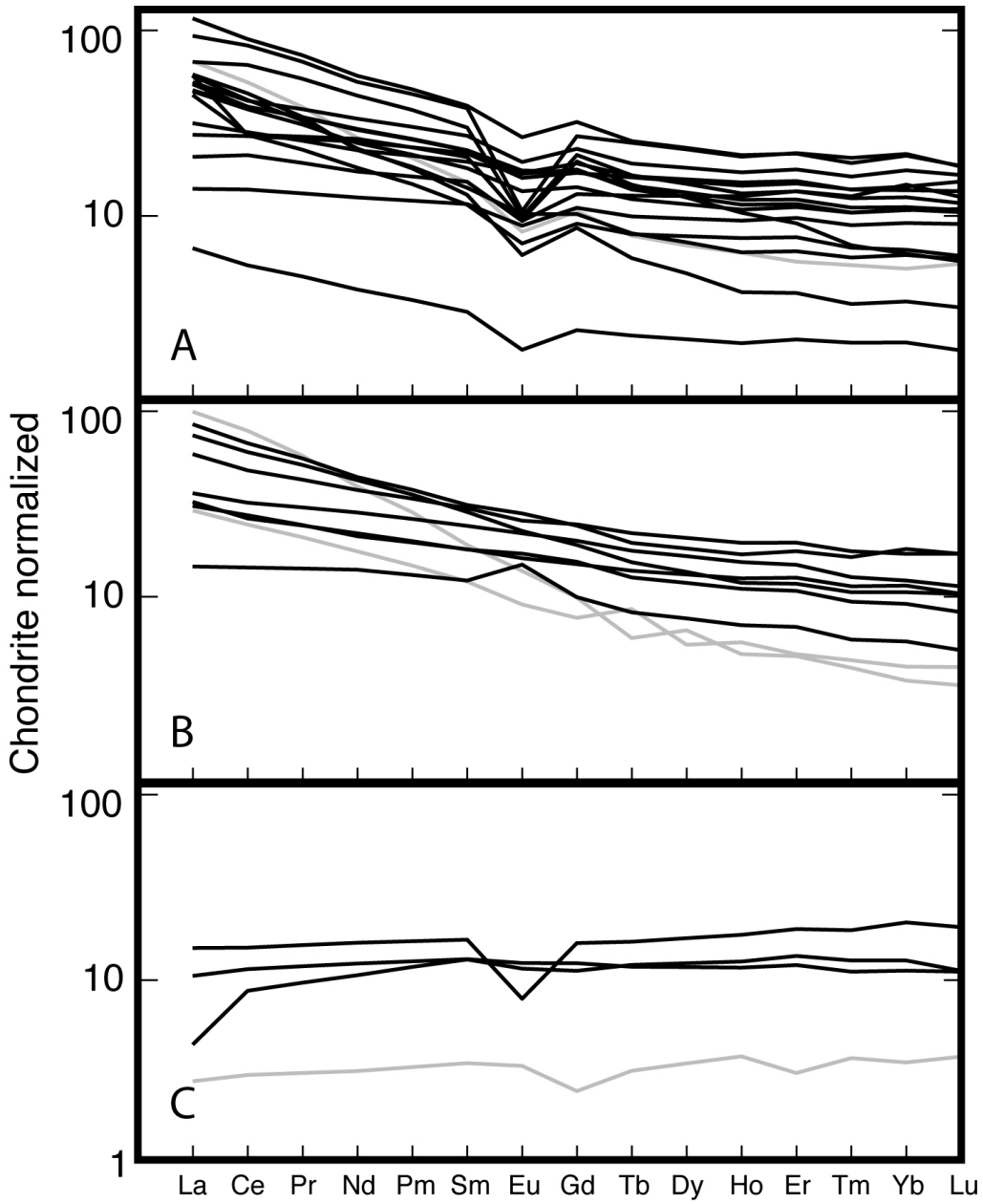
100
10
A
100
10
B
Chondrite normalized
100
10
1
C
La Ce Pr Nd Pm Sm Eu Gd Tb Dy Ho Er Tm Yb Lu

Figure 4.7.

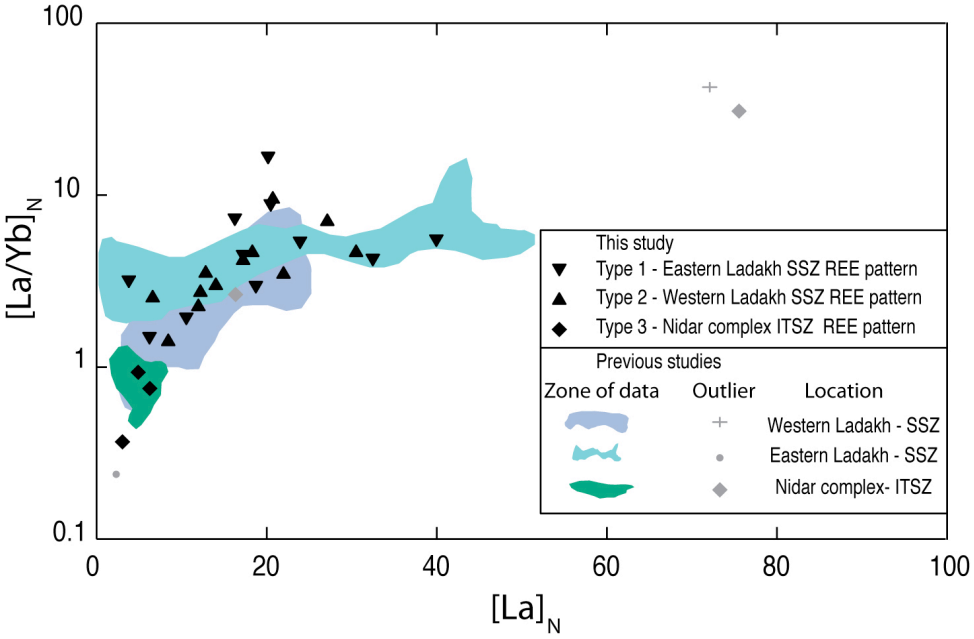
100
10
1
0.1
0
20
40
60
80
100
[La/Yb]N
[La]N
This study
Type 1 - Eastern Ladakh SSZ REE pattern
Type 2 - Western Ladakh SSZ REE pattern
Type 3 - Nidar complex ITSZ REE pattern
Previous studies
Zone of data
Outlier
Location
Western Ladakh - SSZ
Eastern Ladakh - SSZ
Nidar complex- ITSZ

Figure 4.8.

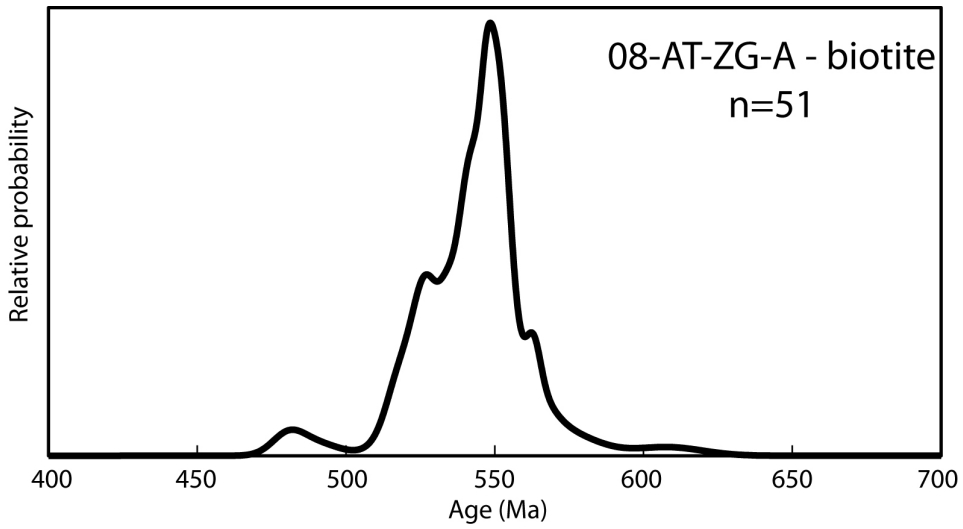
08-AT-ZG-A - biotite
n=51
Relative probability
400
450
500
550
600
650
700
Age (Ma)

# CHAPTER 5

# TIMING OF NORTH-VERGENT DEFORMATION IN LADAKH, NORTHWESTERN INDIA, AND IMPLICATIONS FOR THE ALONG-STRIKE CONTINUITY OF THE GREAT COUNTER THRUST SYSTEM


## ABSTRACT

Backthrusting is thought to play an important role in accommodating Cenozoic convergence between India and Eurasia north of the Himalayan range crest and south of central Tibet. In particular, backthrusts located near the Indus - Tsangpo suture zone have been postulated to represent a major structural system – the Great Counter Thrust system – that may persist many hundreds of kilometers along strike. However, the ages of many structures grouped into the Great Counter Thrust system are not well constrained, complicating our understanding of the role of the system in Himalayan tectonics. In the Ladakh region of NW India, we used new apatite (U-Th)/He dates and published $^{40}Ar/^{39}Ar$ dates to constrain the timing of backthrusting to between 19 and 7 Ma. Zircon (U-Th)/He systematics were not fully reset during the backthrusting event. Modeling of these results in light of the conditions of anchizonal metamorphism related to backthrusting provides a better estimate of the timing of metamorphism (11 to 7 Ma) and suggests a 3 to 3.5 my duration for the event. Comparison of this result with data from elsewhere along the suture suggests either differences in the function of backthrusting along the length of the orogen, implying that the Great Counter Thrust system does not include the backthrusts in NW India, or

diachroneity in the timing of backthrust structures along what is mapped as the Great Counter Thrust system.

**1. Introduction**

In compressional orogens, foreland-directed thrust faults and associated fold trains tend to dominate the tectonic architecture of the system. However, the timing, duration and function of hinterland-directed backthrusts are typically less well understood despite the fact that they are common structural elements of many compressional orogens [*Schmid et al*., 1989; *McQuarrie et al.,* 2001; *Yin*, 2006].

In the Himalayan-Tibetan orogenic system, numerous north-vergent, hinterland-directed structures have been identified in the vicinity of the Indus-Tsangpo suture zone (ITSZ). Present along much of the strike-length of the suture, the Great Counter Thrust system (GCTS) is so named because its structures verge counter to the dominant foreland-directed features [*Heim and Gansser*, 1939]. Its initiation age and duration of activity are not well constrained in most locations, and its relationship with other major Himalayan fault systems (e.g. the Main Central Thrust system, or MCTS, Figure 5.1) is, as a consequence, speculative. At present, age estimates for GCTS activity range from Early-Middle Miocene in eastern Tibet [*Quidelleur et al.,* 1997] to Plio-Pleistocene in the Ladakh region [*Searle et al.,* 1997], implying that the backthrusts may have been active concurrently with a variety of major foreland-vergent fault systems on the south side of the Himalayan range (see *Hodges* [2000] for a general review). Considering the range of age estimates, it is unclear if the GCTS is best regarded

as a fundamental orogen-scale feature, as suggested by *Yin* [2006], or if backthrusts developed at different times in different places along the ITSZ and do not actually constitute a single, well-defined structural system. In order to understand the role of the GCTS and its relationship to other major structures in the orogen, and to differentiate among competing models, it is valuable to better constrain the timing of backthrusting along multiple segments of the ITZS.

In this paper, we take a unique approach to developing information regarding the age and duration of GCTS deformation by obtaining detrital apatite and zircon (U-Th)/He dates from the Indus Basin. A spectacularly exposed molasse in the ITSZ of the Ladakh region of NW India (Figure 5.1), the Indus basin sedimentary rocks display complex north-vergent deformation patterns that we refer to as the Zanskar backthrust system (ZBS). Related anchizonal metamorphism reached high enough temperatures (≥180˚C, *Clift et al.* [2002]) to reset (U-Th)/He isotopic systematics in detrital apatite, but not $^{40}Ar/^{39}Ar$ systematics in detrital white micas, thereby providing an opportunity to bracket the age of ZBS deformation in the Ladakh region with these thermochronometers. Thus, we combined published $^{40}Ar/^{39}Ar$ dates with newly obtained apatite (U-Th)/He data to establish the maximum age range during which backthrusting must have occurred. We then used these constraints and the (U-Th)/He cooling age distributions of detrital zircon (n=122) from the same region to model the duration of ZBS-related metamorphism**.** Using these new constraints, we address the temporal relationship between the ZBS and other major Himalayan fault systems.

## 2. Structural character and timing constraints along the GCTS

Although reconnaissance studies have demonstrated that backthrusts and associated folds are common features of the ITSZ, such structures have been described in detail only in two areas in southern Tibet and one in NW India. Here we briefly describe each region from east to west, and use the regional name of the fault system to differentiate between the various locations.

### 2.1. Renbu-Zedong thrust system

In the Renbu and Zedong region, although the Renbu-Zedong thrust system (RZTS) is buried beneath alluvium in many places, it is well exposed east of Zedong and clearly places phyllites directly atop molasse on a south-dipping plane [*Harrison et al.,* 1993]. *Quidelleur et al.* [1997] collected samples from a 25 km traverse through the footwall, beginning near the exposed fault contact where intrusive rock in the footwall is penetratively deformed and recrystallized to greenschist facies. This deformation and recrystallization decreases away from the fault contact and is not detectable ~5 km north of the thrust. The mineral assemblage of the higher grade hanging wall rocks indicate temperatures of ~450°C, inferred to be the maximum temperature attained during thrusting [*Quidelleur et al.,* 1997]. Hornblende $^{40}Ar/^{39}Ar$ dates from the hanging wall are between 17-18 Ma, which is interpreted to record the time of initial motion of the RZTS. From the footwall, biotite laser total fusion $^{40}Ar/^{39}Ar$ analyses from the transect show dates increasing from 12.3 Ma at the fault to 60 Ma greater than 5 km away from the fault. K-feldspar step-heating experiments yield dates between 8-15 Ma for the initial gas released, and by applying multiple domain diffusion

(MDD) modeling to their step heating spectra, *Quidelleur et al.* [1997] interpreted that the RZTS was active between 19 and 11 Ma.

**2.2. South Kailas thrust system**

In the Kailas region of southwest Tibet, *Heim and Gansser* [1939] recognized a south dipping thrust that places flysch atop molasse type-conglomerates, and coined the term "Great Counter Thrust." Named the South Kailas thrust system (SKTS) in this area, multiple backthrusts successively place rocks of the suture zone above one other, with the structurally highest (southernmost) thrust placing ophiolitic serpentinite over flysch [*Yin et al.,* 1999].

Estimates for movement along the SKTS are broadly bracketed as less than 20 Ma, but greater than 4 Ma [*Yin et al.,* 1999]. The upper boundary derives from MDD models of K-feldspar separated from a volcanic cobble in the Kailas conglomerate that was sampled directly below the frontal thrust. The most robust model allowed *Yin et al.* [1999] to interpret that the sample was at 350°C at 19 Ma, and remained at this temperature until 13 Ma, which they attributed to faulting. The lower boundary of 4 Ma is based upon crosscutting relationships with the Karakoram fault [*Searle*, 1996]. Because the age range broadly overlaps that of the RZTS, *Yin et al.* [1999] correlated the backthrusting between both regions, and preferred the interpretation that the SKTS was active contemporaneously with the RZTS, between 19-10 Ma.

**2.3. Zanskar backthrust system**

First described in detail by *Searle* [1986], the 30-km wide belt of south-dipping backthrusts in the ITSZ in the Ladakh region of NW India affects not

only the ITSZ, but also the northernmost shelf sequence of the Tibetan sedimentary sequence (TSS) [*Searle*, 1986; *Searle et al.,* 1997]. The southern boundary of the ITSZ is formed by the steeply south-dipping Main Zanskar backthrust, whereas the northern boundary of the ITSZ is a less steeply dipping north vergent contact where molassic sedimentary strata of the Indus Basin are thrust upon the Ladakh batholith [*Searle et al.,* 1997]. These boundaries, as well as all other intervening backthrusts, are interpreted to be part of the same system of faults [*Searle*, 1986], which we refer to as the Zanskar backthrust system (ZBS). This system is estimated to have accommodated ~36 km of shortening in the molasse strata alone [*Searle et al.,* 1990], and 150-170 km across the entirety of the ITSZ [*Searle et al.,* 1997].

Because all Eocene-Miocene Indus Basin rocks are cut by the ZBS, *Searle et al.* [1997] suggest that the ZBS is Plio-Pleistocene in age. More recently, *Clift et al.* [2002] presented apatite fission track data from the Indus Group in the Zanskar Gorge, and interpreted their *ca.*14 Ma apatite fission track dates to be evidence of thermal resetting by backthrusting, implying that activity on the ZBS is Middle Miocene.

## 3. Sedimentary rocks of the Indus Basin

### 3.1. Stratigraphy and age constraints

Within the ITSZ, Indus Basin sedimentary rocks, exposed along two transects - the Zanskar Gorge and Leh-Manali road - record the transition from marine to non-marine sedimentation within the paleo-intermontane basin between the Indian and Eurasian plates [*Brookfield and Andrews-Speed,* 1984; *Garzanti*

*and Van Haver,* 1988; *Sinclair and Jaffey*, 2001]. These strata are bounded to the south by the Chilling Group, which comprises a fault-bounded amalgamation of complexly juxtaposed ophiolitic and sedimentary rocks, and to the north by the Ladakh batholith, onto which Indus Basin strata have been thrust (Figure 5.1).

Based upon Advanced Spaceborne Thermal Emission Radiometer and Reflection (ASTER) image analysis, *Tripathy et al.* [in prep.; Chapter 2] demonstrated that the Indus Basin has a relatively simple stratigraphy that can be divided into four macrostratigraphic units, in spite of its highly deformed nature and inaccessible contacts (Figures 5.1 and 5.2). These include the predominantly marine Tar Group that is complexly folded with the terrestrial overlying Lower Indus Group. Based on biostratigraphy and detrital zircon U-Pb geochronology, the Tar Group is upper Ypresian (*ca.* 52-48 Ma) [*Henderson et al., 2010*; 2011]. The Lower Indus Group extends into the Lutetian, where the maximum age of deposition of its uppermost strata is *ca.* 46 Ma [*Henderson et al.,* 2010]. Above the Lower Indus Group and bounded by backthrust structures, the Upper Indus Group comprises several distinct stratigraphic units, all of which are fault bounded. The oldest Choksti Formation is at least Lutetian (*ca.* 48-40 Ma), but may be younger [*Wu et al.,* 2007], and is overlain by the uppermost Lutetian to Priabonian (Middle to Upper Eocene, *ca.* 40-34 Ma) Hemis Formation that is only exposed to the east along the Leh-Manali road transect [*Tripathy et al.,* in prep; Chapter 2]. Above both the Choksti and the Hemis Formations lies the Nimu Formation, which is at least as young as Rupelian (Early Oligocene, *ca.* 30 Ma) [*Tripathy et al.,* in prep; Chapter 2]. North of the Nimu Formation is the final

macrostratigraphic unit, the Basgo Group, which is only exposed near and west of the Zanskar Gorge transect. Bounded by backthrusts to both the north and south, the Basgo Group comprises the Upper Oligocene Basgo Formation [*Bajpai et al.,* 2004], as well as the conformably overlying Temesgam Formation. The depositional history of the latter formation extends into Early Miocene time, as estimated from the maximum age of deposition provided by detrital muscovite $^{40}Ar/^{39}Ar$ thermochronology, *ca.* 19 Ma [*Henderson et al.,* 2010].

**3.2. Provenance**

Detrital zircon U-Pb geochronology provides a valuable constraint on provenance for the Indus Basin clastic rocks because distinctive zircon crystallization age populations characterize both Indian and Eurasian sources [e.g., *Gehrels et al.,* 2011]. Most detrital U-Pb datasets for most of the units in the Indus Basin suggest derivation from Eurasia [*Wu et al., 2007*; *Henderson et al.,* 2010; 2011]. An important exception is the Basgo Formation; although many conglomeratic clasts suggest derivation from Eurasian sources, finer grained clastic units contains an abundance of Indian plate zircons [*Tripathy et al.,* in review; Chapter 3]. *Henderson et al.* [2010, 2011] noted that parts of the Lower Indus Group, and the entirety of the Upper Indus Group, contain detrital muscovite, a mineral that is sparse in exposed sections of the Eurasian plate in the vicinity of the Indus Basin, suggesting to those authors derivation from India. We regard the Indus Basin as predominantly recording the increased dissection of the Ladakh arc to the north, while subtly preserving information about the

exhumation of the Indian plate associated with continental collision [*Tripathy et al*., in review; Chapter 3].

### 3.3. Deformation and metamorphism

The simplest interpretation of the available age constraints on Indus Basin units is that basin deposition was semi-continuous from Early Eocene to Miocene time. As such, it is unlikely that backthrusting began during deposition of Indus Basin strata, particularly because there is no obvious field evidence of syn-deformation sedimentation. Therefore, the timing of ZBS deformation, which affects all rocks enclosed in the ITSZ as pointed out by *Searle* [1986], must be younger than the Early Miocene Temesgam Formation. This provides a maximum age constraint of 19 Ma [*Henderson et al.,* 2010]. Achieving a better estimate of the age of backthrusting requires a different approach.

*Clift et al.* [2002] determined the maximum temperatures throughout the Zanskar Gorge section (Figure 5.2) using illite crystallinity. Of particular importance is the spatial correlation among the highest metamorphic temperatures and the concentration of backthrusts and fold trains; specifically, the highest temperatures were obtained for samples collected in the noses of backthrust-propagation folds. We thus infer a direct relationship between ZBS deformation and anchizonal metamorphism.

To determine how much younger ZBS deformation could be than *ca.*19 Ma, and to obtain information about the duration of metamorphism related to backthrusting, we used detrital mineral thermochronology to elucidate both the minimum age of backthrusting based on reset apatite (U-Th)/He (hereafter

referred to as AHe) systematics, and the duration of reheating, based upon thermal modeling of a partially reset zircon (U-Th)/He (hereafter referred to as ZHe) dataset.

## 4. Analytical methods and results

### 4.1. (U-Th)/He analytical methods

All (U-Th)/He data were obtained in the Noble Gas, Geochronology and Geochemistry Lab ($NG^3L$) at Arizona State University (ASU). Seven samples from the Zanskar Gorge and six samples from the Leh-Manali road transect were crushed, sieved, and separated using standard magnetic and heavy liquid mineral separation techniques. From each sample, a minimum of four, but generally at least ten, euhedral grains were selected, measured, and loaded into Nb microcrucibles for analysis of $^4$He using an ASI *Alphachron* system. Each grain was heated with a 980 nm diode laser, and the released gas was spiked with $^3$He, purified, and expanded into a quadrupole mass spectrometer for $^4$He/$^3$He measurement by electron multiplier. For apatite, after initial heating and measurement, the grain is re-extracted, or reheated such that a second round of gas is released. If, upon re-extraction, the amount of gas released is greater than blank levels, we excluded the analysis due to the likely presence of microinclusions. For zircon analyses, each grain was re-extracted to less than 0.5% of the initial released gas. For U and Th analyses of apatite, each grain was spiked with a $^{235}$U + $^{230}$Th solution and digested using nitric acid. For zircon, samples were spiked and digested using concentrated hydrofluoric, hydrochloric and nitric acids in Parr digestion vessels. The final solutions were analyzed on a

Thermo *X-Series* quadrupole mass spectrometer in the W. M. Keck Foundation Laboratory for Environmental Biogeochemistry at ASU. Each grain was corrected for loss of $^{4}$He by alpha ejection using the methods of Farley et al. [1996] for apatite and of *Hourigan et al.* [2005] for zircon. For a more detailed description of our analytical techniques, see *van Soest et al.* [2011].

**4.2. Data presentation**

Apatite of sufficient quality to be considered datable was recovered from only one sample, 07-AT-ZG-O (Figure 5.1). This sample was collected from an outcrop known to have experienced anchizonal metamorphic temperatures high enough to have likely resulted in the complete resetting of the apatite (U-Th)/He thermochronometer during metamorphism. Six grains from this sample yielded a narrow range of AHe cooling ages between 8.68 ± 0.42 to 6.47 ± 0.19 Ma (2σ). While the dispersion in these dates is greater than what might be expected from analytical imprecision alone – the mean squared weighted deviation, or MSWD, of the error-weighted mean is 27.08 – we interpret these inconsistencies to reflect slight variations in resetting kinetics of the different grains or the uncorrected effects of variable U+Th zoning [*Flowers et al.,* 2009; *Hourigan et al.*, 2005; *Farley et al*., 2011]. For our purposes, we estimate an effective age of resetting based on the error-weighted mean age of the six grains, with a 2σ uncertainty modified by multiplication by the square-root of the MSWD [*Ludwig and Titterington,* 1994] 6.87 ± 0.63 Ma, calculated using Matlab program written at ASU. The complete dataset is located in Supplementary Material Appendix J.

For ZHe analyses, zircons were abundant in all samples. We present 122 dates in total – 91 dates from the Zanskar Gorge transect, and 31 dates from the Leh-Manali road transect (Figures 5.3a and b; Supplementary Material Appendix J; 2σ errors). Somewhat surprisingly, the cooling age frequency distribution from both transects were quite similar, suggesting a similar thermal history for the basin during the backthrusting event. As a consequence, we combined both datasets for the diffusive loss modeling exercise described below (Figure 5.3c).

The range of ZHe dates obtained from these samples (37.32 ± 1.87 to 7.83 ± 0.40 Ma) is too large to be explained by variations of intracrystalline zoning patterns causing incorrect alpha ejection corrections [*Hourigan et al.,* 2005]. Moreover, there is no variation between grain size and ZHe age, such that grain size variation also cannot be invoked as an explanation for the observed range of ZHe dates [*Reiners et al.,* 2004]. Although some dispersion in (U-Th)/He apatite datasets can be traced to different amounts of radiation damage [*Flowers et al.*, 2009], we found no correlation between effective uranium concentration (eU) and apparent age for the Indus Basin zircons. Therefore, we consider it likely that the ZHe data are partially reset during anchizonal metamorphism, such that the age dispersion reflects the primary age frequency distribution in the ZHe detrital zircons before the metamorphic event, as well as the timing of heating and exhumation due to deformation.

**5. Broadly bracketing the age of deformation and metamorphism**

As mentioned above, the detrital muscovite $^{40}Ar/^{39}Ar$ results from *Henderson et al.* [2010] constrain the maximum age of initiation of backthrusting

to be less than *ca.* 19 Ma. The AHe date of 6.87 ± 0.63 Ma (2σ) is interpreted as the minimum age of metamorphism, and, therefore, backthrusting. This is a minimum because first, the apatite (U-Th)/He system has the lowest resetting temperature for any thermochronometer applicable to these samples and second, because the thermal pulse associated with backthrusting had to end prior to *ca.* 7 Ma in order to record this cooling age. Therefore, we consider the range between 19-7 Ma to be a robust bracket around the timing of ZBS deformation.

**6. Additional constraints on the thermal history**

If we assume that resetting of an isotope thermochronometer reflects daughter product ($^4$He) diffusive loss as described by Fick's Law during a heating event, then the extent of resetting is a function of the temperature and duration of that event. Assuming volumetric diffusion, different zircons will experience different degrees of diffusive loss depending on grain size. For a detrital dataset, which would have been characterized by a dispersion of (U-Th)/He apparent ages prior to partial resetting simply because the source regions for the grains would have had variable cooling histories, partially reset ages would also show considerable dispersion regardless of grain size variation. Here we present a method by which a partially reset dataset can be used to derive a range of synthetic "pre-event" cooling age frequency diagrams consistent with different ages and durations for the thermal event. We explain how comparison of these results with other types of detrital thermochronologic and geochronologic data can be used to place additional constraints on the resetting event.

### 6.1. Requirements for estimating a range of possible durations

We determined permissible combinations of duration and $t_{reheat}$, the time of onset of reheating (metamorphism), by applying a series of known inputs and assumed boundary conditions. We point out that this calculation is predicated on data from a single grain, and does not allow the use of multiple grains because it requires input parameters that are unique to each individual grain – namely, grain size and measured U, Th and $^4$He concentrations. Furthermore, we must assume a simple thermal history for this grain that involves crystallization, exhumation, transportation, deposition, instantaneous reheating, and cooling. As such, we calculated the combinations of duration and $t_{reheat}$ for multiple grains to assess the fidelity of the final durations.

The boundary conditions required for the calculation include a range of $t_{reheat}$ for which we calculate unique durations, a range of estimates for maximum temperature ($T_{max}$), and an estimate for the theoretical initial ZHe age of the grain to be modeled. The goal is to combine these assumptions and known parameters to determine, for a given grain, which unique combinations of duration and $t_{reheat}$, for a theoretical initial ZHe age and $T_{max}$, will give the same $^4$He concentration as measured, $^4He_{meas}$.

#### 6.1.1. Defining a range of $t_{reheat}$

From the AHe data, the reheating event as experienced by these grains was completed by ~7 Ma, so we assumed that the initiation of metamorphism can be no younger than 7 Ma, thereby setting a lower boundary for $t_{reheat}$. For the upper boundary, the time at which reheating began cannot be significantly older

than the youngest ZHe age, which is ~8 Ma. Therefore, we assumed that the maximum age of backthrusting is 11 Ma, to account for the possibility of a protracted thermal event. Moreover, if a maximum age of backthrusting of greater than *ca*. 11 Ma is assumed, the duration calculated for each value of $t_{reheat}$ is so short that the grains would actually not be partially reset, but rather preserve their their source area cooling age, which is unlikely considering $T_{max}$ and range of ZHe dates. Hence, using 100,000-year increments for $t_{reheat}$, we calculated 41 possible unique combinations of $t_{reheat}$ and duration for each set of $T_{max}$ and theoretical initial ZHe ages, defined below.

### 6.1.2. Defining a range of maximum temperature, $T_{max}$

Although relative temperatures presented in the illite crystallinity dataset by *Clift et al.* [2002] are likely meaningful, the errors associated with the data are not reported. In general, errors associated with the method are between 12-14% (1σ) [e.g., *Robinson et al.,* 1990]. As such, we did not use absolute temperatures obtained from *Clift et al.* [2002]. Rather, we applied a range of temperatures between 160-200°C, which encompasses much of the range of temperatures obtained by *Clift et al.* [2002].

This range is supported empirically by the ZHe dataset presented herein. If the lower boundary for the $T_{max}$ were much less than ~160°C, partial resetting would require unreasonably long durations based on our calculations. Furthermore, if the temperature of metamorphism were significantly greater than 200°C, the majority of the zircon grains would be reset for the ZHe thermochronometer, in particular because the appropriate range of grain sizes and

heating rates yield resetting temperatures of 210-240°C [*Gardés and Montel*, 2009]. Thus, we consider 200°C to be the $T_{max}$ obtained anywhere within either transect through the Indus Basin.

### 6.1.3. Defining the theoretical initial ZHe age

To determine the most appropriate theoretical initial ZHe age, we first determined the population of grains to which the model should be applied. We used a combination of the published detrital zircon U-Pb data for the region, presented in Figure 5.4 as a relative probability density curve, because these data provide information regarding the source area of the ZHe dates presented in this study, which were collected from the same units within the Indus Basin.

A visual comparison between Figures 5.3c and 5.4 highlights the bimodal nature of both of the curves. The ZHe data presented in Figure 5.3a contain important modes at 10 and 14 Ma, whereas the U-Pb data in Figure 5.4 shows major modes at 55 and 100 Ma. Although the difference between these peaks is significant, we hypothesized that the youngest grains in the ZHe dataset are likely to correspond to the youngest U-Pb dates, implying that if we were to double date the youngest grains dated by U-Pb geochronology with ZHe thermochronology, they would yield dates comparable to the youngest ZHe dates obtained in our dataset. Therefore, we assumed the six youngest grains, which are statistically indistinguishable from one another, are sourced from the *ca.* 50 Ma population of U-Pb dates. Assuming cooling rates between 35-75°C/Ma based on the range of estimates for active orogens, which can be as high as 120°C/Ma in incipiently active orogens [*Liu et al.,* 2000], we obtained theoretical initial ages of 30 and 40

Ma, respectively. These six grains were then individually modeled to determine the durations required to obtain the age that we measure today, described below.

**6.2. Calculating the permissible durations of metamorphism**

Our goals here was to apply a variety of thermal histories at a particular temperature to a single grain with known U and Th concentration, grain size, and an assumed theoretical initial age ($t_{initial}$), where the thermal histories comprise all possible combinations of duration and $t_{reheat}$, in order to determine which thermal history would yield the amount of $^4$He that we analytically measure, $^4He_{meas}$. This allows for unique combinations of duration and $t_{reheat}$. The details of these calculations are presented in the Supplementary Material Appendix K.

All models were run at $T_{max}$ = 180°C and 200°C for theoretical initial ages of 30 and 40 Ma for the six youngest grains. We then averaged the durations obtained from each grain for each model to average any variability imparted by the complexity of zircon diffusion systematics (Table 5.1). The durations from individual grains are reported in Supplementary Material Appendix L. From Table 5.1, it is evident that the difference between 180°C and 200°C is significant, such that the durations for equivalent models vary by 3-4 million years. In contrast to $T_{max}$, the theoretical initial age assumed for these models, 30 Ma versus 40 Ma, has little impact on the calculated duration when comparing otherwise equivalent models.

Based on the AHe data, backthrusting and related metamorphism must have ceased by ~7 Ma. Therefore, the time at which closed system behavior of $^4$He commenced ($t_{close}$) must be greater than 7 Ma for that particular sample, and

is assumed to extrapolate to the remaining samples. This implies that any duration that yields an age that is younger than 7 Ma when subtracted from $t_{reheat}$ is an invalid result. This stipulation eliminates all models associated with a $T_{max}$ of 180°C, and eliminates many of the duration and $t_{reheat}$ combinations for a $T_{max}$ of 200°C (Table 5.1). We are left with durations of metamorphism-related backthrusting that range from 2.5-3.3 my.

**6.3. Removing the thermal history**

In order to further constrain possible durations, we calculated theoretical initial ZHe ages for each remaining set of boundary conditions. To calculate theoretical initial ages, the equations used for the model in section 6.2 are simply inverted such that the known thermal history is subtracted from the system and the $^4$He that was lost from each grain is added back, which corresponds to the theoretical initial age. This yields 122 theoretical initial ZHe ages for each of the remaining thermal histories within both models, for which the initial 6 grains yield their assumed theoretical initial age as a check for the model.

Associated errors for each theoretical initial ZHe age are propagated using Monte Carlo methods, and are never greater than ~5% of the calculated value. Thus we assign each age a 5% error (2σ), and plot their probability density curves in Figure 5.5. This error does not include the uncertainty associated with the diffusivity parameters, but includes all other known and estimatable sources of error.

To assess the fidelity of these curves, we compared them to the topology of the U-Pb probability density curve in Figure 5.4. In this comparison, we

expected the model curves in Figure 5.5 to mimic the U-Pb probability density curve. Thus, modeled peaks must be shifted to lower ages, and peak intensities must be similar such that we expected the youngest peak to be the highest, as is the case for the U-Pb data (Figure 5.4). Moreover, if any major modes for the theoretical initial ZHe age curves were older than the U-Pb modes, those curves must be eliminated as well. For ease of comparison, we plotted major modes from the U-Pb data as gray bars in Figure 5.5. Perhaps the most important mode is the oldest one, depicted by the gray bar centered at ~140 Ma. Based on the U-Pb curve, there should be few to no ZHe dates beyond this point, but only four possible curves meet this criterion, highlighted in Figure 5.5b. This implies that the duration of the thermal event was most likely between 3-3.5 my, and that $t_{reheat}$ = ~11 Ma.

**6.4. Age and duration of backthrusting**

Although dating the exact age of initiation, termination and nuances of the intervening history for a fault is often challenging, if not impossible, it is reasonable to bracket the timing of activity. It is certain that backthrusting is younger than 19 Ma because the muscovite $^{40}Ar/^{39}Ar$ data provide us the maximum age of deposition of the uppermost Temesgam Formation. AHe data further constrains that backthrusting ceased by ~7 Ma. Our preferred interpretation, based on modeling of partially reset ZHe data, is that backthrusting must have commenced around 11 Ma, and lasted for between 3-3.5 my.

The argument could be made that backthrusting continued past 7 Ma to bring the rock to the surface. If $t_{reheat}$ = 11 Ma and the thermal event lasted for 3

my at $T_{max}$ = 200°C, the rock must have begun to cool from $T_{max}$ at 8 Ma. Furthermore, we know that at least some of the rocks were at ~80°C by 7 Ma, which yields a cooling rate of 120°C/Ma. We interpret this very fast cooling rate to be correlated with backthrusting. If backthrusting continued past 7 Ma to bring the rocks to the surface at this cooling rate, 0.5 my would be required, which is within the error of the AHe date itself. If slow cooling commenced, we infer that to imply a cessation of backthrusting. Therefore, 7 Ma should be a robust estimate for the lower boundary for the timing of backthrusting.

We find no evidence that backthrusting in this region is older than 11 Ma, although our data does not preclude the possibility. Therefore, although backthrusting *must* have occurred between ~19-7 Ma, it most likely occurred between 11-7 Ma. Additional evidence that backthrusting is very young comes from the youngest population of ZHe dates that are as young as ~8 Ma (Figure 5.3), implying that backthrusting must be only slightly older than these youngest grains.

This estimate for the age of backthrusting-related deformation and metamorphism is younger than that estimated by *Clift et al.* [2002], based upon AFT dates. They dated two samples from the Zanskar Gorge transect, which yielded dates of 13.8 ± 1.9 and 13.7 ± 3.2 Ma. This age range encompasses the majority of the ZHe data presented herein, aside from the very youngest and oldest populations. However, because *Clift et al.* [2002] had difficulty obtaining track length data, we cannot fully interpret their data.

**7. Orogen-scale backthrusting**

*Yin* [2006] correlated the ZBS with the RZTS and SKTS, and stated that of all the orogenic-scale features in the Himalaya, the GCTS is the most robust in terms of consistency of history along strike. With our new data, we can begin to address possible scenarios regarding the continuity of this system. First, if all 3 regions are part of a single system, we could expect the amount of shortening, the timing of fault activity, the duration of the event, and its relationship with other large-scale structures, to be similar. Importantly, even if the former three criteria are met, if the overall function of the structure varies, it should be considered a different structure. *Yin* [2006] points out that in Tibet, there is evidence for large magnitude slip (>120 km) along the GCTS, which is similar to the 150-170 km estimate for the ZBS from *Searle et al.* [1997]. Regarding timing, all three regions broadly overlap, with the RZTS active between 19-11 Ma, the SKTS best constrained to 20-4 Ma, and ZBS active between 11-7 Ma. However, between the ZBS and the SKTS, the estimated duration of reheating is very different. The maximum duration for the ZBS is 3.5 Ma, whereas the SKTS was heated to 350°C for ~ 6 Ma [*Yin et al.,* 1999].

Regarding the relationship between backthrusting and observed activity on other major Himalayan fault systems, *Yin* [2006] postulated that the RZTS and the SKTS acted synchronously with the South Tibetan fault system (STFS) and the MCT at depth, which is temporally permitted by the broad constraints of backthrusting in both Tibetan locales [*Quidelleur et al.,* 1997; *Yin et al.,* 1999]. However, the STFS in the Zanskar region was active between 22.2-19.8 Ma

[*Dèzes et al.,* 1999], contemporaneous with the MCT, which was active between 23-17 Ma [*Stephenson et al.,* 2001]. Our data presented herein show no evidence that the ZBS was coeval with STFS or MCT activity in the western Himalaya. This calls into question the role of the ZBS in accommodating shortening in conjunction with other major Himalayan fault systems.

Thus, if the RZTS and the SKTS are active contemporaneously with the STFS and MCTS, as suggested by*Yin* [2006], then it is unlikely that the ZBS functioned in the same role, implying that it is not part of the same system. However, it is also possible that the timing along the RZTS and SKTS are not known well enough to accurately assess their relationships with activity the most proximal strands of the MCTS and STFS. Moreover, the timing of activity along the MCTS and STFS need to be known reasonably well south of the Kailas and Zedong regions in order to truly assess this issue. Another possibility is diachroneity of backthrusting-related deformation along strike, based on the difference in timing between the RZTS and the ZBS. This is supported by the variation in interpreted relationships with other Himalayan fault systems.

**8. Conclusion**

Based on a comprehensive analysis of various low-temperature thermochronologic data, we conclude that backthrusting and associated deformation occurred between 19-7 Ma in the Indus Basin region. Based on interpretations drawn from thermal modeling of partially reset zircon (U-Th)/He data, we refined that estimate to 11-7 Ma. This event most likely lasted for 3 to 3.5 million years. Our findings do not negate the hypothesis that the GCTS is an

orogen-scale system, but instead illustrate the need for better constraints in other areas to test the hypothesis that the GCTS is a singular, orogen-scale feature in the Himalayan-Tibetan orogenic system.

## 9. References


Bajpai, S., R. C. Whatley, G. V. R. Prasad, and J. E. Whittaker (2004), An Oligocene non-marine ostracod fauna from the Basgo Formation (Ladakh Molasse), NW Himalaya, India, *J. Micropalaeontol., 23*, 3-9.

Brookfield, M. E., and C. P. Andrews-Speed (1984), Sedimentology, petrography and tectonic significant of the shelf, flysch and molasse clastic deposits across the Indus suture zone, Ladakh NW India, *Sediment. Geol., 40*, 249-286.

Clift, P. D., A. Carter, M. Krol, and E. Kirby (2002), Constraints on India-Eurasia collision in the Arabian Sea region taken from the Indus Group, Ladakh Himalaya, India, in *The Tectonic and Climatic Evolution of the Arabian Sea Region,* edited by P. D. Clift et al., *Geol. Soc. Spec. Publ., 195,* 97-116.

Dèzes, P. J. , J.-C Vannay, A. Steck, F. Bussy, and M. Cosca (1999), Synorogenic extension: Quantitative constraints on the age and displacement of the Zanskar shear zone (northwest Himalaya), *Geol. Soc. Am. Bull., 111,* 364-374.

Farley, K. A., R. A. Wolf, and L. T. Silver (1996), The effects of long alpha-stopping distances on (U-Th)/He ages, *Geochim. Cosmochim. Acta, 60,* 4223-4229.

Farley, K. A., D. L. Shuster, and R. A. Ketcham (2011), U and Th zonation in apatite observed by laser ablation ICPMS, and implications for the (U-Th)/He system, *Geochim. Cosmochim. Acta, 75*, 16, 4515-4530.

Flowers, R. M., R. A. Ketcham, D. L. Shuster and K. A. Farley (2009), Apatite (U-Th)/He thermochronometry using a radiation damage accumulation and annealing model, *Geochim. Cosmochim. Acta*, *73*, 2347-2365.

Gardés, E., and J.-M. Montel (2009), Opening and resetting temperatures in heating and geochronologic systems, *Contrib. Mineral. Petrol., 158*, 185-195.

Garzanti, E., and T. Van Haver (1988), The Indus clastics: forearc basin sedimentation in the Ladakh Himalaya (India), *Sediment. Geol., 59*, 237-249.

Gehrels, G. E., P. Kapp, P. DeCelles, A. Pullen, R. Blakely, A. Weislgel, L. Ding, J. Guynn, A. Marin, N. McQuarrie, and A. Yin (2011), Detrital zircon geochronology of pre-Tertiary strata in the Tibetan-Himalayan orogen, *Tectonic, 30*, TC5016, doi:10.1029/2011TC002868.

Harrison, T. M., P. Copeland, S. Hall, J. Quade, S. Burner, T.P. Ojha, and W. S. F. Kid (1993), Isotopic preservation of Himalayan/Tibetan uplift, denudation and climatic histories in two molasse deposits, *J. Geol., 101*, 159-173.

Henderson, A. L., Y. Najman, R. Parrish, M. BouDagher-Fadel, D. Barford, E. Garzanti, and S. Ando (2010), Geology of the Cenozoic Indus Basin sedimentary rocks: paleoenvironmental interpretation of sedimentation from the western Himalaya during the early phases of India-Eurasia collision, *Tectonics, 29,* TC6015, doi:10.1029/2009TC002651.

Henderson, A. L., Y. Najman, R. Parrish, D. F. Mark, and G. L. Foster (2011), Constraints to the timing of India-Eurasia collision; a re-evaluation of evidence from the Indus Basin sedimentary rocks of the Indus-Tsangpo Suture Zone, Ladakh, India, *Earth-Sci. Rev., 106*, 265-292.

Heim, A., and A. Gansser (1939), Central Himalaya – Geological observations of Swiss expedition, 1936, *Mem. Soc. Helv. Sci. Nat., 73*, 1-245.

Hodges K. V. (2000), Tectonics of the Himalaya and southern Tibet from two perspectives, *Geol. Soc. Am. Bull., 112*, 324-350.

Hourigan, J. K., P. W. Reiners, and M. T. Brandon (2005), U-Th zonation-dependent alpha-ejection in (U-Th)/He chronometry, *Geochim. Cosmochim Acta, 69*, 3349-3365.

Liu, T.-K., Y.-G. Chen, W.-S. Chen and S.-H. Jiang (2000), Rates of cooling and denudation of the Early Penglai Orogeny, Taiwan, as assessed by fission-track constraints, *Tectonophysics, 30*, 69-82.

Ludwig, K. R. and D. M. Titterington (1994), Calculation of 230Th/U Isochrons, ages and errors, *Geochim. Cosmochim. Acta, 58*, 5031-5042.

Quidelleur, X., M. Grove, O. M. Lovera, T. M. Harrison, A. Yin, and F.J. Ryerson (1997), Thermal evolution and slip history of the Renbu-Zedong thrust, southeastern Tibet*, J. Geophys. Res., 102*, 2659-2679.

Reiners, P. W., T. L. Spell, S. Nicolescu, and K. A. Zanetti (2004), Zircon (U-Th)/He thermochronometry: He diffusion and comparisons with $^{40}Ar/^{39}Ar$ dating, *Geochim. Cosmochim. Acta, 68*, 1857-1887, doi: 10.1016/j.gca.2003.10.021.

Robinson, D., L. N. Warr, and R. E. Bevins (1990), The illite 'crystallinity' technique: a critical appraisal of its precision, *J. Metamorph. Geol., 8*, 333-344.

Searle, M. (1986), Structural evolution and sequence of thrusting in the High Himalayan Tibetan-Tethys and Indus suture zones of Zanskar and Ladakh, Western Himalaya, *J. Struct. Geol., 8*, 923-936.

Searle, M. P. (1996), Geological evidence against large-scale pre-Holocene off-sets along the Karakoram fault: implications for the limited extrusion of the Tibetan Plateau, *Tectonics, 15*, doi:10.1029/95TC01693**.**

Searle, M. P., K. T. Pickering, and D. J. W. Cooper (1990), Restoration and evolution of the intermontane Indus molasse basin, Ladakh Himalaya, India, *Tectonophysics, 174*, 301-314.

Searle, M., R. I. Corfield, B. Stephenson, and K. McCarron (1997), Structures of the North Indian continental margin in the Ladakh Zanskar Himalayas: implications for the timing of the obduction of the Spontang ophiolite, India-Asia collision and deformational events in the Himalaya, *Geol. Mag., 134,* 297-316.

Sinclair, H. D. and N. Jaffey (2001), Sedimentation of the Indus Group, Ladakh, northern India: implications for the timing of initiation of the palaeo-Indus River, *J. Geol. Soc., 158*, 151-162.

Stephenson, B. J., M. P. Searle, D. J. Waters and D. C. Rex (2001), Structure of the Main Central thrust zone and extrusion of the High Himalayan deep crustal wedge, Kishtwar-Zanskar Himalaya*, J. Geol. Soc., 158*, 637-652.

Tripathy, A. K., K. V. Hodges, M. C van Soest, and T. Ahmad (2011), Pre-Oligocene emergence of the Indian passive margin and the timing of Indian-Eurasian collision, *submitted to Geology.*

Tripathy, A. K., C. S. Edwards, K. V. Hodges, J.-A. Wartho, and F. J. Cooper, Lithologic mapping of complexly deformed sedimentary strata using

ASTER multispectral imagery: Implications for the evolution of Indus Basin depocenters, Ladakh, NW India, *in preparation.*

Van Soest, M. C., K. V Hodges, J.-A. Wartho, M. B Biren, B. D. Monteleone, J. Ramezani, J. G. Spray, and L. M. Thompson (2011), (U-Th)/He dating of terrestrial impact structures: the Manicouagan example, *Geochem., Geophys., Geosyst., 12*, Q0AA16, doi:10.29/2010GC003465.

Wu, F.-Y., P. D. Clift, and J.-H. Yang (2007), Zircon Hf isotopic constraints on the sources of the Indus Molasse, Ladakh Himalaya, India, *Tectonics, 26*, TC2014, doi:10.1029/2006TC002051.

Yin, A. (2006), Cenozoic tectonic evolution of the Himalayan orogen as constrained by along-strike variation of structural geometry, exhumation history and foreland sedimentation, *Earth-Sci. Rev., 76*, 1-131.

Yin, A., T. M. Harrison, M. A. Murphy, M. Grove, S. Nie, F. J. Ryerson, X. F. Wang, and Z. L. Chen (1999), Tertiary deformational history of southeastern and southwestern Tibet during the Indo-Asian collision, *Geol. Soc. Am. Bull. 111*, 1644-1664.

## 10. Figure captions

Figure 5.1. (a) Shaded relief map derived from GTOPO30 (30m/pixel DEM) overlain with ASTER DEM (15m/pixel) showing major Himalayan fault systems. GCTS – Great Counter Thrust system, MBTS – Main Boundary Thrust system, MCTS – Main Central Thrust system, MFTS – Main Frontal Thrust system, STFS – South Tibetan Fault system. Box shows location of b. Fault locations from *Yin et al*. [1999] and *Hodges* [2000]. (b) Geologic map of the Indus Basin, showing sample locations. Zanskar Gorge transect and Leh-Manali road transect labeled with "ZG" and "LM" in sample names, respectively. Tibetan sedimentary sequence and Ladakh batholith labeled for reference. After *Tripathy et al*. [in prep.].

Figure 5.2. Stratigraphy of the Indus Basin, with summary of age constraints. Sample locations are listed by approximate stratigraphic location, with range of ZHe dates obtained in this study. After *Tripathy et al.* [in prep].

Figure 5.3. Probability density curves for ZHe datasets. (a) Zanskar Gorge ZHe dataset. (b) Leh-Manali road ZHe dataset. (c) All ZHe data from both transects, combined.

Figure 5.4. Probability density curve of published detrital U-Pb geochronologic samples from the Lower and Upper Indus Group rocks. Data from *Wu et al.* [2007] and *Henderson et al.* [2010; 2011].

Figure 5.5. Probability density curves of synthetic theoretical initial ZHe ages calculated from durations derived from the youngest grain population. Each model, run for a specific temperature and theoretical initial age of the youngest grains, produced 41 possible durations for each $t_{reheat}$. Of those, we only plot permissible curves that are shown in bold in Table 5.1 and explained in the text. The gray boxes are major modes taken from the U-Pb dataset in Figure 4 for ease of comparison. (a) Synthetic curves produced by applying durations obtained from $T_{max}$ = 200°C and theoretical initial age (T.I.A.) = 30 Ma. All curves are shown in gray because none of them match the U-Pb curve due to many theoretical initial ZHe ages calculated that are older than the gray box centered at 140 Ma. (b) Synthetic curves produced by applying durations obtained from $T_{max}$

= 200°C and theoretical initial age (T.I.A.) = 40 Ma. The four curves shown in black are permissible based on their offsets toward younger ages when compared to the U-Pb dataset.

Table 5.1. Results from calculation of duration, averaged for the six youngest grains.

| | $T_{max}$=200°C[b] | | $T_{max}$=200°C[b] | | $T_{max}$=180°C[b] | | $T_{max}$=180°C[b] | |
|---|---|---|---|---|---|---|---|---|
| | T.I.A.=30 Ma[c] | | T.I.A.=40 Ma[c] | | T.I.A.=30 Ma[c] | | T.I.A.=40 Ma[c] | |
| $t_{reheat}$ (Ma)[a] | duration (my)[d] | $t_{close}$ (Ma)[e] | duration (my)[d] | $t_{close}$ (Ma)[e] | duration (my)[d] | $T_{close}$ (Ma)[e] | duration (my)[d] | $t_{close}$ (Ma)[e] |
| 7 | 1.7 | 5.3 | 1.9 | 5.1 | 5.3 | 1.7 | 5.4 | 1.6 |
| 7.1 | 1.7 | 5.4 | 1.9 | 5.2 | 5.3 | 1.8 | 5.4 | 1.8 |
| 7.2 | 1.7 | 5.5 | 1.9 | 5.3 | 5.4 | 1.8 | 5.9 | 1.8 |
| 7.3 | 1.8 | 5.5 | 2 | 5.3 | 5.4 | 1.9 | 5.9 | 1.9 |
| 7.4 | 1.8 | 5.6 | 2 | 5.4 | 5.4 | 2 | 5.9 | 2 |
| 7.5 | 1.8 | 5.7 | 2 | 5.5 | 5.5 | 2 | 6 | 2 |
| 7.6 | 1.8 | 5.8 | 2 | 5.6 | 5.5 | 2.1 | 6 | 2.1 |
| 7.7 | 1.9 | 5.8 | 2.1 | 5.6 | 5.5 | 2.2 | 6 | 2.2 |
| 7.8 | 1.9 | 5.9 | 2.1 | 5.7 | 5.6 | 2.2 | 6.1 | 2.2 |
| 7.9 | 1.9 | 6 | 2.1 | 5.8 | 5.6 | 2.3 | 6.1 | 2.3 |
| 8 | 1.9 | 6.1 | 2.1 | 5.9 | 5.7 | 2.3 | 6.1 | 2.3 |
| 8.1 | 2 | 6.1 | 2.2 | 5.9 | 5.7 | 2.4 | 6.6 | 2.4 |
| 8.2 | 2 | 6.2 | 2.2 | 6 | 5.7 | 2.5 | 6.6 | 2.5 |
| 8.3 | 2 | 6.3 | 2.2 | 6.1 | 5.8 | 2.5 | 6.6 | 2.5 |
| 8.4 | 2.1 | 6.3 | 2.3 | 6.1 | 5.8 | 2.6 | 6.7 | 2.6 |
| 8.5 | 2.1 | 6.4 | 2.3 | 6.2 | 5.8 | 2.7 | 6.7 | 2.7 |
| 8.6 | 2.1 | 6.5 | 2.3 | 6.3 | 5.9 | 2.7 | 6.8 | 2.7 |
| 8.7 | 2.2 | 6.5 | 2.3 | 6.4 | 5.9 | 2.8 | 6.8 | 2.8 |
| 8.8 | 2.2 | 6.6 | 2.4 | 6.4 | 6 | 2.8 | 6.8 | 2.8 |
| 8.9 | 2.2 | 6.7 | 2.4 | 6.5 | 6 | 2.9 | 6.9 | 2.9 |
| 9 | 2.3 | 6.7 | 2.4 | 6.6 | 6 | 3 | 6.9 | 3 |
| 9.1 | 2.3 | 6.8 | 2.5 | 6.6 | 6.1 | 3 | 7.3 | 3 |
| 9.2 | 2.3 | 6.9 | 2.5 | 6.7 | 6.1 | 3.1 | 7.3 | 3.1 |
| 9.3 | 2.4 | 6.9 | 2.6 | 6.7 | 6.2 | 3.1 | 7.4 | 3.1 |
| 9.4 | 2.4 | 7 | 2.6 | 6.8 | 6.2 | 3.2 | 7.4 | 3.2 |
| 9.5 | 2.5 | 7 | 2.6 | 6.9 | 6.2 | 3.3 | 7.5 | 3.3 |
| 9.6 | 2.5 | 7.1 | 2.7 | 6.9 | 6.3 | 3.3 | 7.5 | 3.3 |
| 9.7 | 2.6 | 7.1 | 2.7 | 7 | 6.3 | 3.4 | 7.5 | 3.4 |
| 9.8 | 2.6 | 7.2 | 2.8 | 7 | 6.4 | 3.4 | 7.6 | 3.4 |
| 9.9 | 2.7 | 7.2 | 2.8 | 7.1 | 6.4 | 3.5 | 7.6 | 3.5 |
| 10 | 2.7 | 7.3 | 2.9 | 7.1 | 6.5 | 3.5 | 7.7 | 3.5 |
| 10.1 | 2.8 | 7.3 | 2.9 | 7.2 | 6.5 | 3.6 | 7.7 | 3.6 |
| 10.2 | 2.8 | 7.4 | 3 | 7.2 | 6.5 | 3.7 | 7.8 | 3.7 |
| 10.3 | 2.9 | 7.4 | 3 | 7.3 | 6.6 | 3.7 | 7.8 | 3.7 |
| 10.4 | 2.9 | 7.5 | 3.1 | 7.3 | 6.6 | 3.8 | 7.8 | 3.8 |
| 10.5 | 3 | 7.5 | 3.1 | 7.4 | 6.7 | 3.8 | 7.9 | 3.8 |
| 10.6 | 3.1 | 7.5 | 3.2 | 7.4 | 6.7 | 3.9 | 7.9 | 3.9 |
| 10.7 | 3.1 | 7.6 | 3.3 | 7.4 | 6.8 | 3.9 | 8 | 3.9 |
| 10.8 | 3.2 | 7.6 | 3.3 | 7.5 | 6.8 | 4 | 8 | 4 |
| 10.9 | 3.2 | 7.7 | 3.4 | 7.5 | 6.9 | 4 | 8.1 | 4 |
| 11 | 3.3 | 7.7 | 3.4 | 7.6 | 6.9 | 4.1 | 8.1 | 4.1 |

[a]All values of $t_{reheat}$ for which duration was calculated.

[b]Maximum temperature assumed for thermal model.
[c]Theoretical initial age (T.I.A.) assumed for the model.
[d]Average duration for the six youngest grains, calculated based upon model parameters listed above
[e]Calculated from the subtraction of $t_{reheat}$ from duration, which must be greater than 7 Ma for the model to be considered permissible.

Figure 5.1.

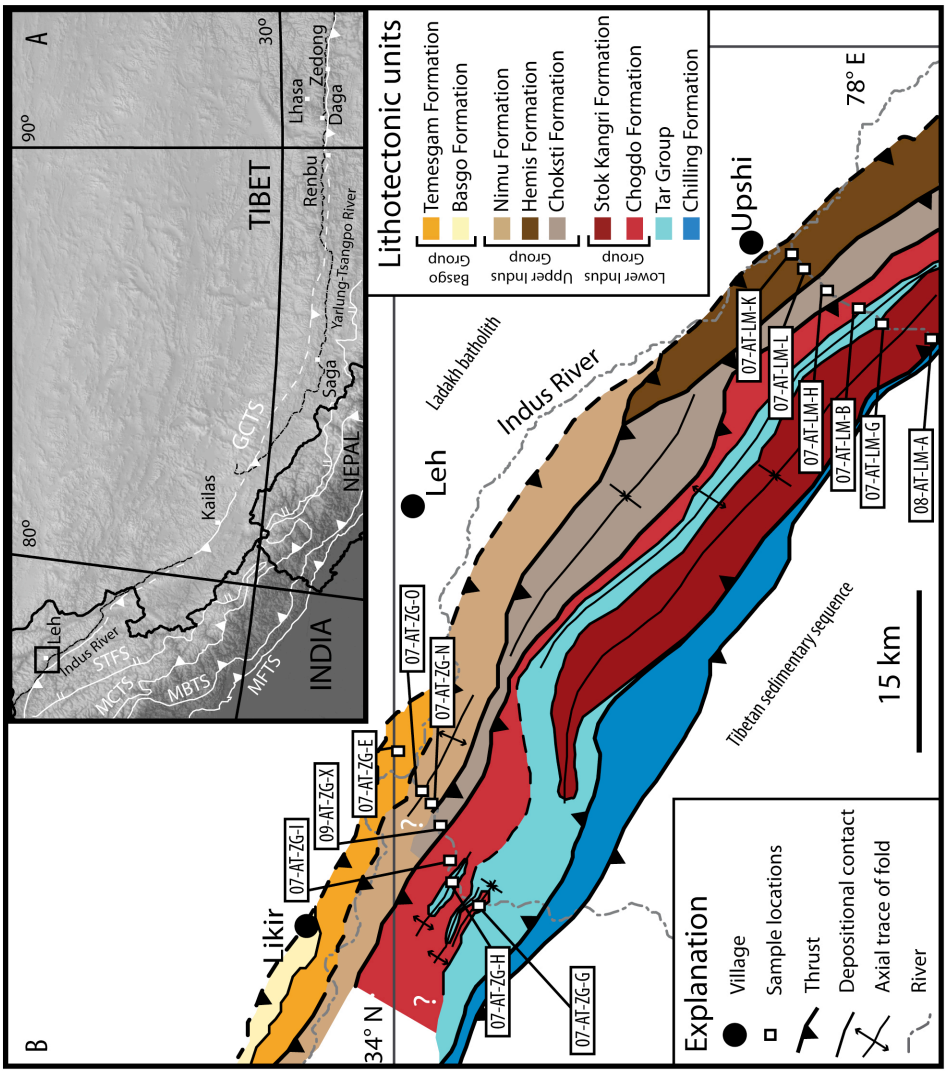
A
B
80°
90°
30°
TIBET
INDIA
NEPAL
Leh
Indus River
Kailas
GCTS
STFS
MCTS
MBTS
MFTS
Saga
Yarlung-Tsangpo River
Renbu
Lhasa
Zedong
Daga
Lithotectonic units
Temesgam Formation
Basgo Formation
Basgo Group
Nimu Formation
Hemis Formation
Choksti Formation
Upper Indus Group
Stok Kangri Formation
Chogdo Formation
Tar Group
Chilling Formation
Lower Indus Group
Likir
Leh
Upshi
Ladakh batholith
Indus River
Tibetan sedimentary sequence
34° N
78° E
15 km
07-AT-ZG-I
09-AT-ZG-X
07-AT-ZG-E
07-AT-ZG-O
07-AT-ZG-N
07-AT-ZG-H
07-AT-ZG-G
07-AT-LM-K
07-AT-LM-L
07-AT-LM-H
07-AT-LM-B
07-AT-LM-G
08-AT-LM-A
Explanation
Village
Sample locations
Thrust
Depositional contact
Axial trace of fold
River

Figure 5.2.

| | Stratigraphic Unit | Biostratigraphy | Detrital zircon | Detrital muscovite | Source | Sample location | ZHe age range (2σ) |
|---|---|---|---|---|---|---|---|
| Basgo Group | Temesgam | | < 41.3 Ma | < 19.1 Ma<br>< 34.5 Ma | *Henderson et al.* (2010)<br>*Henderson et al.* (2010) | 07-AT-ZG-E | 9.48 ± 0.32-28.08 ± 0.82 |
| | Basgo | 28.4-23.03 Ma | *< 29.6 Ma* | | *Tripathy et al.* (submitted)<br>*Bajpai et al.* (2004) | | |
| Upper Indus Group | Nimu | | < 41.1 Ma | <38 Ma<br>< 29.2 Ma | *Henderson et al.* (2010)<br>*Tripathy et al.* (in prep.)<br>*Wu et al.* (2007) | 07-AT-ZG-N<br>07-AT-ZG-O | 9.05 ± 0.28-16.12 ± 0.47<br>10.31 ± 0.33-21.70 ± 1.12 |
| | Hemis | | | < 34.7 Ma<br>< 33 Ma<br>< 50 Ma<br>< 37.6 Ma | *Henderson et al.* (2011)<br>*Tripathy et al.* (in prep.)<br>*Tripathy et al.* (in prep.)<br>*Henderson et al.* (2011) | 07-AT-LM-L<br>07-AT-LM-K | 9.38 ± 0.35-13.71 ± 0.44<br>8.30 ± 0.29-17.09 ± 0.56 |
| | Choksti | | < 45 Ma | | *Wu et al.* (2007) | 07-AT-LM-H<br>09-AT-ZG-X | 8.03 ± 0.27-17.92 ± 0.56<br>8.46 ± 0.26-15.85 ± 0.52 |
| Lower Indus Group | Stok Kangri *south limb* | | < 48.4 Ma | | *Henderson et al.* (2011) | 07-AT-LM-G<br>08-AT-LM-A | 9.72 ± 0.32-20.36 ± 0.66<br>12.51 ± 0.43-18.47 ± 0.55 |
| | Chogdo *north limb* | | < 46.1 Ma | | *Henderson et al.* (2010) | | |
| | | | < 51.1 Ma | | *Henderson et al.* (2010) | | |
| | | | < 50.8 Ma<br>< 52 Ma<br>< 60 Ma | | *Henderson et al.* (2010)<br>*Wu et al.* (2007)<br>*Wu et al.* (2007) | 07-AT-ZG-I<br>07-AT-LM-B<br>07-AT-ZG-G | 8.77 ± 0.27-37.32 ± 1.87<br>8.40 ± 0.26-18.49 ± 0.59<br>9.23 ± 0.29-27.95 ± 0.84 |
| Tar Group | Sumda and Nummulitic Limestone | late Ypresian<br>late Ypresian | < 52.5 Ma | | *Henderson et al.* (2010)<br>*Henderson et al.* (2010)<br>*Henderson et al.* (2010) | 07-AT-ZG-H | 7.83 ± 0.40-38.97 ± 1.13 |
| | Jurutze | | < 53.4 Ma<br>< 54.3 Ma | | *Henderson et al.* (2010)<br>*Henderson et al.* (2011) | | |
| | Nindam | | | | | | |

Figure 5.3.

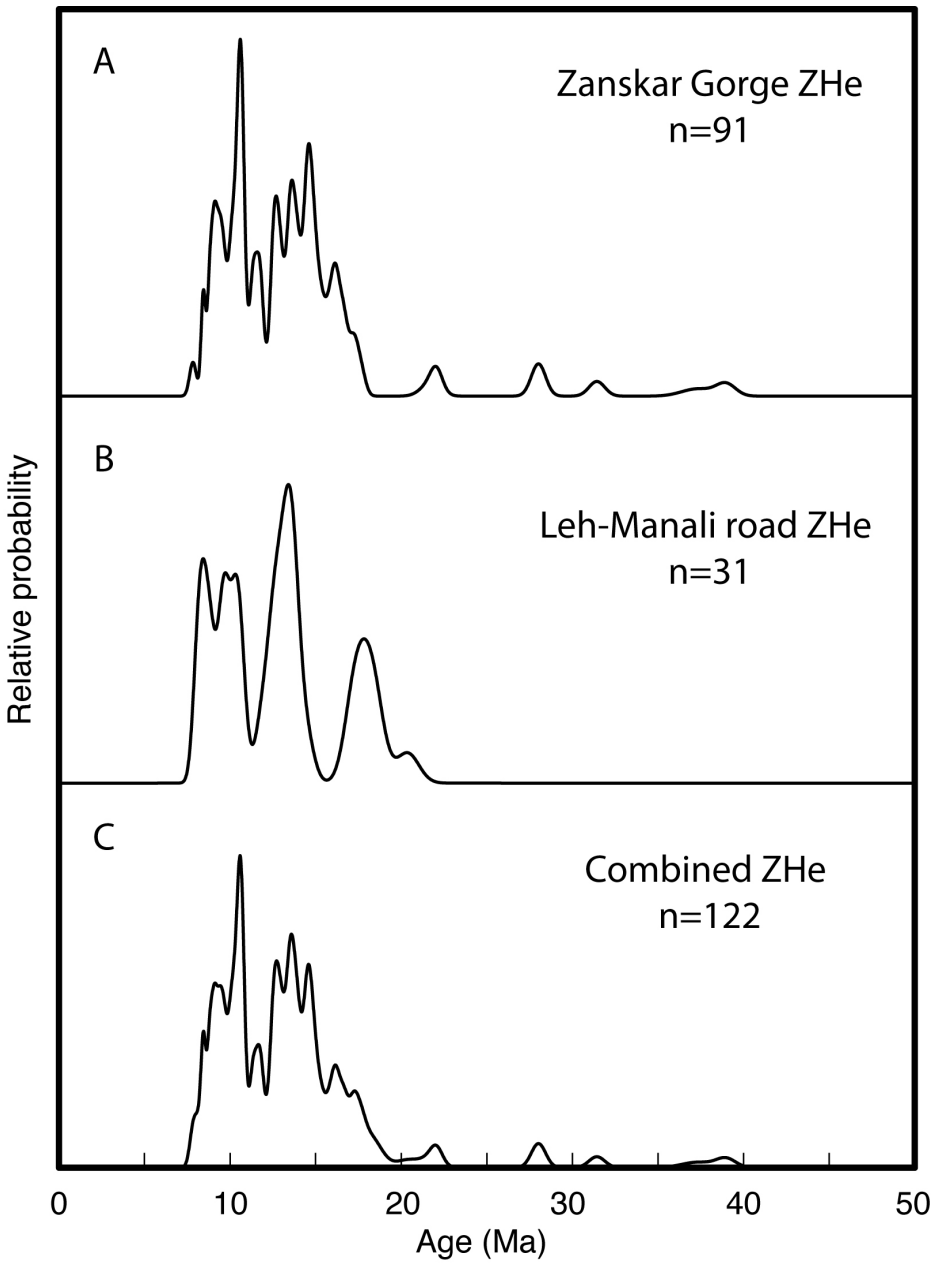
A
Zanskar Gorge ZHe
n=91
B
Leh-Manali road ZHe
n=31
C
Combined ZHe
n=122
Relative probability
0
10
20
30
40
50
Age (Ma)

Figure 5.4.

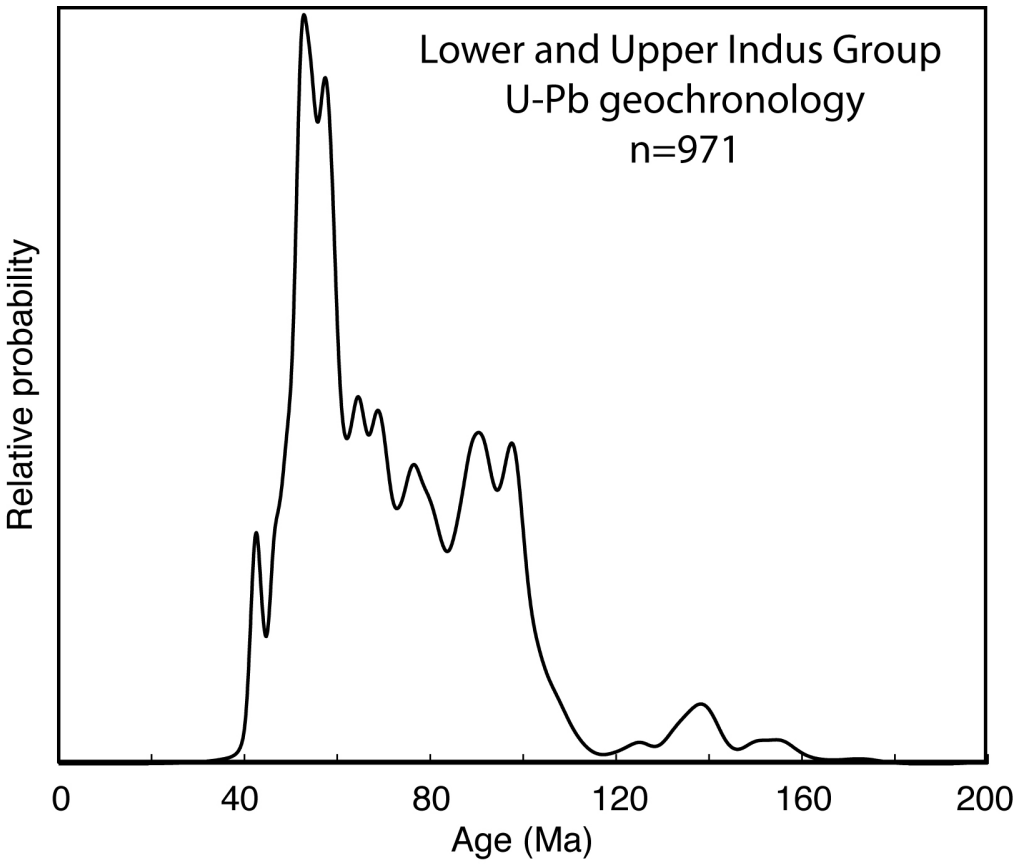
Lower and Upper Indus Group
U-Pb geochronology
n=971
Relative probability
0
40
80
120
160
200
Age (Ma)

Figure 5.5.

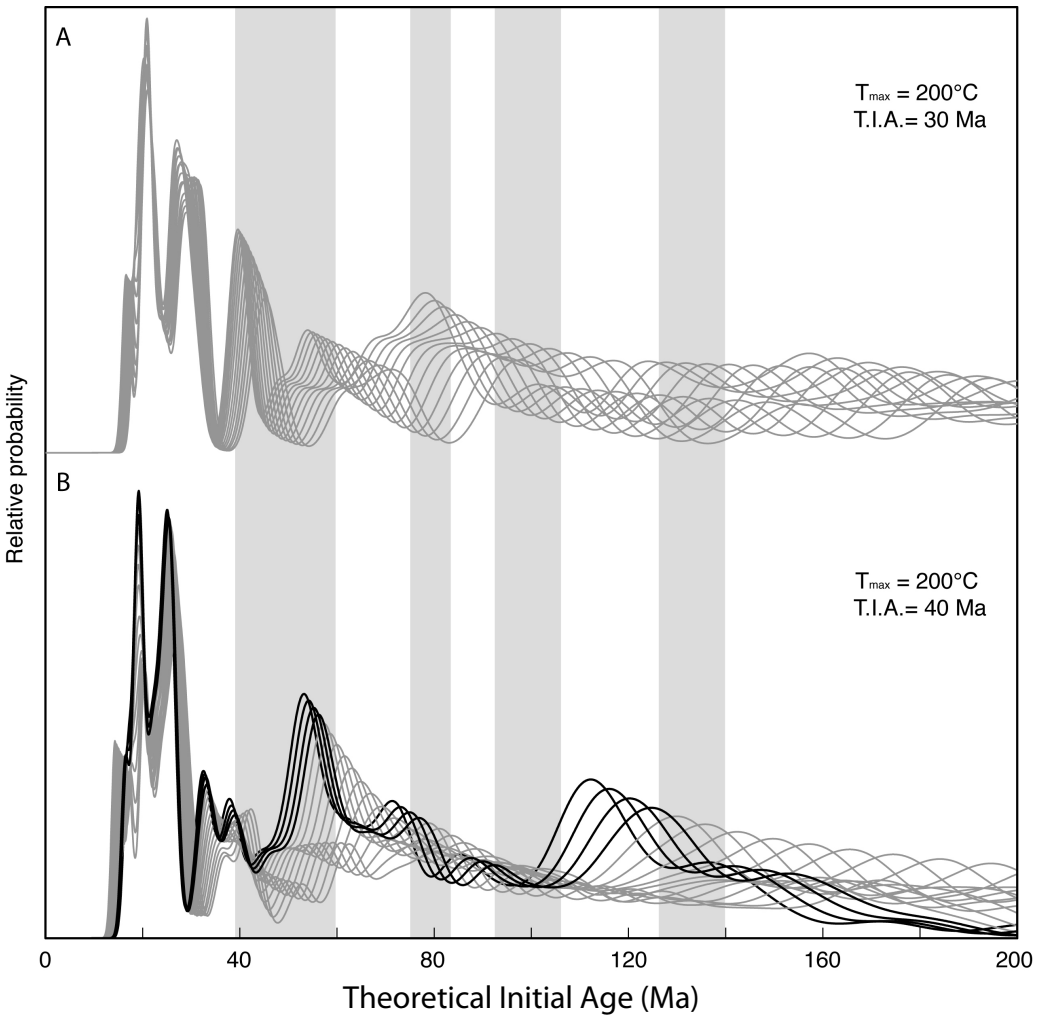
A
$T_{max}$ = 200°C
T.I.A.= 30 Ma
B
$T_{max}$ = 200°C
T.I.A.= 40 Ma
Relative probability
0
40
80
120
160
200
Theoretical Initial Age (Ma)

# CHAPTER 6

# ROBUST DETRITAL MINERAL (U-TH)/HE THERMOCHRONOLOGY IN NON-STEADY-STATE SETTINGS


## ABSTRACT

Detrital mineral thermochronology of modern sediments is a valuable tool for assessing catchment-wide exhumation rates, but only for catchments that have achieved an erosional and thermal steady state. It is possible to assess the likelihood of steady-state conditions – as well as other necessary assumptions – through statistical comparisons of the distribution of thermochronologic dates in a detrital population to catchment hypsometry [e.g., *Ruhl and Hodges*, 2005]. This approach presumes that the thermochronologic dataset is representative of the overall distribution of bedrock dates in the catchment. Due to the time-intensive nature of conventional (U-Th)/He thermochronology, most previous studies of this kind have relied on data for a few tens of grains, even though conventional wisdom holds that a substantially larger number might be necessary for a robust characterization of the population of cooling ages in a sample. We explore here the question of how many grain dates may be necessary and sufficient for such studies in a known non-steady–state setting by comparing subsamples of a large (n = 113) (U-Th)/He zircon dataset for a sediment sample from NW India. Our results indicate that, even for a basin with a complex thermal history, only ~ 35 grains may be enough to reveal that complexity and dissuade a researcher from inadvertently (and incorrectly)

concluding that the catchment had achieved steady state. We also introduce the use of laser microprobe (U-Th)/He for detrital studies, showing that it yields comparable information about cooling age distributions and minimizes unwanted bias toward pristine, unabraded crystals.

**1. Introduction**

Detrital mineral thermochronology has been applied in a variety of settings to address a range of topics, which include, but are not limited to, determining provenance, evaluating cooling histories of source regions, calculating lag time associated with sediment transport, and assessing both long- and short-term catchment wide erosion rates [e.g., *Brewer et al.,* 2003; *Rahl et al.,* 2003; *Hodges et al.,* 2005; *Ruhl and Hodges,* 2005; *McPhillips and Brandon*, 2010]. All of these applications require dating a statistically significant number of grains per sample to appropriately characterize the total population, but the number of grains typically dated in any given study has evolved with the advent of more efficient analytical techniques, as well as revised statistics.

Prior to 2004, most workers dated no more than 60 grains per sample because this number had been deemed sufficient to obtain a representative sampling of the total population of grains [*Dodson et al.,* 1988]. At that point, analytical techniques had evolved such that high throughput of single grain analyses was becoming routine. In particular, laser ablation-inductively coupled plasma mass spectrometry (LA-ICPMS) allowed detrital zircon U-Pb geochronologic studies to become standard methods for provenance studies

[e.g., *Dickinson and Gehrels*, 2003], while laser total fusion of single mica grains opened the door for routine detrital $^{40}Ar/^{39}Ar$ studies (as reviewed by *Hodges et al.* [2005]), which focused not only on provenance, but also on inverting detrital datasets for thermal histories, as first suggested by *Stock and Montgomery* [1996].

Vermeesch (2004) published a statistically rigorous treatment regarding the number of grains required for dating at least one grain from all subsets that compose at least 5% of a uniformly distributed population. He concluded that 117 grains is the minimum number that meets this criterion, and most workers in the field of detrital geochronology and thermochronology have aspired to produce ~100 dates per sample.

Adding detrital (U-Th)/He thermochronology to the arsenal of tools used for studying long- and short-term exhumation rates is important because of the low closure temperatures associated with both zircon (~180°C) [*Reiners et al.,* 2004] and apatite (~80°C) [*Farley*, 2000]. Detrital studies focused on assessing basin-wide erosion rates utilizing these data fill the temporal gap between cosmogenic radionuclide (CRN) studies, which illuminate basin-wide millenial-scale erosion rates, and $^{40}Ar/^{39}Ar$ studies, which elucidate long-term (million year-scale) erosion rates.

However, (U-Th)/He thermochronometry is both labor- and time-intensive due to the inability to simultaneously measure $^{4}He$ by gas-source mass spectrometry, and U and Th by solution ICPMS [*Wolf et al.,* 1996]. As such, most studies rarely date more than 50 and frequently fewer grains per

sediment sample [e.g., *Rahl et al.,* 2003; *Stock et al.,* 2005]. The conventional approach is further complicated by the need to analyze only euhedral grains to allow accurate geometric correction for alpha particle ejection from the outer ~20 microns of each grain [*Hourigan et al.,* 2005], inherently biasing all conventional (U-Th)/He detrital datasets. Moreover, the majority of these studies have focused on detrital apatite (U-Th)/He dating, in part because it is less time consuming, labor intensive, and expensive than detrital zircon studies. The few detrital zircon (U-Th)/He studies that do exist have been limited in scope, focusing more on provenance than quantification of erosion rates of the source area [e.g., *Rahl et al.*, 2003; *Reiners et al.*, 2005*; Campbell et al.,* 2005*; McInnes et al.,* 2009].

Because of the difficulty inherent to obtaining very large datasets using the conventional (U-Th)/He technique, the question of whether or not a particular dataset is truly representative becomes extremely important. Most recently, *Avdeev et al*. [2011] demonstrated that smaller datasets (<20 grains) reliably estimate long-term exhumation rates when cooling histories are simple and especially when there is at least some *a priori* knowledge of the geologic history of the catchment. *Avdeev et al.* [2011] also point out that a standard sample size applicable to all detrital studies is difficult to generalize because it should be dictated by a variety of different parameters, including the catchment size, complexity and exhumation history.

Instead of focusing on a simple situation in which few grains can approximate a plausible erosion rate and yield valid interpretations, we

address here the issue of a complex scenario, in which the standard assumptions associated with calculating basin-wide erosion rates, as described by *Ruhl and Hodges* (2005), are inappropriate. In cases such as these, there exists the distinct possibility that too few cooling ages will lead to a false interpretation of thermal and topographic steady state, leading the researcher to mistakenly believe that estimating basin-wide erosion rate from the data is justified.

In this paper, we present a conventionally acquired zircon (U-Th)/He dataset that was obtained from a modern river sand collected from the Ladakh batholith in the northwestern Indian Himalaya. Based on previously published bedrock (U-Th)/He data from this region [*Kirstein*, 2006; 2009], we expected a complex exhumation history for the catchment. We were not disappointed: the diagnostic technique described by *Ruhl and Hodges* (2005) confirms that a 113-grain conventional dataset is inconsistent with the ensemble of assumptions necessary to use it to calculate a basin-wide erosion rate. We then derived a series of smaller "synthetic" datasets from the conventional dataset to illustrate that small datasets (with fewer than 30-35 dates) frequently yield "false positives", a false sense of comfort by which erosion rates could be erroneously calculated.

A second zircon dataset (n = 44) from the same sample was acquired using the laser microprobe (U-Th)/He method [*Boyce et al.,* 2006]. With these data, we verified that 44 cooling ages is, in fact, sufficient to demonstrate that the catchment violated the assumptions of thermal and

topographic steady state. In this paper, we compare the conventional and laser microprobe datasets and show that the latter is better at recovering the variation of (U-Th)/He ages in the catchment, probably because it permits a less biased sampling of the detrital zircon population than the conventional approach that requires the use of euhedral grains.

## 2. Detrital mineral thermochronology applied to basin-wide erosion rates

*Brewer et al.* [2003] and *Ruhl and Hodges* [2005] discussed the relationship between the frequency distribution of detrital cooling ages and hypsometry of a modern river catchment, demonstrating that the thermochronometric data can be inverted to estimate erosion rates, provided that several assumptions withstand scrutiny. If we ignore the effects of lateral rock advection and assume vertical particle trajectories, the range of measured detrital cooling ages from a single catchment should be proportional to the time needed to erode the relief of the source area [*Stock and Montgomery*, 1996]. Erosion rate ($E$) can be calculated by dividing the elevation range of the catchment (relief, $R$), by the range of measured cooling ages ($t_{range}$).

$$E = \frac{R}{t_{range}} \quad (1)$$

While this equation is simple, its practical utility depends on several assumptions that, as it happens, can be collectively tested by comparing the distribution of elevation within the catchment (the hypsometry) with the distribution of apparent ages of grains collected from the eroded sediment

(*Ruhl and Hodges,* 2005). Specifically, the spatial distribution of erosion can be quantified by comparing the measured cooling ages to a model constructed by assigning cooling ages to each elevation in a digital elevation model (DEM; Figure 6.1). To describe the distribution of measured detrital cooling ages, we plot a synoptic probability density function for each dataset (SPDF; Figure 6.2), which comprises the normalized summation of individual cooling ages and their associated Gaussian uncertainties, such that the area under the curve is 1 [*Ruhl and Hodges*, 2005; *Stock et al.,* 2006]. If erosion is proportional to the surface area, then basin-wide erosion is spatially uniform and the measured SPDF should exactly match that of the hypsometry-derived model SPDF. Deviations between the measured and model SPDFs suggest that at least one of three basic assumptions is invalid.

**2.1. Assumption 1: Thermal and topographic steady state**

For Equation 1 to be applicable, the catchment must have achieved and maintained thermal and topographic steady states at appropriate times during the erosional history of the catchment. "Appropriate", in this case, corresponds to the range of cooling ages determined from the sample. These two steady states are not independent because topographic steady state is required at long wavelengths and over million year timescales to maintain thermal steady state [*Mancktelow and Grasemann*, 1997]. This is particularly true when dealing with low temperature thermochronometers. If the predicted and measured SPDFs topologically match one another, a plausible interpretation is that the catchment is in both topographic and thermal

steady state. Thus, throughout the remainder of this paper, we define our usage of the term "steady state" to include both topographic and thermal steady state, and do not discuss other types of steady state conditions.

### 2.2. Assumption 2: Uniform basin-wide erosion rates

During the range of time between the oldest cooling age and erosion of the sediment, erosion rates must have been temporally and spatially uniform throughout the catchment. Therefore, if the erosion rate within the basin has changed significantly, a mismatch will result. Moreover, if, within a single catchment, there are spatial gradients in uplift or erosion regimes, and if lithologic variations cause preferential erosion in parts of the catchment, the result will be a mismatch between the modeled and measured SPDFs [*Ruhl and Hodges,* 2005].

### 2.3. Assumption 3: Representative sampling of the total population

Although any successful detrital mineral thermochronologic study requires enough cooling ages to ensure an adequate representation of the total population of cooling ages within a sample, *Ruhl and Hodges* [2005] point out that the sediment sample itself must contain a hypsometrically weighted distribution of cooling ages from the bedrock within the catchment, which requires no lag time between erosion and deposition in temporary storage in river channels. Thus, a match between the measured and predicted SPDFs would suggest that the complete range of bedrock cooling ages is present in the detrital sample. Furthermore, departures between the measured and modeled SPDF related to unrepresentative sampling bias can

be caused by a variety of different processes, including sediment storage or focused erosion due to rockfalls, landslides, or glacial erosion.

Using these concepts, we focus much of the remainder of this paper upon comparing hypsometry to measured cooling ages. However, instead of using this method to determine whether any of these assumptions apply to a given catchment, we focus on a catchment in which at least one of these assumptions, that of steady state, was almost certainly violated.

**3. Application to the Ladakh batholith in the NW Indian Himalaya**

The Ladakh batholith of NW India represents a portion of the Andean-type continental arc that developed in Mesozoic to early Cenozoic time, along the southern margin of Eurasia, prior to the India-Eurasia collisional event that resulted in development of the Himalayan-Tibetan orogenic system (Figure 6.1) [*Honegger et al.*, 1982]. Previously published conventional (U-Th)/He analyses of multigrain zircon aliquots from samples of various parts of the batholith yield dates ranging from 30.9 ± 5.8 to 13.5 ± 1.2 Ma (2σ) [*Kirstein et al.,* 2006, 2009]. These and other low-temperature bedrock thermochronometric data (including (U-Th)/He apatite and fission track zircon and apatite analyses) show an unusual pattern: apparent ages do not simply correlate with sample elevation, but instead are oldest at lower elevation along the southern edge of the batholith and become progressively younger at higher elevations and to the north. *Kirstein et al.* [2009] interpreted this pattern as a result of southward tilting of the batholith about a horizontal axis. They also suggested that this might hav e been

accompanied by doming to explain the observed age distribution. This model was further refined to include a sequence of northward and southward tilts to explain Al-in-hornblende geobarometric results for the batholith [*Kirstein*, 2011].

Our study focused on the Basgo catchment, a small (~ 100 $km^2$) basin developed along the southern margin of the batholith (Figure 6.1). Elevations range from 3359 m at the mouth to 4550 at the crest. Kirstein et al. (2009) obtained two bedrock apatite fission track dates from this catchment: 34.9 ± 6.8 Ma at an elevation of 3550 m, and 33.8 ± 9.6 Ma, at an elevation of 4001 m. Statistically indistinguishable from one another, these dates are both older than all published zircon (U-Th)/He bedrock data from the rest of the range, which implies substantial variability of the thermal and erosional structure within the batholith during the Cenozoic. However, $^{10}Be$ cosmogenic radionuclide dates from the main stem of the Basgo catchment yield three statistically indistinguishable estimates for erosion rate between 29.2 ± 8.0 to 39 ± 16 m/Ma, which collectively imply little areal variation in erosion rate over the last ~300 ka (Figure 6.1) [*Dortch et al.,* 2011].

For this study, we collected a modern river sand from the mouth of the Basgo catchment (Figure 6.1, sample 07-AT-LB-B; 34°14'45.05" N, 77°17'1.8"E), which was sampled not only for its proximity to previous thermochronologic and cosmogenic radionuclide sampling localities, but also because the catchment comprises monotonous granite and granodioritic

lithologies common to the Ladakh batholith, as discerned from Advanced Spaceborne Thermal Emission and Reflection Radiometer (ASTER) image analysis. Because zircon is common to these lithologies, we considered it likely that if we obtained a very large dataset, any inconsistency found between the measured and predicted SPDFs would be a result of departure from steady state conditions. As a consequence of previous work by *Kirstein et al*. [2006, 2009], we anticipated that such an inconsistency would be found.

## 4. Analytical Methods

### 4.1. Catchment Hypsometry

Analysis of the relief of the Basgo catchment was performed using an ASTER-based, 30-m per pixel digital elevation model. We derived the hypsometry using ArcInfo drainage area sampling routines with 100-m elevation bins [e.g., *Brocklehurst and Whipple*, 2004; *Ruhl and Hodges,* 2005].

### 4.2. Detrital zircon (U-Th)/He thermochronology

The modern river sand required wet sieving and the application of standard magnetic and density-based mineral separation procedures. Once the fraction containing only zircon was isolated, it was panned in ethanol and split in half. Each half was then prepared for either conventional or laser microprobe dating.

#### 4.2.1 Conventional Approach

Standard procedures for the Noble Gas, Geochronology and Geochemistry Laboratory ($NG^3L$) at Arizona State University (ASU) have

been described in detail by *van Soest et al.* [2011]. For this study, we separated 113 from the conventional split. All grains were carefully examined under high magnification to minimize analyzing grains that contained inclusions, fractures or other imperfections. These opitcally satisfactory and euhedral grains were then measured for alpha ejection correction [*Hourigan et al.,* 2005] and loaded into Nb tubes for isotopic measurement.

$^{4}$He was measured for each individual grain using the ASI AlphaChron at NG$^{3}$L, whereby tubes were loaded into an ultrahigh vacuum (UHV) laser chamber and heated with a 980 nm diode laser. The released gas was spiked with $^{3}$He and measured on a quadrupole mass spectrometer. The packets were removed from the AlphaChron, spiked, and digested using concentrated acids in Parr digestion vessels. The final solutions were analyzed on a Thermo X series quadrupole ICP-MS in the W. M. Keck Foundation Laboratory for Environmental Biogeochemistry at ASU for measurement of U and Th. The resulting data and calculated dates are reported in Supplementary Material Appendix M.

### 4.2.2. Laser Microprobe Approach

The application of laser microprobe technologies for (U-Th)/He monazite thermochronology was pioneered by *Boyce et al*. [2006] and has now been employed to successfully date monazites as young as Pleistocene [*Boyce et al.,* 2009]. Here we describe the first application of this method to detrital zircons.

From the laser micrprobe split mentioned above, we randomly selected a relatively large number of zircon grains that were greater than 60 μm in their shortest dimension from the 50-250 μm zircon size fraction. This minimum grain size was selected because we intended to extract $^{4}$He from the core of each grain using a focused laser beam that would produce a ~ 20-35 μm-diameter ablation pit. As a consequence, dates for ≥ 60 μm grains would not require the alpha correction procedure that requires the selection of euhedral grains for conventional analysis.

The grains were then mounted in Torr Seal, a high vacuum resin made by Varian that is ideal for noble gas work because of its low vapor pressure under UHV. To minimize bubbles on the mount surface, the Torr Seal was stirred atop the grains while heated to no greater than 60°C. Once cured, the mount was polished to submicron levels and ultrasonicated in acetone for 30 minutes to remove any excess Torr Seal residue.

The mount was lightly gold-coated and loaded into the JEOL 840 SEM in the Leroy Eyring Center for Solid State Science (LE-CSSS) at ASU to obtain cathodoluminesence (CL) images, which serve as a proxy for U and Th zoning patterns [e.g., *Dobson et al.,* 2008]. Using these images, we were able to carefully target the least zoned parts of each grain while avoiding the alpha ejection zone, which comprises the outer 20 μm of the grain. We concomitantly collected secondary electron (SE) images, which aided the identification of microinclusions that might have been missed during the

picking process; if found, grains with such inclusions were deemed inappropriate for laser microprobe dating.

After SEM work, the mount was lightly polished to submicron levels to remove the gold coat, ultrasonicated in acetone for 30 minutes, and placed under a temperature-calibrated heat lamp to drive off any remaining volatiles in the Torr Seal. Gold coat removal allowed us to see through the grains, thus maximizing both the usefulness of Torr Seal and our ability to find inclusions in conjunction with the CL and SE images. To ensure that we only remove a thin layer without altering the zoning pattern, we compared pre-and post-analytical CL images; in all cases, the patterns remained unchanged.

The mount was then loaded into an UHV laser chamber, and grains were ablated using a New Wave 193 nm (ArF) Excimer laser with 20-35 μm ablation pit sizes. For a 20 μm diameter pit, 100 shots were fired for a depth of approximately 10 μm, whereas for a 35 μm diameter pit, 175 shots were fired for a depth of approximately 17 μm. The repetition rate of the laser was 5 Hz and the main energy output of the laser was kept constant at 6 mJ. Once the gas was liberated from the grain, it was purified using a SAES GP50 getter and cryogenically trapped such that only $^{4}He$ was released into a Thermo Scientific Helix SFT (Split Flight Tube) mass spectrometer for isotopic measurement using an electron multiplier in ion-counting mode. Sensitivity was monitored using slabs of Durango apatite of known age and U and Th concentration, and was, on average, 58,400 ± 4100 atoms $^{4}He$/cps. Blanks

generally ranged from 3.4 x $10^6$ to 6.0 x $10^7$atoms $^4$He. The volume and depth of each laser-He pit was measured using an ADE PhaseShift MicroXAM interferometric microscope coupled with a Matlab program developed specifically for volume calculations and error determnation, which allows for conversion of $^4$He abundances to $^4$He concentrations. We report volumes and $^4$He concentrations in Supplementary Material Appendix N.

Prior to U and Th analysis, the ejecta blanket around the laser-He pit was lightly polished using submicron abrasive to minimize the amount of removed material. The mount was again ultrasonicated in acetone to remove any Torr Seal that had flaked into the laser ablation pits during polishing. The mount was then gold coated in preparation for secondary ionization mass spectrometry (SIMS).

U and Th concentrations were measured using the Cameca IMS 6f at ASU. For standardization, a calibration curve was created with two natural zircons (Mahenge and ASU Sri Lanka) as well as synrock, a zircon powder made from a single natural zircon that has been sintered together using a piston cylinder furnace at 20 kbar and 1100°C to create a rock [*Monteleone et al*., 2009]. We used a ~20 nA $^{16}O^-$ primary beam and measured the following secondary ions: $^{30}Si^+$, $^{91}Zr^+$, $^{232}Th^+$, $^{238}U^+$, $^{248}ThO^+$, and $^{254}UO^+$, and ratio to $^{30}Si^+$. The primary beam was focused to 60 μm in diameter with a pre-sputter time of 4200 seconds, and energy filtering was applied using a -75 V offset with a 40 eV window. The purpose of using the large primary beam was to obtain an area-integrated measurement of the total U and Th contributing

$^4$He to the region of the laser ablation $^4$He analysis; we accomplished this by centering the broad ion beam directly on the laser ablation pit. While this method assumes no additional U+Th zoning complexity in the third dimension, it is operationally consistent with the approach to dealing with U and Th inhomogeneities that was advocated recently by *Farley et al.* [2011]. The resulting U and Th concentrations are reported in Supplementary Material Appendix N.

Throughout the analytical procedure, we monitored Mg (which is present in much greater concentrations in Torr Seal than in zircon) to ensure that Torr Seal was not contributing either U or Th to the analysis. As we developed this method, a slab of Sri Lanka zircon with an age of 443 ± 9 Ma [*Nasdala et al*., 2004] was analyzed, and for 20 spots, we obtained a weighted mean age of 437 ± 7 Ma (2$\sigma$), which is within error of the published age. This is a relatively homogeneous zircon, given its size, and demonstrates the fidelity of the laser-microprobe (U-Th)/He method.

**5. Conventional (U-Th)/He results**

Figure 6.2b demonstrates a narrow distribution of (U-Th)/He zircon cooling dates for the Basgo catchment and implies moderately paced exhumation over the Middle Eocene (40.0 ± 1.2 Ma) to Early Miocene (19.78 ± 0.60 Ma) interval. The most frequently encountered dates are Late Oligocene. To facilitate comparison between the SPDF produced from the conventional data and the modeled SPDF derived from the hypsometry, we

plot the cumulative SPDF (CSPDF) versus dimensionless age, t*, on a $CSPDF_{t^*}$ plot, where:

$$t^* = \frac{(t_m - t_{m_{\min}})}{t_{range}} \qquad (2)$$

and $t_{m_{\min}}$ is the minimum cooling age from this sample (Figure 6.3a) [*Ruhl and Hodges,* 2005]. While $t_{range}$ was explicitly defined as the difference between the oldest and youngest measured age for a sample in Equation (1), this is impractical when outliers exist, particularly because young grains often have large analytical errors, which will skew the tail of the distribution. Following *Ruhl and Hodges* [2005], we assigned values to $t_{range}$ such that the interval comprises 99% of the area under the cooling age SPDF, and the assigned value minimizes the mismatch, quantified as root mean square error (RMSE), between the shapes of $CSPDF_{t^*}$ versus the model curve derived from hypsometry, $CSPDF_{z^*}$ (Figure 6.3a). To create $CSPDF_{z^*}$, we plot the cumulative normalized SPDF derived from hypsometry, versus dimensionless elevation, z*, where

$$z^* = \frac{(z - z_{\min})}{R} \qquad (3)$$

and $z_{min}$ is the minimum elevation [*Brocklehurst and Whipple*, 2004].

To visually assess the significance of any mismatch between the dimensionless distributions, we follow the procedure of *Ruhl and Hodges* [2005] and produce 300 model curves, $CSPDF_{t^*m}$, from *n* points randomly selected from the $CSPDF_{z^*}$ distribution, where *n* is the number of grains

analyzed from the sample (Figure 6.3). If $CSPDF_{t^*}$ lies within the range of $CSPDF_{t^*m}$, then it is reasonable to infer that all assumptions necessary for the application of Equation 1 are appropriate, and that the catchment was at steady state during the closure interval for the (U-Th)/He thermochronometer as represented by the range of dates in the sample.

### 5.1. Visually assessing the assumption of steady state

As mentioned above, the bedrock data of Kirstein and co-workers led us to expect a mismatch between the $CSPDF_{z^*}$ predicted from hypsometry and the measured (U-Th)/He cooling age distribution, $CSPDF_{t^*}$. Indeed, in Figure 6.3a, $CSPDF_{t^*}$ is well outside the bounds of $CSPDF_{z^*}$ and its derived $CSPDF_{t^*m}$ curves. Close inspection of $CSPDF_{t^*}$ suggests that the mismatch is caused by oversampling of older grains, which, in a simple case, would imply a reduction in catchment relief with more grains being sourced from higher elevations [*Stock et al.,* 2006]. However, if we assume that the interpretation of bedrock data from *Kirstein et al.* [2009] is correct, older ages should be sourced from lower elevations, which would imply oversampling at lower elevation.

### 5.2. Statistically assessing sample size for non-steady state scenarios

Because we have an unprecedented conventional zircon (U-Th)/He dataset, we can explore the ramifications of dating fewer than 114 grains. We used Monte Carlo methods, whereby we randomly subsample the conventional dataset for different values of subsample size, $s$, where $s$ = 10, 50, and 100 grains. We performed this calculation 2000 times for each value

of *s*, and plot the results as $CSPDF_{t^*s=10}$, $CSPDF_{t^*s=50}$ and $CSPDF_{t^*s=100}$ in Figure 6.4, with both $CSPDF_{t^*}$ and $CSPDF_{z^*}$ plotted for reference.

A basic observation is that, as the subsample size *s* increases, the family of $CSPDF_{t^*s}$ curves do not overlap $CSPDF_{z^*}$. However, upon close examination of $CSPDF_{t^*s=10}$ in Figure 6.4a, $CSPDF_{z^*}$ overlaps at least some of the subsampled curves. This important observation implies that it is possible to obtain an incorrect interpretation of steady state when dating so few grains.

In order to quantify how often the subsampled cooling age curves, $CSPDF_{t^*s,}$ are statistically indistinguishable from $CSPDF_{z^*}$, we applied a one-sample Kuiper test [*Kuiper*, 1962]. This method was chosen because it gives equal sensitivity to both the median and tails of a distribution. We calculated the Kuiper statistic, *V*, which involves the maximum deviation both above and below the cumulative distributions that are being compared (Equation 5 of *Ruhl and Hodges* [2005]).

In this case, we compared each $CSPDF_{t^*s}$ curve to $CSPDF_{z^*}$ in an effort to determine the probability, *P*, that one cannot exclude that a sample $CSPDF_{t^*s}$ has been drawn from the given distribution, $CSPDF_{z^*}$ at a threshold of $\alpha$ =0.05. Therefore, if $P > 0.05$, the result is consistent with the two curves being equivalent at the 95% significance level, whereas if $P < 0.05$, the probability that $CSPDF_{t^*s}$ was drawn from $CSPDF_{z^*}$ is less than 5%.

We calculated the Kuiper statistic for each of 10,000 subsampled curves with subsets containing *s*=5 to *s*=100 at 5 grain intervals. The results

are listed in Table 6.1 and displayed in Figure 6.5, where we plot the number of grains in each subsampled population, *s*, on the ordinate, and the percent of false positive matches between $CSPDF_{t^*s}$ and $CSPDF_{z^*}$ versus total number of runs (10,000) on the abscissa.

For ten randomly selected grains, there is a ~70% chance of yielding a $CSPDF_{t^*s}$ curve that is statistically indistinguishable from $CSPDF_{z^*}$ at the 95% confidence level. Thus, the likelihood of incorrectly concluding that the catchment was at steady state is ~70%. In practice, dating only ten grains would probably encourage researchers to calculate basin-wide erosion rates from the non-steady–state Basgo catchment. However, by analyzing more than 35 grains, the probability of obtaining a false positive match decreases to ~5% and any amount over 50 grains is well within the 95% confidence limit of yielding statistically distinguishable $CSPDF_{z^*}$ and $CSPDF_{t^*s}$ curves.

Because the Basgo catchment likely experienced a complex exhumation history [*Kirstein*, 2011], we extrapolate our results to any catchment of similar size and uniform lithology, and conclude that a minimum of 30 to 35 grains should be dated, particularly in the situation where no prior knowledge exists regarding the cooling history. Any dataset that comprises fewer grains should be interpreted with caution, and should be supplemented with alternate datasets, as discussed by *Avdeev et al.*, [2011]. It is also apparent from Figure 6.5 that any sample size greater than 50 grains will not necessarily provide any additional useful information for this particular catchment, and so we suggest that studies that produce

between 50 and 60 cooling ages will robustly characterize the distribution of cooling ages exposed within the catchment under examination so long as it is of comparable size to the Basgo catchment [e.g., *Stock et al.,* 2006].

**6. Laser microprobe results and analysis**

Figures 6.2b and 6.3b show the SPDF and $CSPDF_{t^*}$ curves for 44 single zircons from the same detrital sample. As expected, the overall shapes of the SPDFs for the laser ablation and conventional datasets are similar. The laser ablation dates spread between Middle Eocene (45.1 ± 3.3 Ma) and Middle Miocene (16.3 ± 1.2 Ma), with most dates in the Late Oligocene – Early Miocene interval. Although the means of both datasets are equivalent, the laser ablation dataset shows more skew towards younger dates. This is more apparent when the $CSPDF_{t^*}$ curves for the two datasets are compared (Figure 6.3). As the analysis in the previous section would predict, the 44-grain laser ablation dataset permits us to reject the steady-state assumption for the Basgo catchment even though it is based on a much smaller number of (U-Th)/He dates. Moreover, we consider it likely that the laser ablation dataset provides a less biased sampling of the distribution of bedrock cooling ages in the catchment.

The bedrock data of *Kirstein et al.* [2009] show that higher elevations along the south side of the Ladakh batholith yield younger (U-Th)/He dates, and we would thus predict that younger zircon grains would have to be transported farther downstream in the Basgo catchment to the collection site for our sediment sample. The higher proportion of younger grains in the

laser ablation sample probably reflects the fact that younger grains are more often broken or abraded during their longer transport distance than older grains and thus less likely to be euhedral and selected out of a population for conventional analysis. For the laser microprobe work, we did not selectively choose euhedral grains for analysis but instead selected grains at random for dating.

**7. The case for laser microprobe dating in detrital (U-Th)/He studies**

Evidence that the laser microprobe dataset is more representative than the conventional dataset for the Basgo catchment suggests that the laser microprobe technique may be a better approach to detrital (U-Th)/He thermochronology. However, as is the case with all microanalytical techniques, increased spatial resolution comes at a cost of analytical precision. Our laser microprobe dates for the Basgo catchment have average 2σ analytical uncertainties of ~7.5%, whereas the conventional analyses have average uncertainties of ~3.3%. However, it should be noted that errors associated with the alpha ejection correction that must be applied in conventional (U-Th)/He work are seldom propagated into published datasets (including ours) because they are so difficult to quantify. *Spiegel et al.* [2009] did so by estimating a 5 μm uncertainty in their grain size measurements, and report an approximate 1σ analytical uncertainty of ~6.2% for their data, but even this does not account for uncertainties in overall grain geometry or the possibility of heterogeneous U and Th distribution. Such uncertainties are

effectively eliminated in the laser ablation method because we avoid the alpha ejection zone, and – at least from a two-dimensional perspective that presumes no zoning complexities in the third dimension [*Farley et al.,* 2011] – measure all U and Th that contributed $^{4}$He to the laser ablation pit. We feel confident that the current level of uncertainty associated with laser microprobe (U-Th)/He thermochronology will improve as we continue our efforts to improve the analytical technique.

There have been relatively few published detrital (U-Th)/He studies compared with the number of published detrital $^{40}$Ar/$^{39}$Ar studies. This discrepancy largely reflects the relative simplicity of laser fusion techniques (commonly applied in $^{40}$Ar/$^{39}$Ar studies [*Hodges et al.,* 2005]) as compared with the conventional method of (U-Th)/He dating that involves $^{4}$He analysis by isotope dilution quadrupole mass spectrometry and U+Th analysis by solution ICPMS. The laser microprobe technique described here is also complex, but much of the time associated with the procedure reflects SIMS analysis for U+Th. We are in the process of transitioning our approach to the use of LA-ICPMS, which should increase throughput significantly.

**8. Conclusions**

A paired conventional and laser microprobe study of detrital zircon crystals in a sediment sample from the mouth of the Basgo catchment demonstrates that the laser microprobe technique described here is at least as good as (and likely less biased than) the conventional technique for establishing (U-Th)/He cooling age distributions in detrital mineral

populations. We applied the metrics of *Ruhl and Hodges* [2005] to the two datasets developed for the Basgo catchment to confirm our instinct that the catchment was not at thermal and erosional steady state throughout its Eocene-Miocene interval of cooling through the (U-Th)/He closure temperature. Monte Carlo subsampling of the large conventional dataset suggests that roughly 35 (U-Th)/He dates may be sufficient to characterize the cooling age distributions in detrital mineral populations adequately for application of the *Ruhl and Hodges* [2005] method of assessing the feasibility of employing Equation 1 [*Stock and Montgomery,* 1996] to determine catchment-wide erosion rates for steady-state landscapes.

## 9. References


Avdeev, B., N. A. Niemi, and M. K. Clark (2011), Doing more with less: Bayesian estimation of erosion models with detrital thermochronometric data, *Earth Planet. Sci. Lett., 305,* 385-395.

Boyce J. W., K. V. Hodges, W. J. Olszewski, M. J. Jercinovic, and P. W. Reiners (2006), Laser microprobe (U-Th)/He thermochronology, *Geochim. Cosmochim. Acta, 70,* 3031-3039.

Boyce, J. W., K. V. Hodges, D. King, J. L. Crowley, M. Jercinovic, N. Chatterjee, S. A. Bowring, and M. Searle (2009), Improved confidence in (U-Th)/He thermochronology using the laser microprobe: An example from a Pleistocene leucogranite, Nanga Parbat, Pakistan. *Geochem. Geophys. Geosyst., 10*, QAA01, doi.10.1029/2009GC002497.

Brewer, I. D., D. W. Burbank, and K. V. Hodges (2003), Modeling detrital cooling-age populations: insights from two Himalayan catchments, *Basin Res., 15*, 305-320.

Brocklehurst, S. H. and K. X. Whipple (2004), Hypsometry of glaciated landscapes, *Earth Surf. Processes Landforms, 29*, 907-926.

Campbell, I. H., P. W. Reiners, C. M. Allen, S. Nicolescu, and R. Upadhyay (2005), He-Pb double dating of detrital zircons from the Ganges and Indus Rivers: Implications for quantifying sediment recycling and provenance studies, *Earth Planet. Sci. Lett., 237*, 402-432.

Dickinson, W. R. and G. E. Gehrels (2003), U-Pb ages of detrital zircons from Permian and Jurassic eolianite sandstones of the Colorado Plateau, USA: Paleogeographic implications, *Sediment. Geol., 163*, 29-66.

Dobson, K. J., F. M. Stuart, T. J. Dempster, and EIMF (2008), U and Th zonation in Fish Canyon Tuff zircons: Implications for a zircon (U-Th)/He standard, *Geochim. Cosmochim. Acta, 72*, 4745-4755.

Dodson, M. H., W. Compston, I. S. Williams, and J. F. Wilson (1988), A search for ancient detrital zircons in Zimbabwean sediments, *J. Geol. Soc., 145*, 977-983.

Dortch, J. M., L. A. Owen, L. M. Schoenbohm, and M. W. Caffee (2011), Asymmetrical erosion and morphological development of the central Ladakh Range, northern India, *Geomorphology*, doi:10.1016/j.geomorph.2011.08.014.

Farley, K. A. (2000), Helium diffusion from apatite: General behavior as illustrated by Durango fluroapatite, *J.Geophys. Res., 105*, 2903-2914.

Farley, K. A., D. L. Shuster, and R. A. Ketcham (2011), U and Th zonation in apatite observed by laser ablation ICPMS, and implications for the (U-Th)/He system, *Geochim. Cosmochim. Acta, 75*, 16, 4515-4530.

Hodges, K. V., K. W. Ruhl, C. W. Wobus, and M. S. Pringle (2005), $^{40}Ar/^{39}Ar$ thermochronology of detrital minerals, in *Low-Temperature Thermochronology: Techniques, Interpretations, and Applications*, edited by P. W. Reiners et al., *Rev. Mineral. Geochem., 58*, 239-257.

Honegger, K., V. Dietrich, W. Frank, A. Gansser, M. Thöni, and V. Trommsdorf (1982), Magmatism and metamorphism in the Ladakh Himalayas (the Indus-Tsangpo suture zone), *Earth Planet. Sci. Lett., 60*, 253-292.

Hourigan, J. K., P. W. Reiners, and M. T. Brandon (2005), U-Th zonation-dependent alpha-ejection in (U-Th)/He chronometry, *Geochim. Cosmochim. Acta, 69*, 3349-3365.

Kirstein, L. A. (2011), Thermal evolution and exhumation of the Ladakh Batholith, northwest Himalaya, India, *Tectonophysics, 503*, 222-233.

Kirstein, L. A., H. Sinclair, F. M. Stuart, and K. Dobson (2006), Rapid early Miocene exhumation of the Ladakh batholith, western Himalaya, *Geology, 34*, 1049-1052.

Kirstein, L. A., J. P. T. Foeken, P. van der Beek, F. M. Stuart, and R. J. Phillips (2009), Cenozoic unroofing history of the Ladakh Batholith, western Himalaya, constrained by thermochronology and numerical modeling, *J. Geol. Soc., 166*, 667-678.

Mancktelow, N. S. and B. Grasemann (1997), Time dependent effects of heat advection and topography on cooling histories during erosion, *Tectonophysics, 270*, 167-195.

McInnes, B. I. A., N. J Evans, B. J. McDonald, P. D. Kinny, and J. Jakimowicz (2009), Zircon U-Th-Pb-He double dating of the Merlin kimberlite field, Northern Territory, Australia, *Lithos, 1125,* 592-599.

McPhillips, D. and M. T. Brandon (2010), Using tracer thermochronology to measure modern relief chance in the Sierra Nevada, California, *Earth Planet. Sci. Lett.,, 296*, 373-383.

Monteleone, B. D., M. C. van Soest, K. Hodges, G. M. Moore, J. W. Boyce, and R. L. Hervig (2009), Assessment of alternative [U] and [Th] zircon standards for SIMS, *Eos Trans. AGU, 90(52),* Fall Meet. Suppl., V31E-2017.

Nasdala, L., P. W. Reiners, J. I. Garver, A. K. Kennedy, R. A. Stern, E. Balan, and R. Wirth (2004), Incomplete retention of radiation damage in zircon from Sri Lanka, *Am. Mineral.*, *89*, 219-231.

Rahl, J. M., P. W. Reiners, I. H. Campbell, S. Nicolescu, and C. M. Allen (2003), Combined single-grain (U-Th)/He and U-Pb dating of detrital zircons from the Navajo Sandstone, Utah, *Geology, 31*, 761-764.

Reiners, P. W., I. H. Campbell, S. Nicolescu, C. M. Allen, J. K. Hourigan, J. I. Garver, J. M. Mattinson, and D. S. Cowan (2005), (U-Th)/(He-Pb) double dating of detrital zircons, *Am. J. Sci., 305*, 259-311.

Ruhl, K. W., and K. V. Hodges (2005), The use of detrital mineral cooling ages to evaluate steady-state assumptions in active orogens: An example from the central Nepalese Himalaya, *Tectonics, 24*, TC4015.

Stock, G. M., T. A. Ehlers, and K. A. Farley (2006), Where does sediment come from? Quantifying catchment erosion with detrital apatite (U-Th)/He thermochronometry, *Geology, 34*, 725-728.

Stock, J. D. and D. R. Montgomery (1996), Estimating paleorelief from detrital mineral age ranges, *Basin Res., 8*, 317-327.

Spiegel, C., B. Kohn, D. Belton, Z. Berner, and A. Gleadow (2009), Apatite (U-Th-Sm)/He thermochronology of rapidly cooled samples: The effect of He implantation, *Earth Planet. Sci. Lett.,, 285*, 105-114.

Vermeesch, P. (2004), How many grains are needed for a provenance study?, *Earth Planet. Sci. Lett., 224*, 441-451.

Wolf, R. A., K. A. Farley, and L. T. Silver (1996), Helium diffusion and low-temperature thermochronometry of apatite, *Geochim. Cosmochim. Acta, 60*, 4231-4240.

## 10. Figure captions

Figure 6.1. (a) Shaded relief map derived from GTOPO30 (30m/pixel DEM) overlain with ASTER DEM (15m/pixel), with white box showing location of b. (b) Simplified geologic map after *Tripathy et al*. [in prep.] with black box showing location of c. (c) ASTER DEM of Basgo catchment draped over shaded relief map, with all samples plotted. CRN samples from *Dortch et al.*, [2011], and AFT samples from *Kirstein et al.* [2009]. We plot our detrital zircon (U-Th)/He sample for completeness.

Figure 6.2. Probability density curves of (a) conventional and (b) laser microprobe data presented herein. Outliers are included for completeness.

Figure 6.3. Comparison of cumulative hypsometric curve $CSPDF_{z^*}$ (solid black lines) and non-dimensionalized cooling age curves $CSPDF_{t^*}$ (dashed black

lines), with 300 model $CSPDF_{t^*m}$ curves plotted for the catchment (see Ruhl and Hodges, 2005). For each dataset, *n* describes the number of zircon (U-Th)/He dates represented by $CSPDF_{t^*}$. The root mean square error (RMSE) is calculated between the $CSPDF_{z^*}$ and each $CSPDF_{t^*}$. (a) Conventional dataset, and (b) laser-microprobe dataset.

Figure 6.4. Dashed black line denotes $CSPDF_{t^*}$ calculated from the conventional data. We resampled these data 2000 times for various subset sizes (*s*), and plot their $CSPDF_{t^*s}$ curves (gray lines). We include $CSPDF_{z^*}$ (solid black line) to visually demonstrate the lack of significant difference between some $CSPDF_{t^*s=10}$ curves, and the complete lack of overlap for all $CSPDF_{t^*s=100}$.

Figure 6.5. Graphical depiction of number of grains for different subsets, *s*, of the total population of conventional (U-Th)/He dates versus the percent, out of 10,000 random selections, that the $CSPDF_{t^*s}$ erroneously matches $CSPDF_{z^*}$. In scenarios where *s* is greater than or equal to 40 grains, confidence levels of over 95% are reached such that it is very unlikely that any dataset would yield a topologic match to the hypsometric curve.

Figure 6.6. Comparison between laser-microprobe dataset (solid black line) and conventional dataset (dashed black line). To create the gray lines, we randomly subsampled the conventional dataset to the same size as the laser-

microprobe dataset (n=44). These curves topologically match the laser-microprobe CSPDF fewer than 4% of the time, implying that the two datasets are statistically distinguishable from one another.

Figure 6.1.

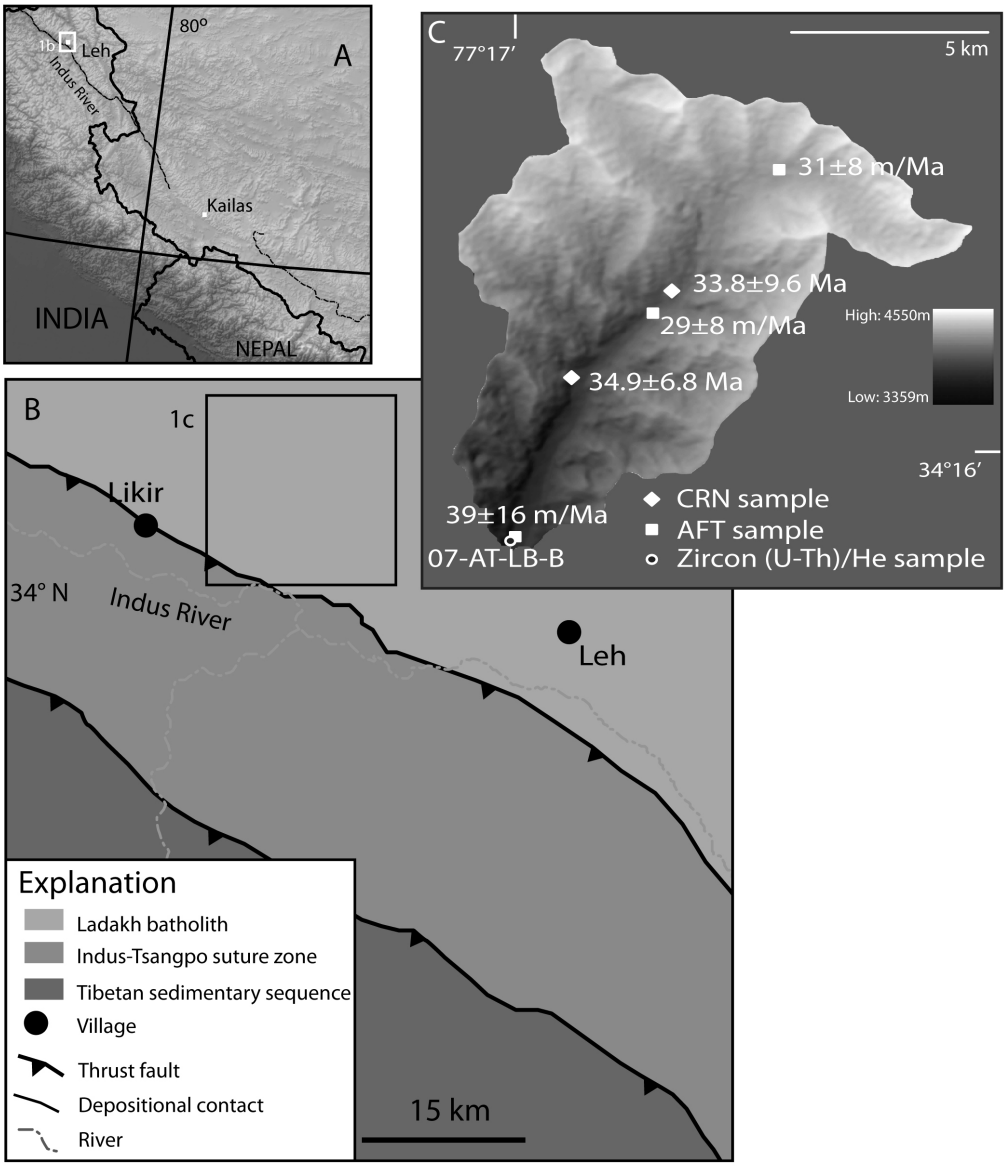
A
80°
1b
Leh
Indus River
Kailas
INDIA
NEPAL
B
1c
Likir
34° N
Indus River
Leh
Explanation
Ladakh batholith
Indus-Tsangpo suture zone
Tibetan sedimentary sequence
Village
Thrust fault
Depositional contact
River
15 km
C
77°17′
5 km
31±8 m/Ma
33.8±9.6 Ma
29±8 m/Ma
34.9±6.8 Ma
High: 4550m
Low: 3359m
34°16′
39±16 m/Ma
07-AT-LB-B
CRN sample
AFT sample
Zircon (U-Th)/He sample

Figure 6.2.

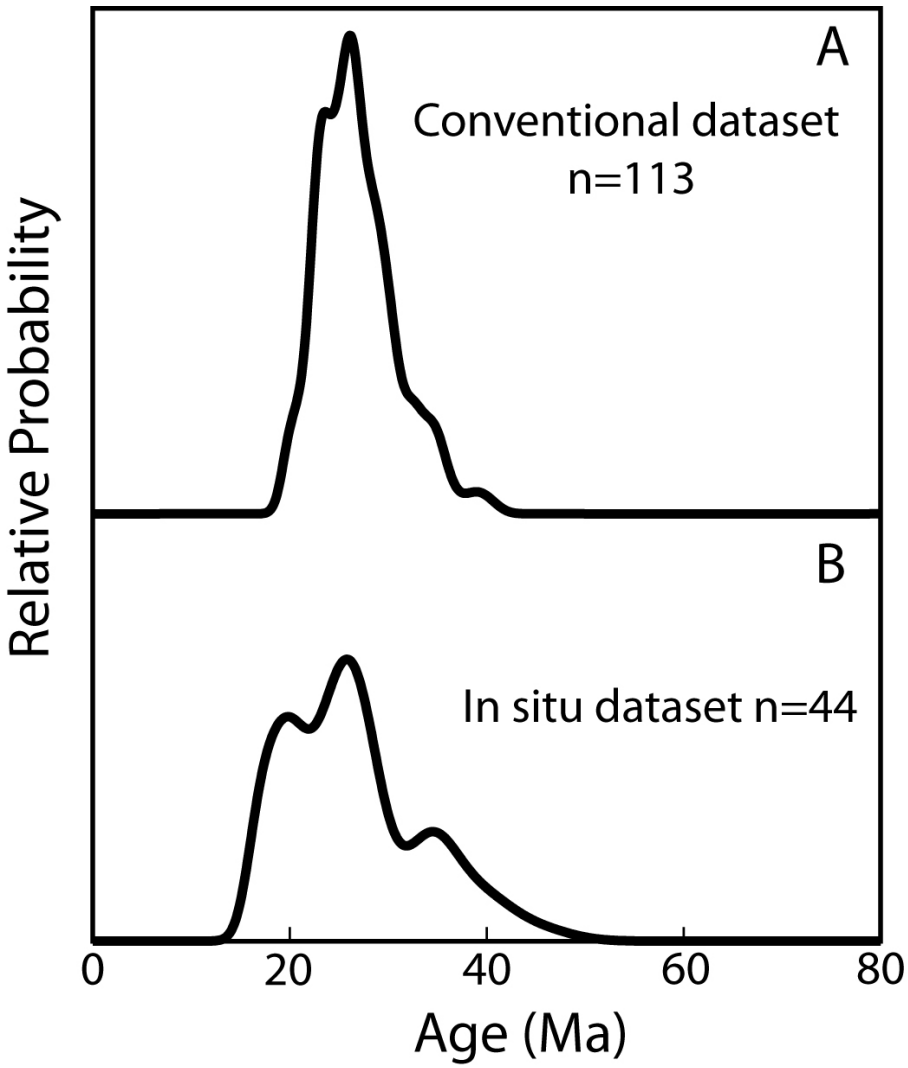
A
Conventional dataset
n=113
B
In situ dataset n=44
Relative Probability
0
20
40
60
80
Age (Ma)

Figure 6.3.

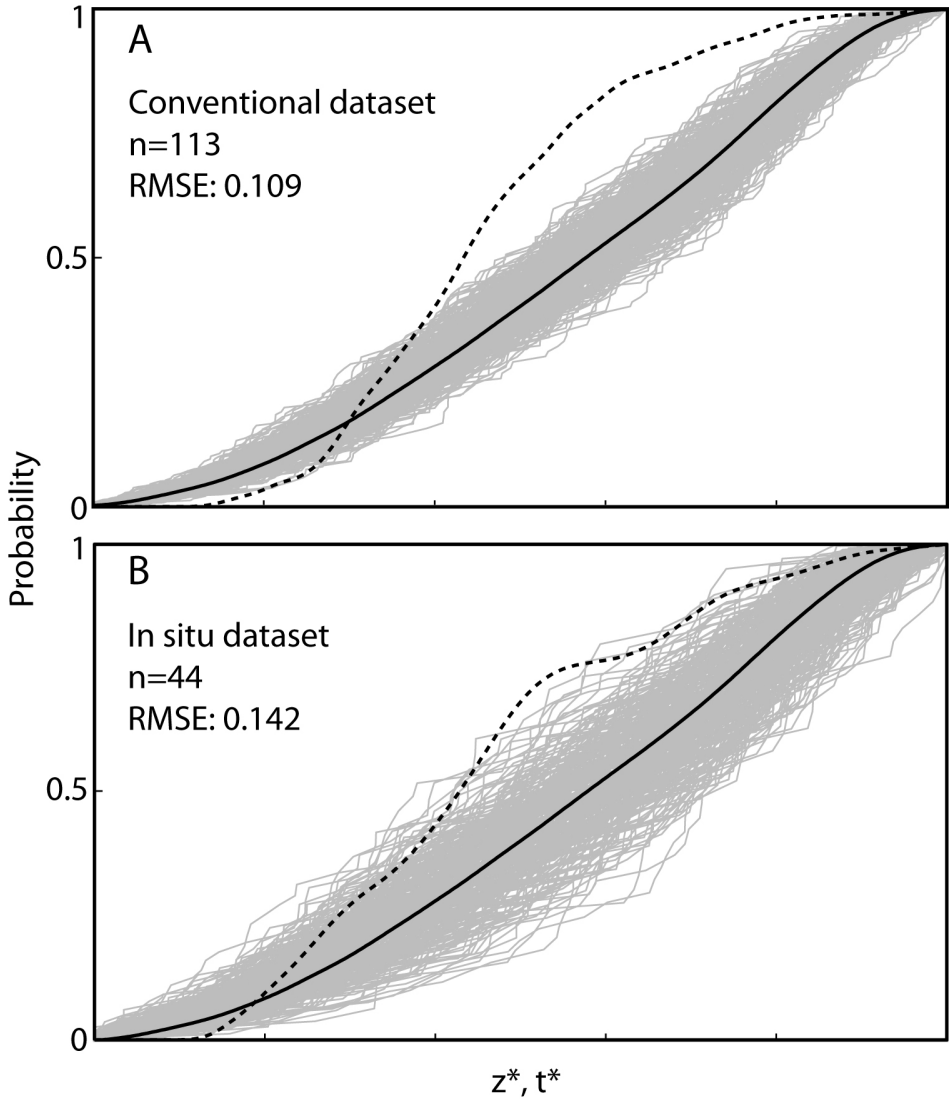
A
Conventional dataset
n=113
RMSE: 0.109
B
In situ dataset
n=44
RMSE: 0.142
Probability
1
0.5
0
z*, t*

Figure 6.4.

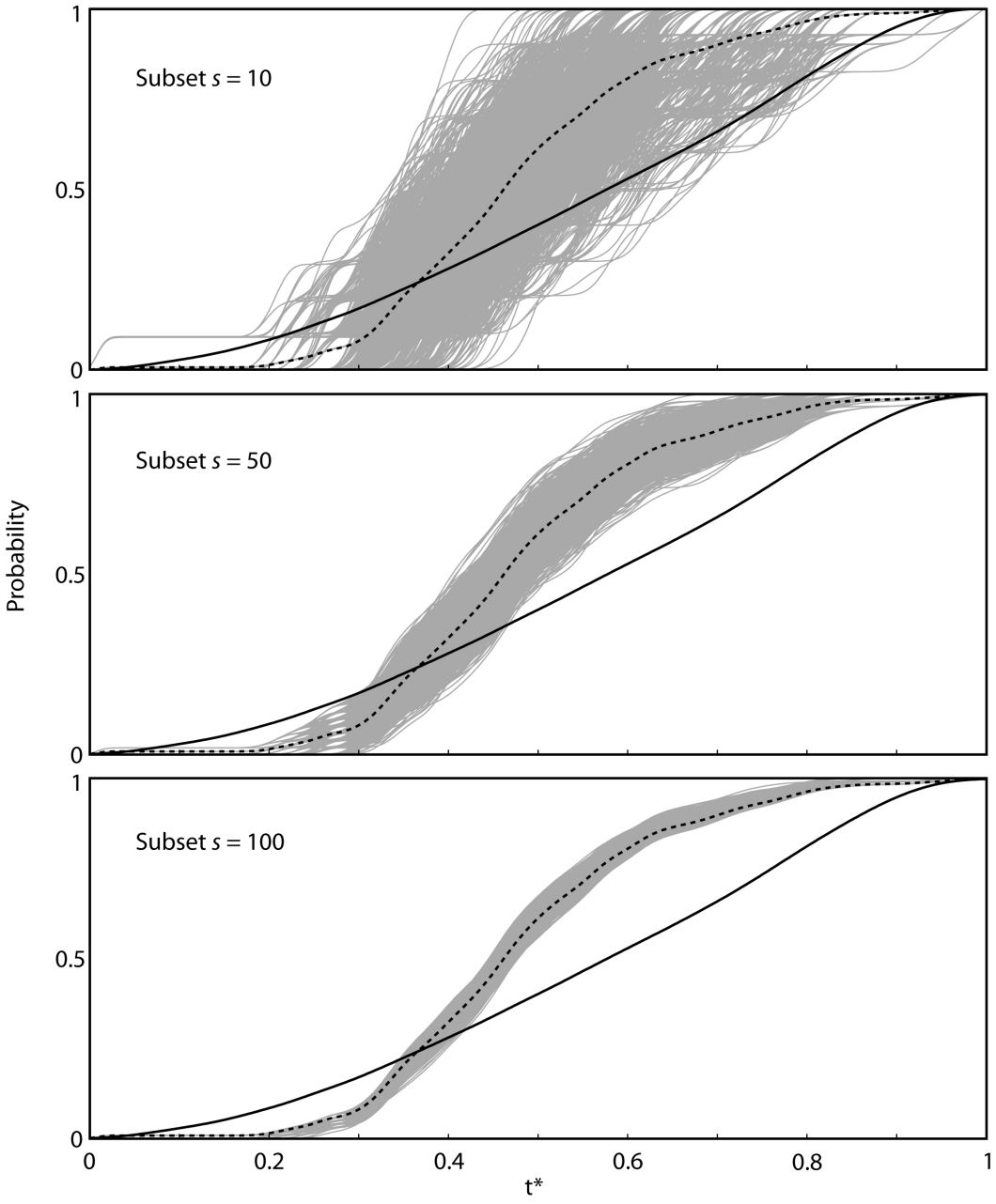
Subset s = 10
Subset s = 50
Subset s = 100
Probability
t*
0
0.5
1
0.2
0.4
0.6
0.8

Figure 6.5.

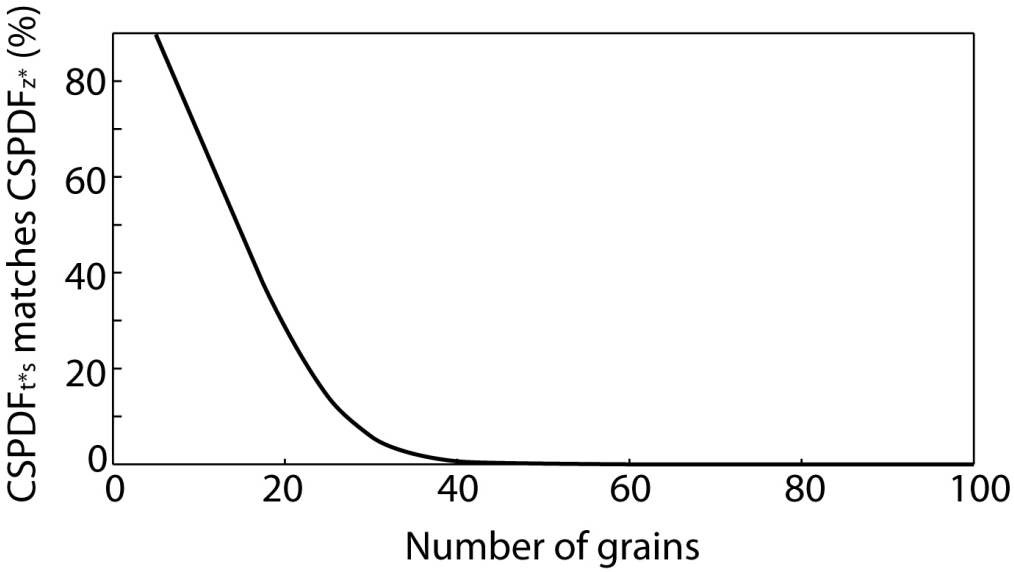
CSPDF$_{t^*s}$ matches CSPDF$_{z^*}$ (%)
0
20
40
60
80
0
20
40
60
80
100
Number of grains

Figure 6.6.

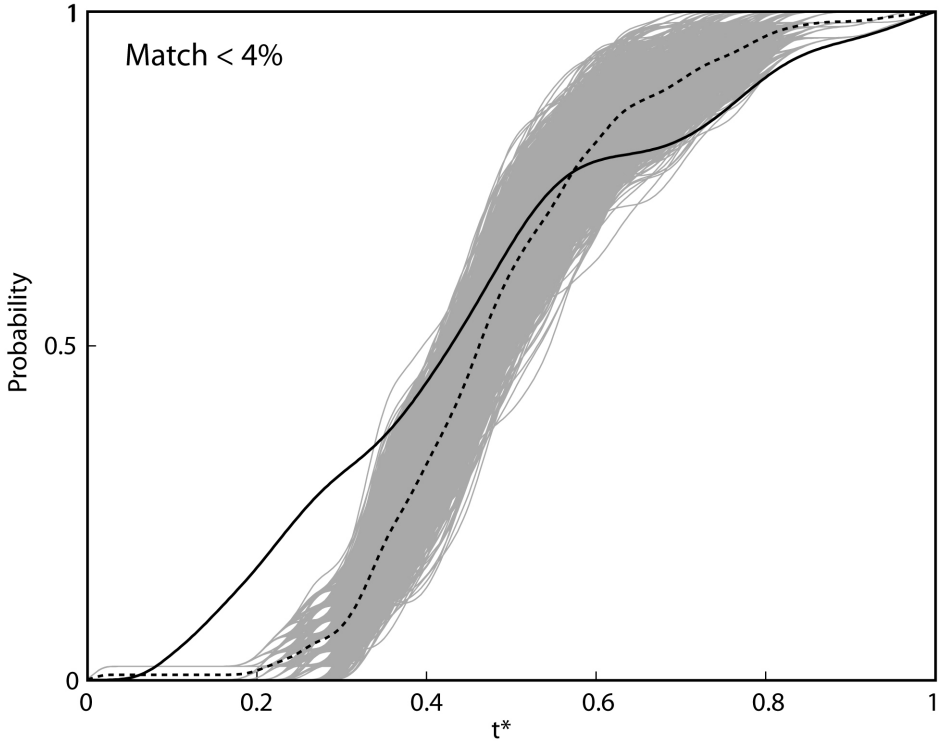

# CHAPTER 7

# SYNTHESIS

The studies described in previous chapters demonstrated the power of using a multi-faceted approach to interrogate a geologically complex area. Here, I summarize the major contributions made in the course of my work and speculate on possible research projects at different scales, ranging from locally focused projects in the Indus Basin to general applications of techniques introduced in this dissertation, that could extend my work.

## 1. Major contributions

For the benefit of those who work in the Ladakh region, I have developed an internally consistent regional-scale geologic map and coherent stratigraphy that eliminated the unnecessary complexity of previous interpretations of Indus Basin geology.

Evidence for mixed Indian-Eurasian detritus has been found throughout the Indus Basin succession, counter to conclusions of previous workers [e.g., *Henderson et al.,* 2010; 2011]. This observation, coupled with previous and newly presented constraints on the depositional ages of different elements of the stratigraphy, requires that the primary tectonic event of the Himalayan-Tibetan orogenic system – collision between India and Eurasia – must have occurred by late Ypresian (late Early Eocene, *ca.* 52-48 Ma) time at this longitude. Thermochronology of some of the youngest (Early Oligocene) continental clastics in the succession confirms that their source, the Indian passive margin south of the suture, was emergent and eroding by Eocene time.

On a scale significant to Himalayan tectonics, my results indicate a previously unappreciated complexity in the post-collisional deformation of the Transhimalayan region in India and southern Tibet. One of the principal deformational styles in this region is north-vergent backfolding and backthrusting that has been assumed to be of exclusively Early-Middle Miocene age (19-11 Ma) based on work done several hundred kilometers to the east of Ladakh. However, my estimates for the age of backthrusting and backfolding in Ladakh, obtained through thermal modeling of partially reset zircon (U-Th)/He systematics, are younger: 11 to 7 Ma. This result suggests diachroneity in backthrusting and backfolding along the length of the orogen.

Two final contributions are in the application of satellite remote sensing data to geologic mapping, and the application of both conventional and laser microprobe technology to detrital mineral (U-Th)/He thermochronology. I demonstrated the integrative use of visible to thermal infrared wavelengths of multispectral data to map stratigraphy and complex structure in poorly accessible and complexy deformed sedimentary basins. I contributed to an ongoing debate regarding the number of grains in a sediment sample that must be dated to fully characterize detrital age distributions in the sample (fewer than previously assumed). I showed for the first time how laser-microprobe techniques (pioneered by *Boyce et al.* [2006, 2009] for monazite dating) can be used to date the important accessory phase zircon and, especially, to characterize detrital zircon (U-Th)/He age distributions in sedimentary samples.

## 2. Opportunities for future work in the Himalaya

### 2.1. Along-strike variation of the timing of Indian-Eurasian collision

Other intermontane basins in Tibet record the first appearance of mixed Indian-Asian detritus at varying times in their depositional histories. For example, in easternmost Tibet, the minimum age of collision is between Oligocene and Miocene time for the Luobusa Formation [*Badengzhu,* 1981], whereas sediments from the next basin to the west for which data exist, the Liuqu conglomerates, provide a minimum age estimate of Middle Eocene collision [*Wang et al.,* 2010]. The oldest record of collision comes from the Qianbulin Formation, which contains mixed Indian-Eurasian detritus in Late Cretaceous time [*Wang et al.,* 2010]. This contrasts with the Kailas Formation, which does not record mixed provenance until Miocene time according to researchers who have studied those rocks [*Aitchison et al.*, 2002]. It is difficult to envisage a paleotectonic scenario consistent with such variable and not spatially progressive variations in the age of collision. I think it is more probable that the collision occurred in the Eocene (or possibly earlier) and that the studies necessary to establish evidence for earlier mixed detritus in depocenters simply have not yet been done.

Even the Indus Basin merits further study. The Tar Group, representing mostly marine strata at the bottom of the Indus Basin, becomes increasingly sand-rich upsection because of the gradual elimination of marine conditions and a transition into a deltaic setting [*Garzanti and Van Haver*, 1988]. Although we have demonstrated that the uppermost part of this sequence provides a minimum age of collision of late Ypresian, the majority of the Tar Group sandstones have

not been studied in detail, and could contain evidence for an even older signal of mixed detritus.

### 2.2. The Timing of Initial Uplift of the Indian Passive Margin

My data record evidence of uplift and erosional unroofing of the Indian passive margin by Eocene time, but that conclusion is based on a small detrital dataset (n = 20). More dates should be obtained from this sequence for the purpose of determining not only the range of cooling dates recorded by these grains, but also to explore whether or not the data are uni- or multi-modal. If India slowed relative to Eurasia after collision and maintained a relatively constant northward velocity, new data would likely be unimodal with an age distribution skewed toward younger dates. However, if, subsequent to collision, the Indian plate velocity (relative to stable Eurasia) varied episodically, as suggested by *White and Lister* [2011], then the cooling age distribution should show distinct peaks, reflecting distinct episodes uplift and erosion.

### 2.3. Exhumation Kinematics of the Ladakh batholith

*Kirstein* [2011] hypothesized that the Ladakh batholith experienced multiple episodes of northward and southward tilting of the range during its Cretaceous-Cenozoic exhumation. Based on a small number of bedrock samples, she concluded that (U-Th)/He dates on bedrock samples from the southern flank of the Ladakh Range showed an unusual pattern: youngest dates at the highest elevations, with dates aging progressively toward lower elevations. The (U-Th)/He detrital zircon age distribution in the Basgo catchment sediment sample is generally consistent with such a pattern, but the hypothesis (and my detrital

thermochronologic results) could be tested in more detail through a systematic bedrock thermochronologic study of the Ladakh batholith. The resulting dataset would also have regional significance because the possible affects on Ladakh Range uplift of oblique slip on the Karakoram fault zone is not well understood.

### 2.4. Mapping Himalayan-Tibetan Geology with ASTER Image Analysis

The mapping challenges encountered by workers in the Indus Basin are common throughout much of the Himalaya, suggesting that the techniques used in Chapter 2 might be valuable for a range of Himalayan studies. This approach is likely to be most valuable in high elevation regions with little vegetation and snowpack such as the Tibetan Plateau, although a recent ASU study of a moderately forested region of western Bhutan yielded valuable insights regarding geologic relationships there [*Cooper et al.,* in prep]. Of particular interest are regions near international borders where access for fieldwork is restricted. Cursory analysis of ASTER imagery of one such region near the Indus Basin– the incompletely mapped Tso Morari ultra-high pressure metamorphic complex – reveals a rich variation of mappable lithologies and should be a target for study.

## 3. Laser Microprobe (U-Th)/He Thermochronology

### 3.1. Improving Laser Microprobe (U-Th)/He Thermochronology

When using the Helix SFT in the NG$^3$L facility for laser microprobe dating, we do not measure $^4$He abundances by isotope dilution. Instead, we convert $^4$He signals to abundances using an abundance sensitivity monitored by replicate analysis of the Durango fluorapatite standard. This results in a 4-7% error ($2\sigma$) for the measurement of $^4$He used in the age determination, partly

because the standard itself is not of completely uniform composition [*Boyce et al*., 2005]. In the future, we intend to abandon this approach and instead use a gas volume with known $^4$He abundance for sensitivity determination, a practice that should reduce the sensitivity error by 50% or more.

The major error associated with the measurement of U and Th concentrations stems from uncertainty in standard concentrations, which we know to 7% ($2\sigma$), a level comparable to the error associated with the $^4$He measurement. This error can be improved with further refinement of standard concentrations, which is in progress with development of synthetic materials of varying chemistry.

Finally, because we use SIMS for U and Th concentration measurement, which is a surficial analytical technique, we do not fully average the U and Th concentration that contributed $^4$He to the laser ablation pit volume. However, with the adaptation of LA-ICPMS for U and Th concentration measurements in the future, it should be possible to volumetrically integrate all U and Th that contributed $^4$He to the ablation pit volume.

Although the laser microprobe method has many steps, we have found that the time for laser microprobe analyses is significantly less than that required for conventional analyses in NG$^3$L. For example, dating 100 zircon grains by the laser microprobe method requires approximately three weeks of analytical time, whereas the conventional method requires approximately 6 weeks. Although procedures vary among conventional laboratories, it's probably a general rule that

the laser microprobe zircon thermochronology is twice as efficient as conventional work.

If it is possible to eliminate our reliance on the SIMS method for U and Th analyses by switching to the much faster LA-ICPMS approach, we would be able to greatly improve our current overall throughput. This would increase the viability of detrital zircon (U-Th)/He as a tool to study provenance thermal and erosional histories. Because laser microprobe thermochronology consumes only a small volume of material within a grain, the potential exists to simultaneously determine the U-Pb age of each zircon grain during the LA-ICPMS procedure. Additionally, if the grain is large enough, "triple dating" – supplementing the U-Pb and (U-Th)/He dates with zircon fission track dates – is also possible.

**3.2. Future Applications of Laser Microprobe (U-Th)/He Thermochronology**

This laser microprobe method opens the door to a variety of research projects in addition to detrital studies, particularly if double- or triple-dating becomes viable. An interesting application would be to address the formation of tectonic mélange in order to understand the interesting juxtaposition of blueschists and eclogites with essentially unmetamorphosed rocks in a block-in-matrix pattern, as is found in the Franciscan of California [*Ernst,* 1970].

Another important aspect of this method is that it is less destructive in comparison to the conventional (U-Th)/He method. *Min et al*. [2004] have examined U- and Th- bearing minerals in Martian meteorites using conventional methods in hopes of understanding their low-temperature history, including the time of shock metamorphism, interpreted as the age of ejection from Mars. Laser

microprobe (U-Th)/He thermochronology has multiple advantages relative to the conventional method for such precious samples. For example, the laser microprobe method does not require extraction of individual whole grains, but rather, can be done using a thick section containing the mineral in question. Additionally, as the precision of the method increases, it will likely surpass that of conventional methods, which will only allow for better constraints on the thermal history of any given meteorite.

**4. References**


Aitchison, J. C, A. M. Davis, Badengzhu, and H. Luo, (2002), New constraints on the Indian-Asia collision: The lower Miocene Gangrinboche conglomerates, Yarlung Tsangpo suture zone, SE Tibet, *J. Asian Earth Sci., 21,* 253-265.

Badengzhu (1981), (Compiler) Xizang Autonomous Region Sangri–Jiacha Regional Geology Reconnaissance Map 1:50,000, *Xizang Geol. Survey Geol. Team #2, Lhasa.*

Boyce, J. W., and K. V. Hodges (2005), U and Th zoning in Cerro de Mercado (Durango, Mexico) fluorapatite: Insights regarding the impact of recoil redistribution of radiogenic $^{4}$He on (U–Th)/He thermochronology, *Chem. Geol., 219*, 261-274

Boyce J. W., K. V. Hodges, W. J. Olszewski, M. J. Jercinovic, and P. W. Reiners (2006), Laser microprobe (U-Th)/He thermochronology, *Geochim. Cosmochim. Acta, 70,* 3031-3039.

Boyce, J. W., K. V. Hodges, D. King, J. L. Crowley, M. Jercinovic, N. Chatterjee, S. A. Bowring, and M. Searle (2009), Improved confidence in (U-Th)/He thermochronology using the laser microprobe: An example from a Pleistocene leucogranite, Nanga Parbat, Pakistan, *Geochem. Geophys. Geosyst., 10*, QAA01, doi.10.1029/2009GC002497.

Cooper, F. J., B. A. Adams, C. S. Edwards, and K. V. Hodges (2011), Large-scale displacement on the South Tibetan fault system in the eastern Himalaya, *in preparation.*

Ernst, W. G. (1970), Tectonic contact between the Franciscan mélange and the Great Valley sequence – crustal expression of a Late Mesozoic Benioff zone, *J. Geophys. Res., 75,* 886-901.

Garzanti, E., and T. Van Haver (1988), The Indus clastics: forearc basin sedimentation in the Ladakh Himalaya (India), *Sediment. Geol., 59*, 237-249.

Henderson, A. L., Y. Najman, R. Parrish, M. BouDagher-Fadel, D. Barford, E. Garzanti, and S. Ando (2010), Geology of the Cenozoic Indus Basin sedimentary rocks: paleoenvironmental interpretation of sedimentation from the western Himalaya during the early phases of India-Eurasia collision, *Tectonics, 29,* TC6015, doi:10.1029/2009TC002651.

Henderson, A. L., Y. Najman, R. Parrish, D. F. Mark, and G. L. Foster (2011), Constraints to the timing of India-Eurasia collision; a re-evaluation of evidence from the Indus Basin sedimentary rocks of the Indus-Tsangpo Suture Zone, Ladakh, India, *Earth-Sci. Rev., 106*, 265-292.

Kirstein, L. A. (2011), Thermal evolution and exhumation of the Ladakh Batholith, northwest Himalaya, India, *Tectonophysics, 503*, 222-233.

Min, K., P. W. Reiners, S. Nicolescu, and J. P. Greenwood (2004), Age and temperature of shock metamorphism of Marian meteorite Los Angeles from (U-Th)/He thermochronology, *Geology, 32*, 677-680.

Wang, J.-G., X.-M. Hu, F.-Y. Wu, and L. Jansa (2010), Provenance of the Liuqu Conglomerate in southern Tibet: A Paleogene erosional record of the Himalayan-Tibetan orogen, *Sediment. Geol., 231*, 74-84.

White, L. T. and G. S. Lister (2011), The collision of India with Asia, *J. Geodyn.*, in press.

REFERENCES

Acton, G. D., 1999, Apparent polar wander of India since the Cretaceous with implications for regional tectonics and true polar wander, in *The Indian subcontinent and Gondwana: A paleomagnetic and rock magnetic perspective,* edited by T. Radhakrishna et al., *geol. Soc. India Mem., 44,* 129-175.

Ahmad, T., T. Tanaka, H. K. Sachan, Y. Asahara, R. Islam, and P. P. Khanna (2008), Geochemical and isotopic constraints on the age and origin of the Nidar Ophiolitic Complex, Ladakh, India: Implications for the Neo-Tethyan subduction along the Indus suture zone, *Tectonophysics, 451*, 206-224.

Aitchison, J. C, A. M. Davis, Badengzhu, and H. Luo (2002), New constraints on the Indian-Asia collision: The lower Miocene Gangrinboche conglomerates, Yarlung Tsangpo suture zone, SE Tibet, *J. Asian Earth Sci., 21*, 253-265.

Aitchison, J. C., J. R. Ali, and A. M. Davis (2007), When and where did India and Asia collide?, *J. Geophys. Res.*, *112*, B05423, doi: 10.1029/2006JB004706.

Aubry, M.-P., K. Ouda, C. Dupuis, W. A. Berggren, J. A. Van Couvering, and Members of the Working Group on the Paleocene/Eocene Boundary (2007), The Global Standard Stratotype-section and Point (GSSP) for the base of the Eocene Series in The Dababiya section (Egypt), *Episodes, 30,* 271-286.

Avdeev, B., N. A. Niemi, and M. K. Clark (2011), Doing more with less: Bayesian estimation of erosion models with detrital thermochronometric data, *Earth Planet. Sci. Lett., 305,* 385-395.

Badengzhu (1981), (Compiler) Xizang Autonomous Region Sangri–Jiacha Regional Geology Reconnaissance Map 1:50,000, *Xizang Geol. Survey Geol. Team #2, Lhasa.*

Bajpai, S., R. C. Whatley, G. V. R. Prasad, and J. E. Whittaker (2004), An Oligocene non-marine ostracod fauna from the Basgo Formation (Ladakh Molasse), NW Himalaya, India, *J. Micropalaeontol., 23*, 3-9.

Bandfield, J. L., D. Rogers, M. D. Smith, and P. R. Christensen (2004), Atmospheric correction and surface spectral unit mapping using Thermal Emission Imaging System data, *J. Geophys. Res., 109*, 10.1029/2004JE002289.

Bertoldi, L., M. Massironi, Visona, R. Carosi, C. Montomoli, F. Gubert, G. Naletto, and M. G. Pelizzo (2011), Mapping the Buraburi granite in the Himalaya of Western Nepal: Remote sensing analysis in a collisional belt with vegetation cover and extreme variation of topography, *Remote Sens. Environ., 115*, 1129-1144.

Bohon, W., K. Hodges, and J. R. Arrowsmith (2011), Refining estimates of Quaternary slip on the Karakoram fault system, Ladakh, northwest India, *submitted to Geology*.

Bouilhol, P., O. Jagoutz, F. O. Dudas, and J. M. Hanchar (2011), Dating the India-Eurasia collision through arc magmatic records, *Geophys. Res. Abstr., 13*, Abstract 1662.

Boyce, J. W., and K. V. Hodges (2005), U and Th zoning in Cerro de Mercado (Durango, Mexico) fluorapatite: Insights regarding the impact of recoil redistribution of radiogenic $^{4}$He on (U–Th)/He thermochronology, *Chem. Geol., 219*, 261-274

Boyce J. W., K. V. Hodges, W. J. Olszewski, M. J. Jercinovic, and P. W. Reiners (2006), Laser microprobe (U-Th)/He thermochronology, *Geochim. Cosmochim. Acta, 70,* 3031-3039.

Boyce, J. W., K. V. Hodges, D. King, J. L. Crowley, M. Jercinovic, N. Chatterjee, S. A. Bowring, and M. Searle (2009), Improved confidence in (U-Th)/He thermochronology using the laser microprobe: An example from a Pleistocene leucogranite, Nanga Parbat, Pakistan. *Geochem. Geophys. Geosyst., 10*, QAA01, doi.10.1029/2009GC002497.

Brewer, I. D., D. W. Burbank, and K. V. Hodges (2003), Modeling detrital cooling-age populations: insights from two Himalayan catchments, *Basin Res., 15*, 305-320.

Brocklehurst, S. H. and K. X. Whipple (2004), Hypsometry of glaciated landscapes, *Earth Surf. Processes Landforms, 29*, 907-926.

Brookfield, M. E., and C. P. Andrews-Speed (1984), Sedimentology, petrography and tectonic significant of the shelf, flysch and molasse clastic deposits across the Indus suture zone, Ladakh NW India, *Sediment. Geol., 40*, 249-286.

Burchfiel, B. C., Z. Chen, K. V. Hodges, Y. Liu, L. H. Royden, C. Deng, and J. Xu (1992), The South Tibetan detachment system, Himalayan orogen:

Extension contemporaneous with and parallel to shortening in a collisional mountain belt, *Spec. Pap. Geol. Soc. Am., 269,* 41 pp.

Burbank, D. W., J. Leland, E. Fielding, R. S. Anderson, N. Brozovic, M. R. Reid, and C. Duncan (1996), Bedrock incision, rock uplift and threshold hillslopes in the northwestern Himalayas, *Nature, 379*, 505-510.

Cai, F., L. Ding, and Y. Yue (2011), Provenance analysis of upper Cretaceous strata in the Tethys Himalaya, southern Tibet: Implications for timing of India-Asia collision, *Earth Planet. Sci. Lett., 305,* 195-206.

Campbell, I. H., P. W. Reiners, C. M. Allen, S. Nicolescu, and R. Upadhyay (2005), He-Pb double dating of detrital zircons from the Ganges and Indus Rivers: Implications for quantifying sediment recycling and provenance studies, *Earth Planet. Sci. Lett., 237*, 402-432.

Chavez, P. S., and A. Y. Kwarteng (1989), Extractive spectral contrast in Landsat Thematic Mapper Image data using selective principal component analysis, *Photogramm. Eng. Remote Sens, 55,* 339-348.

Chen, J., B. Huang, and L. Sun (2010), New constraints to the onset of the India-Asia collision: paleomagnetic reconnaissance on the Linzizong Group in the Lhasa Block, China, *Tectonophysics, 489*, 189-209.

Clift, P. D., N. Shimizu, G. Layne, and J. Blusztain (2001), Tracing patterns of unroofing in the Early Himalaya through microprobe Pb isotope analysis of detrital K-feldspars in the Indus Molasse, India, *Earth Planet. Sci. Lett., 188*, 475-491.

Clift, P. D., A. Carter, M. Krol, and E. Kirby (2002), Constraints on India-Eurasia collision in the Arabian Sea region taken from the Indus Group, Ladakh Himalaya, India, in *The Tectonic and Climatic Evolution of the Arabian Sea Region,* edited by P. D. Clift et al., *Geol. Soc. Spec. Publ., 195,* 97-116.

Clift, P. D., K. Hodges, D. Heslop, R. Hannigan, L. V. Hoang, and G. Calves (2008), Correlation of Himalayan exhumation rates and Asian monsoon intensity, *Nat. Geosci., 1*, doi:10.1038/ngeo1351.

Cooper, F. J., B. A. Adams, C. S. Edwards, and K. V. Hodges, Large-scale displacement on the South Tibetan fault system in the eastern Himalaya, *in preparation.*

Corrie, R. K., Y. Ninomiya, and J. C. Aitchison (2010), Applying Advanced Spaceborne Thermal Emission and Reflection Radiometer (ASTER)

spectra indices for geological mapping and mineral identification on the Tibetan plateau, *Int. Arch. Photogramm., Remote Sens. Spat. Information Sci., XXXVIII*, 464-469.

DeCelles, P. G., D. M. Robinson, J. Quade, T. P. Ojha, C. N. Garzione, P. Copeland, and B. N. Upreti (2001), Stratigraphy, structure, and tectonic evolution of the Himalayan fold-thrust belt in western Nepal, *Tectonics, 20*, 487-509.

DeCelles, P. G., P. Kapp, J. Quade, and G. E. Gehrels (2011), Oligocene-Miocene Kailas basin, southwestern Tibet: Record of postcollisional upper-plate extension in the Indus-Yarlung suture zone, *Geol. Soc. Am. Bull., 123*, 1337-1362.

Dewey, J. F. (1988), Extensional collapse of orogens, *Tectonics, 7,* 1123-1139.

Dèzes, P. J., J.-C Vannay, A. Steck, F. Bussy, and M. Cosca (1999), Synorogenic extension: Quantitative constraints on the age and displacement of the Zanskar shear zone (northwest Himalaya), *Geol. Soc. Am. Bull., 111,* 364-374.

Dickinson, W. R., and C. A. Suczek (1979), Plate tectonics and sandstone compositions*, AAPG Bull., 63*, 2164-2182.

Dickinson, W. R. and G. E. Gehrels (2003), U-Pb ages of detrital zircons from Permian and Jurassic eolianite sandstones of the Colorado Plateau, USA: Paleogeographic implications, *Sediment. Geol., 163*, 29-66.

Dobson, K. J., F. M. Stuart, T. J. Dempster, and EIMF (2008), U and Th zonation in Fish Canyon Tuff zircons: Implications for a zircon (U-Th)/He standard, *Geochim. Cosmochim. Acta, 72*, 4745-4755.

Dodson, M. H., W. Compston, I. S. Williams, and J. F. Wilson (1988), A search for ancient detrital zircons in Zimbabwean sediments, *J. Geol. Soc., 145*, 977-983.

Dortch, J. M., L. A. Owen, L. M. Schoenbohm, and M. W. Caffee (2011), Asymmetrical erosion and morphological development of the central Ladakh Range, northern India, *Geomorphology*, doi:10.1016/j.geomorph.2011.08.014.

Dunlap, W. J. and R. Wysoczanski (2002), Thermal evidence for early Cretaceous metamorphism in the Shyok suture zone and age of the Khardung volcanic rocks, Ladakh, India, *J. Asian Earth Sci., 20,* 481-490.

Ernst, W. G. (1970), Tectonic contact between the Franciscan mélange and the Great Valley sequence – crustal expression of a Late Mesozoic Benioff zone, *J. Geophys. Res., 75,* 886-901.

Farley, K. A. (2000), Helium diffusion from apatite: General behavior as illustrated by Durango fluroapatite, *J.Geophys. Res., 105*, 2903-2914.

Farley, K. A., R. A. Wolf, and L. T. Silver (1996), The effects of long alpha-stopping distances on (U-Th)/He ages, *Geochim. Cosmochim. Acta, 60,* 4223-4229.

Farley, K. A., D. L. Shuster, and R. A. Ketcham (2011), U and Th zonation in apatite observed by laser ablation ICPMS, and implications for the (U-Th)/He system, *Geochim. Cosmochim. Acta, 75*, 16, 4515-4530.

Flowers, R. M., R. A. Ketcham, D. L. Shuster and K. A. Farley (2009), Apatite (U-Th)/He thermochronometry using a radiation damage accumulation and annealing model, *Geochim. Cosmochim. Acta*, *73*, 2347-2365.

Fuchs, G. (1984), Note on the geology of the Markha-Nimaling Area in Ladakh (India), *Jahrb. Geol. Bundesanst., 127*, 5-12.

Gansser, A. (1980), The significance of the Himalayan suture zone, *Tectonophysics, 62*, 37-52.

Gardés, E., and J.-M. Montel (2009), Opening and resetting temperatures in heating and geochronologic systems, *Contrib. Mineral. Petrol., 158*, 185-195.

Garzanti, E., and T. Van Haver (1988), The Indus clastics: forearc basin sedimentation in the Ladakh Himalaya (India), *Sediment. Geol., 59*, 237-249.

Gehrels, G. E., V. Valencia, and A. Pullen (2006), Detrital zircon geochronology by Laser-Ablation Multicolector ICPMS at the Arizona LaserChron Center, in *Geochronology: Emerging Opportunities, Paleontological Society Short Course, October 21, 2006, Philadelphia, PA,* edited by T. Olszewski et al., *Paleontol. Soc. Pap., I2,* 1-10.

Gehrels, G. E., V. Valencia, and J. Ruiz (2008), Enhanced precision, accuracy, efficiency and spatial resolution of U-Pb ages by laser ablation-multicollector-inductively coupled plasma-mass spectrometry*, Geochem., Geophys., Geosyst., 9*, Q03017, doi:10.1029/2007GC001805.

Gehrels, G. E., P. Kapp, P. DeCelles, A. Pullen, R. Blakely, A. Weislgel, L. Ding, J. Guynn, A. Marin, N. McQuarrie, and A. Yin (2011), Detrital zircon geochronology of pre-Tertiary strata in the Tibetan-Himalayan orogen, *Tectonic, 30*, TC5016, doi:10.1029/2011TC002868.

Gillespie, A. R., A. B. Kahle, and R. E. Walker (1986), Color enhancement of highly correlated images. I. Decorrelation and HSI contrast stretches, *Remote Sens. the Environ., 20*, 209-235.

Gillespie, A., S. Rokugawa, T. Matsunaga, J. S. Cothern, S. Hook, and A. B. Kahle (1998), A temperature and emissivity separation algorithm for Advanced Spaceborne Thermal Emission and Reflection Radiometer (ASTER) images, *IEEE Trans. Geosci. Remote Sens., 36*, 1113-1126.

Gradstein, F. M., J. G. Ogg, and A. G. Smith (2004), *A Geologic Time Scale,* 588 pp., Cambridge Univ. Press, Cambridge, U. K.

Green, O. R., M. P. Searle, R. I. Corfield, and R. M. Corfield (2008), Cretaceous-Tertiary carbonate platform evolution an the age of the India-Asia collision along the Ladakh Himalaya (Northwest India), *J. Geol., 116*, 331-353.

Harrison, T. M., P. Copeland, S. Hall, J. Quade, S. Burner, T.P. Ojha, and W. S. F. Kid (1993), Isotopic preservation of Himalayan/Tibetan uplift, denudation and climatic histories in two molasse deposits, *J. Geol., 101*, 159-173.

Heim, A., and A. Gansser (1939), Central Himalaya – Geological observations of Swiss expedition, 1936, *Mem. Soc. Helv. Sci. Nat., 73*, 1-245.

Henderson, A. L., Y. Najman, R. Parrish, M. BouDagher-Fadel, D. Barford, E. Garzanti, and S. Ando (2010), Geology of the Cenozoic Indus Basin sedimentary rocks: paleoenvironmental interpretation of sedimentation from the western Himalaya during the early phases of India-Eurasia collision, *Tectonics, 29,* TC6015, doi:10.1029/2009TC002651.

Henderson, A. L., Y. Najman, R. Parrish, D. F. Mark, and G. L. Foster (2011), Constraints to the timing of India-Eurasia collision; a re-evaluation of evidence from the Indus Basin sedimentary rocks of the Indus-Tsangpo Suture Zone, Ladakh, India, *Earth-Sci. Rev., 106*, 265-292.

Hodges K. V. (2000), Tectonics of the Himalaya and southern Tibet from two perspectives, *Geol. Soc. Am. Bull., 112*, 324-350.

Hodges, K. V. (2006), A synthesis of the Channel Flow–Extrusion hypothesis as developed for the Himalayan-Tibetan orogenic system, in *Chanel Flow, Ductile Extrusion and Exhumation in Continental Collision Zones,* edited by R. D. Law et al., *Geol. Soc Spec. Publ., 268*, 71-90.

Hodges, K. V., K. W. Ruhl, C. W. Wobus, and M. S. Pringle (2005), $^{40}Ar/^{39}Ar$ thermochronology of detrital minerals, in *Low-Temperature Thermochronology: Techniques, Interpretations, and Applications*, edited by P. W. Reiners et al., *Rev. Mineral. Geochem., 58*, 239-257.

Honegger, K., V. Dietrich, W. Frank, A. Gansser, M. Thöni, and V. Trommsdorf (1982), Magmatism and metamorphism in the Ladakh Himalayas (the Indus-Tsangpo suture zone), *Earth Planet. Sci. Lett., 60*, 253-292.

Hourigan, J. K., P. W. Reiners, and M. T. Brandon (2005), U-Th zonation-dependent alpha-ejection in (U-Th)/He chronometry, *Geochim. Cosmochim Acta, 69*, 3349-3365.

Jaeger J.-J., V. Courtillot, and P. Tapponnier (1989), Paleontological view of the ages of the Deccan Traps, the Cretaceous/Tertiary boundary and the India-Asia collision, *Geology, 17*, 316-319.

Ji, W. H., S. J. Chen, Z. M. Zhao, R. S. Li, S. P. He, and C. Wang (2009) Discovery of the Cambrian volcanic rocks in the Xainza area, Gangdese orogenic belt, Tibet, China, and its significance, *Geol. Bull. China, 28,* 1350-1354.

Kirstein, L. A. (2011), Thermal evolution and exhumation of the Ladakh Batholith, northwest Himalaya, India, *Tectonophysics, 503*, 222-233.

Kirstein, L. A., H. Sinclair, F. M. Stuart, and K. Dobson (2006), Rapid early Miocene exhumation of the Ladakh batholith, western Himalaya, *Geology, 34*, 1049-1052.

Kirstein, L. A., J. P. T. Foeken, P. Van der Beek, F. M. Stuart, and R. J. Phillips (2009), Cenozoic unroofing history of the Ladakh Batholith, western Himalaya, constrained by thermochronology and numerical modeling, *J. Geol. Soc., 166*, 667-678.

Klootwijk, C. T., J. S. Gee, J. W. Pierce, G. M. Smith, and P. L. McFadden (1992), An early India-Asia contact; paleomagnetic constraints from Ninetyeast Ridge, ODP Leg 121, *Geology, 20*, 395-398.

Kosler, J., H. Fonneland, P. Sylvester, M. Tubrett, and R.-B. Pedersen (2002), U-Pb dating of detrital zircons for sediment provenance studies – comparison

of laser ablation ICPMS and SIMS techniques, *Chem. Geol., 182,* 605-618.

Leech, M. L., S. Singh, A. K. Jain, S. L. Klemperer, and R. M. Manickavasagam (2005), The onset of India-Asia continental collision: Early, steep subduction required by the timing of UHP metamorphism in the western Himalaya, *Earth Planet. Sci. Lett., 234*, 83-97.

Le Fort, P. (1975), Himalayas: The collided range. Present knowledge of the continental arc, *Am. J. Sci., 275-1*, 1-44.

Le Fort, P., M. Cuney, C. Ceniel, C. France-Lanord, S. M. F. Sheppard, B. N. Upreti, and P. Vidal (1987), Crustal generation of the Himalayan leucogranites, *Tectonophysics, 134*, 39-57.

Li, J.-G., Z.-Y. Guo, D. J. Batten, H.-W. Cai, and Y.-Y. Zhang (2010), Palynological stratigraphy of Late Cretaceous and Cenozoic collision related conglomerates at Qiabulin, Xigaze, Xizang (Tibet) and its bearing on palaeoenvironmenta development, *J. Asian Earth Sci., 28*, 86-95.

Liu, T.-K., Y.-G. Chen, W.-S. Chen and S.-H. Jiang (2000), Rates of cooling and denudation of the Early Penglai Orogeny, Taiwan, as assessed by fission-track constraints, *Tectonophysics, 30*, 69-82.

Ludwig, K. R. and D. M. Titterington (1994), Calculation of 230Th/U Isochrons, ages and errors, *Geochim. Cosmochim. Acta, 58*, 5031-5042.

Mancktelow, N. S. and B. Grasemann (1997), Time dependent effects of heat advection and topography on cooling histories during erosion, *Tectonophysics, 270*, 167-195.

McInnes, B. I. A., N. J Evans, B. J. McDonald, P. D. Kinny, and J. Jakimowicz (2009), Zircon U-Th-Pb-He double dating of the Merlin kimberlite field, Northern Territory, Australia, *Lithos, 1125,* 592-599.

McPhillips, D. and M. T. Brandon (2010), Using tracer thermochronology to measure modern relief chance in the Sierra Nevada, California, *Earth Planet. Sci. Lett.,, 296*, 373-383.

Miller, C., M. Thöni, W. Frank, B. Grasemann, U. Klötzli, P. Guntli, and E. Draganits (2001), The early Paleozoic magmatic event in the Northwest Himalaya, India: source, tectonic setting and age of emplacement, *Geol. Mag., 138*, 237-251.

Min, K., P. W. Reiners, S. Nicolescu, and J. P. Greenwood (2004), Age and temperature of shock metamorphism of Marian meteorite Los Angeles from (U-Th)/He thermochronology, *Geology, 32*, 677-680.

Monteleone, B. D., M. C. van Soest, K. Hodges, G. M. Moore, J. W. Boyce, and R. L. Hervig (2009), Assessment of alternative [U] and [Th] zircon standards for SIMS, *Eos Trans. AGU, 90(52),* Fall Meet. Suppl., V31E-2017.

Myrow, P. M., N. C. Hughes, J. W. Goodge, C. M. Fanning, I. S. Williams, S. Peng, O. N. Bhargava, S. K. Parcha, and K. R. Pogue (2010), Extraordinary transport and mixing of sediment across Himalayan central Gondwana during the Cambrian-Ordovician, *Geol. Soc. Am. Bull.*, 122, 1660-1670.

Najman, Y., M. Bickle, M. BouDagher-Fadel, A. Carter, E. Garzanti, M. Paul, J. Wijbrans, E. Willett, G. Oliver, R. Parrish, S. H. Akhter, R. Allen, S. Ando, E. Chisty, L. Reisberg, and G. Vezzoli (2008), The Paleogene record of Himalayan erosion: Bengal Basin, Bangladesh, *Earth Planet. Sci. Lett., 273*, 1-14.

Najman, Y., E. Appel, M. Boudagher-Fadel, P. Bown, A. Carter, E. Garzanti, L. Godin, J. Han, U. Liebke, G. Oliver, R. Parrish, and G. Vezzoli (2010), Timing of India-Asia collision: Geological, biostratigrphic and palaeomagnetic constraints, *J. Geophys. Res.*, *115*, B12416, doi:10.1029/2010JB007673.

NASA Earth Observatory site, accessed March 2011, Measuring Vegetation (NDVI & EVI), http://earthobservatory.nasa.gov/Features/MeasuringVegetation/measuringvegetation_2.php.

Nasdala, L., P. W. Reiners, J. I. Garver, A. K. Kennedy, R. A. Stern, E. Balan, and R. Wirth (2004), Incomplete retention of radiation damage in zircon from Sri Lanka, *Am. Mineral., 89*, 219-231.

Ninomiya, Y., B. Fu, and T. J. Cudahy (2005), Detecting lithology with Advanced Spaceborne Thermal Emission and Reflection Radiometer (ASTER) multispectral thermal infrared "radiance-at-sensor" data, *Remote Sens. Environ., 99,* 127-139.

Nowicki, K. J., and P. R. Christensen (2011), Removal of Line- and Row-Correlated Noise in THEMIS Multi-Spectral Infrared Data, *submitted to Mars.*

Patriat, P., and J. Achache (1984), India-Eurasia collision chronology has implications for crustal shortening and driving mechanism of plates, *Nature, 311*, p. 615-621.

Quidelleur, X., M. Grove, O. M. Lovera, T. M. Harrison, A. Yin, and F.J. Ryerson (1997), Thermal evolution and slip history of the Renbu-Zedong thrust, southeastern Tibet*, J. Geophys. Res., 102*, 2659-2679.

Rahl, J. M., P. W. Reiners, I. H. Campbell, S. Nicolescu, and C. M. Allen (2003), Combined single-grain (U-Th)/He and U-Pb dating of detrital zircons from the Navajo Sandstone, Utah, *Geology, 31*, 761-764.

Raymo, M. E., and W. F. Ruddimann (1992), Tectonic forcing of late Cenozoic climate, *Nature, 359*, 117-122.

Reiners, P. W., T. L. Spell, S. Nicolescu, and K. A. Zanetti (2004), Zircon (U-Th)/He thermochronometry: He diffusion and comparisons with $^{40}Ar/^{39}Ar$ dating, *Geochim. Cosmochim. Acta, 68*, 1857-1887, doi: 10.1016/j.gca.2003.10.021.

Reiners, P. W., I. H. Campbell, S. Nicolescu, C. M. Allen, J. K. Hourigan, J. I. Garver, J. M. Mattinson, and D. S. Cowan (2005), (U-Th)/(He-Pb) double dating of detrital zircons, *Am. J. Sci., 305*, 259-311.

Robertson, A. and P. Degnan (1994), The Dras arc Complex: lithofacies and reconstruction of a Late Cretaceous oceanic volcanic arc in the Indus Suture Zone, Ladakh Himalaya, *Sediment. Geol., 92*, 117-145.

Robinson, D., L. N. Warr, and R. E. Bevins (1990), The illite 'crystallinity' technique: a critical appraisal of its precision, *J. Metamorph. Geol., 8*, 333-344.

Rolland, Y., A. Pecher, and C. Picard (2000), Middle Cretaceous back-arc formation and arc evolution along the Asian margin: the Shyok Suture Zone in northern Ladakh (NW Himalaya), *Tectonophysics, 325*, 145-173.

Rolland, Y., C. Picard, A. Pecher, H. Lapierre, D. Bosch, and F. Keller (2002), The Cretaceous Ladakh arc of NW Himalaya – slab melting and melt-mantle interaction during fast northward drift of Indian Plate, *Chem. Geol., 182*, 139-178.

Rowan, L. C., and J. C. Mars (2003), Lithological mapping in the Mountain Pass, California area using Advanced Spaceborne Thermal Emission and Reflection Radiometer (ASTER) data, *Remote Sens. Environ., 84*, 350-366.

Rowley, D. B. (1996), Age of initiation of collision between India and Asia: A review of stratigraphic data, *Earth Planet. Sci. Lett., 145*, 1-13.

Ruhl, K. W., and K. V. Hodges (2005), The use of detrital mineral cooling ages to evaluate steady-state assumptions in active orogens: An example from the central Nepalese Himalaya, *Tectonics, 24,* TC4015.

Sabins, F. F. (1997), *Remote Sensing, Principles and Interpretation*, 512 pp., Waveland Press, Inc.

Schlup, M., A. Carter, M. Cosco, and A. Steck (2003), Exhumation history of eastern Ladakh revealed by $^{40}Ar/^{39}Ar$ and fission-track ages: the Indus River – Tso Morari transect, NW Himalaya, *J. Geol. Soc.*, 160, 385-399.

Searle, M. (1986), Structural evolution and sequence of thrusting in the High Himalayan Tibetan-Tethys and Indus suture zones of Zanskar and Ladakh, Western Himalaya, *J. Struct. Geol., 8*, 923-936.

Searle, M. P. (1996), Geological evidence against large-scale pre-Holocene off-sets along the Karakoram fault: implications for the limited extrusion of the Tibetan Plateau, *Tectonics, 15*, doi:10.1029/95TC01693**.**

Searle, M. P., K. T. Pickering, and D. J. W. Cooper (1990), Restoration and evolution of the intermontane Indus molasse basin, Ladakh Himalaya, India, *Tectonophysics, 174*, 301-314.

Searle, M., R. I. Corfield, B. Stephenson, and K. McCarron (1997), Structures of the North Indian continental margin in the Ladakh Zanskar Himalayas: implications for the timing of the obduction of the Spontang ophiolite, India-Asia collision and deformational events in the Himalaya, *Geol. Mag., 134,* 297-316.

Serra-Kiel, J., L. Hottinger, E. Caus, K. Drobne, C. Ferrandez, A. K. Jauhri, G. Less, R. Pavlovec, J. Pignatti, J. N. Samso, H. Schaub, E. Sirel, A. Strougo, Y. Tambareau, J. Tosquella, and E. Zakrevskaya (1998), Larger foraminiferal biostratigraphy of the Tethyan Paleocene and Eocene, *Bull. Soc. Geol. Fr., 169*, 281-299.

Sinclair, H. D. and N. Jaffey (2001), Sedimentation of the Indus Group, Ladakh, northern India: implications for the timing of initiation of the palaeo-Indus River, *J. Geol. Soc., 158*, 151-162.

Singh, S., R. Kumar, M. E. Barley, and A. K. Jain (2007), SHRIMP U-Pb ages and depth of emplacement of Ladakh batholith, Eastern Ladakh, India, *J. Asian Earth Sci., 30,* 490-503.

Stacey, J. S., and J. D. Kramers (1975), Approximation of terrestrial lead isotope evolution by a two stage model, *Earth Planet. Sci. Lett., 26,* 207-221, doi:10.1016/002-821X(75)90088-6.

Steck, A. (2003), Geology of the NW Indian Himalaya, *Eclogae Geol. Helv.*, 96, 147-196.

Steiger, R. H. and E. Jäger (1977), Subcommission on geochronology: Convention on the use of decay constants in geo- and cosmochronology, *Earth Planet. Sci. Lett., 36*, 21-23.

Stephenson, B. J., M. P. Searle, D. J. Waters and D. C. Rex (2001), Structure of the Main Central thrust zone and extrusion of the High Himalayan deep crustal wedge, Kishtwar-Zanskar Himalaya*, J. Geol. Soc., 158*, 637-652.

Stock, G. M., T. A. Ehlers, and K. A. Farley (2006), Where does sediment come from? Quantifying catchment erosion with detrital apatite (U-Th)/He thermochronometry, *Geology, 34*, 725-728.

Stock, J. D. and D. R. Montgomery (1996), Estimating paleorelief from detrital mineral age ranges, *Basin Res.,* 8*,* 317-327.

St.-Onge, M. R., N. Rayner, and M. P. Searle (2010), Zircon age determinations of the Ladakh batholith at Chumathang (Northwest India): Implications for the age of the India-Asia collision in the Ladakh Himalaya, *Tectonophysics, 495*, 171-183.

Spiegel, C., B. Kohn, D. Belton, Z. Berner, and A. Gleadow (2009), Apatite (U-Th-Sm)/He thermochronology of rapidly cooled samples: The effect of He implantation, *Earth Planet. Sci. Lett.,, 285*, 105-114.

Sun, S.-S. and W. F. McDonough (1989), Chemical and Isotopic Systematics of oceanic basalts: implications for Mantle Composition and Processes, in *Magmatism in the Ocean Basings,* edited by A. D. Saunders et al., *Geol. Soc. Spec. Publ., 42,* 313-345.

Swartz, W. H. and M. Trieloff (2007), Intercalibration of $^{40}$Ar-$^{39}$Ar age standards NL-25, HB3gr hornblende, GA1550, SB-3, HD-B1 biotite and BMus/2 muscovite, *Chem. Geol. 242*, 218-231.

Treloar, P. J., D. C. Rex, P. G. Guise, M. P. Coward, M. P. Searle, B. F. Windley, M. G. Peterson, M. Q. Jan, and I. W. Luff (1989), K-Ar and Ar-Ar geochronology of the Himalayan collision in NW Pakistan: constraints on the timing of suturing, deformation, metamorphism and uplift, *Tectonics, 8*, 881-909.

Tripathy, A. K., K. V. Hodges, M. C van Soest, and T. Ahmad (2011), Pre-Oligocene emergence of the Indian passive margin and the timing of Indian-Eurasian collision, *submitted to Geology.*

Tripathy, A. K., C. S. Edwards, K. V. Hodges, J.-A. Wartho, and F. J. Cooper, Lithologic mapping of complexly deformed sedimentary strata using ASTER multispectral imagery: Implications for the evolution of Indus Basin depocenters, Ladakh, NW India, *in preparation.*

Van Soest, M. C., K. V Hodges, J.-A. Wartho, M. B Biren, B. D. Monteleone, J. Ramezani, J. G. Spray, and L. M. Thompson (2011), (U-Th)/He dating of terrestrial impact structures: the Manicouagan example, *Geochem., Geophys., Geosyst., 12*, Q0AA16, doi:10.29/2010GC003465.

Vaughan, R. G., S. J. Hook, W. M. Calvin and J. V. Taranik (2005), Surface mineral mapping at Steamboat Springs, Nevada with multi-watelength Thermal Infrared Images, *Remote Sens. Environ., 99.,* 140-158.

Vermeesch, P. (2004), How many grains are needed for a provenance study?, *Earth Planet. Sci. Lett., 224,* 441-451.

Wang, C. S., X. H. Li, X. M. Hu, and L. F. Jansa (2002), Latest marine horizon north of Qomolangma (Mt Everest): Implications for closure of Tethys seaway and collisional tectonic, *Terra Nova, 14*, 114-120.

Wang, J.-G., X.-M. Hu, F.-Y. Wu, and L. Jansa (2010), Provenance of the Liuqu Conglomerate in southern Tibet: A Paleogene erosional record of the Himalayan-Tibetan orogen, *Sediment. Geol., 231*, 74-84.

Watts, D. R., and N. B. Harris (2005), Mapping granite and gneiss in domes along the North Himalayan antiform with ASTER SWIR band ratios, *Geol. Soc. Am. Bull., 117*, 879-886.

White, L. T. and G. S. Lister (2011), The collision of India with Asia, *J. Geodyn.*, in press.

Wobus, C. W., K. V. Hodges, and K. X. Whipple (2003), Has focused denudation sustained active thrusting at the Himalayan topographic front?, *Geology, 31*, 861-864.

Wolf, R. A., K. A. Farley, and L. T. Silver (1996), Helium diffusion and low-temperature thermochronometry of apatite, *Geochim. Cosmochim. Acta, 60*, 4231-4240.

Wu, F.-Y., P. D. Clift, and J.-H. Yang (2007), Zircon Hf isotopic constraints on the sources of the Indus Molasse, Ladakh Himalaya, India, *Tectonics, 26*, TC2014, doi:10.1029/2006TC002051.

Xiao, X., Z. Shen, and X. Qin (2001), Assessing the potential of VEGETATION sensor data for mapping snow and ice cover: a Normalized Difference Snow and Ice Index, *Int. J. Remote Sens., 22*, 2479–2487.

Yeats, R. S., T. Nakata, A. Farah, M. Fort, M. A. Mirza, M. R. Pandey, and R. S. Stein (1992), The Himalayan frontal fault system, *Ann. Tectonicae, 6*, 85-98.

Yin, A. (2006), Cenozoic tectonic evolution of the Himalayan orogen as constrained by along-strike variation of structural geometry, exhumation history and foreland sedimentation, *Earth-Sci. Rev., 76*, 1-131.

Yin, A. and T. M. Harrison (2000), Geologic evolution of the Himalayan-Tibetan Orogen, *Ann. Rev. of Earth and Planet. Sci., 28,* 211-280.

Yin, A., T. M. Harrison, M. A. Murphy, M. Grove, S. Nie, F. J. Ryerson, X. F. Wang, and Z. L. Chen (1999), Tertiary deformational history of southeastern and southwestern Tibet during the Indo-Asian collision, *Geol. Soc. Am. Bull. 111*, 1644-1664.

Zhu, B., W. S. F. Kidd, D. B. Rowley, B. S. Currie, and N. Shafique (2005), Age of initiation of the India-Asia collision in the east-central Himalaya, *J. Geol., 113*, 265-285.

# APPENDIX A

# CHAPTER 2 SUPPLEMENT:

# UNINTERPRETED ASTER IMAGES

Figure A2.1. Uninterpreted ASTER images that correspond to Figure 2.5.

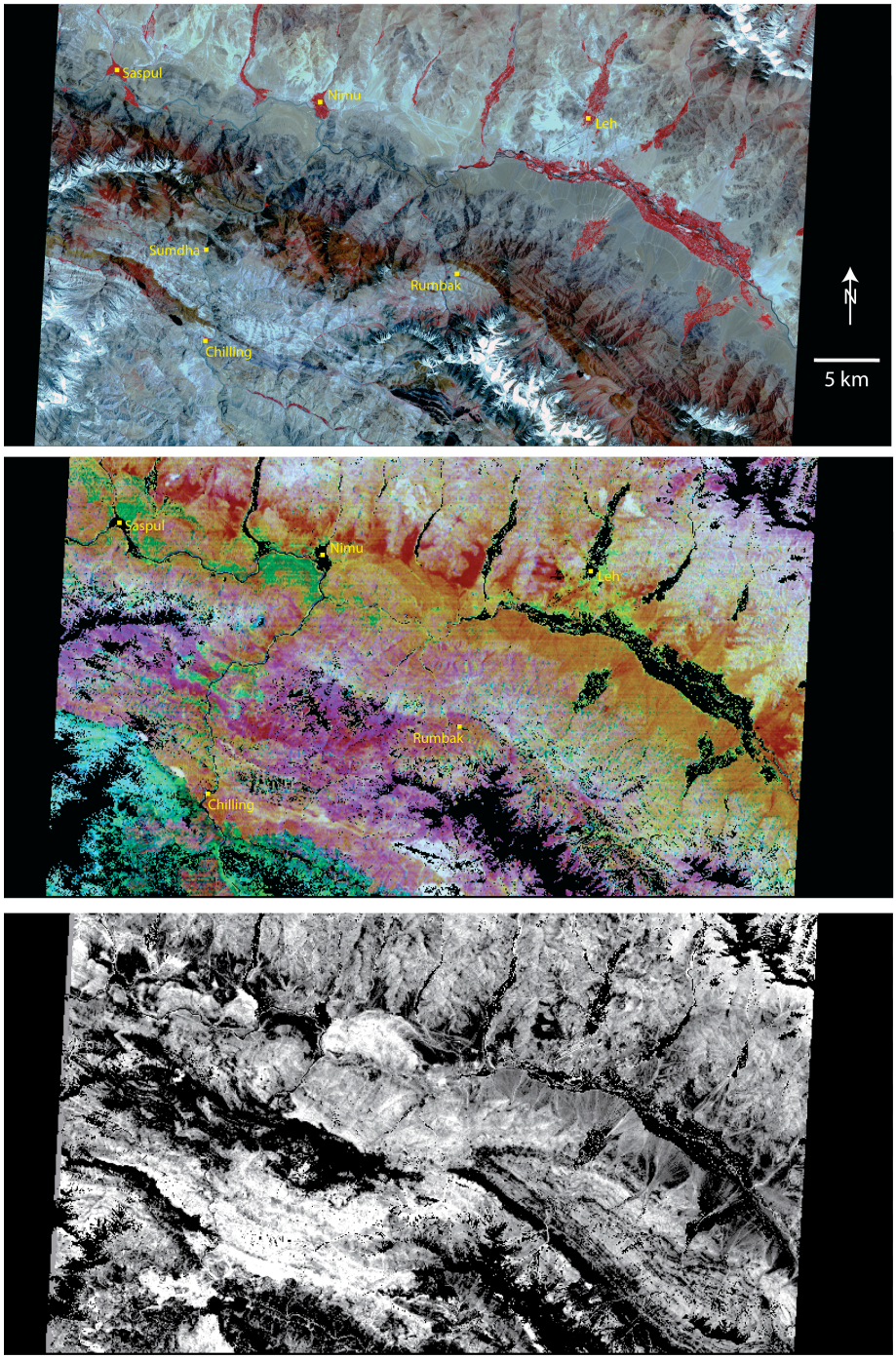

# APPENDIX B

# CHAPTER 2 SUPPLEMENT:

# $^{40}AR/^{39}AR$ METHODS

Muscovite grains from samples 07-AT-ZG-O, O7-AT-LM-K and 07-AT-LM-L were handpicked from the 250-100 μm aliquot, cleaned in acetone, methanol, and deionised water, and individually wrapped in aluminium foil packets. For the irradiation package, sample packets were regularly interspersed with packets of biotite age standard HD-B1 (24.18 ± 0.09 Ma, *Schwarz and Trieloff,* [2007]) to monitor the neutron flux gradient, along with natural and synthetic salts to determine interfering nuclear production ratios. The small aluminium disks into which the packets were loaded were then stacked and secured together to make up the irradiation package, which was then Cd shielded and irradiated for 1.2 hours at a near-core position (5C) within the McMaster University nuclear reactor, Hamilton, Ontario, Canada.

Upon return, individual age standard and unknown sample grains were loaded into a 61 mm diameter aluminium palette containing a series of 2 x 2 x 2 mm holes. The palette and a glass coverslip were loaded into an ultra-high vacuum 4.5" laser chamber with a Kovar glass viewport and baked at 120°C for one day and then pumped at ultrahigh vacuum for one day to remove adsorbed atmospheric argon from the samples and chamber walls.

To degas and melt each grain, a 60 W IPG Photonics infrared (970 nm) diode laser, with computer-controlled Photon Machines optics and X-Y-Z stages linked to a Newport controller, was fired such that two minutes of lasing with a 50 W, 0.6 mm diameter beam was sufficient to ensure total fusion of each grain. The gases released by laser heating were purified for an

additional two minutes using two SAES NP10 getter pumps (one at 400°C and one at room temperature) to remove all active gases. The remaining gases were equilibrated into a high sensitivity multi-collector mass spectrometer (Nu Instruments *Noblesse*), containing a Nier-type source operated at 400 mA. The Ar isotopes were measured using a 1 x $10^{11}$-Ohm Faraday detector or an ETP ion counting multiplier, depending upon the $^{40}$Ar signal size. Detector intercalibration for $^{40}$Ar was performed using multiple air shots. Laser heating, X-Y stage movement, automated valve operation, and data acquisition was automated and computer controlled using the *Mass Spec* software program. Errors throughout this paper are quoted at the 2σ confidence level. $^{40}$Ar/$^{39}$Ar ages were calculated using the decay constant, branching ratio, and atmospheric $^{40}$Ar/$^{36}$Ar ratio recommended by *Steiger and Jäger* [1977]. J-values and errors are noted in data tables in the supplementary materials.

The mean 4 minute extraction system blank Ar isotope measurements obtained during the experiments were 1.41 x $10^{-16}$, 1.70 x $10^{-18}$, 1.93 x $10^{-19}$, 1.14 x $10^{-18}$, and 7.95 x $10^{-19}$ moles STP (standard temperature and pressure) for sample 07-AT-LM-K, 1.66 x $10^{-16}$, 1.61 x $10^{-18}$, 2.07 x $10^{-19}$, 3.18 x $10^{-18}$, and 8.60 x $10^{-19}$ moles STP for sample 07-AT-LM-L, and 1.80 x $10^{-16}$, 1.69 x $10^{-18}$, 2.23 x $10^{-19}$, 1.08 x $10^{-18}$, and 9.14 x $10^{-19}$ moles STP for sample 07-AT-ZG-O, for $^{40}$Ar, $^{39}$Ar, $^{38}$Ar, $^{37}$Ar, and $^{36}$Ar, respectively. The sensitivities of the Faraday and ion counting detectors were 8.2729 x $10^{-13}$ moles/V and 1.4702 x $10^{-20}$ moles/cps for sample 07-AT-ZG-O, and 8.3019 x 10-13 moles/V and

1.4899 x 10-20 moles/cps for samples 07-AT-LM-L and 07-AT-LM-K, respectively. Unknown analyses were corrected for mass spectrometer discrimination using air shots. The measured $^{40}Ar/^{36}Ar$ air ratios varied from 295.17±1.97 to 306.80±1.87 (1σ errors) during the 8 days analyses of sample 07-AT-ZG-O, and 293.41±1.83 to 307.29± 2.21 for the 14 days of analyses of samples 07-AT-LM-L and 07-AT-LM-K. Nuclear interference correction factors were as follows: $^{40}Ar/^{39}Ar_K$ = 0.027945, $^{36}Ar/^{38}Ar_{Cl}$ = 316, Ca/K = 1.92234, and Cl/K = 0.16863. We interpreted no data for experiments yielding less than 90% $^{40}Ar^*$ or having $^{40}Ar^*$ signals less than ten times the level of the $^{40}Ar$ blank. Errors are quoted at 1σ, and the $^{40}Ar/^{39}Ar$ ages were calculated using the decay constant quoted by *Steiger and Jäger* [1977]. J values and errors are noted in the sample $^{40}Ar/^{39}Ar$ data tables in Appendix C.

**REFERENCES**

Steiger, R. H. and E. Jäger (1977), Subcommission on geochronology: Convention on the use of decay constants in geo- and cosmochronology, *Earth Planet. Sci. Lett., 36*, 21-23.

Swartz, W. H. and M. Trieloff (2007), Intercalibration of $^{40}Ar$-$^{39}Ar$ age standards NL-25, HB3gr hornblende, GA1550, SB-3, HD-B1 biotite and BMus/2 muscovite, *Chem. Geol.*, *242*, 218-231.

# APPENDIX C

# CHAPTER 2 SUPPLEMENT:

# $^{40}AR/^{39}AR$ DATA

Table A2.3. $^{40}Ar/^{39}Ar$ data tables

| Lab ID# | $^{40}Ar^*/^{39}Ar$ ± 2σ | | $^{40}Ar/^{39}Ar$ ± 2σ | | $^{36}Ar/^{39}Ar$ ± 2σ | | $^{39}Ar$ (moles) | $\%^{40}Ar^*$ | Age (Ma)[1] ± 2σ | |
|---|---|---|---|---|---|---|---|---|---|---|
| *07-AT-LM-K - 33°48'49.8"N, 77°48'35.9"E* | | | | | | | | | | |
| 406-63 | 63.525 | 0.569 | 64.139 | 0.533 | 0.0020 | 0.0007 | 1.16E-16 | 99.09 | 48.93 | 0.43 |
| 406-80 | 68.998 | 0.709 | 69.428 | 0.629 | 0.0014 | 0.0011 | 6.86E-17 | 99.42 | 53.08 | 0.54 |
| 406-37 | 69.439 | 0.532 | 70.549 | 0.503 | 0.0037 | 0.0006 | 1.18E-16 | 98.47 | 53.41 | 0.40 |
| 406-06 | 72.491 | 0.544 | 73.373 | 0.518 | 0.0029 | 0.0006 | 1.38E-16 | 98.84 | 55.73 | 0.41 |
| 406-11 | 73.654 | 0.621 | 74.485 | 0.571 | 0.0027 | 0.0009 | 8.66E-17 | 98.92 | 56.61 | 0.47 |
| 406-23 | 75.046 | 0.677 | 77.345 | 0.638 | 0.0077 | 0.0009 | 9.24E-17 | 97.06 | 57.66 | 0.51 |
| 406-13 | 76.774 | 0.633 | 77.604 | 0.585 | 0.0027 | 0.0009 | 9.07E-17 | 98.97 | 58.96 | 0.48 |
| 406-97 | 78.356 | 1.265 | 79.304 | 1.016 | 0.0031 | 0.0026 | 3.04E-17 | 98.84 | 60.16 | 0.96 |
| 406-54 | 78.692 | 0.668 | 79.653 | 0.635 | 0.0032 | 0.0008 | 1.07E-16 | 98.83 | 60.41 | 0.50 |
| 406-64 | 80.855 | 0.803 | 83.043 | 0.730 | 0.0073 | 0.0012 | 7.55E-17 | 97.40 | 62.05 | 0.61 |
| 406-83 | 81.938 | 0.689 | 83.261 | 0.630 | 0.0044 | 0.0010 | 7.77E-17 | 98.44 | 62.86 | 0.52 |
| 406-91 | 83.310 | 1.380 | 86.692 | 1.207 | 0.0114 | 0.0025 | 3.04E-17 | 96.13 | 63.9 | 1.0 |
| 406-24 | 83.722 | 0.665 | 85.643 | 0.616 | 0.0064 | 0.0009 | 9.33E-17 | 97.79 | 64.21 | 0.50 |
| 406-46 | 83.862 | 0.395 | 86.206 | 0.386 | 0.0078 | 0.0004 | 3.00E-16 | 97.31 | 64.31 | 0.30 |
| 406-03 | 84.156 | 0.651 | 84.978 | 0.630 | 0.0027 | 0.0006 | 1.37E-16 | 99.06 | 64.53 | 0.49 |
| 406-69 | 84.630 | 0.593 | 85.301 | 0.573 | 0.0022 | 0.0005 | 1.66E-16 | 99.25 | 64.89 | 0.45 |
| 406-28 | 85.839 | 0.894 | 87.942 | 0.845 | 0.0070 | 0.0011 | 7.37E-17 | 97.64 | 65.8 | 0.67 |
| 406-16 | 86.093 | 0.820 | 87.045 | 0.733 | 0.0031 | 0.0013 | 6.75E-17 | 98.94 | 65.99 | 0.62 |
| 406-51 | 86.344 | 0.626 | 86.741 | 0.611 | 0.0013 | 0.0005 | 1.62E-16 | 99.57 | 66.18 | 0.47 |
| 406-70 | 86.436 | 1.008 | 87.585 | 0.856 | 0.0038 | 0.0019 | 4.68E-17 | 98.72 | 66.25 | 0.76 |
| 406-19 | 86.572 | 0.808 | 91.229 | 0.779 | 0.0157 | 0.0011 | 8.26E-17 | 94.92 | 66.35 | 0.61 |
| 406-01 | 87.580 | 0.505 | 88.573 | 0.495 | 0.0033 | 0.0004 | 2.12E-16 | 98.91 | 67.11 | 0.38 |
| 406-60 | 89.101 | 0.696 | 90.763 | 0.672 | 0.0055 | 0.0007 | 1.29E-16 | 98.20 | 68.25 | 0.52 |
| 406-65 | 89.220 | 1.126 | 90.465 | 0.979 | 0.0041 | 0.0020 | 4.03E-17 | 98.65 | 68.34 | 0.85 |
| 406-25 | 89.672 | 0.681 | 90.145 | 0.646 | 0.0015 | 0.0007 | 1.13E-16 | 99.51 | 68.68 | 0.51 |
| 406-57 | 90.522 | 1.460 | 94.470 | 1.203 | 0.0133 | 0.0030 | 2.86E-17 | 95.85 | 69.3 | 1.1 |
| 406-75 | 90.567 | 1.204 | 97.494 | 1.057 | 0.0234 | 0.0024 | 4.20E-17 | 92.92 | 69.36 | 0.90 |
| 406-66 | 91.085 | 1.615 | 92.845 | 1.407 | 0.0059 | 0.0028 | 2.70E-17 | 98.13 | 69.7 | 1.2 |
| 406-04 | 91.588 | 0.482 | 93.848 | 0.470 | 0.0076 | 0.0005 | 2.21E-16 | 97.62 | 70.12 | 0.36 |
| 406-33 | 91.651 | 0.930 | 93.427 | 0.868 | 0.0059 | 0.0013 | 6.09E-17 | 98.13 | 70.17 | 0.70 |
| 406-38 | 91.704 | 1.314 | 93.666 | 1.173 | 0.0065 | 0.0022 | 3.56E-17 | 97.94 | 70.21 | 0.99 |
| 406-74 | 91.901 | 0.729 | 92.929 | 0.702 | 0.0034 | 0.0007 | 1.15E-16 | 98.92 | 70.36 | 0.55 |
| 406-27 | 93.088 | 1.064 | 94.152 | 0.989 | 0.0035 | 0.0014 | 5.62E-17 | 98.90 | 71.25 | 0.80 |
| 406-14 | 93.227 | 0.568 | 94.540 | 0.555 | 0.0044 | 0.0005 | 1.93E-16 | 98.64 | 71.35 | 0.43 |
| 406-10 | 93.356 | 1.182 | 95.615 | 1.041 | 0.0076 | 0.0020 | 3.90E-17 | 97.67 | 71.45 | 0.89 |
| 406-48 | 93.454 | 1.082 | 95.713 | 0.959 | 0.0076 | 0.0018 | 4.48E-17 | 97.67 | 71.52 | 0.81 |
| 406-67 | 93.554 | 0.842 | 94.328 | 0.807 | 0.0025 | 0.0009 | 9.27E-17 | 99.21 | 71.60 | 0.63 |
| 406-17 | 93.915 | 1.110 | 94.959 | 1.015 | 0.0034 | 0.0016 | 5.06E-17 | 98.93 | 71.87 | 0.83 |
| 406-32 | 94.018 | 0.801 | 98.012 | 0.769 | 0.0134 | 0.0010 | 8.87E-17 | 95.95 | 71.95 | 0.60 |
| 406-21 | 94.081 | 0.865 | 97.173 | 0.802 | 0.0104 | 0.0013 | 6.68E-17 | 96.85 | 71.99 | 0.65 |
| 406-52 | 94.144 | 1.710 | 94.843 | 1.420 | 0.0023 | 0.0033 | 2.26E-17 | 99.29 | 72.0 | 1.3 |
| 406-02 | 95.308 | 0.933 | 101.540 | 0.895 | 0.0210 | 0.0013 | 7.08E-17 | 93.89 | 72.91 | 0.70 |
| 406-47 | 95.401 | 0.946 | 97.077 | 0.916 | 0.0056 | 0.0010 | 8.56E-17 | 98.30 | 72.98 | 0.71 |
| 406-34 | 97.700 | 1.052 | 107.927 | 1.012 | 0.0345 | 0.0017 | 6.18E-17 | 90.55 | 74.71 | 0.79 |

| | | | | | | | | | | |
|---|---|---|---|---|---|---|---|---|---|---|
| 406-39 | 98.406 | 0.975 | 99.620 | 0.924 | 0.0040 | 0.0011 | 6.27E-17 | 98.81 | 75.24 | 0.73 |
| 406-36 | 98.579 | 1.000 | 101.175 | 0.946 | 0.0087 | 0.0013 | 6.63E-17 | 97.46 | 75.37 | 0.75 |
| 406-59 | 98.867 | 1.737 | 100.470 | 1.510 | 0.0053 | 0.0030 | 2.45E-17 | 98.43 | 75.6 | 1.3 |
| 406-31 | 99.169 | 1.438 | 104.482 | 1.223 | 0.0179 | 0.0029 | 3.11E-17 | 94.94 | 75.8 | 1.1 |
| 406-30 | 101.218 | 0.912 | 102.612 | 0.869 | 0.0046 | 0.0010 | 8.16E-17 | 98.67 | 77.34 | 0.68 |
| 406-62 | 102.665 | 0.644 | 104.091 | 0.626 | 0.0047 | 0.0006 | 1.54E-16 | 98.66 | 78.42 | 0.48 |
| 406-56 | 103.266 | 1.173 | 104.777 | 1.023 | 0.0050 | 0.0020 | 4.33E-17 | 98.58 | 78.87 | 0.88 |
| 406-29 | 103.656 | 0.780 | 108.229 | 0.756 | 0.0154 | 0.0008 | 1.27E-16 | 95.80 | 79.16 | 0.58 |
| 406-05 | 104.306 | 1.134 | 106.510 | 1.045 | 0.0074 | 0.0017 | 5.24E-17 | 97.96 | 79.65 | 0.85 |
| 406-40 | 104.406 | 0.577 | 105.296 | 0.570 | 0.0029 | 0.0004 | 2.09E-16 | 99.18 | 79.72 | 0.43 |
| 406-87 | 104.498 | 1.054 | 113.316 | 0.936 | 0.0298 | 0.0021 | 5.39E-17 | 92.24 | 79.79 | 0.79 |
| 406-98 | 104.590 | 1.259 | 105.792 | 1.103 | 0.0040 | 0.0021 | 3.77E-17 | 98.89 | 79.86 | 0.94 |
| 406-22 | 104.790 | 0.860 | 106.430 | 0.834 | 0.0055 | 0.0008 | 9.71E-17 | 98.48 | 80.01 | 0.64 |
| 406-09 | 105.336 | 0.956 | 107.206 | 0.892 | 0.0062 | 0.0013 | 6.12E-17 | 98.28 | 80.42 | 0.71 |
| 406-68 | 105.993 | 1.030 | 106.598 | 0.985 | 0.0020 | 0.0011 | 7.97E-17 | 99.46 | 80.91 | 0.77 |
| 406-45 | 106.317 | 0.960 | 108.283 | 0.934 | 0.0066 | 0.0009 | 1.04E-16 | 98.21 | 81.15 | 0.72 |
| 406-77 | 106.855 | 1.412 | 109.065 | 1.167 | 0.0074 | 0.0028 | 2.91E-17 | 98.00 | 81.6 | 1.1 |
| 406-08 | 108.547 | 0.950 | 118.019 | 0.954 | 0.0320 | 0.0010 | 1.28E-16 | 92.00 | 82.81 | 0.71 |
| 406-85 | 109.141 | 1.387 | 110.104 | 1.269 | 0.0032 | 0.0020 | 4.11E-17 | 99.15 | 83.3 | 1.0 |
| 406-58 | 109.201 | 1.441 | 110.301 | 1.310 | 0.0036 | 0.0021 | 3.77E-17 | 99.03 | 83.3 | 1.1 |
| 406-18 | 110.094 | 0.824 | 110.909 | 0.809 | 0.0027 | 0.0006 | 1.33E-16 | 99.29 | 83.97 | 0.61 |
| 406-26 | 111.060 | 0.854 | 112.245 | 0.834 | 0.0039 | 0.0007 | 1.27E-16 | 98.97 | 84.69 | 0.64 |
| 406-07 | 111.776 | 1.422 | 113.959 | 1.279 | 0.0073 | 0.0023 | 3.52E-17 | 98.11 | 85.2 | 1.1 |
| 406-61 | 112.102 | 1.503 | 116.682 | 1.352 | 0.0154 | 0.0026 | 3.71E-17 | 96.10 | 85.5 | 1.1 |
| 406-81 | 112.718 | 1.875 | 124.072 | 1.812 | 0.0383 | 0.0031 | 3.07E-17 | 90.87 | 85.9 | 1.4 |
| 406-86 | 113.388 | 1.488 | 114.597 | 1.333 | 0.0040 | 0.0023 | 3.60E-17 | 98.97 | 86.4 | 1.1 |
| 406-76 | 113.422 | 1.252 | 116.244 | 1.087 | 0.0095 | 0.0022 | 3.98E-17 | 97.60 | 86.45 | 0.93 |
| 406-42 | 113.516 | 1.681 | 116.194 | 1.484 | 0.0090 | 0.0029 | 2.62E-17 | 97.72 | 86.5 | 1.3 |
| 406-53 | 113.962 | 1.401 | 116.337 | 1.291 | 0.0079 | 0.0020 | 4.02E-17 | 97.98 | 86.8 | 1.0 |
| 406-20 | 113.938 | 0.571 | 114.349 | 0.562 | 0.0013 | 0.0004 | 2.20E-16 | 99.66 | 86.83 | 0.42 |
| 406-43 | 114.223 | 1.271 | 117.687 | 1.186 | 0.0116 | 0.0018 | 4.49E-17 | 97.08 | 87.04 | 0.95 |
| 406-55 | 114.567 | 1.650 | 116.998 | 1.438 | 0.0081 | 0.0029 | 2.98E-17 | 97.95 | 87.3 | 1.2 |
| 406-78 | 76.156 | 0.771 | 76.704 | 0.698 | 0.0018 | 0.0011 | 6.81E-17 | 99.32 | 58.50 | 0.58 |
| 406-15 | 92.491 | 0.498 | 93.793 | 0.483 | 0.0043 | 0.0005 | 2.03E-16 | 98.64 | 70.80 | 0.37 |

*07-AT-ZG-L - 33°48'13.9"N, 77°47'52.37"E*

| | | | | | | | | | | |
|---|---|---|---|---|---|---|---|---|---|---|
| 408-32 | 43.021 | 0.313 | 43.951 | 0.274 | 0.0031 | 0.0005 | 1.66E-16 | 97.94 | 32.36 | 0.23 |
| 408-88 | 45.146 | 0.385 | 46.703 | 0.344 | 0.0052 | 0.0006 | 1.41E-16 | 96.72 | 33.94 | 0.29 |
| 408-80 | 45.390 | 0.314 | 45.841 | 0.292 | 0.0014 | 0.0004 | 2.06E-16 | 99.08 | 34.13 | 0.23 |
| 408-44 | 45.582 | 0.334 | 47.657 | 0.299 | 0.0069 | 0.0006 | 1.75E-16 | 95.70 | 34.27 | 0.25 |
| 408-03 | 45.619 | 0.386 | 49.989 | 0.344 | 0.0147 | 0.0007 | 1.54E-16 | 91.31 | 34.30 | 0.29 |
| 408-16 | 45.874 | 0.273 | 46.385 | 0.247 | 0.0016 | 0.0004 | 2.19E-16 | 98.96 | 34.49 | 0.20 |
| 408-25 | 46.105 | 0.492 | 46.962 | 0.397 | 0.0028 | 0.0010 | 7.72E-17 | 98.23 | 34.66 | 0.37 |
| 408-68 | 46.121 | 0.428 | 47.792 | 0.383 | 0.0056 | 0.0007 | 1.40E-16 | 96.56 | 34.67 | 0.32 |
| 408-57 | 46.203 | 0.347 | 47.019 | 0.320 | 0.0027 | 0.0005 | 1.70E-16 | 98.32 | 34.73 | 0.26 |
| 408-61 | 46.245 | 0.301 | 46.617 | 0.281 | 0.0012 | 0.0004 | 2.09E-16 | 99.26 | 34.76 | 0.22 |
| 408-81 | 46.283 | 0.316 | 47.000 | 0.292 | 0.0023 | 0.0004 | 1.95E-16 | 98.53 | 34.79 | 0.24 |
| 408-48 | 46.456 | 0.356 | 48.203 | 0.310 | 0.0058 | 0.0006 | 1.40E-16 | 96.43 | 34.92 | 0.26 |

| | | | | | | | | | | |
|---|---|---|---|---|---|---|---|---|---|---|
| 408-56 | 46.545 | 0.328 | 50.978 | 0.282 | 0.0149 | 0.0006 | 1.64E-16 | 91.35 | 34.99 | 0.24 |
| 408-70 | 47.120 | 0.335 | 48.961 | 0.311 | 0.0061 | 0.0005 | 1.98E-16 | 96.29 | 35.41 | 0.25 |
| 408-22 | 47.286 | 0.352 | 47.808 | 0.340 | 0.0017 | 0.0003 | 2.30E-16 | 98.97 | 35.54 | 0.26 |
| 408-53 | 47.327 | 0.223 | 48.025 | 0.213 | 0.0023 | 0.0002 | 3.67E-16 | 98.60 | 35.57 | 0.17 |
| 408-76 | 47.368 | 0.369 | 49.176 | 0.350 | 0.0060 | 0.0004 | 2.23E-16 | 96.38 | 35.60 | 0.27 |
| 408-45 | 47.660 | 0.329 | 48.139 | 0.302 | 0.0015 | 0.0005 | 1.69E-16 | 99.06 | 35.82 | 0.24 |
| 408-14 | 47.710 | 0.372 | 48.731 | 0.325 | 0.0034 | 0.0006 | 1.39E-16 | 97.96 | 35.85 | 0.28 |
| 408-58 | 47.991 | 0.332 | 52.163 | 0.312 | 0.0140 | 0.0004 | 2.76E-16 | 92.05 | 36.06 | 0.25 |
| 408-29 | 48.021 | 0.241 | 48.679 | 0.228 | 0.0021 | 0.0003 | 3.22E-16 | 98.70 | 36.08 | 0.18 |
| 408-21 | 48.110 | 0.275 | 49.095 | 0.248 | 0.0032 | 0.0004 | 2.00E-16 | 98.05 | 36.15 | 0.20 |
| 408-52 | 48.218 | 0.322 | 49.310 | 0.310 | 0.0036 | 0.0003 | 2.86E-16 | 97.84 | 36.23 | 0.24 |
| 408-08 | 48.367 | 0.423 | 51.688 | 0.400 | 0.0112 | 0.0006 | 1.54E-16 | 93.62 | 36.34 | 0.31 |
| 408-41 | 48.713 | 0.652 | 53.876 | 0.478 | 0.0174 | 0.0017 | 5.75E-17 | 90.46 | 36.60 | 0.48 |
| 408-07 | 48.792 | 0.330 | 49.004 | 0.315 | 0.0006 | 0.0003 | 2.12E-16 | 99.63 | 36.66 | 0.25 |
| 408-43 | 48.851 | 0.352 | 49.200 | 0.337 | 0.0011 | 0.0004 | 2.39E-16 | 99.35 | 36.70 | 0.26 |
| 408-40 | 48.913 | 0.552 | 50.167 | 0.399 | 0.0042 | 0.0013 | 6.58E-17 | 97.55 | 36.75 | 0.41 |
| 408-34 | 48.935 | 0.429 | 49.667 | 0.361 | 0.0024 | 0.0008 | 1.02E-16 | 98.58 | 36.76 | 0.32 |
| 408-72 | 49.017 | 0.633 | 50.390 | 0.506 | 0.0046 | 0.0013 | 5.76E-17 | 97.33 | 36.83 | 0.47 |
| 408-28 | 49.074 | 0.727 | 50.482 | 0.544 | 0.0047 | 0.0017 | 5.16E-17 | 97.26 | 36.87 | 0.54 |
| 408-90 | 49.292 | 0.424 | 51.109 | 0.334 | 0.0061 | 0.0009 | 1.01E-16 | 96.50 | 37.03 | 0.32 |
| 408-17 | 49.348 | 0.389 | 49.757 | 0.306 | 0.0013 | 0.0008 | 1.01E-16 | 99.23 | 37.07 | 0.29 |
| 408-02 | 49.393 | 0.329 | 50.883 | 0.307 | 0.0050 | 0.0004 | 2.10E-16 | 97.13 | 37.11 | 0.24 |
| 408-64 | 49.517 | 0.594 | 51.156 | 0.473 | 0.0055 | 0.0013 | 6.33E-17 | 96.85 | 37.20 | 0.44 |
| 408-51 | 49.519 | 0.429 | 50.890 | 0.345 | 0.0046 | 0.0009 | 8.35E-17 | 97.36 | 37.20 | 0.32 |
| 408-55 | 49.540 | 0.661 | 51.324 | 0.499 | 0.0059 | 0.0015 | 5.24E-17 | 96.58 | 37.21 | 0.49 |
| 408-71 | 49.545 | 0.539 | 52.430 | 0.392 | 0.0097 | 0.0013 | 6.50E-17 | 94.55 | 37.22 | 0.40 |
| 408-19 | 49.640 | 0.236 | 49.930 | 0.224 | 0.0009 | 0.0003 | 3.62E-16 | 99.48 | 37.29 | 0.18 |
| 408-84 | 49.741 | 0.205 | 50.755 | 0.198 | 0.0033 | 0.0002 | 5.05E-16 | 98.06 | 37.36 | 0.15 |
| 408-37 | 49.772 | 0.571 | 52.335 | 0.425 | 0.0086 | 0.0014 | 6.35E-17 | 95.15 | 37.39 | 0.42 |
| 408-36 | 49.833 | 0.381 | 50.555 | 0.328 | 0.0024 | 0.0007 | 1.16E-16 | 98.63 | 37.43 | 0.28 |
| 408-04 | 49.835 | 0.730 | 51.163 | 0.538 | 0.0044 | 0.0017 | 4.83E-17 | 97.46 | 37.43 | 0.54 |
| 408-39 | 49.879 | 0.572 | 52.209 | 0.412 | 0.0078 | 0.0014 | 6.52E-17 | 95.59 | 37.47 | 0.43 |
| 408-63 | 49.895 | 0.425 | 50.671 | 0.351 | 0.0025 | 0.0008 | 9.12E-17 | 98.52 | 37.48 | 0.32 |
| 408-93 | 49.917 | 0.390 | 50.297 | 0.341 | 0.0012 | 0.0007 | 1.16E-16 | 99.30 | 37.49 | 0.29 |
| 408-69 | 49.979 | 0.436 | 51.286 | 0.349 | 0.0043 | 0.0009 | 1.04E-16 | 97.50 | 37.54 | 0.32 |
| 408-65 | 50.015 | 0.543 | 51.044 | 0.400 | 0.0034 | 0.0013 | 6.05E-17 | 98.04 | 37.57 | 0.40 |
| 408-12 | 50.442 | 0.509 | 54.074 | 0.410 | 0.0122 | 0.0011 | 8.46E-17 | 93.33 | 37.88 | 0.38 |
| 408-50 | 50.484 | 0.341 | 51.817 | 0.288 | 0.0044 | 0.0007 | 1.23E-16 | 97.48 | 37.92 | 0.25 |
| 408-42 | 50.544 | 0.392 | 51.096 | 0.338 | 0.0018 | 0.0007 | 1.16E-16 | 98.97 | 37.96 | 0.29 |
| 408-73 | 50.550 | 0.586 | 51.810 | 0.443 | 0.0042 | 0.0013 | 6.34E-17 | 97.62 | 37.96 | 0.44 |
| 408-95 | 50.858 | 0.250 | 54.562 | 0.239 | 0.0124 | 0.0003 | 4.22E-16 | 93.26 | 38.19 | 0.19 |
| 408-85 | 50.917 | 0.743 | 51.441 | 0.539 | 0.0017 | 0.0017 | 4.73E-17 | 99.03 | 38.24 | 0.55 |
| 408-82 | 50.934 | 0.519 | 52.459 | 0.435 | 0.0051 | 0.0010 | 8.16E-17 | 97.14 | 38.25 | 0.39 |
| 408-11 | 51.002 | 0.615 | 51.935 | 0.423 | 0.0031 | 0.0015 | 5.08E-17 | 98.26 | 38.30 | 0.46 |
| 408-83 | 51.208 | 0.614 | 55.314 | 0.459 | 0.0138 | 0.0015 | 6.09E-17 | 92.62 | 38.45 | 0.46 |
| 408-15 | 51.407 | 0.961 | 56.372 | 0.653 | 0.0167 | 0.0026 | 3.32E-17 | 91.24 | 38.60 | 0.71 |
| 408-92 | 51.436 | 0.585 | 56.498 | 0.477 | 0.0170 | 0.0013 | 7.14E-17 | 91.09 | 38.62 | 0.43 |
| 408-66 | 51.526 | 0.573 | 53.360 | 0.474 | 0.0061 | 0.0012 | 7.05E-17 | 96.61 | 38.69 | 0.43 |

| | | | | | | | | | | |
|---|---|---|---|---|---|---|---|---|---|---|
| 408-05 | 51.540 | 0.901 | 55.005 | 0.605 | 0.0116 | 0.0024 | 3.24E-17 | 93.75 | 38.70 | 0.67 |
| 408-46 | 51.626 | 0.774 | 53.558 | 0.593 | 0.0064 | 0.0018 | 4.32E-17 | 96.44 | 38.76 | 0.58 |
| 408-24 | 51.729 | 0.655 | 53.428 | 0.502 | 0.0057 | 0.0015 | 5.22E-17 | 96.87 | 38.84 | 0.49 |
| 408-75 | 51.745 | 0.570 | 52.519 | 0.438 | 0.0025 | 0.0013 | 6.95E-17 | 98.58 | 38.85 | 0.42 |
| 408-54 | 51.935 | 0.714 | 53.971 | 0.545 | 0.0068 | 0.0016 | 5.05E-17 | 96.28 | 38.99 | 0.53 |
| 408-20 | 52.088 | 0.687 | 57.826 | 0.497 | 0.0193 | 0.0018 | 5.22E-17 | 90.12 | 39.11 | 0.51 |
| 408-31 | 52.121 | 0.346 | 53.879 | 0.332 | 0.0059 | 0.0004 | 2.76E-16 | 96.79 | 39.13 | 0.26 |
| 408-35 | 52.282 | 0.375 | 53.138 | 0.322 | 0.0028 | 0.0007 | 1.23E-16 | 98.44 | 39.25 | 0.28 |
| 408-18 | 52.617 | 0.468 | 54.847 | 0.403 | 0.0075 | 0.0009 | 1.05E-16 | 95.98 | 39.50 | 0.35 |
| 408-01 | 52.682 | 0.620 | 53.779 | 0.490 | 0.0036 | 0.0013 | 5.92E-17 | 98.01 | 39.55 | 0.46 |
| 408-98 | 52.696 | 0.605 | 54.589 | 0.466 | 0.0063 | 0.0014 | 5.82E-17 | 96.58 | 39.56 | 0.45 |
| 408-13 | 52.735 | 0.439 | 54.842 | 0.390 | 0.0070 | 0.0008 | 1.15E-16 | 96.21 | 39.59 | 0.33 |
| 408-38 | 52.740 | 0.790 | 53.720 | 0.583 | 0.0032 | 0.0018 | 4.82E-17 | 98.23 | 39.59 | 0.59 |
| 408-10 | 52.794 | 0.396 | 57.635 | 0.357 | 0.0163 | 0.0007 | 1.65E-16 | 91.64 | 39.63 | 0.29 |
| 408-67 | 52.877 | 0.742 | 54.368 | 0.565 | 0.0050 | 0.0017 | 4.73E-17 | 97.31 | 39.69 | 0.55 |
| 408-96 | 52.888 | 0.781 | 59.750 | 0.606 | 0.0231 | 0.0019 | 4.62E-17 | 88.56 | 39.70 | 0.58 |
| 408-26 | 53.196 | 0.481 | 56.349 | 0.365 | 0.0106 | 0.0011 | 8.32E-17 | 94.45 | 39.93 | 0.36 |
| 408-87 | 53.592 | 0.848 | 58.165 | 0.661 | 0.0154 | 0.0020 | 4.32E-17 | 92.18 | 40.22 | 0.63 |
| 408-47 | 53.645 | 0.799 | 54.516 | 0.600 | 0.0029 | 0.0018 | 4.42E-17 | 98.45 | 40.26 | 0.59 |
| 408-79 | 53.678 | 0.403 | 55.856 | 0.321 | 0.0073 | 0.0009 | 1.17E-16 | 96.15 | 40.29 | 0.30 |
| 408-30 | 53.730 | 0.992 | 59.776 | 0.662 | 0.0204 | 0.0027 | 3.34E-17 | 89.93 | 40.33 | 0.74 |
| 408-86 | 53.901 | 0.606 | 56.498 | 0.461 | 0.0087 | 0.0014 | 6.87E-17 | 95.45 | 40.45 | 0.45 |
| 408-23 | 58.619 | 0.527 | 62.359 | 0.493 | 0.0126 | 0.0008 | 1.21E-16 | 94.05 | 43.95 | 0.39 |
| 408-09 | 61.682 | 0.510 | 63.418 | 0.459 | 0.0058 | 0.0008 | 1.16E-16 | 97.31 | 46.22 | 0.38 |
| 408-78 | 66.277 | 0.452 | 66.634 | 0.431 | 0.0011 | 0.0005 | 1.92E-16 | 99.51 | 49.62 | 0.33 |
| 408-89 | 68.353 | 0.737 | 83.158 | 0.654 | 0.0500 | 0.0016 | 8.13E-17 | 82.22 | 51.15 | 0.54 |
| 408-49 | 71.383 | 0.331 | 75.330 | 0.326 | 0.0133 | 0.0003 | 3.91E-16 | 94.80 | 53.38 | 0.24 |
| 408-59 | 72.960 | 0.419 | 75.436 | 0.407 | 0.0083 | 0.0004 | 2.56E-16 | 96.75 | 54.54 | 0.31 |

*07-AT-ZG-0 - 34°9'13.1"N, 77°18'55.6"E*

| | | | | | | | | | | |
|---|---|---|---|---|---|---|---|---|---|---|
| 398-81 | 38.959 | 0.276 | 40.257 | 0.230 | 0.0043 | 0.0005 | 1.71E-16 | 96.84 | 29.23 | 0.21 |
| 398-89 | 39.719 | 0.292 | 41.441 | 0.259 | 0.0057 | 0.0005 | 1.91E-16 | 95.91 | 29.80 | 0.22 |
| 398-45 | 40.201 | 0.257 | 40.732 | 0.236 | 0.0017 | 0.0004 | 2.24E-16 | 98.76 | 30.16 | 0.19 |
| 398-50 | 40.268 | 0.305 | 43.364 | 0.277 | 0.0104 | 0.0005 | 2.22E-16 | 92.92 | 30.21 | 0.23 |
| 398-79 | 40.638 | 0.351 | 41.753 | 0.274 | 0.0037 | 0.0008 | 1.26E-16 | 97.39 | 30.48 | 0.26 |
| 398-78 | 40.672 | 0.308 | 42.118 | 0.274 | 0.0048 | 0.0005 | 1.75E-16 | 96.63 | 30.51 | 0.23 |
| 398-40 | 41.144 | 0.307 | 43.575 | 0.279 | 0.0081 | 0.0005 | 2.04E-16 | 94.48 | 30.86 | 0.23 |
| 398-23 | 41.351 | 0.264 | 42.258 | 0.226 | 0.0030 | 0.0005 | 1.83E-16 | 97.92 | 31.01 | 0.20 |
| 398-102 | 42.169 | 0.609 | 43.646 | 0.413 | 0.0049 | 0.0016 | 5.71E-17 | 96.68 | 31.62 | 0.45 |
| 398-48 | 42.322 | 0.398 | 44.218 | 0.335 | 0.0063 | 0.0008 | 1.40E-16 | 95.77 | 31.73 | 0.30 |
| 398-49 | 42.567 | 0.304 | 46.110 | 0.284 | 0.0119 | 0.0004 | 2.89E-16 | 92.37 | 31.92 | 0.23 |
| 398-22 | 42.659 | 0.444 | 45.524 | 0.427 | 0.0096 | 0.0006 | 1.69E-16 | 93.76 | 31.98 | 0.33 |
| 398-66 | 42.686 | 0.320 | 45.174 | 0.287 | 0.0083 | 0.0005 | 1.79E-16 | 94.55 | 32.01 | 0.24 |
| 398-27 | 43.150 | 0.296 | 45.499 | 0.256 | 0.0079 | 0.0005 | 1.60E-16 | 94.90 | 32.35 | 0.22 |
| 398-08 | 43.461 | 0.385 | 46.317 | 0.351 | 0.0096 | 0.0006 | 1.43E-16 | 93.89 | 32.58 | 0.29 |
| 398-33 | 43.594 | 0.661 | 44.970 | 0.442 | 0.0046 | 0.0017 | 4.93E-17 | 97.00 | 32.68 | 0.49 |
| 398-93 | 43.598 | 0.350 | 47.787 | 0.304 | 0.0141 | 0.0007 | 1.53E-16 | 91.29 | 32.68 | 0.26 |
| 398-21 | 43.685 | 0.673 | 47.046 | 0.509 | 0.0113 | 0.0016 | 5.54E-17 | 92.91 | 32.75 | 0.50 |

| | | | | | | | | | | |
|---|---|---|---|---|---|---|---|---|---|---|
| 398-103 | 43.813 | 0.351 | 48.942 | 0.303 | 0.0173 | 0.0007 | 1.55E-16 | 89.57 | 32.84 | 0.26 |
| 398-82 | 43.885 | 0.311 | 44.788 | 0.267 | 0.0030 | 0.0006 | 1.62E-16 | 98.04 | 32.90 | 0.23 |
| 398-73 | 44.076 | 0.319 | 45.112 | 0.290 | 0.0034 | 0.0005 | 1.70E-16 | 97.76 | 33.04 | 0.24 |
| 398-28 | 44.267 | 0.506 | 46.875 | 0.389 | 0.0087 | 0.0012 | 7.53E-17 | 94.49 | 33.18 | 0.38 |
| 398-43 | 44.418 | 0.455 | 46.522 | 0.351 | 0.0070 | 0.0010 | 8.22E-17 | 95.53 | 33.29 | 0.34 |
| 398-31 | 44.501 | 0.300 | 45.444 | 0.268 | 0.0031 | 0.0005 | 1.70E-16 | 97.99 | 33.35 | 0.22 |
| 398-68 | 44.513 | 0.325 | 46.085 | 0.280 | 0.0052 | 0.0006 | 1.47E-16 | 96.65 | 33.36 | 0.24 |
| 398-25 | 44.641 | 0.371 | 48.366 | 0.335 | 0.0125 | 0.0006 | 1.75E-16 | 92.35 | 33.46 | 0.28 |
| 398-65 | 44.802 | 0.321 | 46.198 | 0.306 | 0.0046 | 0.0004 | 2.67E-16 | 97.04 | 33.58 | 0.24 |
| 398-01 | 44.905 | 0.407 | 48.539 | 0.320 | 0.0122 | 0.0009 | 1.02E-16 | 92.57 | 33.65 | 0.30 |
| 398-56 | 45.219 | 0.322 | 47.007 | 0.282 | 0.0060 | 0.0006 | 1.62E-16 | 96.25 | 33.89 | 0.24 |
| 398-18 | 45.236 | 0.236 | 48.047 | 0.224 | 0.0094 | 0.0003 | 3.54E-16 | 94.20 | 33.90 | 0.18 |
| 398-06 | 45.405 | 0.318 | 46.322 | 0.303 | 0.0030 | 0.0004 | 2.56E-16 | 98.08 | 34.02 | 0.24 |
| 398-02 | 45.558 | 0.305 | 49.246 | 0.309 | 0.0124 | 0.0003 | 4.38E-16 | 92.56 | 34.14 | 0.23 |
| 398-109 | 45.654 | 0.463 | 47.974 | 0.326 | 0.0078 | 0.0012 | 8.64E-17 | 95.22 | 34.21 | 0.34 |
| 398-12 | 45.820 | 0.409 | 48.594 | 0.337 | 0.0093 | 0.0009 | 1.16E-16 | 94.35 | 34.33 | 0.30 |
| 398-95 | 45.984 | 0.334 | 47.254 | 0.311 | 0.0042 | 0.0004 | 1.95E-16 | 97.37 | 34.45 | 0.25 |
| 398-107 | 46.128 | 0.327 | 48.015 | 0.314 | 0.0063 | 0.0004 | 2.76E-16 | 96.13 | 34.56 | 0.24 |
| 398-72 | 46.410 | 0.311 | 49.240 | 0.295 | 0.0095 | 0.0004 | 2.21E-16 | 94.31 | 34.77 | 0.23 |
| 398-29 | 46.422 | 0.367 | 47.477 | 0.286 | 0.0035 | 0.0008 | 1.05E-16 | 97.84 | 34.78 | 0.27 |
| 398-41 | 46.526 | 0.287 | 46.947 | 0.277 | 0.0013 | 0.0003 | 3.23E-16 | 99.16 | 34.86 | 0.21 |
| 398-106 | 46.529 | 0.631 | 48.549 | 0.436 | 0.0067 | 0.0016 | 5.35E-17 | 95.89 | 34.86 | 0.47 |
| 398-94 | 46.587 | 0.338 | 47.703 | 0.306 | 0.0037 | 0.0005 | 1.73E-16 | 97.72 | 34.90 | 0.25 |
| 398-26 | 46.676 | 0.322 | 48.108 | 0.292 | 0.0048 | 0.0005 | 1.82E-16 | 97.08 | 34.97 | 0.24 |
| 398-15 | 46.771 | 0.305 | 47.745 | 0.289 | 0.0032 | 0.0004 | 2.72E-16 | 98.02 | 35.04 | 0.23 |
| 398-35 | 46.835 | 0.342 | 49.840 | 0.325 | 0.0101 | 0.0004 | 2.53E-16 | 94.02 | 35.09 | 0.25 |
| 398-90 | 46.963 | 0.405 | 50.063 | 0.373 | 0.0104 | 0.0006 | 1.70E-16 | 93.86 | 35.18 | 0.30 |
| 398-05 | 47.011 | 0.300 | 48.405 | 0.287 | 0.0046 | 0.0003 | 2.94E-16 | 97.17 | 35.22 | 0.22 |
| 398-09 | 47.018 | 0.300 | 48.812 | 0.277 | 0.0060 | 0.0004 | 2.49E-16 | 96.38 | 35.22 | 0.22 |
| 398-92 | 47.036 | 0.357 | 50.817 | 0.335 | 0.0127 | 0.0005 | 2.31E-16 | 92.61 | 35.24 | 0.26 |
| 398-104 | 47.071 | 0.429 | 47.890 | 0.337 | 0.0027 | 0.0009 | 9.30E-17 | 98.35 | 35.26 | 0.32 |
| 398-75 | 47.331 | 0.433 | 48.567 | 0.352 | 0.0041 | 0.0009 | 9.49E-17 | 97.51 | 35.45 | 0.32 |
| 398-86 | 47.469 | 0.281 | 51.674 | 0.256 | 0.0141 | 0.0005 | 3.12E-16 | 91.91 | 35.56 | 0.21 |
| 398-20 | 47.583 | 0.543 | 51.385 | 0.410 | 0.0128 | 0.0013 | 6.66E-17 | 92.65 | 35.64 | 0.40 |
| 398-67 | 47.721 | 0.538 | 49.621 | 0.438 | 0.0063 | 0.0011 | 7.07E-17 | 96.23 | 35.74 | 0.40 |
| 398-14 | 47.730 | 0.444 | 52.277 | 0.442 | 0.0153 | 0.0005 | 2.49E-16 | 91.35 | 35.75 | 0.33 |
| 398-62 | 47.733 | 0.419 | 52.586 | 0.340 | 0.0163 | 0.0010 | 1.20E-16 | 90.82 | 35.75 | 0.31 |
| 398-83 | 48.029 | 0.348 | 51.259 | 0.297 | 0.0108 | 0.0007 | 1.32E-16 | 93.75 | 35.97 | 0.26 |
| 398-46 | 48.469 | 0.745 | 51.006 | 0.547 | 0.0085 | 0.0018 | 4.42E-17 | 95.08 | 36.30 | 0.55 |
| 398-52 | 48.579 | 0.642 | 48.857 | 0.477 | 0.0009 | 0.0015 | 5.22E-17 | 99.49 | 36.38 | 0.48 |
| 398-112 | 48.591 | 0.437 | 49.725 | 0.340 | 0.0037 | 0.0010 | 8.82E-17 | 97.77 | 36.39 | 0.32 |
| 398-99 | 48.883 | 0.286 | 49.871 | 0.272 | 0.0033 | 0.0003 | 3.12E-16 | 98.07 | 36.60 | 0.21 |
| 398-85 | 48.926 | 0.900 | 52.159 | 0.610 | 0.0108 | 0.0023 | 3.71E-17 | 93.85 | 36.64 | 0.67 |
| 398-80 | 48.977 | 0.487 | 53.904 | 0.375 | 0.0166 | 0.0012 | 9.41E-17 | 90.91 | 36.67 | 0.36 |
| 398-44 | 48.988 | 0.642 | 53.969 | 0.459 | 0.0168 | 0.0017 | 5.87E-17 | 90.82 | 36.68 | 0.48 |
| 398-61 | 49.198 | 0.407 | 50.161 | 0.327 | 0.0032 | 0.0008 | 1.20E-16 | 98.13 | 36.84 | 0.30 |
| 398-30 | 49.208 | 0.394 | 53.249 | 0.340 | 0.0136 | 0.0008 | 1.16E-16 | 92.46 | 36.85 | 0.29 |
| 398-42 | 49.227 | 0.192 | 51.684 | 0.182 | 0.0082 | 0.0002 | 5.68E-16 | 95.30 | 36.86 | 0.14 |

| | | | | | | | | | | |
|---|---|---|---|---|---|---|---|---|---|---|
| 398-111 | 49.351 | 0.699 | 52.843 | 0.492 | 0.0117 | 0.0018 | 5.21E-17 | 93.44 | 36.95 | 0.52 |
| 398-63 | 49.432 | 0.623 | 49.651 | 0.440 | 0.0007 | 0.0015 | 6.04E-17 | 99.62 | 37.01 | 0.46 |
| 398-19 | 49.451 | 0.379 | 53.241 | 0.307 | 0.0127 | 0.0008 | 1.23E-16 | 92.93 | 37.03 | 0.28 |
| 398-98 | 49.481 | 0.459 | 54.507 | 0.368 | 0.0169 | 0.0011 | 1.04E-16 | 90.83 | 37.05 | 0.34 |
| 398-70 | 49.628 | 0.487 | 52.617 | 0.399 | 0.0100 | 0.0010 | 8.64E-17 | 94.37 | 37.16 | 0.36 |
| 398-101 | 49.660 | 0.768 | 49.972 | 0.560 | 0.0010 | 0.0018 | 4.60E-17 | 99.43 | 37.18 | 0.57 |
| 398-105 | 49.728 | 0.791 | 50.860 | 0.544 | 0.0037 | 0.0020 | 4.24E-17 | 97.83 | 37.23 | 0.59 |
| 398-03 | 49.753 | 0.444 | 50.791 | 0.362 | 0.0034 | 0.0009 | 8.59E-17 | 98.01 | 37.25 | 0.33 |
| 398-55 | 49.753 | 0.372 | 53.802 | 0.308 | 0.0136 | 0.0008 | 1.14E-16 | 92.52 | 37.25 | 0.28 |
| 398-84 | 49.764 | 0.371 | 51.860 | 0.281 | 0.0070 | 0.0009 | 1.11E-16 | 96.01 | 37.26 | 0.27 |
| 398-24 | 49.847 | 0.379 | 52.587 | 0.286 | 0.0092 | 0.0009 | 1.10E-16 | 94.84 | 37.32 | 0.28 |
| 398-04 | 50.027 | 0.521 | 53.348 | 0.433 | 0.0111 | 0.0011 | 7.45E-17 | 93.82 | 37.45 | 0.39 |
| 398-116 | 50.110 | 0.748 | 50.231 | 0.543 | 0.0003 | 0.0017 | 4.57E-17 | 99.82 | 37.51 | 0.55 |
| 398-114 | 50.461 | 0.791 | 56.240 | 0.570 | 0.0195 | 0.0020 | 4.59E-17 | 89.77 | 37.77 | 0.59 |
| 398-57 | 50.590 | 0.529 | 51.443 | 0.416 | 0.0028 | 0.0011 | 7.54E-17 | 98.40 | 37.87 | 0.39 |
| 398-110 | 50.740 | 0.823 | 55.201 | 0.569 | 0.0150 | 0.0021 | 4.54E-17 | 91.96 | 37.98 | 0.61 |
| 398-113 | 50.867 | 0.968 | 55.441 | 0.688 | 0.0154 | 0.0025 | 3.76E-17 | 91.80 | 38.07 | 0.72 |
| 398-97 | 52.417 | 0.716 | 56.078 | 0.529 | 0.0123 | 0.0017 | 5.22E-17 | 93.52 | 39.22 | 0.53 |
| 398-115 | 52.739 | 0.986 | 56.744 | 0.679 | 0.0135 | 0.0026 | 3.44E-17 | 92.99 | 39.46 | 0.73 |
| 398-16 | 52.821 | 0.565 | 56.434 | 0.408 | 0.0121 | 0.0014 | 7.11E-17 | 93.64 | 39.52 | 0.42 |
| 398-108 | 53.387 | 0.497 | 56.593 | 0.351 | 0.0108 | 0.0013 | 7.33E-17 | 94.38 | 39.94 | 0.37 |
| 398-39 | 54.912 | 0.473 | 55.604 | 0.373 | 0.0023 | 0.0010 | 8.92E-17 | 98.80 | 41.07 | 0.35 |
| 398-76 | 58.094 | 0.455 | 59.871 | 0.417 | 0.0059 | 0.0007 | 1.38E-16 | 97.08 | 43.42 | 0.34 |
| 398-91 | 59.098 | 0.475 | 62.733 | 0.440 | 0.0122 | 0.0007 | 1.45E-16 | 94.25 | 44.16 | 0.35 |
| 398-100 | 59.418 | 0.363 | 63.545 | 0.339 | 0.0139 | 0.0005 | 2.42E-16 | 93.55 | 44.40 | 0.27 |

[1]J values (2σ):07-AT-LM-K - 4.327E-4±7.9910E-6; 07-AT-LM-L - 4.2070E-4±1.7900E-6; 07-AT-ZG-O - 4.1930E-4±6.422E-6

# APPENDIX D

# CHAPTER 3 SUPPLEMENT:

# U-PB METHODS

Zircon crystals were extracted from crushed samples by traditional gravimetric and magnetic susceptibility methods. A large split of the grains was incorporated into a 1" epoxy mount together with fragments of University of Arizona Sri Lanka standard zircon. The mounts were polished, imaged both photographically and with cathodoluminescence at Arizona State University, and cleaned prior to isotopic analysis.

U-Pb geochronology was conducted by laser ablation multicollector inductively coupled plasma mass spectrometry (LA-MC-ICPMS) at the Arizona LaserChron Center [*Gehrels et al.,* 2006, 2008]. The analyses involved ablation of zircons with a New Wave UP193HE Excimer laser using a spot diameter of 30 μm. The ablated material was carried in helium into the plasma source of a Nu HR ICPMS for simultaneous measurement of U, Th, and Pb isotopes. All measurements were made in static mode, using Faraday detectors with $3x10^{11}$ ohm resistors for $^{238}U$, $^{232}Th$, $^{208}Pb$, $^{207}Pb$, $^{206}Pb$, and discrete dynode ion counters for $^{204}Pb$ and $^{202}Hg$. Ion yields were ~0.8 mv per ppm. Each analysis consisted of one 15-second integration on peaks with the laser off (for backgrounds), 15 one-second integrations with the laser firing, and a 30-second delay to purge the previous sample and prepare for the next analysis. The ablation pits were ~15 μm in depth.

For each analysis, the errors in determining $^{206}Pb/^{238}U$ and $^{206}Pb/^{204}Pb$ generally resulted in a measurement error of ~1-2% (at 2σ level) in the $^{206}Pb/^{238}U$ age. The errors in measurement of $^{206}Pb/^{207}Pb$ and $^{206}Pb/^{204}Pb$ generally also resulted in ~1-2% (at 2σ level) uncertainty in age for grains that are >1.0 Ga, but

were substantially larger for younger grains due to low intensity of the $^{207}Pb$ signal. For most analyses, the cross-over in precision of $^{206}Pb/^{238}U$ and $^{206}Pb/^{207}Pb$ ages occurred at ~1.0 Ga.

$^{204}Hg$ interference with $^{204}Pb$ was accounted for by measurement of $^{202}Hg$ during laser ablation and subtraction of $^{204}Hg$ according to the natural $^{202}Hg/^{204}Hg$ of 4.35. This Hg is correction was not significant for most analyses because our Hg backgrounds were low (generally ~150 cps at mass 204).

Common Pb correction was done using the Hg-corrected $^{204}Pb$ and assuming an initial Pb composition from *Stacey and Kramers* [1975]. Uncertainties of 1.5 for $^{206}Pb/^{204}Pb$ and 0.3 for $^{207}Pb/^{204}Pb$ were applied to these compositional values based on the variation in Pb isotopic composition in modern crystal rocks.

Inter-element fractionation of Pb/U was generally ~5%, whereas apparent fractionation of Pb isotopes was generally <0.2%. In-run analysis of fragments of a large Sri Lanka zircon crystal (generally every fifth measurement) with known age of 563.5 ± 3.2 Ma (2σ error) was used to correct for this fractionation. The uncertainty resulting from the calibration correction was generally 1-2% (2σ) for both $^{206}Pb/^{207}Pb$ and $^{206}Pb/^{238}U$ ages.

Concentrations of U and Th were calibrated relative to the same zircon standard, which contains ~518 ppm of U and 68 ppm Th.

The analytical data are reported in Appendix E. Uncertainties shown in these tables are at the 1σ level, and include only analytical errors. Analyses that are >20% discordant (by comparison of $^{206}Pb/^{238}U$ and $^{206}Pb/^{207}Pb$ ages) or >5%

reverse discordant are not considered further.

The resulting interpreted ages are shown in relative age-probability diagrams using a Matlab program written at Arizona State University. The age-probability diagrams show the age and its uncertainty (for analytical error only) as a normal distribution, and sum all ages from a sample into a single curve. The area under each curve is normalized to 1 according to the number of constituent analyses. The ordinate for the curves plotted in Figure 3.2a have the same scale, such that the relative peak heights not only within but also between different curves have significance.

## REFERENCES


Gehrels, G. E., V. Valencia, and A. Pullen (2006), Detrital zircon geochronology by Laser-Ablation Multicolector ICPMS at the Arizona LaserChron Center, in *Geochronology: Emerging Opportunities, Paleontological Society Short Course, October 21, 2006, Philadelphia, PA,* edited by T. Olszewski et al., *Paleontol. Soc. Pap., I2,* 1-10.

Gehrels, G. E., V. Valencia, and J. Ruiz (2008), Enhanced precision, accuracy, efficiency and spatial resolution of U-Pb ages by laser ablation-multicollector-inductively coupled plasma-mass spectrometry, *Geochem., Geophys., Geosyst., 9*, Q03017, doi:10.1029/2007GC001805.

Stacey, J. S., and J. D. Kramers (1975), Approximation of terrestrial lead isotope evolution by a two stage model, *Earth Planet. Sci. Lett., 26,* 207-221, doi:10.1016/002-821X(75)90088-6.

# APPENDIX E

# CHAPTER 3 SUPPLEMENT:

# U-PB DATA

Table A3.2a. Detrital U-Pb geochronologic analyses, raw data

| Analysis | U[1] (ppm) | $^{206}Pb/^{204}Pb$[2] | U/Th[1] | Isotope ratios | | | | | | error corr. |
|---|---|---|---|---|---|---|---|---|---|---|
| | | | | $^{206}Pb^*/^{207}Pb^*$ | ± (%) | $^{207}Pb^*/^{235}U$ | ± (%) | $^{206}Pb^*/^{238}U$ | ± (%) | |
| *TRD* | | | | | | | | | | |
| 07ATTRD-48 | 100 | 19655 | 2.5 | 16.2594 | 24.6 | 0.1279 | 25.9 | 0.0151 | 8.0 | 0.31 |
| 07ATTRD-85 | 214 | 43350 | 2.6 | 23.1634 | 28.1 | 0.0948 | 28.2 | 0.0159 | 3.2 | 0.11 |
| 07ATTRD-44 | 315 | 103802 | 2.0 | 19.4537 | 12.7 | 0.1232 | 13.1 | 0.0174 | 3.4 | 0.26 |
| 07ATTRD-21 | 132 | 171136 | 1.1 | 17.2778 | 3.3 | 0.6501 | 5.2 | 0.0815 | 4.0 | 0.77 |
| 07ATTRD-33 | 58 | 57081 | 0.6 | 17.7629 | 11.3 | 0.6363 | 14.0 | 0.0820 | 8.3 | 0.59 |
| 07ATTRD-4 | 42 | 6017 | 0.6 | 12.3696 | 26.6 | 0.9155 | 28.0 | 0.0821 | 8.9 | 0.32 |
| 07ATTRD-67 | 212 | 654333 | 0.7 | 16.9696 | 4.1 | 0.6718 | 6.8 | 0.0827 | 5.4 | 0.80 |
| 07ATTRD-62 | 285 | 368219 | 2.4 | 17.0689 | 2.2 | 0.6757 | 3.4 | 0.0837 | 2.5 | 0.75 |
| 07ATTRD-89 | 66 | 79760 | 1.1 | 16.6213 | 8.5 | 0.6957 | 10.1 | 0.0839 | 5.3 | 0.53 |
| 07ATTRD-80 | 122 | 165031 | 1.7 | 17.2423 | 8.5 | 0.6754 | 9.0 | 0.0845 | 3.1 | 0.35 |
| 07ATTRD-18 | 152 | 277323 | 0.7 | 17.3775 | 3.0 | 0.6788 | 4.5 | 0.0855 | 3.3 | 0.74 |
| 07ATTRD-82 | 83 | 85330 | 0.7 | 17.5040 | 8.5 | 0.6778 | 9.0 | 0.0860 | 3.0 | 0.34 |
| 07ATTRD-68 | 872 | 2390001 | 25.4 | 17.0463 | 1.1 | 0.7016 | 2.9 | 0.0867 | 2.7 | 0.93 |
| 07ATTRD-30 | 302 | 426977 | 0.6 | 17.2843 | 2.0 | 0.6948 | 3.8 | 0.0871 | 3.2 | 0.84 |
| 07ATTRD-60 | 1037 | 2556786 | 71.4 | 17.1572 | 0.8 | 0.7040 | 2.4 | 0.0876 | 2.3 | 0.95 |
| 07ATTRD-38 | 635 | 684392 | 0.7 | 17.0302 | 0.9 | 0.7124 | 2.3 | 0.0880 | 2.1 | 0.92 |
| 07ATTRD-40 | 220 | 268366 | 1.0 | 17.3758 | 4.3 | 0.6991 | 4.5 | 0.0881 | 1.4 | 0.31 |
| 07ATTRD-8 | 287 | 545989 | 1.5 | 17.2944 | 1.3 | 0.7094 | 2.1 | 0.0890 | 1.6 | 0.76 |
| 07ATTRD-81 | 112 | 32096 | 0.9 | 15.9463 | 7.5 | 0.7714 | 8.6 | 0.0892 | 4.2 | 0.49 |
| 07ATTRD-61 | 967 | 1441737 | 3.0 | 17.1414 | 0.6 | 0.7330 | 1.4 | 0.0911 | 1.3 | 0.92 |
| 07ATTRD-46 | 112 | 201945 | 1.4 | 14.2158 | 30.1 | 0.8876 | 30.3 | 0.0915 | 3.5 | 0.11 |
| 07ATTRD-74 | 489 | 806422 | 3.1 | 16.9350 | 1.1 | 0.7479 | 3.1 | 0.0919 | 2.8 | 0.93 |
| 07ATTRD-28 | 109 | 113402 | 1.8 | 16.5771 | 3.3 | 0.7765 | 4.9 | 0.0934 | 3.6 | 0.74 |
| 07ATTRD-100 | 100 | 93454 | 1.3 | 16.6027 | 4.1 | 0.8267 | 6.1 | 0.0995 | 4.5 | 0.74 |
| 07ATTRD-70 | 90 | 116726 | 2.3 | 16.2374 | 5.2 | 0.8516 | 6.7 | 0.1003 | 4.3 | 0.63 |
| 07ATTRD-5 | 507 | 844908 | 21.6 | 16.3747 | 1.1 | 0.8622 | 2.5 | 0.1024 | 2.3 | 0.91 |
| 07ATTRD-72 | 294 | 154013 | 3.2 | 15.5249 | 1.9 | 0.9199 | 5.6 | 0.1036 | 5.3 | 0.94 |
| 07ATTRD-95 | 655 | 1878398 | 3.6 | 16.4424 | 1.3 | 0.8779 | 2.2 | 0.1047 | 1.8 | 0.81 |
| 07ATTRD-10 | 227 | 274184 | 5.7 | 16.2337 | 2.4 | 0.9055 | 4.2 | 0.1066 | 3.5 | 0.83 |
| 07ATTRD-76 | 108 | 195807 | 2.2 | 16.0626 | 4.4 | 0.9304 | 5.1 | 0.1084 | 2.6 | 0.51 |
| 07ATTRD-34 | 349 | 410055 | 4.8 | 15.1812 | 2.5 | 1.0355 | 4.0 | 0.1140 | 3.1 | 0.78 |
| 07ATTRD-6 | 275 | 542255 | 2.9 | 14.1026 | 1.0 | 1.1722 | 6.1 | 0.1199 | 6.0 | 0.99 |
| 07ATTRD-23 | 904 | 2318596 | 12.3 | 15.5784 | 0.8 | 1.0956 | 2.1 | 0.1238 | 1.9 | 0.92 |
| 07ATTRD-51 | 505 | 159982 | 6.6 | 14.6807 | 0.8 | 1.1975 | 4.3 | 0.1275 | 4.2 | 0.98 |
| 07ATTRD-101 | 255 | 444700 | 1.6 | 15.3693 | 1.0 | 1.1470 | 2.7 | 0.1279 | 2.5 | 0.92 |
| 07ATTRD-14 | 241 | 431140 | 13.5 | 15.0828 | 1.2 | 1.1911 | 3.4 | 0.1303 | 3.2 | 0.94 |
| 07ATTRD-39 | 249 | 404360 | 2.1 | 15.1718 | 0.9 | 1.2044 | 1.7 | 0.1325 | 1.4 | 0.84 |
| 07ATTRD-1 | 100 | 356813 | 0.8 | 14.6844 | 5.3 | 1.3550 | 7.3 | 0.1443 | 5.0 | 0.69 |
| 07ATTRD-22 | 533 | 2255388 | 8.7 | 14.4692 | 0.9 | 1.4366 | 2.2 | 0.1508 | 2.0 | 0.90 |
| 07ATTRD-86 | 118 | 337830 | 2.5 | 14.2851 | 2.5 | 1.5165 | 3.7 | 0.1571 | 2.7 | 0.74 |
| 07ATTRD-59 | 36 | 173364 | 0.7 | 14.2592 | 6.8 | 1.4166 | 8.5 | 0.1465 | 5.1 | 0.60 |
| 07ATTRD-79 | 316 | 783619 | 2.8 | 14.2364 | 0.8 | 1.5366 | 2.3 | 0.1587 | 2.2 | 0.94 |
| 07ATTRD-78 | 76 | 252319 | 2.5 | 14.2134 | 3.3 | 1.4556 | 5.1 | 0.1500 | 3.9 | 0.76 |
| 07ATTRD-105 | 282 | 622523 | 8.3 | 14.1360 | 1.1 | 1.4841 | 2.5 | 0.1522 | 2.3 | 0.90 |
| 07ATTRD-17 | 149 | 369296 | 2.1 | 14.1349 | 1.5 | 1.4810 | 2.5 | 0.1518 | 2.0 | 0.80 |
| 07ATTRD-2 | 43 | 122079 | 1.8 | 14.1225 | 5.6 | 1.6200 | 6.1 | 0.1659 | 2.3 | 0.38 |
| 07ATTRD-58 | 154 | 366191 | 5.6 | 14.1211 | 2.1 | 1.5417 | 2.3 | 0.1579 | 1.0 | 0.43 |
| 07ATTRD-35 | 148 | 620705 | 1.6 | 14.1130 | 2.0 | 1.5722 | 2.9 | 0.1609 | 2.1 | 0.73 |
| 07ATTRD-106 | 323 | 577481 | 2.6 | 14.0677 | 1.1 | 1.5761 | 2.3 | 0.1608 | 2.0 | 0.88 |
| 07ATTRD-69 | 96 | 320890 | 2.4 | 14.0096 | 3.6 | 1.5555 | 4.4 | 0.1581 | 2.5 | 0.57 |
| 07ATTRD-71 | 214 | 890109 | 1.9 | 13.9745 | 1.4 | 1.5599 | 2.3 | 0.1581 | 1.9 | 0.80 |
| 07ATTRD-88 | 187 | 489072 | 4.0 | 13.9685 | 1.2 | 1.6445 | 2.4 | 0.1666 | 2.1 | 0.86 |
| 07ATTRD-53 | 90 | 163581 | 1.2 | 13.9360 | 3.5 | 1.5265 | 5.5 | 0.1543 | 4.2 | 0.76 |
| 07ATTRD-49 | 54 | 110596 | 2.2 | 13.9056 | 2.7 | 1.3697 | 3.5 | 0.1381 | 2.1 | 0.61 |
| 07ATTRD-65 | 365 | 868556 | 4.4 | 13.8898 | 1.1 | 1.6055 | 3.6 | 0.1617 | 3.4 | 0.95 |
| 07ATTRD-77 | 53 | 162419 | 0.9 | 13.8283 | 5.6 | 1.6027 | 6.2 | 0.1607 | 2.7 | 0.44 |
| 07ATTRD-92 | 160 | 373477 | 0.9 | 13.8167 | 1.8 | 1.7167 | 2.9 | 0.1720 | 2.3 | 0.80 |
| 07ATTRD-64 | 122 | 653139 | 1.6 | 13.7420 | 1.7 | 1.7393 | 3.8 | 0.1734 | 3.4 | 0.90 |
| 07ATTRD-108 | 606 | 343709 | 4.0 | 13.7180 | 0.5 | 1.4826 | 4.2 | 0.1475 | 4.2 | 0.99 |
| 07ATTRD-56 | 100 | 359759 | 0.7 | 13.7067 | 3.0 | 1.7572 | 5.6 | 0.1747 | 4.7 | 0.84 |
| 07ATTRD-93 | 303 | 1939734 | 4.9 | 13.6314 | 2.0 | 1.7329 | 3.1 | 0.1713 | 2.4 | 0.76 |

| | | | | | | | | | | |
|---|---|---|---|---|---|---|---|---|---|---|
| 07ATTRD-54 | 110 | 192046 | 1.5 | 13.2425 | 1.6 | 1.9016 | 2.7 | 0.1826 | 2.2 | 0.82 |
| 07ATTRD-41 | 407 | 1504112 | 1.1 | 13.1955 | 0.6 | 2.0063 | 1.5 | 0.1920 | 1.4 | 0.92 |
| 07ATTRD-83 | 281 | 1202720 | 5.3 | 13.1337 | 1.0 | 1.9599 | 2.5 | 0.1867 | 2.3 | 0.91 |
| 07ATTRD-63 | 94 | 469267 | 3.6 | 13.0078 | 2.6 | 2.0513 | 6.3 | 0.1935 | 5.7 | 0.91 |
| 07ATTRD-29 | 222 | 493409 | 2.3 | 12.7758 | 1.2 | 2.1426 | 2.1 | 0.1985 | 1.8 | 0.83 |
| 07ATTRD-15 | 373 | 1733328 | 11.4 | 12.6171 | 0.6 | 2.1462 | 2.0 | 0.1964 | 1.9 | 0.96 |
| 07ATTRD-12 | 329 | 1085943 | 5.6 | 12.6089 | 0.5 | 2.1792 | 1.6 | 0.1993 | 1.5 | 0.95 |
| 07ATTRD-87 | 621 | 3560633 | 1.5 | 12.2770 | 1.2 | 2.2528 | 2.7 | 0.2006 | 2.4 | 0.89 |
| 07ATTRD-98 | 126 | 499287 | 3.8 | 12.1873 | 1.1 | 2.4135 | 2.4 | 0.2133 | 2.1 | 0.88 |
| 07ATTRD-52 | 237 | 865343 | 4.8 | 11.8175 | 1.0 | 2.5297 | 1.9 | 0.2168 | 1.5 | 0.83 |
| 07ATTRD-57 | 83 | 258614 | 1.9 | 10.3778 | 2.6 | 3.4664 | 3.0 | 0.2609 | 1.6 | 0.53 |
| 07ATTRD-37 | 435 | 2583783 | 2.9 | 9.8411 | 0.9 | 3.4314 | 3.0 | 0.2449 | 2.9 | 0.96 |
| 07ATTRD-19 | 62 | 740233 | 1.7 | 8.7933 | 1.3 | 5.0631 | 4.8 | 0.3229 | 4.6 | 0.96 |
| 07ATTRD-26 | 166 | 821166 | 2.7 | 8.7232 | 0.7 | 5.3885 | 1.5 | 0.3409 | 1.3 | 0.88 |
| 07ATTRD-45 | 346 | 235781 | 5.1 | 7.9208 | 0.2 | 6.3335 | 2.8 | 0.3638 | 2.8 | 1.00 |
| 07ATTRD-107 | 419 | 2451566 | 2.1 | 7.6670 | 0.3 | 6.8260 | 1.3 | 0.3796 | 1.3 | 0.97 |
| 07ATTRD-55 | 588 | 8121931 | 5.9 | 6.5020 | 0.4 | 8.8109 | 7.4 | 0.4155 | 7.4 | 1.00 |
| 07ATTRD-36 | 133 | 762870 | 1.0 | 6.3319 | 0.3 | 9.6692 | 1.5 | 0.4440 | 1.5 | 0.98 |
| 07ATTRD-32 | 213 | 450874 | 2.4 | 6.3110 | 0.9 | 9.4872 | 6.1 | 0.4342 | 6.1 | 0.99 |
| 07ATTRD-42 | 41 | 179035 | 4.1 | 6.2090 | 1.2 | 10.4308 | 2.0 | 0.4697 | 1.6 | 0.81 |
| 07ATTRD-27 | 404 | 5444555 | 2.2 | 6.2068 | 0.2 | 9.5136 | 2.6 | 0.4283 | 2.6 | 1.00 |
| 07ATTRD-24 | 278 | 2081748 | 1.2 | 6.1849 | 0.4 | 9.8813 | 1.3 | 0.4432 | 1.2 | 0.95 |
| 07ATTRD-103 | 267 | 2695398 | 1.4 | 6.1387 | 0.3 | 10.0361 | 2.4 | 0.4468 | 2.4 | 0.99 |
| 07ATTRD-73 | 152 | 1009992 | 1.5 | 6.1152 | 0.4 | 9.8868 | 2.2 | 0.4385 | 2.2 | 0.99 |
| 07ATTRD-47 | 285 | 3594489 | 3.5 | 5.8926 | 0.2 | 10.3724 | 2.3 | 0.4433 | 2.3 | 1.00 |
| 07ATTRD-9 | 66 | 708296 | 1.9 | 5.3480 | 0.9 | 12.8608 | 2.5 | 0.4988 | 2.4 | 0.93 |
| 07ATTRD-102 | 540 | 900381 | 2.5 | 4.5017 | 1.2 | 16.9645 | 2.7 | 0.5539 | 2.4 | 0.89 |
| 07ATTRD-31 | 37 | 290208 | 2.0 | 4.4201 | 0.6 | 17.3220 | 1.6 | 0.5553 | 1.5 | 0.94 |
| 07ATTRD-90 | 23 | 258710 | 1.7 | 3.4297 | 0.4 | 27.3673 | 4.7 | 0.6808 | 4.6 | 1.00 |
| | | | | | | | | | | |
| *TRE* | | | | | | | | | | |
| 07ATTRE-54 | 650 | 182376 | 2.9 | 20.4940 | 11.2 | 0.0931 | 11.4 | 0.0138 | 2.4 | 0.21 |
| 07ATTRE-75 | 533 | 4910063 | 1.3 | 10.0004 | 0.2 | 3.7573 | 1.4 | 0.2725 | 1.4 | 0.99 |
| 07ATTRE-84 | 137 | 909328 | 1.2 | 5.9628 | 0.3 | 11.1479 | 2.9 | 0.4821 | 2.9 | 1.00 |
| 07ATTRE-66 | 767 | 1950967 | 9.8 | 16.6063 | 0.8 | 0.7691 | 1.1 | 0.0926 | 0.8 | 0.73 |
| 07ATTRE-88 | 60 | 629787 | 1.3 | 3.4042 | 0.3 | 28.1681 | 2.2 | 0.6955 | 2.1 | 0.99 |
| 07ATTRE-112 | 547 | 450411 | 1.8 | 16.9712 | 1.4 | 0.7237 | 1.8 | 0.0891 | 1.0 | 0.60 |
| 07ATTRE-22 | 671 | 1479155 | 2.7 | 6.1914 | 0.4 | 9.9863 | 2.2 | 0.4484 | 2.2 | 0.99 |
| 07ATTRE-97 | 479 | 249612 | 0.9 | 18.2175 | 2.8 | 0.4230 | 3.4 | 0.0559 | 1.9 | 0.57 |
| 07ATTRE-26 | 1247 | 979646 | 6.9 | 16.9935 | 0.8 | 0.6269 | 1.7 | 0.0773 | 1.5 | 0.87 |
| 07ATTRE-78 | 222 | 190737 | 0.7 | 17.0632 | 2.2 | 0.6776 | 2.6 | 0.0839 | 1.4 | 0.53 |
| 07ATTRE-21 | 343 | 1932509 | 2.3 | 12.5355 | 0.4 | 2.1054 | 1.8 | 0.1914 | 1.7 | 0.98 |
| 07ATTRE-64 | 215 | 2038759 | 1.7 | 5.3225 | 0.4 | 13.5715 | 2.8 | 0.5239 | 2.8 | 0.99 |
| 07ATTRE-108 | 243 | 490715 | 0.7 | 17.5657 | 2.8 | 0.6154 | 3.2 | 0.0784 | 1.6 | 0.49 |
| 07ATTRE-29 | 376 | 1857298 | 3.5 | 6.3955 | 0.4 | 8.3678 | 3.4 | 0.3881 | 3.4 | 0.99 |
| 07ATTRE-7 | 69 | 39745 | 0.5 | 15.8849 | 16.3 | 0.7090 | 16.4 | 0.0817 | 1.7 | 0.10 |
| 07ATTRE-81 | 329 | 1664660 | 2.2 | 9.9583 | 0.5 | 4.0544 | 1.6 | 0.2928 | 1.5 | 0.96 |
| 07ATTRE-11 | 734 | 729531 | 3.5 | 16.1391 | 1.0 | 0.9055 | 1.8 | 0.1060 | 1.4 | 0.81 |
| 07ATTRE-40 | 463 | 466807 | 1.3 | 17.0374 | 1.1 | 0.7223 | 2.1 | 0.0893 | 1.7 | 0.83 |
| 07ATTRE-70 | 843 | 4092450 | 1.2 | 13.5487 | 0.4 | 1.6752 | 1.8 | 0.1646 | 1.8 | 0.97 |
| 07ATTRE-80 | 393 | 1971538 | 6.7 | 7.4846 | 0.5 | 7.4320 | 3.4 | 0.4034 | 3.4 | 0.99 |
| 07ATTRE-83 | 188 | 177765 | 0.7 | 17.7826 | 2.7 | 0.6580 | 3.3 | 0.0849 | 1.9 | 0.57 |
| 07ATTRE-79 | 271 | 263211 | 6.0 | 17.1637 | 3.4 | 0.7524 | 3.8 | 0.0937 | 1.8 | 0.46 |
| 07ATTRE-19 | 579 | 1050727 | 2.1 | 13.8587 | 0.5 | 1.6318 | 2.5 | 0.1640 | 2.4 | 0.98 |
| 07ATTRE-33 | 392 | 1272665 | 7.4 | 15.7889 | 1.7 | 0.9333 | 2.3 | 0.1069 | 1.6 | 0.70 |
| 07ATTRE-82 | 619 | 1414330 | 16.5 | 14.1316 | 0.5 | 1.6023 | 1.8 | 0.1642 | 1.7 | 0.95 |
| 07ATTRE-35 | 188 | 111236 | 0.9 | 16.5323 | 5.2 | 0.7122 | 5.6 | 0.0854 | 2.2 | 0.39 |
| 07ATTRE-37 | 123 | 113938 | 0.2 | 16.7396 | 5.1 | 0.7513 | 5.5 | 0.0912 | 2.1 | 0.39 |
| 07ATTRE-114 | 490 | 978749 | 16.2 | 14.0307 | 0.6 | 1.5597 | 2.3 | 0.1587 | 2.3 | 0.97 |
| 07ATTRE-104 | 509 | 659634 | 3.4 | 17.2427 | 1.8 | 0.6838 | 3.1 | 0.0855 | 2.5 | 0.81 |
| 07ATTRE-109 | 79 | 58933 | 0.5 | 17.2940 | 5.1 | 0.6369 | 5.8 | 0.0799 | 2.8 | 0.48 |
| 07ATTRE-57 | 192 | 674241 | 2.2 | 9.4937 | 0.8 | 4.4583 | 1.2 | 0.3070 | 0.9 | 0.75 |
| 07ATTRE-105 | 571 | 661059 | 1.7 | 12.5693 | 0.7 | 1.9993 | 2.8 | 0.1823 | 2.7 | 0.97 |
| 07ATTRE-71 | 353 | 1142606 | 1.2 | 15.1096 | 1.5 | 1.1582 | 2.4 | 0.1269 | 1.9 | 0.79 |
| 07ATTRE-58 | 111 | 230593 | 0.5 | 16.8595 | 8.6 | 0.6967 | 9.0 | 0.0852 | 2.7 | 0.30 |
| 07ATTRE-62 | 416 | 2034397 | 2.6 | 11.5093 | 0.8 | 2.3922 | 2.8 | 0.1997 | 2.7 | 0.96 |
| 07ATTRE-14 | 196 | 314911 | 2.7 | 14.4513 | 1.1 | 1.3985 | 2.1 | 0.1466 | 1.8 | 0.86 |
| 07ATTRE-24 | 102 | 76855 | 0.5 | 17.8123 | 6.3 | 0.6981 | 6.9 | 0.0902 | 2.7 | 0.40 |
| 07ATTRE-89 | 80 | 101639 | 0.9 | 17.4053 | 6.3 | 0.7163 | 6.9 | 0.0904 | 2.8 | 0.41 |
| 07ATTRE-44 | 443 | 1314837 | 5.7 | 13.8905 | 0.8 | 1.6545 | 2.3 | 0.1667 | 2.2 | 0.94 |

| | | | | | | | | | | |
|---|---|---|---|---|---|---|---|---|---|---|
| 07ATTRE-17 | 132 | 111474 | 0.8 | 16.3944 | 5.4 | 0.7009 | 6.3 | 0.0833 | 3.2 | 0.50 |
| 07ATTRE-91 | 644 | 2125809 | 35.2 | 14.9360 | 0.5 | 1.2724 | 2.2 | 0.1378 | 2.1 | 0.97 |
| 07ATTRE-96 | 584 | 709673 | 2.7 | 16.7635 | 1.7 | 0.7351 | 3.6 | 0.0894 | 3.2 | 0.89 |
| 07ATTRE-2 | 300 | 245899 | 2.2 | 17.1534 | 3.0 | 0.6986 | 4.5 | 0.0869 | 3.3 | 0.74 |
| 07ATTRE-28 | 66 | 60932 | 0.6 | 18.3090 | 7.2 | 0.6306 | 8.0 | 0.0837 | 3.5 | 0.43 |
| 07ATTRE-32 | 416 | 708521 | 2.1 | 13.9099 | 0.9 | 1.6361 | 2.9 | 0.1651 | 2.7 | 0.95 |
| 07ATTRE-60 | 393 | 519076 | 4.5 | 13.5883 | 0.9 | 1.8508 | 4.7 | 0.1824 | 4.6 | 0.98 |
| 07ATTRE-53 | 397 | 770612 | 6.8 | 14.5585 | 1.2 | 1.2764 | 2.6 | 0.1348 | 2.3 | 0.89 |
| 07ATTRE-94 | 200 | 224977 | 0.9 | 17.2713 | 3.4 | 0.6677 | 4.9 | 0.0836 | 3.5 | 0.72 |
| 07ATTRE-1 | 67 | 42471 | 0.5 | 17.5989 | 14.8 | 0.6276 | 15.3 | 0.0801 | 3.8 | 0.25 |
| 07ATTRE-16 | 417 | 798077 | 4.8 | 14.0115 | 0.9 | 1.5238 | 1.9 | 0.1549 | 1.6 | 0.87 |
| 07ATTRE-90 | 250 | 585800 | 3.7 | 14.4206 | 1.2 | 1.4014 | 2.6 | 0.1466 | 2.3 | 0.88 |
| 07ATTRE-52 | 837 | 1576055 | 117.3 | 13.7200 | 1.0 | 1.7971 | 6.0 | 0.1788 | 6.0 | 0.99 |
| 07ATTRE-36 | 122 | 32388 | 1.0 | 13.8708 | 5.1 | 1.1441 | 5.9 | 0.1151 | 3.0 | 0.51 |
| 07ATTRE-10 | 257 | 349626 | 4.3 | 14.0186 | 1.0 | 1.5947 | 2.6 | 0.1621 | 2.4 | 0.92 |
| 07ATTRE-86 | 50 | 58448 | 0.8 | 18.5570 | 21.0 | 0.5991 | 21.5 | 0.0806 | 4.4 | 0.21 |
| 07ATTRE-115 | 1599 | 367171 | 8.7 | 14.0725 | 0.5 | 1.2288 | 3.1 | 0.1254 | 3.1 | 0.99 |
| 07ATTRE-55 | 188 | 471113 | 1.6 | 14.2551 | 1.1 | 1.5166 | 3.1 | 0.1568 | 2.9 | 0.94 |
| 07ATTRE-73 | 568 | 864616 | 3.1 | 14.1973 | 1.1 | 1.4194 | 4.0 | 0.1462 | 3.9 | 0.96 |
| 07ATTRE-46 | 1062 | 1155068 | 24.9 | 16.7109 | 0.9 | 0.5681 | 5.6 | 0.0689 | 5.6 | 0.99 |
| 07ATTRE-27 | 298 | 1103475 | 0.5 | 13.5874 | 1.1 | 1.5094 | 2.3 | 0.1487 | 2.1 | 0.88 |
| 07ATTRE-25 | 80 | 109789 | 0.6 | 18.1432 | 7.4 | 0.6339 | 8.8 | 0.0834 | 4.7 | 0.54 |
| 07ATTRE-43 | 95 | 94889 | 2.2 | 14.8378 | 27.3 | 0.8688 | 27.7 | 0.0935 | 4.2 | 0.15 |
| 07ATTRE-34 | 991 | 1506130 | 5.0 | 16.5884 | 0.8 | 0.8019 | 4.5 | 0.0965 | 4.5 | 0.98 |
| 07ATTRE-47 | 236 | 436819 | 3.3 | 12.8245 | 1.3 | 2.1910 | 3.7 | 0.2038 | 3.5 | 0.94 |
| 07ATTRE-111 | 406 | 413997 | 12.5 | 16.7676 | 1.2 | 0.7930 | 4.7 | 0.0964 | 4.5 | 0.97 |
| 07ATTRE-85 | 218 | 266702 | 1.8 | 14.3178 | 1.3 | 1.5192 | 1.8 | 0.1578 | 1.3 | 0.72 |
| 07ATTRE-113 | 180 | 326922 | 0.7 | 14.1192 | 1.3 | 1.4988 | 2.0 | 0.1535 | 1.6 | 0.78 |
| 07ATTRE-63 | 171 | 366294 | 1.8 | 13.1744 | 1.3 | 1.9727 | 2.8 | 0.1885 | 2.5 | 0.88 |
| 07ATTRE-13 | 90 | 850032 | 1.2 | 9.4112 | 1.4 | 4.5475 | 3.1 | 0.3104 | 2.7 | 0.89 |
| 07ATTRE-93 | 644 | 170740 | 1.7 | 15.1706 | 1.5 | 1.0541 | 4.1 | 0.1160 | 3.8 | 0.93 |
| 07ATTRE-95 | 59 | 47678 | 0.5 | 18.1251 | 9.4 | 0.6151 | 10.8 | 0.0809 | 5.3 | 0.49 |
| 07ATTRE-49 | 278 | 525852 | 0.8 | 13.9727 | 1.3 | 1.5808 | 1.8 | 0.1602 | 1.2 | 0.67 |
| 07ATTRE-39 | 179 | 320753 | 1.7 | 13.6232 | 1.4 | 1.7771 | 2.3 | 0.1756 | 1.9 | 0.81 |
| 07ATTRE-41 | 369 | 542854 | 3.9 | 13.0474 | 1.4 | 1.8196 | 5.7 | 0.1722 | 5.6 | 0.97 |
| 07ATTRE-20 | 86 | 63044 | 0.9 | 16.3012 | 31.3 | 0.6303 | 31.9 | 0.0745 | 6.5 | 0.20 |
| 07ATTRE-51 | 523 | 1159323 | 4.4 | 15.1965 | 1.1 | 1.1062 | 4.7 | 0.1219 | 4.6 | 0.97 |
| 07ATTRE-72 | 129 | 142307 | 0.5 | 16.4022 | 3.6 | 0.6843 | 8.1 | 0.0814 | 7.2 | 0.90 |
| 07ATTRE-30 | 168 | 667519 | 1.8 | 12.8978 | 1.9 | 1.8565 | 3.1 | 0.1737 | 2.4 | 0.78 |
| 07ATTRE-92 | 138 | 367593 | 0.5 | 12.6578 | 1.9 | 2.1996 | 3.1 | 0.2019 | 2.4 | 0.79 |
| 07ATTRE-56 | 47 | 48799 | 0.5 | 17.1232 | 15.6 | 0.6556 | 17.6 | 0.0814 | 8.2 | 0.46 |
| 07ATTRE-4 | 78 | 220446 | 1.0 | 10.3296 | 2.2 | 3.4803 | 3.5 | 0.2607 | 2.7 | 0.77 |
| 07ATTRE-3 | 176 | 317126 | 1.0 | 14.2668 | 2.0 | 1.4664 | 3.4 | 0.1517 | 2.7 | 0.80 |
| 07ATTRE-61 | 449 | 975112 | 2.6 | 14.3308 | 12.9 | 0.8196 | 15.6 | 0.0852 | 8.7 | 0.56 |
| 07ATTRE-18 | 197 | 265903 | 0.9 | 13.9533 | 2.3 | 1.5368 | 4.1 | 0.1555 | 3.4 | 0.83 |
| 07ATTRE-106 | 195 | 1632830 | 2.5 | 10.0533 | 2.6 | 3.3251 | 4.7 | 0.2424 | 4.0 | 0.84 |
| 07ATTRE-5 | 659 | 764617 | 2.5 | 14.5473 | 0.6 | 1.2768 | 6.7 | 0.1347 | 6.6 | 1.00 |
| 07ATTRE-103 | 284 | 756159 | 4.4 | 12.1601 | 2.7 | 1.8410 | 6.1 | 0.1624 | 5.4 | 0.89 |
| 07ATTRE-77 | 163 | 330871 | 2.0 | 14.2612 | 2.8 | 1.3233 | 7.5 | 0.1369 | 6.9 | 0.93 |
| 07ATTRE-76 | 401 | 949692 | 1.0 | 11.4533 | 2.8 | 2.3986 | 7.2 | 0.1992 | 6.6 | 0.92 |
| 07ATTRE-6 | 80 | 160340 | 1.9 | 14.0657 | 3.4 | 1.4714 | 3.8 | 0.1501 | 1.8 | 0.47 |
| 07ATTRE-74 | 127 | 225094 | 2.2 | 13.7703 | 4.2 | 1.6312 | 6.6 | 0.1629 | 5.1 | 0.77 |
| 07ATTRE-48 | 51 | 123580 | 1.6 | 12.6837 | 4.9 | 1.9715 | 5.4 | 0.1814 | 2.3 | 0.43 |
| 07ATTRE-65 | 73 | 98751 | 2.2 | 13.1744 | 6.5 | 1.7193 | 7.0 | 0.1643 | 2.4 | 0.34 |

*Note:* All uncertainties are reported at the 1σ level, and include only measurement errors. Systematic errors are as follows for $^{206}Pb/^{238}U$ and $^{206}Pb/^{207}Pb$, respectively, at 2σ level: 1.6% and 0.9% for sample TRD and 2.1% and 3.2% for sample TRE. Analyses conducted by LA-MC-ICPMS, as described by Gehrels et al. (2008). U/Pb and $^{206}Pb/^{207}Pb$ fractionation is calibrated relative to fragments of a large Sri Lanka zircon of 563.5±3.2 Ma (2σ). U decay constants and composition as follows: $^{238}U = 9.8485 \times 10^{-10}$, $^{235}U = 1.55125 \times 10^{-10}$, $^{238}U/^{235}U = 137.88$.

[1]U concentration and U/Th are calibrated relative to Sri Lanka zircon standard and are accurate to ~20%.

[2]Common Pb correction is from measured $^{204}Pb$ with common Pb composition interpreted from Stacey and Kramers (1975). Common Pb composition assigned uncertainties of 1.5 for $^{206}Pb/^{204}Pb$, 0.3 for $^{207}Pb/^{204}Pb$, and 2.0 for $^{208}Pb/^{204}Pb$.

Table A3.2b. Detrital U-Pb geochronologic analyses, age data.

| Analysis | Apparent ages (Ma) | | | | | | | |
|---|---|---|---|---|---|---|---|---|
| | $^{206}Pb^*/^{238}U$ | ± | $^{207}Pb^*/^{235}U$ | ± | $^{206}Pb^*/^{207}Pb^*$ | ± | Best age[3] | ± |
| | (Ma) | (Ma) | (Ma) | (Ma) | (Ma) | (Ma) | (Ma) | (Ma) |
| *TRD* | | | | | | | | |
| 07ATTRD-48 | 96.5 | 7.6 | 122 | 30 | 660 | 540 | 96.5 | 7.6 |
| 07ATTRD-85 | 101.9 | 3.2 | 92 | 25 | -160.0 | 710 | 101.9 | 3.2 |
| 07ATTRD-44 | 111.1 | 3.7 | 118 | 15 | 260 | 290 | 111.1 | 3.7 |
| 07ATTRD-21 | 505 | 19 | 509 | 21 | 525 | 73 | 505 | 19 |
| 07ATTRD-33 | 508 | 40 | 500 | 55 | 460 | 250 | 508 | 40 |
| 07ATTRD-4 | 509 | 44 | 660 | 140 | 1220 | 530 | 509 | 44 |
| 07ATTRD-67 | 512 | 27 | 522 | 28 | 564 | 89 | 512 | 27 |
| 07ATTRD-62 | 518 | 13 | 524 | 14 | 552 | 48 | 518 | 13 |
| 07ATTRD-89 | 519 | 27 | 536 | 42 | 610 | 180 | 519 | 27 |
| 07ATTRD-80 | 523 | 16 | 524 | 37 | 530 | 190 | 523 | 16 |
| 07ATTRD-18 | 529 | 17 | 526 | 18 | 513 | 67 | 529 | 17 |
| 07ATTRD-82 | 532 | 15 | 525 | 37 | 500 | 190 | 532 | 15 |
| 07ATTRD-68 | 536 | 14 | 540 | 12 | 555 | 24 | 536 | 14 |
| 07ATTRD-30 | 538 | 16 | 536 | 16 | 524 | 45 | 538 | 16 |
| 07ATTRD-60 | 541 | 12 | 541 | 10 | 540 | 17 | 541 | 12 |
| 07ATTRD-38 | 544 | 11 | 546.2 | 9.7 | 557 | 20 | 544 | 11 |
| 07ATTRD-40 | 544.3 | 7.2 | 538 | 19 | 513 | 95 | 544.3 | 7.2 |
| 07ATTRD-8 | 549.5 | 8.4 | 544.4 | 8.8 | 523 | 30 | 549.5 | 8.4 |
| 07ATTRD-81 | 551 | 22 | 581 | 38 | 700 | 160 | 551 | 22 |
| 07ATTRD-61 | 562.2 | 7.0 | 558.3 | 6.1 | 542 | 12 | 562.2 | 7.0 |
| 07ATTRD-46 | 565 | 19 | 650 | 150 | 940 | 630 | 565 | 19 |
| 07ATTRD-74 | 567 | 15 | 567 | 13 | 569 | 25 | 567 | 15 |
| 07ATTRD-28 | 575 | 20 | 583 | 22 | 615 | 71 | 575 | 20 |
| 07ATTRD-100 | 612 | 26 | 612 | 28 | 612 | 89 | 612 | 26 |
| 07ATTRD-70 | 616 | 25 | 626 | 31 | 660 | 110 | 616 | 25 |
| 07ATTRD-5 | 628 | 14 | 631 | 12 | 642 | 23 | 628 | 14 |
| 07ATTRD-72 | 635 | 32 | 662 | 27 | 755 | 40 | 635 | 32 |
| 07ATTRD-95 | 642 | 11 | 640 | 11 | 633 | 28 | 642 | 11 |
| 07ATTRD-10 | 653 | 22 | 655 | 20 | 660 | 51 | 653 | 22 |
| 07ATTRD-76 | 663 | 17 | 668 | 25 | 683 | 94 | 663 | 17 |
| 07ATTRD-34 | 696 | 21 | 722 | 21 | 802 | 52 | 696 | 21 |
| 07ATTRD-6 | 730 | 41 | 788 | 33 | 955 | 21 | 730 | 41 |
| 07ATTRD-23 | 752 | 14 | 751 | 11 | 748 | 17 | 752 | 14 |
| 07ATTRD-51 | 774 | 31 | 799 | 24 | 872 | 16 | 774 | 31 |
| 07ATTRD-101 | 776 | 19 | 776 | 15 | 776 | 22 | 776 | 19 |
| 07ATTRD-14 | 790 | 24 | 796 | 19 | 816 | 25 | 790 | 24 |
| 07ATTRD-39 | 802 | 10 | 802.6 | 9.2 | 804 | 19 | 802 | 10 |
| 07ATTRD-1 | 869 | 41 | 870 | 43 | 870 | 110 | 869 | 41 |
| 07ATTRD-22 | 905 | 17 | 904 | 13 | 902 | 19 | 902 | 19 |
| 07ATTRD-86 | 941 | 24 | 937 | 22 | 928 | 50 | 928 | 50 |
| 07ATTRD-59 | 881 | 42 | 896 | 50 | 930 | 140 | 930 | 140 |
| 07ATTRD-79 | 949 | 19 | 945 | 14 | 935 | 16 | 935 | 16 |
| 07ATTRD-78 | 901 | 32 | 912 | 31 | 939 | 68 | 939 | 68 |
| 07ATTRD-105 | 913 | 19 | 924 | 15 | 950 | 22 | 950 | 22 |
| 07ATTRD-17 | 911 | 17 | 923 | 15 | 950 | 31 | 950 | 31 |
| 07ATTRD-2 | 990 | 22 | 978 | 38 | 950 | 120 | 950 | 120 |
| 07ATTRD-58 | 945.1 | 8.6 | 947 | 14 | 952 | 42 | 952 | 42 |
| 07ATTRD-35 | 962 | 19 | 959 | 18 | 953 | 40 | 953 | 40 |
| 07ATTRD-106 | 961 | 18 | 961 | 14 | 960 | 22 | 960 | 22 |
| 07ATTRD-69 | 946 | 22 | 953 | 27 | 968 | 73 | 968 | 73 |
| 07ATTRD-71 | 946 | 16 | 954 | 14 | 973 | 29 | 973 | 29 |
| 07ATTRD-88 | 993 | 19 | 987 | 15 | 974 | 24 | 974 | 24 |
| 07ATTRD-53 | 925 | 36 | 941 | 34 | 979 | 72 | 979 | 72 |
| 07ATTRD-49 | 834 | 17 | 876 | 20 | 984 | 56 | 984 | 56 |
| 07ATTRD-65 | 966 | 30 | 972 | 22 | 986 | 23 | 986 | 23 |
| 07ATTRD-77 | 961 | 24 | 971 | 39 | 990 | 110 | 990 | 110 |
| 07ATTRD-92 | 1023 | 22 | 1015 | 19 | 997 | 36 | 997 | 36 |
| 07ATTRD-64 | 1031 | 33 | 1023 | 25 | 1008 | 35 | 1008 | 35 |
| 07ATTRD-108 | 887 | 35 | 923 | 26 | 1011.1 | 9.4 | 1011.1 | 9.4 |
| 07ATTRD-56 | 1038 | 45 | 1030 | 36 | 1013 | 61 | 1013 | 61 |
| 07ATTRD-93 | 1019 | 22 | 1021 | 20 | 1024 | 41 | 1024 | 41 |
| 07ATTRD-54 | 1081 | 22 | 1082 | 18 | 1082 | 31 | 1082 | 31 |
| 07ATTRD-41 | 1132 | 15 | 1118 | 10 | 1089 | 12 | 1089 | 12 |

| | | | | | | | | |
|---|---|---|---|---|---|---|---|---|
| 07ATTRD-83 | 1103 | 23 | 1102 | 17 | 1099 | 21 | 1099 | 21 |
| 07ATTRD-63 | 1140 | 60 | 1133 | 43 | 1118 | 51 | 1118 | 51 |
| 07ATTRD-29 | 1167 | 19 | 1163 | 15 | 1154 | 24 | 1154 | 24 |
| 07ATTRD-15 | 1156 | 20 | 1164 | 14 | 1179 | 11 | 1179 | 11 |
| 07ATTRD-12 | 1171 | 16 | 1174 | 11 | 1179.9 | 9.5 | 1179.9 | 9.5 |
| 07ATTRD-87 | 1178 | 26 | 1198 | 19 | 1232 | 23 | 1232 | 23 |
| 07ATTRD-98 | 1247 | 24 | 1247 | 17 | 1247 | 22 | 1247 | 22 |
| 07ATTRD-52 | 1265 | 18 | 1281 | 14 | 1307 | 20 | 1307 | 20 |
| 07ATTRD-57 | 1494 | 21 | 1520 | 24 | 1555 | 49 | 1555 | 49 |
| 07ATTRD-37 | 1412 | 37 | 1512 | 24 | 1654 | 16 | 1654 | 16 |
| 07ATTRD-19 | 1804 | 72 | 1830 | 40 | 1860 | 24 | 1860 | 24 |
| 07ATTRD-26 | 1891 | 21 | 1883 | 13 | 1874 | 13 | 1874 | 13 |
| 07ATTRD-45 | 2000 | 49 | 2023 | 25 | 2046.4 | 4.3 | 2046.4 | 4.3 |
| 07ATTRD-107 | 2074 | 23 | 2089 | 12 | 2103.7 | 6.0 | 2103.7 | 6.0 |
| 07ATTRD-55 | 2240 | 140 | 2319 | 68 | 2388.6 | 6.6 | 2388.6 | 6.6 |
| 07ATTRD-36 | 2369 | 29 | 2404 | 14 | 2433.6 | 5.0 | 2433.6 | 5.0 |
| 07ATTRD-32 | 2320 | 120 | 2386 | 56 | 2439 | 16 | 2439 | 16 |
| 07ATTRD-42 | 2482 | 34 | 2474 | 19 | 2467 | 20 | 2467 | 20 |
| 07ATTRD-27 | 2298 | 51 | 2389 | 24 | 2467.4 | 4.1 | 2467.4 | 4.1 |
| 07ATTRD-24 | 2365 | 24 | 2424 | 12 | 2473.3 | 6.7 | 2473.3 | 6.7 |
| 07ATTRD-103 | 2381 | 47 | 2438 | 22 | 2486 | 4.9 | 2486 | 4.9 |
| 07ATTRD-73 | 2344 | 43 | 2424 | 20 | 2492.4 | 6.0 | 2492.4 | 6.0 |
| 07ATTRD-47 | 2365 | 45 | 2469 | 21 | 2554.7 | 3.7 | 2554.7 | 3.7 |
| 07ATTRD-9 | 2609 | 51 | 2670 | 24 | 2716 | 15 | 2716 | 15 |
| 07ATTRD-102 | 2841 | 55 | 2933 | 26 | 2996 | 20 | 2996 | 20 |
| 07ATTRD-31 | 2847 | 35 | 2953 | 15 | 3025.6 | 8.8 | 3025.6 | 8.8 |
| 07ATTRD-90 | 3350 | 120 | 3397 | 46 | 3426 | 6.3 | 3426 | 6.3 |
| | | | | | | | | |
| *TRE* | | | | | | | | |
| 07ATTRE-54 | 88.6 | 2.1 | 90.4 | 9.9 | 140 | 260 | 88.6 | 2.1 |
| 07ATTRE-75 | 1554 | 20 | 1584 | 11 | 1624.0 | 3.0 | 1624.0 | 3.0 |
| 07ATTRE-84 | 2536 | 61 | 2536 | 27 | 2534.9 | 4.4 | 2534.9 | 4.4 |
| 07ATTRE-66 | 571.0 | 4.6 | 579.2 | 5.1 | 611 | 17 | 571.0 | 4.6 |
| 07ATTRE-88 | 3403 | 57 | 3425 | 21 | 3437.6 | 5.4 | 3437.6 | 5.4 |
| 07ATTRE-112 | 550.1 | 5.5 | 552.8 | 7.5 | 564 | 31 | 550.1 | 5.5 |
| 07ATTRE-22 | 2388 | 43 | 2434 | 20 | 2471.6 | 6.1 | 2471.6 | 6.1 |
| 07ATTRE-97 | 350.6 | 6.6 | 358 | 10 | 408 | 63 | 350.6 | 6.6 |
| 07ATTRE-26 | 479.8 | 6.7 | 494.2 | 6.5 | 561 | 18 | 479.8 | 6.7 |
| 07ATTRE-78 | 519.1 | 6.8 | 525 | 11 | 552 | 48 | 519.1 | 6.8 |
| 07ATTRE-21 | 1129 | 18 | 1151 | 12 | 1191.4 | 7.3 | 1191.4 | 7.3 |
| 07ATTRE-64 | 2716 | 62 | 2720 | 27 | 2723.7 | 7.3 | 2723.7 | 7.3 |
| 07ATTRE-108 | 486.6 | 7.3 | 487 | 12 | 489 | 61 | 486.6 | 7.3 |
| 07ATTRE-29 | 2114 | 61 | 2272 | 31 | 2416.7 | 7.5 | 2416.7 | 7.5 |
| 07ATTRE-7 | 506.1 | 8.3 | 544 | 69 | 710 | 350 | 506.1 | 8.3 |
| 07ATTRE-81 | 1656 | 22 | 1645 | 13 | 1631.8 | 8.7 | 1631.8 | 8.7 |
| 07ATTRE-11 | 649.4 | 8.9 | 654.7 | 8.5 | 673 | 22 | 649.4 | 8.9 |
| 07ATTRE-40 | 551.1 | 9.0 | 552.0 | 8.8 | 556 | 25 | 551.1 | 9.0 |
| 07ATTRE-70 | 982 | 16 | 999 | 12 | 1036.2 | 9.1 | 1036.2 | 9.1 |
| 07ATTRE-80 | 2185 | 63 | 2165 | 31 | 2145.9 | 9.2 | 2145.9 | 9.2 |
| 07ATTRE-83 | 525.1 | 9.5 | 513 | 13 | 462 | 61 | 525.1 | 9.5 |
| 07ATTRE-79 | 577.2 | 9.7 | 570 | 17 | 540 | 75 | 577.2 | 9.7 |
| 07ATTRE-19 | 979 | 22 | 983 | 16 | 990 | 10 | 990 | 10 |
| 07ATTRE-33 | 655 | 10 | 669 | 11 | 719 | 36 | 655 | 10 |
| 07ATTRE-82 | 980 | 15 | 971 | 11 | 951 | 11 | 951 | 11 |
| 07ATTRE-35 | 528 | 11 | 546 | 24 | 620 | 110 | 528 | 11 |
| 07ATTRE-37 | 563 | 11 | 569 | 24 | 590 | 110 | 563 | 11 |
| 07ATTRE-114 | 950 | 20 | 954 | 14 | 965 | 12 | 965 | 12 |
| 07ATTRE-104 | 529 | 13 | 529 | 13 | 530 | 40 | 529 | 13 |
| 07ATTRE-109 | 495 | 13 | 500 | 23 | 520 | 110 | 495 | 13 |
| 07ATTRE-57 | 1726 | 13 | 1723.2 | 9.5 | 1720 | 14 | 1720 | 14 |
| 07ATTRE-105 | 1079 | 27 | 1115 | 19 | 1186 | 14 | 1186 | 14 |
| 07ATTRE-71 | 770 | 14 | 781 | 13 | 812 | 31 | 770 | 14 |
| 07ATTRE-58 | 527 | 14 | 537 | 38 | 580 | 190 | 527 | 14 |
| 07ATTRE-62 | 1174 | 29 | 1240 | 20 | 1358 | 15 | 1358 | 15 |
| 07ATTRE-14 | 882 | 15 | 888 | 13 | 905 | 23 | 882 | 15 |
| 07ATTRE-24 | 557 | 15 | 538 | 29 | 460 | 140 | 557 | 15 |
| 07ATTRE-89 | 558 | 15 | 548 | 29 | 510 | 140 | 558 | 15 |
| 07ATTRE-44 | 994 | 20 | 991 | 15 | 986 | 16 | 986 | 16 |
| 07ATTRE-17 | 516 | 16 | 539 | 26 | 640 | 120 | 516 | 16 |
| 07ATTRE-91 | 832 | 17 | 833 | 13 | 836 | 11 | 832 | 17 |

| | | | | | | | | |
|---|---|---|---|---|---|---|---|---|
| 07ATTRE-96 | 552 | 17 | 560 | 16 | 591 | 36 | 552 | 17 |
| 07ATTRE-2 | 537 | 17 | 538 | 19 | 541 | 66 | 537 | 17 |
| 07ATTRE-28 | 518 | 17 | 496 | 31 | 400 | 160 | 518 | 17 |
| 07ATTRE-32 | 985 | 25 | 984 | 18 | 983 | 18 | 983 | 18 |
| 07ATTRE-60 | 1080 | 46 | 1064 | 31 | 1030 | 18 | 1030 | 18 |
| 07ATTRE-53 | 815 | 18 | 835 | 15 | 889 | 25 | 815 | 18 |
| 07ATTRE-94 | 518 | 18 | 519 | 20 | 526 | 74 | 518 | 18 |
| 07ATTRE-1 | 497 | 18 | 495 | 60 | 480 | 330 | 497 | 18 |
| 07ATTRE-16 | 928 | 14 | 940 | 11 | 968 | 19 | 968 | 19 |
| 07ATTRE-90 | 882 | 19 | 890 | 16 | 909 | 26 | 882 | 19 |
| 07ATTRE-52 | 1061 | 58 | 1044 | 39 | 1011 | 20 | 1011 | 20 |
| 07ATTRE-36 | 702 | 20 | 774 | 32 | 990 | 100 | 702 | 20 |
| 07ATTRE-10 | 969 | 21 | 968 | 16 | 967 | 21 | 967 | 21 |
| 07ATTRE-86 | 500 | 21 | 477 | 82 | 370 | 480 | 500 | 21 |
| 07ATTRE-115 | 762 | 22 | 814 | 17 | 959 | 10 | 762 | 22 |
| 07ATTRE-55 | 939 | 26 | 937 | 19 | 933 | 22 | 933 | 22 |
| 07ATTRE-73 | 879 | 32 | 897 | 24 | 941 | 22 | 941 | 22 |
| 07ATTRE-46 | 429 | 23 | 457 | 21 | 598 | 21 | 429 | 23 |
| 07ATTRE-27 | 894 | 17 | 934 | 14 | 1030 | 23 | 1030 | 23 |
| 07ATTRE-25 | 516 | 23 | 498 | 35 | 420 | 160 | 516 | 23 |
| 07ATTRE-43 | 576 | 23 | 630 | 130 | 850 | 580 | 576 | 23 |
| 07ATTRE-34 | 594 | 25 | 598 | 21 | 614 | 18 | 594 | 25 |
| 07ATTRE-47 | 1196 | 38 | 1178 | 26 | 1146 | 25 | 1146 | 25 |
| 07ATTRE-111 | 594 | 26 | 593 | 21 | 590 | 25 | 594 | 26 |
| 07ATTRE-85 | 944 | 12 | 938 | 11 | 924 | 26 | 924 | 26 |
| 07ATTRE-113 | 920 | 13 | 930 | 12 | 952 | 26 | 952 | 26 |
| 07ATTRE-63 | 1113 | 25 | 1106 | 19 | 1093 | 26 | 1093 | 26 |
| 07ATTRE-13 | 1743 | 42 | 1740 | 25 | 1736 | 26 | 1736 | 26 |
| 07ATTRE-93 | 707 | 26 | 731 | 22 | 804 | 31 | 707 | 26 |
| 07ATTRE-95 | 501 | 26 | 487 | 42 | 420 | 210 | 501 | 26 |
| 07ATTRE-49 | 958 | 11 | 963 | 11 | 974 | 27 | 974 | 27 |
| 07ATTRE-39 | 1043 | 18 | 1037 | 15 | 1025 | 28 | 1025 | 28 |
| 07ATTRE-41 | 1024 | 53 | 1053 | 38 | 1112 | 28 | 1112 | 28 |
| 07ATTRE-20 | 463 | 29 | 500 | 130 | 650 | 690 | 463 | 29 |
| 07ATTRE-51 | 742 | 32 | 756 | 25 | 800 | 24 | 742 | 32 |
| 07ATTRE-72 | 504 | 35 | 529 | 33 | 638 | 77 | 504 | 35 |
| 07ATTRE-30 | 1032 | 23 | 1066 | 20 | 1135 | 38 | 1135 | 38 |
| 07ATTRE-92 | 1186 | 26 | 1181 | 22 | 1172 | 38 | 1172 | 38 |
| 07ATTRE-56 | 505 | 40 | 512 | 71 | 540 | 340 | 505 | 40 |
| 07ATTRE-4 | 1494 | 36 | 1523 | 27 | 1564 | 41 | 1564 | 41 |
| 07ATTRE-3 | 911 | 23 | 917 | 20 | 931 | 42 | 931 | 42 |
| 07ATTRE-61 | 527 | 44 | 608 | 71 | 920 | 270 | 527 | 44 |
| 07ATTRE-18 | 932 | 30 | 945 | 25 | 976 | 47 | 976 | 47 |
| 07ATTRE-106 | 1399 | 50 | 1487 | 37 | 1614 | 48 | 1614 | 48 |
| 07ATTRE-5 | 815 | 51 | 835 | 38 | 891 | 13 | 815 | 51 |
| 07ATTRE-103 | 970 | 49 | 1060 | 40 | 1251 | 53 | 1251 | 53 |
| 07ATTRE-77 | 827 | 54 | 856 | 43 | 932 | 58 | 827 | 54 |
| 07ATTRE-76 | 1171 | 71 | 1242 | 52 | 1367 | 55 | 1367 | 55 |
| 07ATTRE-6 | 902 | 15 | 919 | 23 | 960 | 69 | 960 | 69 |
| 07ATTRE-74 | 973 | 46 | 982 | 42 | 1003 | 85 | 1003 | 85 |
| 07ATTRE-48 | 1074 | 23 | 1106 | 36 | 1168 | 96 | 1168 | 96 |
| 07ATTRE-65 | 981 | 22 | 1016 | 45 | 1090 | 130 | 1090 | 130 |

[3]Analyses with >10% uncertainty (1σ) in $^{206}Pb/^{238}U$ age are not included. Analyses with >10% uncertainty (1σ) in $^{206}Pb/^{207}Pb$ are not included, unless $^{206}Pb/^{238}U$ age is <500 Ma. Best age is determined from $^{206}Pb/^{238}U$ age for analyses with $^{206}Pb/^{238}U$ age <1000 Ma and from $^{206}Pb/^{207}Pb$ age for analyses with $^{206}Pb/^{238}U$ age >1000 Ma.

# APPENDIX F

# CHAPTER 3 SUPPLEMENT:

# ZHE DATA

Table A3.3. ZHe data

| Sam. name | [$^{4}$He][1] | [$^{238}$U][1] | [$^{232}$Th][1] | Age$_R$[2] | R1[3] | R2[3] | L[3] | T1[3] | T2[3] | $F_T$[4] | Age$_C$[5] | Err. |
|---|---|---|---|---|---|---|---|---|---|---|---|---|
| | | | | (Ma) | (μm) | (μm) | (μm) | (μm) | (μm) | | (Ma) | (2σ)[6] |
| *07-AT-TR-B (34°16'42.37"N, 77°10'55.24"E)* | | | | | | | | | | | | |
| z003 | 0.0977 | 2.1164 | 0.6475 | 24.98 | 38.7 | 38.7 | 138.0 | - | - | 0.745 | 33.5 | 1.9 |
| z004 | 0.3352 | 4.4538 | 3.4689 | 38.76 | 46.2 | 46.2 | 165.5 | - | - | 0.782 | 49.6 | 2.3 |
| z005 | 0.1311 | 1.8270 | 0.4837 | 35.65 | 29.3 | 32.3 | 144.3 | 39.6 | 33.4 | 0.678 | 52.6 | 1.7 |
| *07-AT-TR-D (34°16'30.33"N, 77°11'0.05"E)* | | | | | | | | | | | | |
| z001 | 0.2057 | 3.3611 | 1.7031 | 32.41 | 47.0 | 43.1 | 152.1 | 34.2 | 31.7 | 0.761 | 42.6 | 1.5 |
| z002 | 0.2036 | 4.4802 | 0.8736 | 23.45 | 37.1 | 28.7 | 137.4 | 33.1 | 27.4 | 0.692 | 33.9 | 1.3 |
| z003 | 0.2452 | 4.1966 | 2.9763 | 29.05 | 46.2 | 40.1 | 138.2 | 40.4 | 24.6 | 0.744 | 39.1 | 1.3 |
| z004 | 0.1545 | 3.3536 | 1.4554 | 24.26 | 44.1 | 40.3 | 147.8 | 34.9 | 40.0 | 0.744 | 32.6 | 1.1 |
| z005 | 0.3861 | 6.6678 | 1.8788 | 29.63 | 39.6 | 28.7 | 135.7 | 19.3 | 29.2 | 0.701 | 42.3 | 1.4 |
| *07-AT-TR-E (34°16'32.99"N, 77°11'0.47"E)* | | | | | | | | | | | | |
| z001 | 0.7267 | 13.868 | 0.2595 | 29.46 | 37.9 | 31.5 | 187.7 | 32.6 | 32.4 | 0.726 | 40.6 | 1.4 |
| z003 | 0.0580 | 1.0095 | 0.2226 | 28.20 | 28.9 | 57.3 | 83.9 | 27.6 | 29.3 | 0.663 | 42.5 | 1.9 |
| z004 | 0.1381 | 2.5226 | 0.6938 | 26.29 | 32.8 | 28.1 | 104.9 | 20.8 | 29.3 | 0.656 | 40.1 | 1.5 |
| z005 | 0.1078 | 1.6384 | 1.2416 | 26.83 | 30.3 | 26.8 | 86.3 | 24.5 | 22.5 | 0.616 | 43.6 | 1.7 |
| *08-AT-ST-B (34°17'8.13"N, 77°10'0.69"E)* | | | | | | | | | | | | |
| z001 | 0.3042 | 6.4837 | 6.5190 | 24.73 | 62.7 | 76.7 | 226.3 | 62.3 | 55.4 | 0.835 | 29.6 | 1.1 |
| z002 | 2.4364 | 39.734 | 52.068 | 30.53 | 59.3 | 64.9 | 282.4 | 48.3 | 42.7 | 0.834 | 36.6 | 1.3 |
| z003 | 0.9821 | 15.995 | 35.829 | 26.13 | 61.5 | 67.4 | 259.7 | 70.1 | 50.4 | 0.830 | 31.5 | 1.2 |
| z004 | 1.8170 | 40.098 | 26.753 | 25.49 | 61.4 | 61.1 | 298.8 | 55.0 | 65.3 | 0.834 | 30.6 | 1.1 |
| z005 | 0.6335 | 9.8403 | 7.5803 | 34.76 | 52.1 | 52.7 | 347.0 | 40.6 | 55.3 | 0.818 | 42.5 | 1.4 |
| z006 | 1.1434 | 27.901 | 14.327 | 24.00 | 94.3 | 56.1 | 234.7 | 47.7 | 60.2 | 0.842 | 28.5 | 1.0 |
| z007 | 0.1070 | 1.8848 | 1.4750 | 27.38 | 39.0 | 37.2 | 157.0 | 29.1 | 36.0 | 0.732 | 37.4 | 1.2 |
| z008 | 0.2835 | 5.0716 | 4.1451 | 29.07 | 47.7 | 47.4 | 274.3 | 41.7 | 55.4 | 0.795 | 36.6 | 1.6 |

[1]Absolute measured $^{4}$He, $^{238}$U and $^{232}$Th concentrations are used to calculate the 'Raw Age' that is uncorrected for the effects of $^{4}$He loss due to alpha particle recoil. Measured in pmoles

[2]The 'Raw Age' was calculated with an iterative approach to solving the age equation.

[3]R1 and R2 describe the perpendicular half widths of the zircon crystal. L describes the total length of the zircon crystal and T1 and T2 describe the height of the pyramidal termination of the zircon crystals.

[4]The mean FT correction was calculated following procedures defined by Hourigan et al. (2005).

[5]The FT corrected age of the crystal. The FT correction was applied to the raw age following procedures defined by Farley et al. (1996).

[6]The propagated 1σ and 2σ analytical errors.

**REFERENCES**

Farley, K. A. R. A. Wolf, and L. T. Silver (1996), The effects of long alpha-stopping distances on (U-Th)/He ages, *Geochim. Cosmochim. Acta, 60,* 4223-4229.

Hourigan, J.K., P. W. Reiners, and M. T. Brandon (2005), U-Th zonation-dependent alpha-ejection, *Geochim. Cosmochim. Acta, 69*, 3349-3365.

# APPENDIX G

# CHAPTER 3 SUPPLEMENT:

# CITATIONS FOR FIGURE 3.2

Table A3.4. Sources for Eurasian Oligocene and older U-Pb zircon data.

| Citation | Region | Number of Dates |
|---|---|---|
| Booth et al., 2003 | Lhasa, Gangdese | 231 |
| Chiu et al., 2009 | Lhasa | 24 |
| Chu et al., 2006 | Lhasa, Gangdese | 77 |
| Chung et al., 2003 | Lhasa | 1 |
| Dong et al., 2005 | Gangdese | 4 |
| Dong et al., 2011 | Qiantang | 138 |
| Dong et al., 2011b | Lhasa | 50 |
| Dunap and Wysoczanski, 2002 | Ladakh | 33 |
| Fraser et al., 2001 | Karakoram | 4 |
| Guynn et al., 2006 | Lhasa | 9 |
| Harrison et al., 2000 | Gangese | 3 |
| He et al., 2007 | Gangdese | 161 |
| Honegger et al., 1982 | Ladakh | 1 |
| Hu et al., 2003 | Gangese | 2 |
| Jain and Singh, 2008 | Karakroram | 9 |
| Ji et al., 2009 | Gangese | 42 |
| Kapp et al., 2005 | Lhasa | 60 |
| Krol et al., 1996 | Kohistan | 1 |
| Le Fort, 1983 | Karakoram | 1 |
| Leier et al., 2007 | Lhasa | 729 |
| Leloup et al., 2011 | Karakoram | 2 |
| McDermid et al., 2002 | Lhasa | 6 |
| Miller et al., 2000 | Gangese | 2 |
| Mo et al., 2005 | Gangese | 6 |
| Murphy et al., 1997 | Lhasa | 2 |
| Parrish and Tirrul, 1989 | Karakoram | 22 |
| Pullen et al., 2008 | Qiantang | 432 |
| Quidelleur et al., 1997 | Lhasa | 12 |
| Ravikant et al., 2009 | Ladakh | 12 |
| Schaltagger et al., 2002 | Kohistan | 5 |
| Scharer et al., 1984 | Ladakh | 26 |
| Scharer et al., 1984b | Gangdese | 11 |
| Scharer et al., 1990 | Karakoram | 4 |
| Searle et al., 1989 | Karakoram | 1 |
| Searle et al., 1990 | Karakoram | 5 |
| Searle et al., 1998 | Karakoram | 39 |
| Singh et al., 2007 | Ladakh | 2 |
| St Onge et al., 2010 | Ladakh | 2 |
| Upadhyay et al., 2008 | Ladakh | 5 |
| Volkmer et al., 2007 | Lhasa | 23 |
| Weinberg and Dunlap, 2000 | Ladakh | 3 |
| Weinberg et al., 2000 | Karakoram | 1 |
| Wen et al., 2008 | Gangdese | 25 |
| Xu et al., 1985 | Lhasa | 44 |
| Zhu et al., 2011 | Qiangtang, Lhasa | 507 |

## REFERENCES


Booth, A. L., Zeitler, P. K., Kidd, W. S. F., Wooden, J., Liu, Y., Idleman, B., Hren, M., and Chamberlain, C. P., 2004, U-Pb zircon constraints on the tectonic evolution of the southeastern Tibet, Namche Barwa area: American Journal of Science, v. 304, p. 889-929.

Chiu, H.-Y., Chung, S.-L., Wu, F.-Y., Liu, D., Liang, Y.-H., Lin, I.-J., Iizuka, Y., Xie, L.-W., Wang, Y., and Chu, M.-F., 2009, Zircon U-Pb and Hf isotopic constraints from eastern Transhimalayan batholiths on the precollisional magmatic and tectonic evolution in southern Tibet: Tectonophysics, v. 477, p. 3-19.

Chu, M. F., Chung, S. L., Song, B., Liu, Y., O'Reilly, S. Y., Pearson, N. J., Ji, J.Q., and Wen, D. J., 2006, Zircon U-Pb and Hf isotope constraints on the Mesozoic tectonics and crustal evolution of southern Tibet, Geology, v. 34, p. 745-748.

Chung, S.-L., Liu, D., Ji, J., Chu, M.-F., Lee, H.-Y., Wen, D.-J., Lo, C.-H., Lee, T.-Y., Qian, Q., and Zhang, Q., 2003, Adakites from continental collision zones: melting of thickened lower crust beneath southern Tibet: Geology, v. 31, p. 1021-1024.

Dong, G. C., Mo, X. X., Zhao, Z. D., Guo, T. Y., Wang, L. L., and Chen, T., 2005, Geochronologic constraints on the magmatic underplating of the Gangdese belt in the India-Eurasia collision: Evidence of SHRIMP II zircon U-Pb dating: Acta Geologica Sinica, v. 79, p. 787-794.

Dong, C. Y., Li, C., Wan, Y. S., Wang, W., Wu, Y. W., Xie, H. Q., and Liu, D. Y., 2011, Detrital zircon age model of Ordovician Wenquan quartzite south of Lungmuco-Shuanghu suture in the Qiantang area, Tibet: Constraint on tectonic affinity and source regions: Science China, Earth Sciences, doi: 10.1007/s11430-010-41660x.

Dong, X., Zhang, Z., Liu, F., Wang, W., Yu, F., and Shen, K., 2011, Zircon U-Pb geochronology of the Nyainqentanglha Group from the Lhasa terrane: New constraints on the Triassic orogeny of the south Tibet: Journal of Asian Earth Sciences, v. 42, p. 732-739.

Dunlap, W. J. and Wysoczanski, R., 2002, Thermal evidence for early Cretaceous metamorphism in the Shyok suture zone and age of the Khardung volcanic rocks, Ladakh, India: Journal of Asian Earth Sciences, v. 20, p. 481-490.

Fraser, J. E., Searle, M. P., Parrish, R. R., and Noble, S. R., 2001, Chronology of deformation, metamorphism and magmatism in the southern Karakoram Mountains: Geological Society of America Bulletin, v. 113, p. 1443-1455.

Guynn, J. H., Kapp, P., Pullen, A., Heizler, M., Gehrels, G., and Ding, L., 2006, Tibetan basement rocks near Amdo reveal "missing" Mesozoic tectonism along the Bangong suture, central Tibet: Geology, v. 34, p. 505-508.

Harrison, T. M., Yin, A., Grove, M., Lovera, O., Ryerson, F. J., and Zhou, X., 2000, The Zedong Window: A record of superposed Tertiary convergence in southeastern Tibet: Journal of Geophysical Research, v. 105, p. 19211-19230.

He, S., Kapp, P., DeCelles, P. G., Gehrels, G. E., and Heizler, M., 2007, Cretaceous-Tertiary geology of the Gangdese Arc in the Linzhou area, southern Tibet: Tectonophysics, v. 433, p. 15-37.

Honegger, K., Dietrich, V., Frank, W., Gansser, A., Thöni, M., and Trommsdorff, V., 1982, Magmatism and metamorphism in the Ladakh Himalayas (The Indus-Tsangpo suture zone): Earth and Planetary Science Letters, v. 60, p. 253-292.

Hu, D. G., Wu, Z. H., Ye, P. S., and Jiang, W., 2003, SHRIMP U-Pb ages of zircons from dioritic gneiss in the Nyainqentanglha Mountains, Tibet: Geological Bulletin of China, v. 22, p. 936-940.

Jain, A. K. and Singh, S., 2008, Tectonics of the southern Asian Plate margin along the Karakoram Shear Zone: Constraints from field observations and U–Pb SHRIMP ages: Tectonophysics, v. 451, p. 186-205.

Ji, W.-Q., Wu, F.-Y., Chung, S.-L., Li, J.-X., and Liu, C.-Z., 2009, Zircon U-Pb geochronology and Hf isotopic constraints on petrogenesis of the Gangdese batholith, southern Tibet: Chemical Geology, v. 262, p. 229-245.

Kapp, J. L. D., Harrison, T. M., Kapp, P., Grove, M., Lovera, O. M., and Lin, D., 2005, Nyainqentanglha Shan: A window into the tectonic, thermal and geochemical evolution of the Lhasa block, southern Tibet: Journal of Geophysical Research, v. 110, B08413, doi: 10.1029/2004JB003330.

Krol, M. A., Zeitler, P. K., and Copeland, P., 1996, Episodic unroofing of the Kohistan Batholith, Pakistan: Implications from K-feldspar thermochronology: Journal of Geophysical Research, v. 101, p. 28149-28164.

Le Fort, P., Michard, A., Sonet, J., and Zimmerman, J. L., 1983, Petrography, geochemistry and geochronology of some samples from the Karakoram axial batholith (northern Pakistan), *in* Shams, F. A., ed., Granites of Himalayas, Karakorum and Hindu Kush: Lahore, Pakistan Punjab University, Institute of Geology, p. 377-387.

Leier, A. L., Kapp, P., Gehrels, G. E., and DeCelles, P. G., 2007, Detrital zircon geochronology of Carboniferous-Cretaceous strata in the Lhasa terrane, southern Tibet: Basin Research, v. 19, p. 361-378, doi: 10.111/j.1365-2117.2007.00330.x.

Leloup, P. H., Boutonnet, E., Davis, W. J., and Hattori, K., 2011, Long-lasting intracontinental strike-slip faulting: new evidence fro the Karakorum shear zone in the Himalayas: Terra Nova, v. 23, p. 92-99.

McDermid, I. R. C., Aitchison, J. C., Davis, A. M., Harrison, T. M., and Grove, M., 2002, The Zedong terrane: a late Jurassic intra-oceanic magmatic arc within the Yarlung-Tsangpo suture zone, southeastern Tibet: Chemical Geology, v. 187, p. 267-277.

Miller, C., Schuster, R., Klötzli, U., and Frank, W., 2000, Late Cretaceous-Tertiary magmatic and tectonic events in the Transhimalaya batholith (Kailas area, SW Tibet): Schweizerische Mineralogische und Petrographische Mitteilungen, v. 80, p. 1-20.

Mo, X. X., Dong, G. C., Zhao, Z. D., Guo, T. Y., Wang, L. L., and Chen, T., 2005, Timing of magma mixing in Gangdise magmatic belt during the India-Asia collision: Zircon U-Pb dating: Acta Geologica Sinica, v. 25, p. 719-722.

Murphy, M. A., Yin, A., Harrison, T. M., Durr, S. B., Kidd, W. S. F., Chen, Z., Ryerson, F. J., Wang, X., and Zhou, X., 1997, Significant crustal shortening in south-central Tibet prior to the Indo-Asia collision: Geology, v. 25, p. 719-722.

Parrish, R. R., and Tirrul, R., 1989, U-Pb age of the Baltoro granite, northwest Himalaya, and implications for monazite U-Pb systematics: Geology, v. 17, p. 1076-1079.

Pullen, A., Kapp P., Gehrels, G. E., Vervoort, J. D., and Ding, L., 2008, Triassic continental subduction in central Tibet and Mediterranean-style closure of the Paleo-Tethys Ocean: Geology, v. 36, p. 351-354.

Quidelleur, X., Grove, M., Lovera, O. M., Harrison, T. M., Yin, A., and Ryerson, F. J., 1997, Thermal evolution and slip history of the Renbu-Zedong

thrust, southeastern Tibet: Journal of Geophysical Research, v. 102, p. 2659-2679.

Ravikant, V., Wu, F.-Y., and Ji, W.-Q., 2009, Zircon U-Pb and Hf isotopic constraints on petrogenesis of the Cretaceous-Tertiary granites in eastern Karakoram and Ladakh, India: Lithos, v. 110, p. 153-166.

Schaltegger, U., Zeilinger, G., Frank, M., and Burg, J. P., 2002, Multiple mantle sources during island arc magmatism: U-Pb and Hf isotopic evidence from the Kohistan arc complex, Pakistan: Terra nova, v. 14, p. 461-468.

Schärer, U., Hamet, J., and Allégre, C. J., 1984, The Transhimalaya (Gangdese) plutonism in the Ladakh region: U-Pb and Rb-Sr study: Earth and Planetary Science Letters, v. 67, p. 327-339.

Schärer, U., Xu, R.-H., and Allégre, C. J., 1984, U-Pb geochronology of Gangdese (Transhimalaya) plutonism in the Lhasa-Xigaze region, Tibet: Earth and Planetary Science Letters, v. 69, p. 311-320.

Schärer, U., Copeland, P., Harrison, T. M., and Searle, M. P., 1990, Age, cooling history and origin of post-collisional leucogranite in the Karakoram batholith: A multi-system isotope study: Journal of Geology, v. 98, p. 233-251.

Searle, M. P., Rex, A. J., Tirrul, R., Rex, D. C., Barnicoat, A., and Windley, B. F., 1989, Metamorphic, magmatic and tectonic evolution of the Central Karakoram in the Biafo-Baltoro-Hushe regions of northern Pakistan: Geological Society of America, Special Paper 232, p. 47-73.

Searle, M. P., Parrish, R. R., Tirrul, R., and Rex, D. C., 1990, Age of crystallization and cooling of the K2 gneiss in the Baltoro Karakoram: Journal of the Geological Society of London, v. 147, p. 603-606.

Searle, M. P., Weinberg, R. F., and Dunlap, W. J., 1998, Transpressional tectonics along the Karakoram fault zone, northern Ladakh: Constraints on Tibetan extrusion, *in* Holdsworth, R. E., Strachan, R. A., and Dewey, J. F., eds., Continental Transpressional and Transtensional Tectonics: Geological Society of London Special Publication 135, p. 307-325.

Singh, S., Kumar, R., Barley, M. E., and Jain, A .K., 2007, SHRIMP U-Pb ages and depth of emplacement of Ladakh Batholith, Eastern Ladakh, India: Journal of Asian Earth Sciences, v. 30, p. 490-503.

St-Onge, M. R., Rayner, N., and Searle, M. P., 2010, Zircon age determinations of the Ladakh batholith at Chumathang (Northwest India): Implications for

the age of the India-Asia collision in the Ladakh Himalaya: Tectonophysics, v. 495, p. 171-183.

Upadhyay, R., Frisch, W., and Siebel, W., 2008, Tectonic implications of new U-Pb zircon ages of the Ladakh batholith, Indus suture zone, northwest Himalaya, India: Terra Nova, v. 20, p. 309-317.

Volkmer, J. E., Kapp, P., Guynn, J. H., and Lai, Q., 2007, Cretaceous-Tertiary structural evolution of the north central Lhasa terrane, Tibet: Tectonics, v. 26, TC6007, doi:10.1029/2005TC001832.

Weinberg, R. F. and Dunlap, W. J., 2000, Growth and deformation of the Ladakh Batholith, Northwest Himalayas: Implications for timing of continental collision and origin of calc-alkaline batholiths: Journal of Geology, v. 108, p. 303-320.

Weinberg, R. F., Dunlap, W. J., and Whitehouse, M., 2000, New field, structural and geochronological data from the Shyok and Nubra valleys, northern Ladakh: Linking Kohistan to Tibet, *in* Khan, M. A., Treloar, P. J., Searle, M. P. and Jan, M. Q., eds., Tectonics of the Nanga Parbat Syntaxis and the Western Himalaya: London, Geological Society of London Special Publication 170, p. 253-275.

Wen, D.-R., Liu, D., Chung, S.-L., Chu, M.-F., Ji, J., Zhang, Q., Song, B., Lee, T.-Y., Yeh, M.-W., and Lo, C.-H., 2008, Zircon SHRIMP U-Pb ages of the Gangdese Batholith and implications for Neotethyan subduction in southern Tibet: Chemical Geology, v. 252, p. 191-201.

Xu, R.-H., Schärer, U., and Allégre, C. J., 1985, Magmatism and metamorphism in the Lhasa Block (Tibet): a geochronological study: Journal of Geology, v. 93, p. 41-57.

Zhu, D.-C., Zhao, Z.-D., Niu, Y., Dilek, Y., and Mo, X.-X., 2011, Lhasa terrane in southern Tibet came from Australia: Geology, v. 39, p. 727-730.

# APPENDIX H

## CHAPTER 4 SUPPLEMENT:

## U-PB DATA FOR QUARTZITE CLASTS

Table A4.1a. U-Pb geochronologic analyses of zircons from quartzite clasts, raw data.

| Analysis | U[1] (ppm) | $^{206}Pb/^{204}Pb^{2}$ | U/Th[1] | Isotope ratios | | | | | | error corr. |
|---|---|---|---|---|---|---|---|---|---|---|
| | | | | $^{206}Pb^{*}/^{207}Pb^{*}$ | ± (%) | $^{207}Pb^{*}/^{235}U$ | ± (%) | $^{206}Pb^{*}/^{238}U$ | ± (%) | |
| *09-AT-LM-Y* | | | | | | | | | | |
| 09ATLMY17 | 850 | 8426468 | 3.1 | 18.8594 | 2.6 | 0.2366 | 2.9 | 0.0324 | 1.4 | 0.48 |
| 09ATLMY72 | 801 | 4554025 | 1.8 | 17.6529 | 1.6 | 0.5564 | 1.7 | 0.0712 | 0.7 | 0.40 |
| 09ATLMY40 | 273 | 682520 | 1.5 | 19.8946 | 3.6 | 0.2312 | 4.0 | 0.0334 | 1.8 | 0.44 |
| 09ATLMY10 | 114 | 365779 | 0.8 | 20.3798 | 11.0 | 0.2012 | 11.3 | 0.0297 | 2.4 | 0.21 |
| 09ATLMY107 | 1071 | 6932424 | 1.7 | 17.3241 | 1.0 | 0.6586 | 1.4 | 0.0827 | 1.0 | 0.69 |
| 09ATLMY83 | 311 | 385572 | 1.3 | 17.0132 | 9.4 | 0.2798 | 9.7 | 0.0345 | 2.4 | 0.25 |
| 09ATLMY89 | 844 | 2475414 | 7.0 | 19.9383 | 0.8 | 0.2395 | 2.7 | 0.0346 | 2.5 | 0.95 |
| 09ATLMY48 | 68 | 369555 | 0.8 | 20.6751 | 4.9 | 0.2252 | 5.6 | 0.0338 | 2.7 | 0.48 |
| 09ATLMY64 | 255 | 886579 | 0.7 | 19.8833 | 2.0 | 0.2331 | 3.4 | 0.0336 | 2.7 | 0.80 |
| 09ATLMY41 | 302 | 522917 | 2.6 | 19.2536 | 3.4 | 0.2157 | 4.6 | 0.0301 | 3.1 | 0.67 |
| 09ATLMY65 | 296 | 746945 | 1.9 | 19.6510 | 2.0 | 0.2295 | 3.6 | 0.0327 | 3.0 | 0.84 |
| 09ATLMY28 | 698 | 986707 | 1.9 | 19.7548 | 2.4 | 0.2702 | 3.7 | 0.0387 | 2.8 | 0.75 |
| 09ATLMY101 | 212 | 486899 | 2.3 | 18.0119 | 3.6 | 0.4088 | 4.1 | 0.0534 | 2.0 | 0.49 |
| 09ATLMY49 | 327 | 1061045 | 1.7 | 19.8822 | 8.8 | 0.2243 | 9.5 | 0.0323 | 3.4 | 0.36 |
| 09ATLMY79 | 1065 | 2073124 | 2.5 | 15.6397 | 0.7 | 1.0081 | 1.3 | 0.1143 | 1.1 | 0.84 |
| 09ATLMY33 | 208 | 947627 | 1.2 | 15.6565 | 0.6 | 1.0874 | 1.2 | 0.1235 | 1.1 | 0.88 |
| 09ATLMY36 | 660 | 744763 | 1.9 | 17.3160 | 1.9 | 0.6471 | 2.5 | 0.0813 | 1.6 | 0.63 |
| 09ATLMY73 | 224 | 438525 | 0.7 | 17.9009 | 4.0 | 0.6244 | 4.4 | 0.0811 | 1.8 | 0.41 |
| 09ATLMY52 | 297 | 834351 | 1.6 | 17.1850 | 1.6 | 0.6794 | 2.4 | 0.0847 | 1.9 | 0.76 |
| 09ATLMY45 | 295 | 904168 | 1.7 | 17.1154 | 2.6 | 0.6503 | 3.3 | 0.0807 | 2.0 | 0.61 |
| 09ATLMY24 | 349 | 851925 | 6.6 | 17.1239 | 2.5 | 0.6711 | 3.1 | 0.0833 | 1.9 | 0.62 |
| 09ATLMY59 | 219 | 114240 | 3.7 | 17.2854 | 7.5 | 0.7501 | 7.8 | 0.0940 | 2.0 | 0.26 |
| 09ATLMY44 | 3038 | 830106 | 10.8 | 15.9863 | 2.4 | 0.8736 | 3.1 | 0.1013 | 2.0 | 0.63 |
| 09ATLMY-2 | 250 | 69215 | 2.3 | 18.3508 | 12.6 | 0.6731 | 12.8 | 0.0896 | 2.3 | 0.18 |
| 09ATLMY20 | 1263 | 1119298 | 4.4 | 12.7453 | 0.7 | 1.9654 | 1.4 | 0.1817 | 1.2 | 0.86 |
| 09ATLMY99 | 93 | 208847 | 2.0 | 16.3455 | 10.5 | 0.7421 | 10.8 | 0.0880 | 2.4 | 0.22 |
| 09ATLMY90 | 523 | 945069 | 5.7 | 12.2091 | 0.6 | 2.2791 | 1.3 | 0.2018 | 1.2 | 0.90 |
| 09ATLMY82 | 529 | 1298895 | 1.0 | 18.6661 | 6.7 | 0.4848 | 7.5 | 0.0656 | 3.3 | 0.44 |
| 09ATLMY11 | 1512 | 3413043 | 3.7 | 13.4703 | 1.4 | 1.6514 | 2.0 | 0.1613 | 1.5 | 0.74 |
| 09ATLMY19 | 156 | 867496 | 2.7 | 14.2935 | 1.2 | 1.3901 | 2.0 | 0.1441 | 1.7 | 0.82 |
| 09ATLMY102 | 648 | 1232207 | 1.2 | 12.5031 | 1.5 | 2.2215 | 2.0 | 0.2015 | 1.3 | 0.64 |
| 09ATLMY14 | 56 | 33787 | 0.6 | 22.8703 | 27.8 | 0.5237 | 27.9 | 0.0869 | 2.8 | 0.10 |
| 09ATLMY51 | 241 | 492482 | 5.6 | 16.5359 | 0.9 | 0.7616 | 3.0 | 0.0913 | 2.9 | 0.95 |
| 09ATLMY22 | 1092 | 1565769 | 2.0 | 12.5190 | 1.9 | 2.1912 | 2.4 | 0.1990 | 1.5 | 0.62 |
| 09ATLMY67 | 562 | 291077 | 2.8 | 18.9741 | 6.0 | 0.3807 | 7.8 | 0.0524 | 5.0 | 0.65 |
| 09ATLMY98 | 121 | 627307 | 1.6 | 17.2863 | 3.5 | 0.7004 | 4.7 | 0.0878 | 3.1 | 0.67 |
| 09ATLMY23 | 505 | 989997 | 3.4 | 10.2589 | 0.7 | 3.6369 | 1.6 | 0.2706 | 1.4 | 0.90 |
| 09ATLMY29 | 432 | 654505 | 2.8 | 13.2043 | 1.5 | 1.7891 | 2.6 | 0.1713 | 2.1 | 0.81 |
| 09ATLMY71 | 144 | 399522 | 0.6 | 13.1641 | 1.7 | 1.8040 | 2.8 | 0.1722 | 2.2 | 0.78 |
| 09ATLMY7 | 598 | 525559 | 2.4 | 12.7454 | 2.1 | 2.0161 | 3.0 | 0.1864 | 2.0 | 0.69 |
| 09ATLMY12 | 370 | 621963 | 2.5 | 12.5190 | 1.0 | 1.7599 | 2.6 | 0.1598 | 2.4 | 0.92 |
| 09ATLMY74 | 289 | 257552 | 1.9 | 14.4776 | 1.1 | 1.3718 | 2.8 | 0.1440 | 2.6 | 0.93 |
| 09ATLMY87 | 632 | 599210 | 1.2 | 10.2624 | 0.8 | 3.7038 | 1.9 | 0.2757 | 1.7 | 0.91 |
| 09ATLMY100 | 288 | 806454 | 0.9 | 13.3915 | 0.5 | 1.7786 | 2.6 | 0.1727 | 2.5 | 0.98 |
| 09ATLMY5 | 180 | 754856 | 1.4 | 9.6623 | 0.9 | 4.1820 | 2.0 | 0.2931 | 1.7 | 0.88 |
| 09ATLMY68 | 235 | 380287 | 2.1 | 10.1751 | 1.6 | 3.5645 | 2.6 | 0.2631 | 2.0 | 0.77 |
| 09ATLMY-3 | 390 | 1185756 | 3.5 | 14.1149 | 1.2 | 1.4614 | 3.4 | 0.1496 | 3.1 | 0.93 |
| 09ATLMY109 | 196 | 250239 | 1.1 | 12.4145 | 0.8 | 2.2858 | 2.6 | 0.2058 | 2.4 | 0.95 |
| 09ATLMY39 | 90 | 396589 | 3.7 | 14.6493 | 1.6 | 1.0735 | 4.4 | 0.1141 | 4.1 | 0.93 |
| 09ATLMY93 | 127 | 230561 | 1.3 | 14.8277 | 1.5 | 1.1861 | 4.2 | 0.1276 | 3.9 | 0.93 |
| 09ATLMY42 | 151 | 120222 | 1.3 | 10.7887 | 3.2 | 3.1465 | 3.9 | 0.2462 | 2.3 | 0.58 |
| 09ATLMY86 | 155 | 334076 | 1.2 | 11.1488 | 2.0 | 2.9752 | 3.1 | 0.2406 | 2.4 | 0.76 |
| 09ATLMY88 | 78 | 128618 | 1.2 | 13.4931 | 2.0 | 1.6621 | 3.8 | 0.1627 | 3.3 | 0.85 |
| 09ATLMY56 | 754 | 677714 | 1.4 | 12.8847 | 2.5 | 1.9027 | 4.1 | 0.1778 | 3.2 | 0.79 |

| | | | | | | | | | | |
|---|---|---|---|---|---|---|---|---|---|---|
| 09ATLMY15 | 175 | 734424 | 2.0 | 8.3461 | 0.2 | 5.5415 | 1.9 | 0.3354 | 1.9 | 1.00 |
| 09ATLMY21 | 252 | 866118 | 1.8 | 14.0394 | 0.6 | 1.5954 | 3.6 | 0.1624 | 3.5 | 0.99 |
| 09ATLMY104 | 453 | 264166 | 17.4 | 12.5202 | 1.6 | 2.0819 | 3.7 | 0.1890 | 3.3 | 0.90 |
| 09ATLMY62 | 1254 | 408996 | 1.3 | 12.1664 | 1.0 | 2.3436 | 3.4 | 0.2068 | 3.2 | 0.95 |
| 09ATLMY78 | 276 | 170863 | 1.5 | 12.6886 | 0.9 | 1.7987 | 4.0 | 0.1655 | 3.9 | 0.97 |
| 09ATLMY31 | 1138 | 457142 | 1.1 | 10.6038 | 0.4 | 2.7662 | 3.2 | 0.2127 | 3.2 | 0.99 |
| 09ATLMY66 | 421 | 604045 | 3.3 | 5.4334 | 0.4 | 12.6604 | 1.7 | 0.4989 | 1.7 | 0.98 |
| 09ATLMY-4 | 312 | 212174 | 1.9 | 10.6730 | 1.4 | 3.2746 | 3.2 | 0.2535 | 2.8 | 0.89 |
| 09ATLMY94 | 203 | 407402 | 1.6 | 9.2281 | 0.8 | 4.5507 | 2.7 | 0.3046 | 2.6 | 0.96 |
| 09ATLMY81 | 409 | 571754 | 1.8 | 6.0799 | 0.2 | 10.5324 | 1.9 | 0.4644 | 1.9 | 0.99 |
| 09ATLMY63 | 71 | 106426 | 1.1 | 10.2688 | 1.4 | 3.4570 | 3.3 | 0.2575 | 3.0 | 0.90 |
| 09ATLMY108 | 801 | 668339 | 2.7 | 10.1017 | 1.2 | 3.2165 | 3.6 | 0.2357 | 3.4 | 0.94 |
| 09ATLMY-1A | 746 | 520288 | 9.1 | 5.1430 | 0.3 | 13.1034 | 2.2 | 0.4888 | 2.2 | 0.99 |
| 09ATLMY55 | 536 | 329533 | 3.1 | 6.0595 | 0.3 | 10.0450 | 2.5 | 0.4415 | 2.5 | 0.99 |
| 09ATLMY77 | 1841 | 150167 | 1.6 | 5.0763 | 0.8 | 12.1358 | 2.7 | 0.4468 | 2.6 | 0.95 |
| 09ATLMY34 | 907 | 277939 | 1.9 | 6.0204 | 0.5 | 10.0937 | 2.7 | 0.4407 | 2.7 | 0.98 |
| 09ATLMY103 | 559 | 144281 | 3.9 | 8.6561 | 0.5 | 5.3535 | 3.5 | 0.3361 | 3.4 | 0.99 |
| 09ATLMY50 | 199 | 141099 | 1.7 | 12.2493 | 1.3 | 2.3582 | 5.3 | 0.2095 | 5.1 | 0.97 |
| 09ATLMY8 | 149 | 91391 | 1.8 | 9.2794 | 1.7 | 3.9782 | 4.8 | 0.2677 | 4.5 | 0.94 |
| 09ATLMY30 | 429 | 35460 | 2.4 | 13.1058 | 0.6 | 1.8638 | 6.6 | 0.1772 | 6.6 | 1.00 |
| 09ATLMY53 | 298 | 80386 | 1.9 | 8.2642 | 0.5 | 5.2547 | 4.7 | 0.3150 | 4.6 | 0.99 |
| 09ATLMY26 | 380 | 90366 | 1.2 | 4.9497 | 0.8 | 15.4482 | 3.2 | 0.5546 | 3.1 | 0.97 |
| 09ATLMY84 | 53 | 32403 | 1.2 | 6.5557 | 2.4 | 9.8838 | 10.3 | 0.4699 | 10.0 | 0.97 |
| | | | *09-AT-LM-Z* | | | | | | | |
| 09ATLMZ-121 | 724 | 73935 | 0.6 | 20.1256 | 8.5 | 0.0518 | 8.9 | 0.0076 | 2.6 | 0.29 |
| 09ATLMZ-69 | 331 | 24776 | 1.0 | 20.3461 | 18.6 | 0.0651 | 18.8 | 0.0096 | 2.8 | 0.15 |
| 09ATLMZ-113 | 601 | 73341 | 1.3 | 22.7373 | 5.9 | 0.0869 | 6.4 | 0.0143 | 2.5 | 0.39 |
| 09ATLMZ-28 | 608 | 42463 | 0.6 | 17.5705 | 6.6 | 0.0756 | 7.7 | 0.0096 | 4.0 | 0.52 |
| 09ATLMZ-80 | 455 | 46053 | 1.3 | 21.2420 | 16.3 | 0.0862 | 16.6 | 0.0133 | 3.0 | 0.18 |
| 09ATLMZ-98 | 733 | 187489 | 4.1 | 19.7535 | 2.8 | 0.2280 | 3.1 | 0.0327 | 1.3 | 0.43 |
| 09ATLMZ-106 | 470 | 70311 | 1.1 | 21.0339 | 12.1 | 0.0869 | 12.6 | 0.0133 | 3.3 | 0.27 |
| 09ATLMZ-21 | 809 | 286408 | 1.5 | 21.7557 | 3.9 | 0.0936 | 4.9 | 0.0148 | 3.0 | 0.62 |
| 09ATLMZ-30 | 368 | 40934 | 1.4 | 23.5213 | 20.3 | 0.0795 | 20.8 | 0.0136 | 4.3 | 0.21 |
| 09ATLMZ-9 | 680 | 769838 | 5.5 | 18.3012 | 2.5 | 0.4343 | 2.9 | 0.0576 | 1.5 | 0.53 |
| 09ATLMZ-64 | 271 | 88179 | 2.5 | 19.0072 | 10.3 | 0.2675 | 10.5 | 0.0369 | 2.4 | 0.23 |
| 09ATLMZ-3 | 525 | 1776917 | 2.8 | 16.5530 | 1.5 | 0.8431 | 1.8 | 0.1012 | 1.0 | 0.54 |
| 09ATLMZ-122 | 227 | 109606 | 1.5 | 18.3185 | 18.4 | 0.2323 | 18.9 | 0.0309 | 4.0 | 0.21 |
| 09ATLMZ-70 | 520 | 310173 | 3.1 | 17.1262 | 2.4 | 0.6766 | 2.9 | 0.0840 | 1.6 | 0.55 |
| 09ATLMZ-43 | 592 | 552424 | 4.8 | 15.8683 | 1.2 | 1.0002 | 1.8 | 0.1151 | 1.2 | 0.71 |
| 09ATLMZ-38 | 132 | 45672 | 1.4 | 19.9393 | 19.4 | 0.2210 | 19.9 | 0.0320 | 4.5 | 0.23 |
| 09ATLMZ-60 | 244 | 399208 | 1.2 | 14.9231 | 1.4 | 1.2252 | 1.9 | 0.1326 | 1.2 | 0.67 |
| 09ATLMZ-27 | 724 | 966655 | 6.5 | 14.7289 | 0.7 | 1.3047 | 1.5 | 0.1394 | 1.3 | 0.87 |
| 09ATLMZ-4 | 194 | 467271 | 1.5 | 13.0075 | 2.0 | 1.9390 | 2.3 | 0.1829 | 1.1 | 0.49 |
| 09ATLMZ-115 | 751 | 625402 | 3.2 | 16.9080 | 1.3 | 0.6763 | 2.7 | 0.0829 | 2.4 | 0.88 |
| 09ATLMZ-39 | 469 | 441771 | 6.6 | 16.8936 | 2.9 | 0.7373 | 3.7 | 0.0903 | 2.3 | 0.63 |
| 09ATLMZ-16 | 187 | 115915 | 0.7 | 17.5327 | 5.7 | 0.6418 | 6.3 | 0.0816 | 2.6 | 0.41 |
| 09ATLMZ-107 | 657 | 645262 | 6.7 | 16.3281 | 0.7 | 0.8529 | 2.5 | 0.1010 | 2.4 | 0.96 |
| 09ATLMZ-117 | 297 | 304627 | 4.0 | 18.9046 | 5.8 | 0.4357 | 7.1 | 0.0597 | 4.1 | 0.58 |
| 09ATLMZ-120 | 168 | 496639 | 2.3 | 14.6096 | 2.1 | 1.2775 | 2.9 | 0.1354 | 2.0 | 0.69 |
| 09ATLMZ-63 | 112 | 123093 | 2.6 | 14.6657 | 2.2 | 1.3217 | 3.0 | 0.1406 | 2.0 | 0.67 |
| 09ATLMZ-1 | 379 | 210217 | 3.1 | 17.4225 | 2.0 | 0.6745 | 3.9 | 0.0852 | 3.4 | 0.86 |
| 09ATLMZ-87 | 793 | 819802 | 3.2 | 16.5201 | 1.3 | 0.8161 | 3.3 | 0.0978 | 3.0 | 0.92 |
| 09ATLMZ-83 | 190 | 325390 | 1.2 | 13.0970 | 1.7 | 1.9087 | 2.4 | 0.1813 | 1.8 | 0.73 |
| 09ATLMZ-102 | 258 | 721286 | 1.2 | 11.0583 | 0.8 | 2.8303 | 1.7 | 0.2270 | 1.5 | 0.88 |
| 09ATLMZ-95 | 167 | 140055 | 2.1 | 16.9921 | 5.9 | 0.7509 | 6.7 | 0.0925 | 3.3 | 0.49 |
| 09ATLMZ-116 | 420 | 1288383 | 2.2 | 13.1128 | 1.2 | 1.8894 | 2.2 | 0.1797 | 1.9 | 0.84 |
| 09ATLMZ-32 | 287 | 303401 | 1.5 | 17.4635 | 2.8 | 0.6579 | 4.9 | 0.0833 | 3.9 | 0.81 |
| 09ATLMZ-119 | 326 | 726198 | 1.1 | 12.4978 | 0.9 | 2.2107 | 2.1 | 0.2004 | 1.9 | 0.90 |
| 09ATLMZ-109 | 743 | 1191881 | 5.5 | 13.6143 | 2.4 | 1.3451 | 3.6 | 0.1328 | 2.7 | 0.75 |
| 09ATLMZ-72 | 976 | 307230 | 2.3 | 13.8173 | 0.9 | 1.5796 | 2.5 | 0.1583 | 2.3 | 0.94 |
| 09ATLMZ-50 | 1005 | 2035079 | 3.1 | 14.3540 | 0.4 | 1.4199 | 2.5 | 0.1478 | 2.5 | 0.99 |
| 09ATLMZ-24 | 192 | 335428 | 1.6 | 13.4605 | 2.0 | 1.8633 | 3.0 | 0.1819 | 2.2 | 0.74 |
| 09ATLMZ-91 | 341 | 766963 | 1.9 | 12.9871 | 0.8 | 1.9693 | 2.3 | 0.1855 | 2.2 | 0.95 |

| | | | | | | | | | | |
|---|---|---|---|---|---|---|---|---|---|---|
| 09ATLMZ-17 | 467 | 722993 | 1.9 | 15.1807 | 1.1 | 1.1804 | 3.3 | 0.1300 | 3.1 | 0.94 |
| 09ATLMZ-25 | 85 | 330421 | 1.5 | 8.9588 | 1.6 | 4.9722 | 2.2 | 0.3231 | 1.5 | 0.66 |
| 09ATLMZ-51 | 136 | 186494 | 2.1 | 12.7117 | 1.6 | 2.1173 | 2.7 | 0.1952 | 2.2 | 0.81 |
| 09ATLMZ-103 | 162 | 152331 | 0.8 | 17.4241 | 5.6 | 0.6523 | 7.4 | 0.0824 | 4.7 | 0.64 |
| 09ATLMZ-44 | 107 | 386759 | 2.2 | 8.8274 | 1.0 | 5.0856 | 1.8 | 0.3256 | 1.5 | 0.84 |
| 09ATLMZ-36 | 97 | 187344 | 1.1 | 10.3197 | 1.3 | 3.5443 | 2.2 | 0.2653 | 1.8 | 0.81 |
| 09ATLMZ-104 | 234 | 375603 | 1.1 | 13.6540 | 0.9 | 1.7805 | 2.8 | 0.1763 | 2.7 | 0.94 |
| 09ATLMZ-10 | 121 | 271441 | 3.9 | 15.0600 | 8.2 | 1.3065 | 8.9 | 0.1427 | 3.2 | 0.36 |
| 09ATLMZ-81 | 157 | 421836 | 1.6 | 12.3838 | 1.7 | 2.0759 | 3.3 | 0.1865 | 2.8 | 0.85 |
| 09ATLMZ-65 | 882 | 1087711 | 2.3 | 14.2986 | 0.6 | 1.4462 | 3.4 | 0.1500 | 3.4 | 0.98 |
| 09ATLMZ-77 | 328 | 334813 | 1.2 | 14.0279 | 1.2 | 1.5560 | 3.5 | 0.1583 | 3.3 | 0.94 |
| 09ATLMZ-40 | 172 | 343712 | 1.4 | 11.8917 | 2.4 | 2.3812 | 3.6 | 0.2054 | 2.7 | 0.74 |
| 09ATLMZ-55 | 230 | 461302 | 1.2 | 13.2479 | 1.2 | 1.9167 | 3.3 | 0.1842 | 3.1 | 0.93 |
| 09ATLMZ-111 | 925 | 2380389 | 2.6 | 14.2512 | 0.9 | 1.3921 | 3.9 | 0.1439 | 3.8 | 0.98 |
| 09ATLMZ-66 | 312 | 1488082 | 0.7 | 5.4708 | 0.3 | 12.6724 | 1.5 | 0.5028 | 1.4 | 0.97 |
| 09ATLMZ-37 | 438 | 653221 | 3.1 | 14.6424 | 1.6 | 1.2087 | 4.6 | 0.1284 | 4.3 | 0.94 |
| 09ATLMZ-112 | 721 | 5362545 | 9.2 | 5.5184 | 0.3 | 11.9009 | 1.6 | 0.4763 | 1.6 | 0.99 |
| 09ATLMZ-59 | 502 | 1676751 | 11.8 | 13.1161 | 0.8 | 1.7941 | 3.6 | 0.1707 | 3.5 | 0.97 |
| 09ATLMZ-97 | 204 | 363274 | 2.0 | 14.1323 | 2.1 | 1.6244 | 4.5 | 0.1665 | 4.0 | 0.88 |
| 09ATLMZ-92 | 288 | 1186626 | 1.4 | 8.3380 | 0.4 | 5.8393 | 2.2 | 0.3531 | 2.2 | 0.98 |
| 09ATLMZ-8 | 165 | 351115 | 1.0 | 8.7526 | 0.7 | 5.0995 | 2.5 | 0.3237 | 2.4 | 0.96 |
| 09ATLMZ-45 | 258 | 3406341 | 2.1 | 4.3721 | 0.6 | 19.1414 | 1.7 | 0.6070 | 1.6 | 0.93 |
| 09ATLMZ-31 | 114 | 382215 | 3.4 | 13.1361 | 2.8 | 1.9717 | 4.7 | 0.1878 | 3.8 | 0.81 |
| 09ATLMZ-53 | 202 | 856590 | 1.2 | 7.5409 | 1.1 | 7.1154 | 2.5 | 0.3892 | 2.2 | 0.90 |
| 09ATLMZ-76 | 279 | 356115 | 2.1 | 13.1100 | 1.9 | 1.7747 | 4.7 | 0.1687 | 4.3 | 0.91 |
| 09ATLMZ-71 | 1076 | 2566751 | 17.4 | 14.4596 | 0.6 | 1.3494 | 5.3 | 0.1415 | 5.2 | 0.99 |
| 09ATLMZ-47 | 779 | 703107 | 7.3 | 12.4802 | 0.9 | 1.9290 | 4.5 | 0.1746 | 4.4 | 0.98 |
| 09ATLMZ-82 | 468 | 3285703 | 2.2 | 3.5233 | 0.7 | 22.3615 | 2.0 | 0.5714 | 1.9 | 0.94 |
| 09ATLMZ-85 | 78 | 259519 | 1.6 | 8.7647 | 1.2 | 5.2334 | 3.2 | 0.3327 | 2.9 | 0.92 |
| 09ATLMZ-7 | 565 | 241165 | 1.6 | 13.4799 | 1.2 | 1.6207 | 5.5 | 0.1584 | 5.4 | 0.98 |
| 09ATLMZ-56 | 518 | 1045189 | 10.0 | 14.0302 | 0.8 | 1.6027 | 5.4 | 0.1631 | 5.3 | 0.99 |
| 09ATLMZ-41 | 274 | 514299 | 2.5 | 14.1260 | 1.7 | 1.4222 | 7.1 | 0.1457 | 6.9 | 0.97 |
| 09ATLMZ-79 | 119 | 221486 | 1.1 | 12.6037 | 1.8 | 2.0756 | 6.2 | 0.1897 | 5.9 | 0.95 |
| 09ATLMZ-49 | 590 | 2669809 | 6.8 | 5.2714 | 0.8 | 12.1344 | 3.5 | 0.4639 | 3.4 | 0.98 |
| 09ATLMZ-29 | 118 | 860461 | 2.8 | 4.0844 | 0.6 | 21.5068 | 2.9 | 0.6371 | 2.8 | 0.98 |
| 09ATLMZ-46 | 140 | 1579346 | 1.2 | 3.6264 | 1.8 | 25.5477 | 4.2 | 0.6719 | 3.8 | 0.91 |
| 09ATLMZ-6 | 360 | 242691 | 2.9 | 5.6242 | 0.3 | 11.0530 | 8.8 | 0.4509 | 8.8 | 1.00 |

*Note:* All uncertainties are reported at the 1σ level, and include only measurement errors. Systematic errors are as follows for $^{206}Pb/^{238}U$ and $^{206}Pb/^{207}Pb$, respectively, at 2σ level: 1.6% and 0.9% for sample TRD and 2.1% and 3.2% for sample TRE. Analyses conducted by LA-MC-ICPMS, as described by Gehrels et al. (2008). U/Pb and $^{206}Pb/^{207}Pb$ fractionation is calibrated relative to fragments of a large Sri Lanka zircon of 563.5±3.2 Ma (2σ). U decay constants and composition as follows: $^{238}U = 9.8485 \times 10^{-10}$, $^{235}U = 1.55125 \times 10^{-10}$, $^{238}U/^{235}U = 137.88$.

[1]U concentration and U/Th are calibrated relative to Sri Lanka zircon standard and are accurate to ~20%.

[2]Common Pb correction is from measured $^{204}Pb$ with common Pb composition interpreted from Stacey and Kramers (1975). Common Pb composition assigned uncertainties of 1.5 for $^{206}Pb/^{204}Pb$, 0.3 for $^{207}Pb/^{204}Pb$, and 2.0 for $^{208}Pb/^{204}Pb$.

Table A4.1b. U-Pb geochronologic analyses of zircons from quartzite clasts, age data.

| Analysis | Apparent ages (Ma) | | | | | | | |
|---|---|---|---|---|---|---|---|---|
| | $^{206}Pb^*/^{238}U$ (Ma) | ± (Ma) | $^{207}Pb^*/^{235}U$ (Ma) | ± (Ma) | $^{206}Pb^*/^{207}Pb^*$ (Ma) | ± (Ma) | Best age[3] (Ma) | ± (Ma) |
| | | | *09-AT-LM-Y* | | | | | |
| 09ATLMY17 | 205.3 | 2.8 | 215.7 | 5.7 | 329.8 | 58.8 | 205.3 | 2.8 |
| 09ATLMY72 | 443.6 | 2.9 | 449.2 | 6.2 | 477.8 | 34.5 | 443.6 | 2.9 |
| 09ATLMY40 | 211.5 | 3.7 | 211.2 | 7.7 | 207.2 | 83.7 | 211.5 | 3.7 |
| 09ATLMY10 | 188.9 | 4.5 | 186.1 | 19.2 | 150.0 | 260.0 | 188.9 | 4.5 |
| 09ATLMY107 | 512.5 | 4.7 | 513.7 | 5.6 | 519.2 | 21.8 | 512.5 | 4.7 |
| 09ATLMY83 | 218.8 | 5.2 | 250.5 | 21.6 | 560.0 | 210.0 | 218.8 | 5.2 |
| 09ATLMY89 | 219.5 | 5.5 | 218.0 | 5.2 | 202.2 | 19.1 | 219.5 | 5.5 |
| 09ATLMY48 | 214.1 | 5.6 | 206.2 | 10.4 | 120.0 | 120.0 | 214.1 | 5.6 |
| 09ATLMY64 | 213.1 | 5.7 | 212.8 | 6.4 | 208.6 | 46.3 | 213.1 | 5.7 |
| 09ATLMY41 | 191.3 | 5.9 | 198.3 | 8.3 | 282.7 | 77.9 | 191.3 | 5.9 |
| 09ATLMY65 | 207.5 | 6.1 | 209.8 | 6.8 | 235.8 | 45.2 | 207.5 | 6.1 |
| 09ATLMY28 | 244.9 | 6.6 | 242.9 | 7.9 | 223.6 | 55.7 | 244.9 | 6.6 |
| 09ATLMY101 | 335.4 | 6.6 | 348.0 | 12.1 | 433.2 | 79.7 | 335.4 | 6.6 |
| 09ATLMY49 | 205.2 | 6.9 | 205.5 | 17.6 | 210.0 | 210.0 | 205.2 | 6.9 |
| 09ATLMY79 | 697.9 | 7.3 | 707.9 | 6.7 | 739.6 | 14.8 | 697.9 | 7.3 |
| 09ATLMY33 | 750.5 | 7.5 | 747.2 | 6.4 | 737.4 | 12.1 | 750.5 | 7.5 |
| 09ATLMY36 | 503.7 | 7.6 | 506.7 | 9.9 | 520.3 | 42.4 | 503.7 | 7.6 |
| 09ATLMY73 | 502.5 | 8.6 | 492.6 | 17.2 | 446.9 | 89.5 | 502.5 | 8.6 |
| 09ATLMY52 | 524.0 | 9.4 | 526.4 | 10.1 | 537.0 | 34.9 | 524.0 | 9.4 |
| 09ATLMY45 | 500.5 | 9.6 | 508.7 | 13.1 | 545.8 | 56.7 | 500.5 | 9.6 |
| 09ATLMY24 | 516.1 | 9.7 | 521.4 | 12.8 | 544.7 | 54.1 | 516.1 | 9.7 |
| 09ATLMY59 | 579.4 | 11.3 | 568.3 | 34.0 | 520.0 | 170.0 | 579.4 | 11.3 |
| 09ATLMY44 | 622.0 | 11.6 | 637.5 | 14.6 | 693.1 | 51.1 | 622.0 | 11.6 |
| 09ATLMY-2 | 553.1 | 12.1 | 522.6 | 52.4 | 390.0 | 280.0 | 553.1 | 12.1 |
| 09ATLMY20 | 1076.1 | 12.1 | 1103.7 | 9.6 | 1158.5 | 14.5 | 1158.5 | 14.5 |
| 09ATLMY99 | 543.5 | 12.6 | 563.6 | 46.7 | 650.0 | 230.0 | 543.5 | 12.6 |
| 09ATLMY90 | 1185.0 | 12.7 | 1205.8 | 9.3 | 1243.3 | 11.4 | 1243.3 | 11.4 |
| 09ATLMY82 | 409.8 | 13.2 | 401.3 | 24.9 | 350.0 | 150.0 | 409.8 | 13.2 |
| 09ATLMY11 | 964.2 | 13.4 | 990.1 | 12.8 | 1047.9 | 27.5 | 1047.9 | 27.5 |
| 09ATLMY19 | 867.9 | 13.6 | 884.7 | 12.1 | 927.2 | 24.1 | 867.9 | 13.6 |
| 09ATLMY102 | 1183.1 | 13.7 | 1187.9 | 14.0 | 1196.5 | 30.3 | 1196.5 | 30.3 |
| 09ATLMY14 | 537.0 | 14.6 | 427.6 | 97.8 | -130.0 | 700.0 | 537.0 | 14.6 |
| 09ATLMY51 | 563.5 | 15.6 | 575.0 | 13.3 | 620.6 | 19.8 | 563.5 | 15.6 |
| 09ATLMY22 | 1169.7 | 15.9 | 1178.3 | 16.6 | 1194.0 | 36.6 | 1194.0 | 36.6 |
| 09ATLMY67 | 329.2 | 16.2 | 327.5 | 21.9 | 320.0 | 140.0 | 329.2 | 16.2 |
| 09ATLMY98 | 542.6 | 16.4 | 539.0 | 19.8 | 524.0 | 77.4 | 542.6 | 16.4 |
| 09ATLMY23 | 1543.8 | 19.6 | 1557.6 | 12.6 | 1576.4 | 12.7 | 1576.4 | 12.7 |
| 09ATLMY29 | 1019.4 | 19.9 | 1041.5 | 16.9 | 1088.0 | 30.1 | 1088.0 | 30.1 |
| 09ATLMY71 | 1024.4 | 20.5 | 1046.9 | 18.2 | 1094.1 | 34.8 | 1094.1 | 34.8 |
| 09ATLMY7 | 1101.6 | 20.7 | 1120.9 | 20.1 | 1158.5 | 42.5 | 1158.5 | 42.5 |
| 09ATLMY12 | 955.6 | 21.1 | 1030.8 | 16.8 | 1194.0 | 20.1 | 1194.0 | 20.1 |
| 09ATLMY74 | 867.5 | 21.4 | 876.9 | 16.7 | 900.9 | 21.9 | 867.5 | 21.4 |
| 09ATLMY87 | 1569.5 | 24.0 | 1572.2 | 15.2 | 1575.7 | 15.0 | 1575.7 | 15.0 |
| 09ATLMY100 | 1027.2 | 24.1 | 1037.7 | 16.8 | 1059.8 | 9.8 | 1059.8 | 9.8 |
| 09ATLMY5 | 1656.8 | 25.2 | 1670.5 | 16.1 | 1687.7 | 17.3 | 1687.7 | 17.3 |
| 09ATLMY68 | 1505.4 | 26.2 | 1541.7 | 20.2 | 1591.7 | 30.6 | 1591.7 | 30.6 |
| 09ATLMY-3 | 898.8 | 26.3 | 914.6 | 20.3 | 953.0 | 25.2 | 953.0 | 25.2 |
| 09ATLMY109 | 1206.4 | 26.7 | 1207.9 | 18.1 | 1210.5 | 16.5 | 1210.5 | 16.5 |
| 09ATLMY39 | 696.3 | 27.1 | 740.5 | 23.1 | 876.5 | 33.1 | 696.3 | 27.1 |
| 09ATLMY93 | 773.9 | 28.4 | 794.2 | 23.1 | 851.4 | 31.9 | 773.9 | 28.4 |
| 09ATLMY42 | 1418.9 | 28.8 | 1444.1 | 30.0 | 1481.5 | 60.0 | 1481.5 | 60.0 |
| 09ATLMY86 | 1389.7 | 29.4 | 1401.3 | 23.4 | 1419.0 | 38.1 | 1419.0 | 38.1 |
| 09ATLMY88 | 971.5 | 29.4 | 994.2 | 24.3 | 1044.5 | 40.4 | 1044.5 | 40.4 |
| 09ATLMY56 | 1055.0 | 31.3 | 1082.0 | 27.1 | 1137.0 | 49.7 | 1137.0 | 49.7 |

| | | | | | | | | |
|---|---|---|---|---|---|---|---|---|
| 09ATLMY15 | 1864.7 | 31.3 | 1907.1 | 16.7 | 1953.5 | 3.0 | 1953.5 | 3.0 |
| 09ATLMY21 | 970.4 | 31.6 | 968.4 | 22.2 | 964.0 | 12.3 | 964.0 | 12.3 |
| 09ATLMY104 | 1116.2 | 33.9 | 1142.9 | 25.3 | 1193.8 | 32.0 | 1193.8 | 32.0 |
| 09ATLMY62 | 1211.7 | 35.3 | 1225.6 | 23.9 | 1250.1 | 19.9 | 1250.1 | 19.9 |
| 09ATLMY78 | 987.4 | 35.9 | 1045.0 | 26.3 | 1167.4 | 18.0 | 1167.4 | 18.0 |
| 09ATLMY31 | 1243.4 | 36.0 | 1346.5 | 24.0 | 1514.2 | 8.2 | 1514.2 | 8.2 |
| 09ATLMY66 | 2609.1 | 36.1 | 2654.7 | 16.2 | 2689.7 | 5.8 | 2689.7 | 5.8 |
| 09ATLMY-4 | 1456.4 | 37.0 | 1475.0 | 24.8 | 1501.9 | 27.3 | 1501.9 | 27.3 |
| 09ATLMY94 | 1714.0 | 38.5 | 1740.3 | 22.3 | 1772.1 | 14.3 | 1772.1 | 14.3 |
| 09ATLMY81 | 2459.1 | 39.1 | 2482.8 | 17.9 | 2502.2 | 4.1 | 2502.2 | 4.1 |
| 09ATLMY63 | 1476.9 | 39.4 | 1517.5 | 26.0 | 1574.6 | 26.4 | 1574.6 | 26.4 |
| 09ATLMY108 | 1364.1 | 42.0 | 1461.1 | 28.0 | 1605.2 | 22.1 | 1605.2 | 22.1 |
| 09ATLMY-1A | 2565.3 | 46.9 | 2687.1 | 21.1 | 2780.1 | 4.8 | 2780.1 | 4.8 |
| 09ATLMY55 | 2357.1 | 49.6 | 2438.9 | 23.4 | 2507.9 | 5.4 | 2507.9 | 5.4 |
| 09ATLMY77 | 2381.0 | 51.9 | 2615.0 | 25.6 | 2801.5 | 13.4 | 2801.5 | 13.4 |
| 09ATLMY34 | 2353.9 | 52.5 | 2443.4 | 25.0 | 2518.7 | 8.1 | 2518.7 | 8.1 |
| 09ATLMY103 | 1867.8 | 55.8 | 1877.4 | 29.8 | 1888.1 | 8.9 | 1888.1 | 8.9 |
| 09ATLMY50 | 1226.2 | 57.0 | 1230.0 | 37.5 | 1236.8 | 24.9 | 1236.8 | 24.9 |
| 09ATLMY8 | 1529.3 | 61.2 | 1629.8 | 39.0 | 1762.0 | 30.9 | 1762.0 | 30.9 |
| 09ATLMY30 | 1051.4 | 63.8 | 1068.3 | 43.6 | 1103.0 | 11.6 | 1103.0 | 11.6 |
| 09ATLMY53 | 1765.0 | 71.7 | 1861.5 | 39.9 | 1971.1 | 9.6 | 1971.1 | 9.6 |
| 09ATLMY26 | 2844.2 | 71.7 | 2843.3 | 30.7 | 2842.7 | 13.0 | 2842.7 | 13.0 |
| 09ATLMY84 | 2480.0 | 210.0 | 2424.0 | 95.1 | 2374.6 | 41.6 | 2374.6 | 41.6 |
| | | | *09-AT-LM-Z* | | | | | |
| 09ATLMZ-121 | 48.6 | 1.3 | 51.3 | 4.5 | 180.0 | 200.0 | 48.6 | 1.3 |
| 09ATLMZ-69 | 61.6 | 1.7 | 64.0 | 11.6 | 150.0 | 440.0 | 61.6 | 1.7 |
| 09ATLMZ-113 | 91.8 | 2.3 | 84.6 | 5.2 | -110.0 | 150.0 | 91.8 | 2.3 |
| 09ATLMZ-28 | 61.8 | 2.5 | 74.0 | 5.5 | 490.0 | 150.0 | 61.8 | 2.5 |
| 09ATLMZ-80 | 85.0 | 2.5 | 83.9 | 13.3 | 50.0 | 390.0 | 85.0 | 2.5 |
| 09ATLMZ-98 | 207.2 | 2.7 | 208.5 | 5.9 | 223.7 | 65.6 | 207.2 | 2.7 |
| 09ATLMZ-106 | 84.9 | 2.8 | 84.6 | 10.2 | 80.0 | 290.0 | 84.9 | 2.8 |
| 09ATLMZ-21 | 94.5 | 2.9 | 90.9 | 4.3 | -4.2 | 93.0 | 94.5 | 2.9 |
| 09ATLMZ-30 | 86.8 | 3.7 | 77.6 | 15.5 | -200.0 | 510.0 | 86.8 | 3.7 |
| 09ATLMZ-9 | 361.3 | 5.4 | 366.2 | 9.0 | 397.5 | 55.5 | 361.3 | 5.4 |
| 09ATLMZ-64 | 233.5 | 5.5 | 240.7 | 22.6 | 310.0 | 230.0 | 233.5 | 5.5 |
| 09ATLMZ-3 | 621.5 | 5.9 | 620.8 | 8.4 | 618.3 | 33.0 | 621.5 | 5.9 |
| 09ATLMZ-122 | 196.0 | 7.8 | 212.1 | 36.1 | 400.0 | 420.0 | 196.0 | 7.8 |
| 09ATLMZ-70 | 520.2 | 7.8 | 524.7 | 11.7 | 544.4 | 52.5 | 520.2 | 7.8 |
| 09ATLMZ-43 | 702.4 | 8.3 | 703.9 | 8.9 | 708.8 | 26.2 | 702.4 | 8.3 |
| 09ATLMZ-38 | 202.8 | 9.0 | 202.7 | 36.7 | 200.0 | 450.0 | 202.8 | 9.0 |
| 09ATLMZ-60 | 802.7 | 9.4 | 812.1 | 10.4 | 838.1 | 28.8 | 802.7 | 9.4 |
| 09ATLMZ-27 | 841.1 | 10.2 | 847.8 | 8.6 | 865.3 | 15.5 | 841.1 | 10.2 |
| 09ATLMZ-4 | 1082.9 | 11.1 | 1094.7 | 15.2 | 1118.1 | 39.3 | 1118.1 | 39.3 |
| 09ATLMZ-115 | 513.6 | 11.9 | 524.5 | 11.2 | 572.4 | 28.4 | 513.6 | 11.9 |
| 09ATLMZ-39 | 557.6 | 12.5 | 560.8 | 16.1 | 574.2 | 63.2 | 557.6 | 12.5 |
| 09ATLMZ-16 | 505.7 | 12.5 | 503.4 | 25.0 | 490.0 | 130.0 | 505.7 | 12.5 |
| 09ATLMZ-107 | 620.3 | 14.1 | 626.2 | 11.7 | 647.8 | 15.7 | 620.3 | 14.1 |
| 09ATLMZ-117 | 374.0 | 15.1 | 367.2 | 21.9 | 320.0 | 130.0 | 374.0 | 15.1 |
| 09ATLMZ-120 | 818.4 | 15.3 | 835.7 | 16.4 | 882.2 | 42.8 | 818.4 | 15.3 |
| 09ATLMZ-63 | 847.9 | 15.9 | 855.2 | 17.2 | 874.2 | 45.5 | 847.9 | 15.9 |
| 09ATLMZ-1 | 527.2 | 17.1 | 523.4 | 16.0 | 506.8 | 43.4 | 527.2 | 17.1 |
| 09ATLMZ-87 | 601.4 | 17.5 | 605.9 | 15.1 | 622.6 | 27.8 | 601.4 | 17.5 |
| 09ATLMZ-83 | 1074.1 | 17.7 | 1084.1 | 16.3 | 1104.3 | 33.4 | 1104.3 | 33.4 |
| 09ATLMZ-102 | 1318.8 | 17.9 | 1363.6 | 12.8 | 1434.6 | 15.3 | 1434.6 | 15.3 |
| 09ATLMZ-95 | 570.5 | 18.1 | 568.7 | 29.3 | 560.0 | 130.0 | 570.5 | 18.1 |
| 09ATLMZ-116 | 1065.3 | 18.2 | 1077.4 | 14.7 | 1102.0 | 24.0 | 1102.0 | 24.0 |
| 09ATLMZ-32 | 516.0 | 19.6 | 513.3 | 19.6 | 501.6 | 62.7 | 516.0 | 19.6 |
| 09ATLMZ-119 | 1177.4 | 20.0 | 1184.4 | 14.4 | 1197.4 | 17.5 | 1197.4 | 17.5 |
| 09ATLMZ-109 | 803.9 | 20.5 | 865.4 | 21.0 | 1026.4 | 47.9 | 1026.4 | 47.9 |
| 09ATLMZ-72 | 947.3 | 20.7 | 962.2 | 15.6 | 996.5 | 17.8 | 996.5 | 17.8 |
| 09ATLMZ-50 | 888.7 | 20.8 | 897.3 | 15.1 | 918.6 | 8.3 | 918.6 | 8.3 |
| 09ATLMZ-24 | 1077.4 | 21.9 | 1068.2 | 19.6 | 1049.4 | 40.2 | 1049.4 | 40.2 |
| 09ATLMZ-91 | 1096.9 | 22.3 | 1105.1 | 15.7 | 1121.2 | 15.2 | 1121.2 | 15.2 |

| | | | | | | | | |
|---|---|---|---|---|---|---|---|---|
| 09ATLMZ-17 | 787.6 | 22.7 | 791.5 | 17.9 | 802.3 | 23.5 | 787.6 | 22.7 |
| 09ATLMZ-25 | 1804.7 | 22.9 | 1814.6 | 18.6 | 1826.0 | 29.9 | 1826.0 | 29.9 |
| 09ATLMZ-51 | 1149.5 | 22.9 | 1154.5 | 18.5 | 1163.8 | 31.2 | 1163.8 | 31.2 |
| 09ATLMZ-103 | 510.6 | 23.2 | 509.9 | 29.5 | 510.0 | 120.0 | 510.6 | 23.2 |
| 09ATLMZ-44 | 1817.0 | 23.7 | 1833.7 | 15.2 | 1852.7 | 17.8 | 1852.7 | 17.8 |
| 09ATLMZ-36 | 1516.8 | 24.0 | 1537.2 | 17.3 | 1565.3 | 23.9 | 1565.3 | 23.9 |
| 09ATLMZ-104 | 1046.8 | 25.8 | 1038.4 | 18.4 | 1020.5 | 19.1 | 1020.5 | 19.1 |
| 09ATLMZ-10 | 859.9 | 25.9 | 848.6 | 51.0 | 820.0 | 170.0 | 859.9 | 25.9 |
| 09ATLMZ-81 | 1102.1 | 28.4 | 1140.9 | 22.5 | 1215.4 | 33.6 | 1215.4 | 33.6 |
| 09ATLMZ-65 | 900.8 | 28.5 | 908.3 | 20.7 | 926.5 | 12.3 | 926.5 | 12.3 |
| 09ATLMZ-77 | 947.4 | 29.2 | 952.9 | 21.7 | 965.7 | 23.9 | 965.7 | 23.9 |
| 09ATLMZ-40 | 1204.1 | 29.6 | 1237.0 | 26.0 | 1294.7 | 47.3 | 1294.7 | 47.3 |
| 09ATLMZ-55 | 1089.7 | 30.6 | 1086.9 | 21.9 | 1081.4 | 24.2 | 1081.4 | 24.2 |
| 09ATLMZ-111 | 866.6 | 31.0 | 885.6 | 23.2 | 933.3 | 17.8 | 866.6 | 31.0 |
| 09ATLMZ-66 | 2625.9 | 31.0 | 2655.6 | 13.9 | 2678.3 | 5.5 | 2678.3 | 5.5 |
| 09ATLMZ-37 | 778.5 | 31.8 | 804.6 | 25.6 | 877.5 | 32.6 | 778.5 | 31.8 |
| 09ATLMZ-112 | 2511.2 | 32.6 | 2596.6 | 14.9 | 2664.0 | 4.5 | 2664.0 | 4.5 |
| 09ATLMZ-59 | 1015.8 | 32.9 | 1043.3 | 23.5 | 1101.4 | 16.9 | 1101.4 | 16.9 |
| 09ATLMZ-97 | 992.8 | 36.9 | 979.7 | 28.6 | 950.5 | 44.0 | 950.5 | 44.0 |
| 09ATLMZ-92 | 1949.5 | 37.0 | 1952.3 | 19.4 | 1955.2 | 7.0 | 1955.2 | 7.0 |
| 09ATLMZ-8 | 1807.8 | 38.3 | 1836.0 | 21.5 | 1868.1 | 13.1 | 1868.1 | 13.1 |
| 09ATLMZ-45 | 3057.8 | 38.5 | 3049.0 | 16.4 | 3043.1 | 10.1 | 3043.1 | 10.1 |
| 09ATLMZ-31 | 1109.7 | 39.1 | 1105.9 | 31.8 | 1098.4 | 55.1 | 1098.4 | 55.1 |
| 09ATLMZ-53 | 2118.9 | 39.8 | 2126.0 | 21.8 | 2132.8 | 18.9 | 2132.8 | 18.9 |
| 09ATLMZ-76 | 1005.2 | 40.4 | 1036.2 | 30.9 | 1102.4 | 38.6 | 1102.4 | 38.6 |
| 09ATLMZ-71 | 853.2 | 41.9 | 867.3 | 30.7 | 903.4 | 11.8 | 853.2 | 41.9 |
| 09ATLMZ-47 | 1037.4 | 42.1 | 1091.2 | 30.0 | 1200.1 | 18.5 | 1200.1 | 18.5 |
| 09ATLMZ-82 | 2913.6 | 44.5 | 3199.6 | 19.6 | 3384.1 | 10.8 | 3384.1 | 10.8 |
| 09ATLMZ-85 | 1851.3 | 47.3 | 1858.1 | 27.2 | 1865.6 | 22.5 | 1865.6 | 22.5 |
| 09ATLMZ-7 | 948.1 | 47.7 | 978.3 | 34.8 | 1046.5 | 24.6 | 1046.5 | 24.6 |
| 09ATLMZ-56 | 973.9 | 48.1 | 971.3 | 33.6 | 965.3 | 16.0 | 965.3 | 16.0 |
| 09ATLMZ-41 | 876.8 | 56.2 | 898.3 | 42.2 | 951.4 | 34.7 | 951.4 | 34.7 |
| 09ATLMZ-79 | 1119.9 | 60.8 | 1140.8 | 42.5 | 1180.7 | 36.4 | 1180.7 | 36.4 |
| 09ATLMZ-49 | 2456.9 | 69.7 | 2614.9 | 32.8 | 2739.6 | 12.6 | 2739.6 | 12.6 |
| 09ATLMZ-29 | 3177.6 | 71.2 | 3161.7 | 28.2 | 3151.7 | 9.7 | 3151.7 | 9.7 |
| 09ATLMZ-46 | 3313.3 | 99.7 | 3329.4 | 41.5 | 3339.1 | 27.9 | 3339.1 | 27.9 |
| 09ATLMZ-6 | 2400.0 | 180.0 | 2527.6 | 82.4 | 2632.5 | 4.3 | 2632.5 | 4.3 |

[3]Analyses with >10% uncertainty (2σ) in $^{206}Pb/^{238}U$ age are not included. Analyses with >10% uncertainty (1σ) in $^{206}Pb/^{207}Pb$ are not included, unless $^{206}Pb/^{238}U$ age is <500 Ma. Best age is determined from $^{206}Pb/^{238}U$ age for analyses with $^{206}Pb/^{238}U$ age <1000 Ma and from $^{206}Pb/^{207}Pb$ age for analyses with $^{206}Pb/^{238}U$ age >1000 Ma.

# APPENDIX I

## CHAPTER 4 SUPPLEMENT:

## $^{40}AR/^{39}AR$ FOR 08-AT-ZG-A

Table A4.2. $^{40}Ar/^{39}Ar$ data for sample 08-AT-ZG-A.

| Lab ID# | $^{40}Ar^*/^{39}Ar$ ± 2s | | $^{40}Ar/^{39}Ar$ ± 2s | | $^{36}Ar/^{39}Ar$ ± 2s | | $^{39}Ar$ (moles) | $\%^{40}Ar^*$ | Age (Ma)[1] ± 2s | |
|---|---|---|---|---|---|---|---|---|---|---|
| | | | | | *08-AT-ZG-A* | | | | | |
| 103-21 | 179.939 | 2.423 | 181.026 | 2.419 | 0.0036 | 0.0010 | 8.52E-17 | 99.41 | 480.5 | 5.3 |
| 103-03 | 179.133 | 1.643 | 183.273 | 1.603 | 0.0139 | 0.0015 | 6.19E-17 | 97.76 | 489.6 | 8.0 |
| 103-08 | 187.445 | 1.793 | 188.811 | 1.773 | 0.0046 | 0.0011 | 7.59E-17 | 99.29 | 516.2 | 5.8 |
| 103-09 | 181.617 | 1.004 | 189.186 | 1.004 | 0.0256 | 0.0008 | 1.55E-16 | 96.01 | 517.2 | 3.9 |
| 103-02 | 190.601 | 4.574 | 193.158 | 4.235 | 0.0086 | 0.0063 | 1.29E-17 | 98.69 | 521.0 | 5.1 |
| 103-63 | 186.909 | 2.301 | 191.150 | 2.206 | 0.0143 | 0.0027 | 3.21E-17 | 97.80 | 523.4 | 8.5 |
| 103-05 | 176.626 | 1.992 | 177.468 | 1.935 | 0.0028 | 0.0017 | 4.36E-17 | 99.54 | 524.7 | 5.5 |
| 103-07 | 188.858 | 1.792 | 191.459 | 1.802 | 0.0087 | 0.0007 | 1.41E-16 | 98.66 | 525.5 | 4.1 |
| 103-11 | 180.412 | 1.783 | 183.659 | 1.756 | 0.0109 | 0.0014 | 6.62E-17 | 98.25 | 526.2 | 4.3 |
| 103-19 | 193.230 | 0.954 | 194.167 | 0.944 | 0.0031 | 0.0005 | 1.90E-16 | 99.53 | 527.4 | 4.2 |
| 103-04 | 184.967 | 1.184 | 185.705 | 1.169 | 0.0024 | 0.0007 | 1.15E-16 | 99.62 | 527.6 | 4.0 |
| 103-01 | 184.342 | 1.445 | 185.345 | 1.431 | 0.0033 | 0.0008 | 9.22E-17 | 99.47 | 529.4 | 6.2 |
| 103-28 | 178.388 | 1.603 | 180.453 | 1.576 | 0.0069 | 0.0012 | 6.86E-17 | 98.87 | 530.6 | 4.5 |
| 103-29 | 174.758 | 2.248 | 176.928 | 2.199 | 0.0073 | 0.0019 | 4.14E-17 | 98.79 | 533 | 13 |
| 103-13 | 183.983 | 1.469 | 184.945 | 1.468 | 0.0032 | 0.0005 | 1.64E-16 | 99.49 | 533.7 | 2.6 |
| 103-18 | 211.425 | 4.779 | 218.176 | 4.799 | 0.0228 | 0.0037 | 2.51E-17 | 96.92 | 537.5 | 4.7 |
| 103-16 | 178.084 | 2.151 | 179.997 | 2.072 | 0.0064 | 0.0022 | 4.19E-17 | 98.95 | 537.5 | 4.3 |
| 103-20 | 185.559 | 1.149 | 193.792 | 1.183 | 0.0278 | 0.0005 | 4.87E-16 | 95.77 | 539.2 | 3.3 |
| 103-60 | 186.136 | 1.492 | 187.333 | 1.494 | 0.0040 | 0.0005 | 2.10E-16 | 99.38 | 539.7 | 3.7 |
| 103-10 | 184.602 | 1.465 | 186.070 | 1.439 | 0.0049 | 0.0011 | 8.27E-17 | 99.23 | 540.6 | 3.7 |
| 103-14 | 183.773 | 1.304 | 185.780 | 1.281 | 0.0067 | 0.0010 | 9.37E-17 | 98.93 | 541.3 | 3.7 |
| 103-69 | 179.227 | 1.584 | 185.081 | 1.553 | 0.0198 | 0.0016 | 5.67E-17 | 96.85 | 541.5 | 4.7 |
| 103-30 | 178.685 | 1.679 | 180.361 | 1.635 | 0.0056 | 0.0015 | 5.12E-17 | 99.09 | 542.2 | 3.0 |
| 103-06 | 183.101 | 1.861 | 188.817 | 1.843 | 0.0193 | 0.0016 | 5.86E-17 | 96.99 | 542.4 | 8.9 |
| 103-32 | 186.867 | 0.761 | 192.189 | 0.765 | 0.0179 | 0.0004 | 4.28E-16 | 97.24 | 543.7 | 2.9 |
| 103-38 | 189.085 | 3.727 | 190.244 | 3.404 | 0.0039 | 0.0053 | 1.68E-17 | 99.41 | 545.2 | 3.8 |
| 103-61 | 175.162 | 1.509 | 178.218 | 1.444 | 0.0103 | 0.0017 | 5.47E-17 | 98.30 | 547.0 | 1.9 |
| 103-33 | 187.192 | 1.617 | 188.549 | 1.593 | 0.0045 | 0.0011 | 7.61E-17 | 99.29 | 547.1 | 5.8 |
| 103-26 | 188.263 | 0.940 | 189.212 | 0.936 | 0.0031 | 0.0004 | 2.24E-16 | 99.51 | 547.8 | 2.6 |
| 103-23 | 181.191 | 5.171 | 188.295 | 5.188 | 0.0240 | 0.0046 | 1.91E-17 | 96.24 | 547.8 | 4.1 |
| 103-68 | 183.111 | 1.712 | 185.186 | 1.680 | 0.0070 | 0.0014 | 5.72E-17 | 98.89 | 548.0 | 3.1 |
| 103-67 | 189.086 | 0.885 | 191.554 | 0.887 | 0.0083 | 0.0003 | 3.33E-16 | 98.73 | 548.1 | 2.4 |
| 103-43 | 184.693 | 1.855 | 186.557 | 1.858 | 0.0063 | 0.0008 | 1.20E-16 | 99.02 | 548.5 | 4.5 |
| 103-36 | 187.288 | 0.946 | 188.905 | 0.940 | 0.0054 | 0.0005 | 1.90E-16 | 99.16 | 549.7 | 2.4 |
| 103-31 | 188.881 | 1.006 | 189.630 | 1.008 | 0.0025 | 0.0002 | 5.30E-16 | 99.62 | 550.5 | 2.4 |
| 103-24 | 199.310 | 3.955 | 210.872 | 3.799 | 0.0391 | 0.0056 | 1.50E-17 | 94.53 | 552.0 | 4.5 |
| 103-17 | 187.184 | 1.039 | 188.444 | 1.034 | 0.0042 | 0.0005 | 1.80E-16 | 99.35 | 552.1 | 2.5 |
| 103-15 | 192.285 | 2.554 | 194.595 | 2.425 | 0.0078 | 0.0030 | 2.70E-17 | 98.83 | 552.6 | 9.4 |
| 103-51 | 190.136 | 0.933 | 190.742 | 0.929 | 0.0020 | 0.0004 | 2.35E-16 | 99.70 | 552.6 | 2.2 |
| 103-53 | 187.928 | 0.952 | 193.052 | 0.959 | 0.0173 | 0.0005 | 2.77E-16 | 97.36 | 553.2 | 2.5 |
| 103-27 | 164.470 | 3.064 | 166.331 | 3.058 | 0.0062 | 0.0016 | 5.25E-17 | 98.90 | 554.9 | 7.2 |
| 103-57 | 189.305 | 0.982 | 190.446 | 0.979 | 0.0038 | 0.0004 | 2.14E-16 | 99.42 | 555.3 | 2.3 |
| 103-42 | 185.019 | 3.513 | 186.695 | 3.432 | 0.0056 | 0.0030 | 2.72E-17 | 99.12 | 556.3 | 8.2 |
| 103-34 | 190.545 | 3.258 | 191.083 | 2.962 | 0.0017 | 0.0046 | 1.72E-17 | 99.73 | 556 | 11 |
| 103-46 | 161.017 | 2.040 | 172.051 | 2.010 | 0.0373 | 0.0025 | 3.89E-17 | 93.60 | 558 | 11 |
| 103-52 | 187.268 | 1.211 | 188.447 | 1.202 | 0.0039 | 0.0007 | 1.23E-16 | 99.39 | 560.7 | 6.4 |
| 103-55 | 192.882 | 2.872 | 198.738 | 2.802 | 0.0198 | 0.0031 | 2.92E-17 | 97.07 | 562.2 | 7.2 |

| | | | | | | | | | | |
|---|---|---|---|---|---|---|---|---|---|---|
| 103-37 | 191.110 | 4.328 | 194.911 | 3.965 | 0.0128 | 0.0064 | 1.33E-17 | 98.06 | 563.0 | 2.4 |
| 103-54 | 177.585 | 3.323 | 183.334 | 3.179 | 0.0194 | 0.0042 | 1.90E-17 | 96.88 | 571 | 10 |
| 103-62 | 190.002 | 2.876 | 193.742 | 2.794 | 0.0126 | 0.0029 | 2.67E-17 | 98.08 | 578.2 | 9.8 |
| 103-40 | 196.328 | 4.184 | 200.561 | 3.748 | 0.0143 | 0.0068 | 1.43E-17 | 97.90 | 608 | 12 |

[1]J value (2s) - 1.8955E-03 ± 0.3399

# APPENDIX J

# CHAPTER 5 SUPPLEMENT:

# (U-TH)/HE THERMOCHRONOLOGIC DATA FROM ZANSKAR GORGE AND LEH-MANALI ROAD

Table A5.1. (U-Th)/He thermochronologic data for samples from Zanskar Gorge and Leh-Manali road transects

| Sample name | $[^4He]^a$ | $[^{238}U]^a$ | $[^{232}Th]^a$ | $Age_R^b$ | $R1^c$ | $R2^c$ | $L^c$ | $T1^c$ | $T2^c$ | $F_T^d$ | $Age_C^e$ | Err. |
|---|---|---|---|---|---|---|---|---|---|---|---|---|
| | ($ncm^3$) | (ng) | (ng) | (Ma) | (μm) | (μm) | (μm) | (μm) | (μm) | | (Ma) | $(2\sigma)^f$ |
| *07-AT-ZG-E zircon* | | | | | | | | | | | | |
| z001 | 0.7913 | 0.8296 | 0.5365 | 6.80 | 36.4 | 39.7 | 133.8 | 33.3 | 34.4 | 0.718 | 9.48 | 0.32 |
| z002 | 3.7055 | 2.5217 | 1.6012 | 10.50 | 67.1 | 65.6 | 277.3 | 58.5 | 75.3 | 0.840 | 12.51 | 0.39 |
| z003 | 2.3102 | 1.4630 | 1.0675 | 11.07 | 67.4 | 49.3 | 224.0 | 44.8 | 46.5 | 0.815 | 13.59 | 0.41 |
| z004 | 7.8350 | 3.7052 | 2.4847 | 15.00 | 66.1 | 68.9 | 331.2 | 58.8 | 58.7 | 0.850 | 17.64 | 0.54 |
| z005 | 1.9605 | 1.3374 | 0.4098 | 11.23 | 45.3 | 41.2 | 150.6 | 34.7 | 44.7 | 0.749 | 14.99 | 0.52 |
| z006 | 0.9326 | 0.8789 | 0.5657 | 7.57 | 51.9 | 47.9 | 185.5 | 47.6 | 36.5 | 0.786 | 9.64 | 0.31 |
| z007 | 1.0817 | 0.8144 | 0.6693 | 9.14 | 25.2 | 40.9 | 160.2 | 49.0 | 37.2 | 0.679 | 13.46 | 0.49 |
| z008 | 5.0395 | 1.6938 | 1.9043 | 19.31 | 29.1 | 34.8 | 155.3 | 35.7 | 33.0 | 0.688 | 28.08 | 0.82 |
| z009 | 1.0091 | 0.4681 | 0.3479 | 15.07 | 30.5 | 30.2 | 162.8 | 32.5 | 34.6 | 0.683 | 22.06 | 0.69 |
| z010 | 2.6819 | 2.0076 | 1.2675 | 9.56 | 55.9 | 51.0 | 247.7 | 56.5 | 54.4 | 0.808 | 11.83 | 0.35 |
| *07-AT-ZG-G zircon* | | | | | | | | | | | | |
| z001 | 4.4637 | 2.5891 | 2.1499 | 11.85 | 55.6 | 65.9 | 234.6 | 51.2 | 60.9 | 0.821 | 14.42 | 0.44 |
| z003 | 2.8390 | 1.6390 | 1.2771 | 12.02 | 42.5 | 58.5 | 235.5 | 54.6 | 50.1 | 0.793 | 15.16 | 0.46 |
| z004 | 4.4502 | 1.3578 | 1.0957 | 22.60 | 50.1 | 54.8 | 276.3 | 50.6 | 62.4 | 0.809 | 27.95 | 0.84 |
| z005 | 4.3045 | 4.0412 | 2.4394 | 7.66 | 65.6 | 57.5 | 263.4 | 47.6 | 61.1 | 0.830 | 9.23 | 0.29 |
| *07-AT-ZG-H zircon* | | | | | | | | | | | | |
| z001 | 1.7648 | 1.1082 | 1.0235 | 10.75 | 42.2 | 28.7 | 254.5 | 46.5 | 35.0 | 0.728 | 14.75 | 0.73 |
| z002 | 5.8421 | 5.0768 | 3.2342 | 8.22 | 104.0 | 86.0 | 303.5 | 86.0 | 74.3 | 0.878 | 9.37 | 0.45 |
| z003 | 8.9036 | 7.4851 | 7.8747 | 7.83 | 70.0 | 45.4 | 280.4 | 68.8 | 49.5 | 0.815 | 9.61 | 0.46 |
| z004 | 4.2821 | 4.7143 | 2.4547 | 6.65 | 70.5 | 69.0 | 320.0 | 82.1 | 84.9 | 0.849 | 7.83 | 0.40 |
| z005 | 3.2830 | 2.4842 | 3.0172 | 8.44 | 79.5 | 79.5 | 312.5 | 96.8 | 106.5 | 0.855 | 9.87 | 0.47 |
| z006 | 5.2236 | 1.2548 | 1.0588 | 28.49 | 40.6 | 31.4 | 217.5 | 28.1 | 47.6 | 0.731 | 38.97 | 1.13 |
| z008 | 0.3879 | 0.4680 | 0.2547 | 6.04 | 31.0 | 32.0 | 128.4 | 39.5 | 28.7 | 0.673 | 8.97 | 0.30 |
| z009 | 1.7666 | 1.5605 | 0.9131 | 8.18 | 53.0 | 50.5 | 169.4 | 42.2 | 45.0 | 0.785 | 10.42 | 0.33 |
| z010 | 2.1406 | 1.5138 | 0.8187 | 10.31 | 44.7 | 32.4 | 121.4 | 32.1 | 30.0 | 0.709 | 14.53 | 0.44 |
| z011 | 0.7238 | 0.9405 | 0.3717 | 5.79 | 36.1 | 34.7 | 103.5 | 24.7 | 26.5 | 0.687 | 8.42 | 0.27 |
| *07-AT-ZG-I zircon* | | | | | | | | | | | | |
| z001 | 16.645 | 3.8028 | 1.9702 | 31.99 | 81.0 | 81.0 | 242.0 | 58.8 | 58.4 | 0.857 | 37.32 | 1.87 |
| z003 | 2.2548 | 1.3673 | 0.8313 | 11.85 | 89.5 | 73.5 | 264.0 | 71.5 | 84.9 | 0.840 | 13.85 | 0.52 |
| z007 | 3.2244 | 1.8858 | 1.4334 | 11.91 | 81.0 | 76.0 | 219.0 | 64.2 | 66.0 | 0.845 | 14.10 | 0.39 |
| z008 | 0.3485 | 0.3427 | 0.1972 | 7.36 | 37.9 | 30.7 | 159.0 | 44.4 | 51.4 | 0.696 | 10.58 | 0.31 |
| z009 | 0.1595 | 0.1823 | 0.1392 | 6.10 | 31.7 | 28.6 | 117.0 | 33.8 | 34.5 | 0.650 | 9.37 | 0.29 |
| z010 | 0.9868 | 0.8541 | 0.6135 | 8.12 | 41.4 | 41.0 | 240.3 | 42.6 | 47.5 | 0.765 | 10.61 | 0.34 |
| z012 | 0.4238 | 0.4089 | 0.3410 | 7.12 | 32.6 | 34.8 | 125.7 | 24.1 | 27.2 | 0.693 | 10.27 | 0.36 |
| z013 | 1.5256 | 0.8099 | 0.5158 | 13.45 | 59.8 | 38.5 | 212.1 | 64.8 | 42.6 | 0.778 | 17.29 | 0.48 |
| z014 | 2.3258 | 0.7311 | 0.7144 | 21.23 | 31.8 | 26.6 | 177.0 | 35.3 | 29.2 | 0.675 | 31.43 | 0.93 |
| z016 | 0.3259 | 0.3183 | 0.1813 | 7.42 | 32.2 | 34.5 | 125.1 | 31.2 | 35.2 | 0.685 | 10.83 | 0.34 |
| z017 | 2.8633 | 1.6243 | 0.7839 | 13.00 | 55.1 | 66.3 | 171.0 | 45.3 | 49.6 | 0.804 | 16.16 | 0.46 |
| z018 | 0.3095 | 0.3439 | 0.2093 | 6.47 | 27.8 | 31.7 | 97.3 | 24.9 | 18.6 | 0.644 | 10.04 | 0.33 |
| z019 | 0.2793 | 0.2315 | 0.2633 | 7.82 | 37.6 | 38.8 | 151.3 | 35.2 | 29.6 | 0.728 | 10.74 | 0.35 |
| z020 | 1.0071 | 1.1141 | 0.5440 | 6.66 | 41.6 | 56.1 | 139.5 | 36.3 | 37.9 | 0.760 | 8.77 | 0.27 |
| z021 | 0.2973 | 0.2610 | 0.1325 | 8.36 | 28.4 | 30.4 | 112.2 | 33.2 | 21.6 | 0.651 | 12.84 | 0.43 |
| z022 | 0.6720 | 0.6035 | 0.4495 | 7.78 | 28.7 | 32.0 | 139.0 | 31.4 | 39.7 | 0.668 | 11.65 | 0.36 |
| z023 | 0.3440 | 0.3477 | 0.2758 | 6.85 | 57.8 | 43.4 | 157.4 | 37.1 | 39.3 | 0.774 | 8.85 | 0.28 |
| *07-AT-ZG-N zircon* | | | | | | | | | | | | |
| z002 | 13.167 | 9.5308 | 3.4388 | 10.46 | 118.0 | 121.0 | 596.5 | 114.5 | 158.5 | 0.913 | 11.46 | 0.60 |
| z003 | 1.8815 | 1.2702 | 0.9041 | 10.42 | 37.4 | 34.8 | 185.0 | 38.2 | 41.6 | 0.727 | 14.34 | 0.74 |
| z004 | 1.1335 | 1.2004 | 0.3047 | 7.32 | 28.3 | 28.5 | 153.0 | 27.3 | 24.5 | 0.671 | 10.92 | 0.59 |
| z005 | 5.2436 | 3.4263 | 2.9532 | 10.45 | 51.0 | 40.3 | 186.0 | 36.7 | 37.6 | 0.770 | 13.57 | 0.67 |
| z006 | 12.530 | 6.5015 | 4.7301 | 13.52 | 56.1 | 73.4 | 284.0 | 52.8 | 48.2 | 0.838 | 16.12 | 0.47 |
| z007 | 6.1700 | 5.2570 | 2.3395 | 8.73 | 42.8 | 27.7 | 123.2 | 22.7 | 30.9 | 0.692 | 12.61 | 0.39 |
| z008 | 1.9359 | 1.6735 | 1.0402 | 8.29 | 64.3 | 57.2 | 209.0 | 51.7 | 52.1 | 0.817 | 10.14 | 0.31 |
| z009 | 5.5171 | 5.4482 | 2.3498 | 7.55 | 83.4 | 60.6 | 201.9 | 44.8 | 50.8 | 0.835 | 9.05 | 0.28 |
| z010 | 0.3611 | 0.3616 | 0.2735 | 6.97 | 35.4 | 35.0 | 141.7 | 34.4 | 40.5 | 0.704 | 9.90 | 0.38 |
| z011 | 9.2964 | 5.9391 | 3.9949 | 11.10 | 54.5 | 50.2 | 212.5 | 42.9 | 43.3 | 0.801 | 13.87 | 0.40 |

*07-AT-ZG-O zircon*

| | | | | | | | | | | | | |
|---|---|---|---|---|---|---|---|---|---|---|---|---|
| z002 | 9.8706 | 8.1061 | 3.6484 | 9.05 | 54.6 | 58.7 | 160.9 | 40.3 | 0.0 | 0.800 | 11.31 | 0.35 |
| z003 | 0.3200 | 0.2526 | 0.2823 | 8.24 | 25.7 | 28.7 | 150.9 | 22.8 | 26.1 | 0.653 | 12.63 | 0.74 |
| z005 | 0.8732 | 0.6694 | 0.4921 | 9.14 | 23.8 | 26.8 | 172.5 | 25.0 | 26.3 | 0.642 | 14.23 | 0.72 |
| z006 | 2.6071 | 1.5867 | 1.6643 | 10.82 | 36.7 | 40.0 | 177.3 | 39.3 | 32.5 | 0.737 | 14.68 | 0.46 |
| z007 | 1.7389 | 1.2640 | 0.6631 | 10.06 | 45.0 | 45.0 | 188.4 | 35.5 | 38.7 | 0.773 | 13.02 | 0.69 |
| z009 | 9.9513 | 4.0999 | 2.8652 | 17.11 | 50.5 | 45.3 | 215.5 | 36.7 | 37.9 | 0.789 | 21.70 | 1.12 |
| z010 | 7.2927 | 4.4098 | 3.2074 | 11.60 | 40.9 | 37.8 | 177.6 | 36.0 | 36.6 | 0.744 | 15.59 | 0.79 |
| z012 | 0.5078 | 0.4618 | 0.3196 | 7.77 | 30.1 | 18.0 | 135.1 | 32.8 | 27.2 | 0.589 | 13.20 | 0.57 |
| z013 | 2.5298 | 1.4599 | 1.8781 | 10.93 | 30.6 | 29.1 | 167.2 | 42.8 | 31.0 | 0.675 | 16.19 | 0.50 |
| z015 | 1.7008 | 1.2255 | 0.3494 | 10.69 | 25.8 | 24.8 | 187.0 | 34.3 | 31.8 | 0.646 | 16.55 | 0.63 |
| z016 | 1.0191 | 0.8420 | 0.6494 | 8.42 | 42.5 | 32.1 | 240.0 | 38.5 | 43.6 | 0.742 | 11.34 | 0.37 |
| z017 | 2.6948 | 1.8352 | 0.8004 | 10.94 | 39.6 | 35.1 | 196.0 | 42.6 | 53.8 | 0.734 | 14.91 | 0.45 |
| z018 | 3.0474 | 1.8696 | 1.9803 | 10.72 | 26.1 | 25.5 | 168.0 | 27.4 | 31.5 | 0.642 | 16.68 | 0.48 |
| z019 | 4.2856 | 3.0299 | 1.4191 | 10.47 | 24.2 | 26.0 | 153.5 | 26.7 | 32.7 | 0.633 | 16.54 | 0.51 |
| z020 | 3.4562 | 2.6386 | 1.5865 | 9.43 | 34.9 | 28.5 | 138.0 | 35.5 | 25.9 | 0.682 | 13.83 | 0.41 |
| z021 | 0.8732 | 0.6629 | 0.6325 | 8.84 | 30.0 | 34.1 | 151.0 | 30.1 | 31.7 | 0.690 | 12.80 | 0.41 |
| z022 | 3.0208 | 1.9213 | 1.1678 | 11.30 | 49.6 | 42.7 | 192.0 | 41.5 | 37.9 | 0.776 | 14.57 | 0.43 |
| z023 | 3.1797 | 2.1668 | 2.0294 | 9.88 | 42.1 | 34.3 | 169.5 | 38.2 | 39.3 | 0.731 | 13.52 | 0.40 |
| z024 | 2.3819 | 1.3270 | 1.1919 | 12.17 | 39.7 | 27.9 | 209.5 | 31.2 | 41.2 | 0.712 | 17.09 | 0.52 |
| z025 | 1.6145 | 1.1256 | 1.5918 | 8.84 | 35.8 | 32.7 | 168.0 | 40.3 | 28.1 | 0.709 | 12.47 | 0.39 |
| z026 | 3.0379 | 2.9324 | 1.2710 | 7.73 | 40.1 | 43.0 | 131.0 | 27.8 | 22.8 | 0.740 | 10.44 | 0.32 |
| z027 | 5.1025 | 3.7459 | 1.7772 | 10.07 | 46.6 | 42.9 | 203.5 | 47.6 | 50.3 | 0.771 | 13.05 | 0.43 |
| z028 | 1.9360 | 1.6598 | 1.1578 | 8.23 | 48.8 | 42.4 | 194.0 | 45.0 | 42.1 | 0.772 | 10.66 | 0.33 |
| z029 | 10.199 | 6.9084 | 1.5191 | 11.53 | 48.5 | 48.8 | 176.0 | 27.1 | 36.8 | 0.785 | 14.70 | 1.84 |
| z030 | 15.258 | 9.4167 | 5.0964 | 11.81 | 61.5 | 51.5 | 222.5 | 40.4 | 41.2 | 0.814 | 14.50 | 0.44 |
| z031 | 0.8919 | 0.8284 | 0.6130 | 7.54 | 37.5 | 38.1 | 158.5 | 30.6 | 33.9 | 0.731 | 10.31 | 0.33 |
| z032 | 1.0778 | 0.7668 | 0.6214 | 9.70 | 45.9 | 40.5 | 189.5 | 35.0 | 32.1 | 0.765 | 12.68 | 0.49 |
| z033 | 0.3160 | 0.2595 | 0.2263 | 8.30 | 34.0 | 37.9 | 148.5 | 33.9 | 35.7 | 0.713 | 11.64 | 0.51 |
| z034 | 1.8492 | 1.6179 | 1.1393 | 8.06 | 42.4 | 39.1 | 182.0 | 31.9 | 32.9 | 0.754 | 10.69 | 0.32 |
| z035 | 2.7769 | 2.0959 | 1.8520 | 9.01 | 42.1 | 43.9 | 186.5 | 34.0 | 34.7 | 0.763 | 11.80 | 0.61 |
| z036 | 1.6656 | 0.9839 | 1.0386 | 11.14 | 44.6 | 37.3 | 181.0 | 32.0 | 33.8 | 0.751 | 14.83 | 0.74 |

*09-AT-ZG-X zircon*

| | | | | | | | | | | | | |
|---|---|---|---|---|---|---|---|---|---|---|---|---|
| z002 | 3.5974 | 1.9584 | 1.5538 | 12.71 | 57.6 | 63.9 | 240.4 | 49.4 | 47.3 | 0.825 | 15.40 | 0.42 |
| z003 | 1.8139 | 1.8348 | 1.4169 | 6.87 | 61.9 | 55.7 | 237.4 | 68.3 | 72.4 | 0.813 | 8.46 | 0.26 |
| z004 | 17.766 | 15.894 | 4.4180 | 8.62 | 64.5 | 50.3 | 189.4 | 42.4 | 41.1 | 0.807 | 10.68 | 0.33 |
| z005 | 4.9951 | 2.9111 | 1.9677 | 12.16 | 65.4 | 56.8 | 238.2 | 56.5 | 53.5 | 0.824 | 14.75 | 0.44 |
| z006 | 3.5717 | 1.9476 | 1.3722 | 12.92 | 64.3 | 54.0 | 246.2 | 50.4 | 59.9 | 0.821 | 15.74 | 0.46 |
| z007 | 1.1965 | 1.1877 | 0.5330 | 7.49 | 64.7 | 62.9 | 223.9 | 72.7 | 71.8 | 0.820 | 9.13 | 0.29 |
| z008 | 1.1210 | 0.9876 | 0.7658 | 7.89 | 45.1 | 34.9 | 197.7 | 33.7 | 39.2 | 0.750 | 10.52 | 0.30 |
| z009 | 2.4505 | 1.7531 | 0.9395 | 10.20 | 34.1 | 47.8 | 205.0 | 39.4 | 37.3 | 0.754 | 13.52 | 0.40 |
| z010 | 0.9480 | 0.5573 | 0.3976 | 11.97 | 36.2 | 61.7 | 183.5 | 63.6 | 60.9 | 0.755 | 15.85 | 0.52 |

*07-AT-ZG-O apatite*

| | | | | | | | | | | | | |
|---|---|---|---|---|---|---|---|---|---|---|---|---|
| a003 | 0.1103 | 0.1520 | 0.1414 | 4.89 | N.D.[g] | 64.7 | 140.0 | N.D. | N.D. | 0.754 | 6.49 | 0.26 |
| a004 | 0.0255 | 0.0237 | 0.0478 | 5.98 | N.D. | 50.3 | 116.3 | N.D. | N.D. | 0.689 | 8.68 | 0.42 |
| a005 | 0.0913 | 0.0822 | 0.2448 | 5.36 | N.D. | 46.5 | 182.5 | N.D. | N.D. | 0.697 | 7.70 | 0.31 |
| a008 | 0.0217 | 0.0285 | 0.0501 | 4.43 | N.D. | 37.7 | 126.6 | N.D. | N.D. | 0.630 | 7.04 | 0.35 |
| a009 | 0.1236 | 0.1098 | 0.3477 | 5.30 | N.D. | 71.7 | 206.0 | N.D. | N.D. | 0.784 | 6.76 | 0.19 |
| a010 | 0.1844 | 0.1962 | 0.4285 | 5.10 | N.D. | 75.7 | 182.1 | N.D. | N.D. | 0.789 | 6.47 | 0.19 |

*08-AT-LM-A zircon*

| | | | | | | | | | | | | |
|---|---|---|---|---|---|---|---|---|---|---|---|---|
| z001 | 1.7712 | 1.0937 | 0.9757 | 10.99 | 70.0 | 51.8 | 204.2 | 46.9 | 41.9 | 0.815 | 13.49 | 0.43 |
| z002 | 13.929 | 10.375 | 2.8929 | 10.35 | 65.7 | 63.5 | 203.5 | 33.7 | 54.2 | 0.828 | 12.51 | 0.43 |
| z003 | 4.7445 | 2.2660 | 1.4300 | 14.97 | 54.5 | 51.4 | 260.8 | 53.0 | 44.7 | 0.811 | 18.47 | 0.55 |
| z004 | 2.4638 | 1.5547 | 1.0503 | 11.23 | 48.0 | 86.0 | 230.4 | 60.9 | 46.9 | 0.824 | 13.63 | 0.43 |
| z005 | 5.0567 | 2.7539 | 0.9414 | 13.96 | 51.1 | 56.3 | 227.5 | 52.4 | 44.7 | 0.808 | 17.28 | 0.55 |

*07-AT-LM-B zircon*

| | | | | | | | | | | | | |
|---|---|---|---|---|---|---|---|---|---|---|---|---|
| z001 | 1.5420 | 1.5443 | 1.5354 | 6.65 | 53.1 | 49.2 | 194.7 | 42.8 | 41.6 | 0.791 | 8.40 | 0.26 |
| z002 | 1.1573 | 0.9936 | 0.9233 | 7.85 | 37.8 | 45.4 | 154.8 | 32.3 | 33.1 | 0.745 | 10.54 | 0.34 |
| z003 | 2.6681 | 1.9380 | 1.1073 | 9.97 | 38.9 | 39.1 | 138.7 | 31.3 | 31.7 | 0.729 | 13.68 | 0.41 |
| z004 | 2.0678 | 1.0797 | 0.6888 | 13.68 | 36.9 | 42.9 | 154.5 | 32.5 | 31.0 | 0.740 | 18.49 | 0.59 |
| z005 | 2.6856 | 2.5264 | 1.2977 | 7.79 | 53.3 | 69.4 | 186.8 | 41.6 | 53.4 | 0.811 | 9.61 | 0.31 |

*07-AT-LM-G zircon*

| | | | | | | | | | | | | |
|---|---|---|---|---|---|---|---|---|---|---|---|---|
| z001 | 2.3824 | 1.0297 | 0.8098 | 16.03 | 45.4 | 47.0 | 251.4 | 50.2 | 41.8 | 0.787 | 20.36 | 0.66 |
| z002 | 11.807 | 5.8820 | 3.5775 | 14.42 | 51.2 | 57.7 | 243.0 | 41.9 | 50.3 | 0.812 | 17.76 | 0.56 |
| z003 | 1.5042 | 1.4041 | 0.7036 | 7.87 | 64.0 | 52.9 | 200.4 | 38.4 | 58.0 | 0.810 | 9.72 | 0.32 |
| z004 | 3.9778 | 2.5841 | 1.7427 | 10.91 | 59.3 | 66.5 | 217.7 | 44.2 | 58.1 | 0.824 | 13.24 | 0.42 |
| z005 | 2.3066 | 1.7515 | 0.9520 | 9.59 | 41.9 | 56.6 | 160.8 | 42.0 | 40.9 | 0.771 | 12.45 | 0.40 |
| *07-AT-LM-H zircon* | | | | | | | | | | | | |
| z001 | 1.9052 | 1.3101 | 0.8496 | 10.37 | 64.7 | 48.6 | 192.6 | 49.8 | 42.6 | 0.802 | 12.92 | 0.42 |
| z003 | 1.7226 | 1.9215 | 0.9609 | 6.59 | 73.9 | 58.7 | 187.5 | 44.5 | 54.4 | 0.821 | 8.03 | 0.27 |
| z004 | 2.5621 | 2.7115 | 1.3521 | 6.95 | 55.2 | 49.4 | 197.2 | 45.2 | 47.3 | 0.796 | 8.73 | 0.28 |
| z005 | 1.7079 | 1.2504 | 0.7010 | 9.91 | 38.7 | 38.5 | 160.6 | 21.1 | 30.2 | 0.739 | 13.41 | 0.47 |
| z006 | 1.1003 | 0.6642 | 0.9037 | 10.31 | 37.4 | 34.2 | 146.8 | 32.3 | 25.3 | 0.713 | 14.45 | 0.45 |
| z007 | 1.8220 | 0.9282 | 1.2276 | 12.29 | 30.8 | 31.3 | 161.9 | 29.8 | 34.4 | 0.686 | 17.92 | 0.56 |
| *07-AT-LM-K zircon* | | | | | | | | | | | | |
| z001 | 19.514 | 9.1050 | 5.6070 | 15.37 | 115.8 | 120.5 | 349.1 | 89.6 | 96.8 | 0.899 | 17.09 | 0.56 |
| z002 | 33.800 | 22.226 | 7.2236 | 11.61 | 124.2 | 116.7 | 451.7 | 102.4 | 89.2 | 0.910 | 12.76 | 0.45 |
| z003 | 1.7295 | 1.9292 | 0.6498 | 6.83 | 64.0 | 59.2 | 211.5 | 51.7 | 47.3 | 0.822 | 8.30 | 0.29 |
| z004 | 16.031 | 10.610 | 5.9182 | 10.97 | 139.9 | 171.3 | 618.6 | 120.4 | 168.0 | 0.929 | 11.81 | 0.39 |
| z005 | 0.7890 | 0.7593 | 0.4209 | 7.55 | 79.0 | 66.2 | 264.1 | 67.7 | 50.7 | 0.849 | 8.90 | 0.31 |
| *07-AT-LM-L zircon* | | | | | | | | | | | | |
| z001 | 3.2467 | 2.7329 | 1.9177 | 8.38 | 59.9 | 57.1 | 231.6 | 66.2 | 48.2 | 0.816 | 10.26 | 0.36 |
| z002 | 3.3601 | 2.0716 | 1.9781 | 10.88 | 45.4 | 52.2 | 272.7 | 68.8 | 56.5 | 0.794 | 13.71 | 0.44 |
| z003 | 0.7587 | 0.7734 | 0.3773 | 7.23 | 28.6 | 29.1 | 178.0 | 24.8 | 19.7 | 0.682 | 10.60 | 0.36 |
| z004 | 0.4220 | 0.4202 | 0.3200 | 7.00 | 39.6 | 39.8 | 180.4 | 31.8 | 44.6 | 0.746 | 9.38 | 0.35 |
| z005 | 1.4409 | 1.3321 | 0.5853 | 8.06 | 56.0 | 42.4 | 226.3 | 45.8 | 44.0 | 0.792 | 10.17 | 0.37 |

[a]Absolute measured $^{4}He$, $^{238}U$ and $^{232}Th$ concentrations are used to calculate the 'Raw Age' that is uncorrected for the effects of $^{4}He$ loss due to alpha particle recoil.

[b]The 'Raw Age' was calculated with an iterative approach to solving the age equation.

[c]R1 and R2 describe the perpendicular half widths of the zircon crystal. L describes the total length of the zircon crystal and T1 and T2 describe the height fo the pyramidal termination of the zircon crystals.

[d]The mean FT correction was calculated following procedures defined by Hourigan et al. (2005).

[e]The FT corrected age of the crystal. The FT correction was applied to the raw age following procedures defined by Farley et al. (1996).

[f]The propagated 1σ and 2σ analytical errors.

[g]N.D. = not determined.

# APPENDIX K

# CHAPTER 5 SUPPLEMENT:

# THERMAL MODEL

First all components of this thermal model are defined, which we facilitate by using a cartoon that demonstrates the evolution of $^4He$ in a given grain over time. We begin with Figure A1a, which shows a simple cooling history that the grain would have undergone had it not been reheated. $^4He_{initial}$, defined as the amount of $^4He$ that the grain should have contained had it not been subject to a thermal event, is labeled, as is the theoretical initial age ($t_{initial}$) of the grain.

Figure A5.2.1 depicts the simple thermal model that we assume for the grain, which we describe in terms of temporal evolution. Beginning at the theoretical initial age ($t_{initial}$), the grain accumulates $^4He$ until $t_{reheat}$, at which time it has accumulated $^4He_{reheat}$. At $t_{reheat}$, the grain is instantaneously heated and subsequently loses some amount of $^4He$, defined as $4He_{lost}$. The grain is then held for some duration before it effectively closes to the diffusive loss of $^4He$, and begins to acquire $^4He$ along a different trajectory. We define this as $t_{close}$, where

$$t_{close} = t_{reheat} - \text{duration} \qquad \text{Eq. A1}$$

The grain evolves along the new trajectory from $t_{close}$ until present, where we measure the concentration of $^4He$ present today, $^4He_{meas}$.

$^4He_{meas}$ can be defined as the sum of the amount of $^4He$ that was not lost during the reheating event ($^4He_{not\_lost}$) and the amount of $^4He$ that has grown into the system since it began to retain $^4He$ after reheating ($^4He_{close}$). Determining the amount of $^4He_{not\_lost}$ requires manipulation of simple equations. The first is the equation for fractional loss (*f*) of a sphere from *Crank* [1975]:

$$f = 1 - (6/\pi^2)\sum_{n=1}^{\infty}(1/n^2)\exp(-n^2\pi^2 Dt/r^2) \qquad \text{Eq. A2}$$

where $D$ is the diffusivity at a specific temperature (diffusivity calculated using Arrhenius parameters from *Reiners et al.* [2004]), $r$ is the measured radius of each grain, and $t$ is the unknown duration of the reheating event. The next two equations indirectly relate $f$ to $^4He_{not\_lost}$:

$$^4He_{reheat} = {}^4He_{not\_lost} + {}^4He_{lost} \qquad \text{Eq. A3}$$

$$f = {}^4He_{lost} / {}^4He_{reheat} \qquad \text{Eq. A4}$$

where $^4He_{reheat}$ is the amount of $^4He$ present at $t_{reheat}$, determined from measured U and Th concentrations by using the age equation for the (U-Th)/He system [*Harrison and Zeitler,* 2005], and $^4He_{lost}$ is the amount of $^4He$ that was diffusively lost during the reheating event. Determining the amount of $^4He_{close}$ is simpler, as it involves using the relationship in Eq. A1, to determine $t_{close}$. Using the age equation with $t_{close}$, $^4He_{close}$ is calculated. Finally, $^4He_{close}$ and $^4He_{not\_lost}$ are summed and compared to $^4He_{meas}$ until the correct combination of durations and $t_{reheat}$ is found.

In order to calculate the theoretical initial ages of the other zircon grains in the dataset, the thermal history, which is a unique combination of $t_{reheat}$ and duration for a given temperature and theoretical initial age of the modeled grain, must be removed such that $^4He_{reheat}$ can be calculated. For this calculation, $t_{close}$ is known from Eq. A1, so $^4He_{close}$ is calculated for every grain from the age equation. To obtain $^4He_{not\_lost}$, $^4He_{close}$ is subtracted from $^4He_{meas}$. Using Eq. A2, $f$ is calculated and to determine $^4He_{lost}$ by combining Eqs. A3 and A4. Finally,

$^4He_{reheat}$ is calculated from Eq. A3, and used with the known U and Th concentrations of each grain, to calculate the time between $t_{initial}$ and $t_{reheat}$.

## REFERENCES


Crank, J., 1975, The mathematics of diffusion: Oxford University Press, London.

Harrison, T. M., and Zeitler, P. K., 2005, Fundamentals of Noble Gas Thermochronometry: Reviews in Mineralogy and Geochemistry, v. 58, p. 123-149.

Reiners, P. W., Spell, T. L., Nicolescu, S., and Zanetti, K. A., 2004, Zircon (U-Th)/He thermochronometry: He diffusion and comparisons with $^{40}Ar/^{39}Ar$ dating: Geochimica et Cosmochimica Acta, v. 68, p. 1857-1887.


## FIGURE CAPTIONS

Figure A5.2.1. (a) $^4He$ evolution over time of a grain that has not experienced a thermal event after it cooled through its bulk closure temperatures. (b) $^4He$ evolution of a grain that has been subject to a metamorphic event, during which it retained some $^4He$. All quantities are described in the text except for $t_{measured}$, which is the date of the grain that we calculate today after measure $^4He$, U and Th and making all appropriate corrections.

Figure A5.2.1

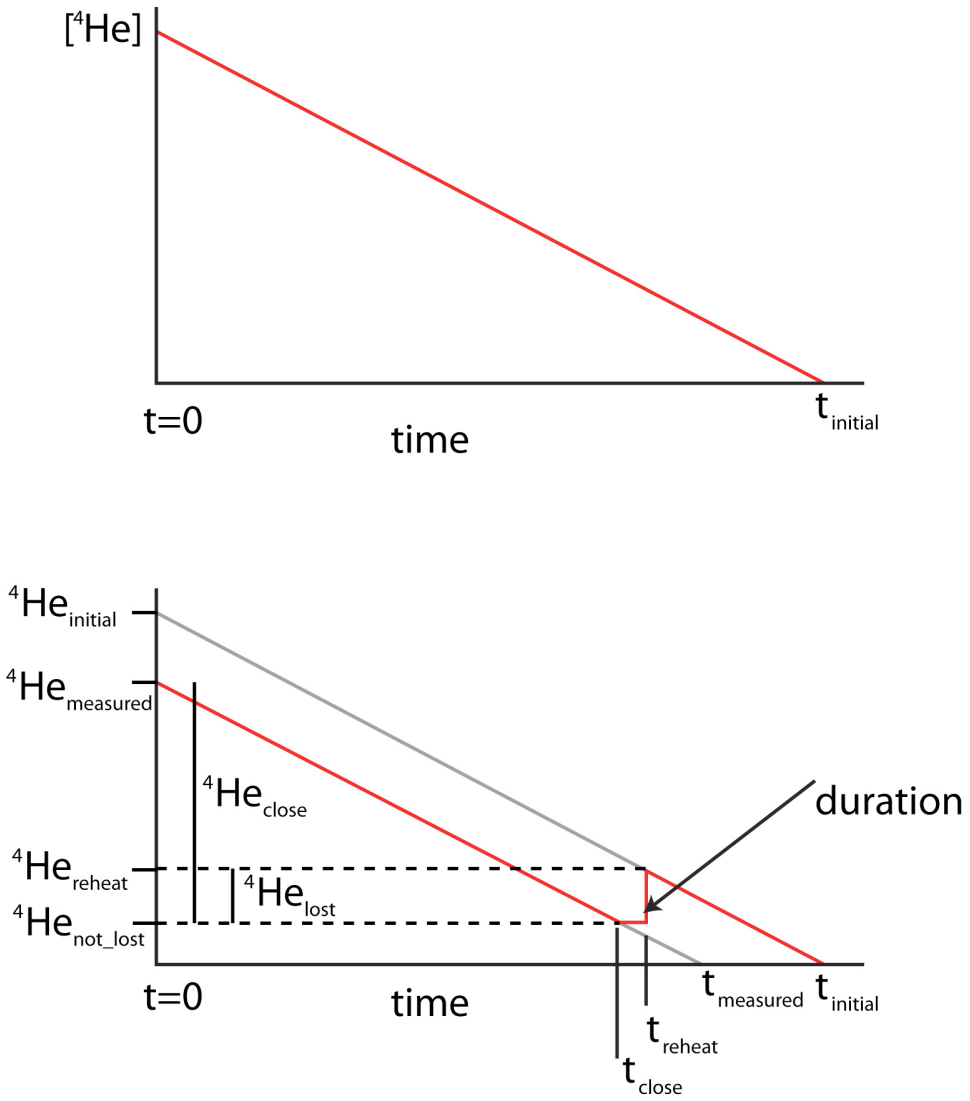
[4He]
t=0
time
t initial
4He initial
4He measured
4He close
4He reheat
4He lost
4He not_lost
duration
t=0
time
t measured
t initial
t reheat
t close

# APPENDIX L

# CHAPTER 5 SUPPLEMENT:

# INDIVIDUAL GRAIN DURATIONS

Table A5.3. Individual grain duration calculations.

| $t_{reheat}$ (Ma) | $T_{max}$=200 T.I.A. = 30 Ma duration (my) | $T_{max}$=200 T.I.A. =40 Ma duration (my) | $T_{max}$=180 T.I.A. = 30 Ma duration (my) | $T_{max}$=180 T.I.A. =40 Ma duration (my) |
|---|---|---|---|---|
| *Grain info: age - 7.83 +/- 0.20 Ma; half-width - 70 (microns)* | | | | |
| 7 | 2.3 | 2.7 | 6.6 | - |
| 7.1 | 2.3 | 2.7 | 6.7 | - |
| 7.2 | 2.3 | 2.7 | 6.7 | - |
| 7.3 | 2.4 | 2.7 | 6.8 | - |
| 7.4 | 2.4 | 2.8 | 6.8 | - |
| 7.5 | 2.4 | 2.8 | 6.8 | - |
| 7.6 | 2.4 | 2.8 | 6.9 | - |
| 7.7 | 2.5 | 2.9 | 6.9 | - |
| 7.8 | 2.5 | 2.9 | 6.9 | - |
| 7.9 | 2.5 | 2.9 | 7 | - |
| 8 | 2.6 | 2.9 | 7 | - |
| 8.1 | 2.6 | 3 | 7.1 | - |
| 8.2 | 2.6 | 3 | 7.1 | - |
| 8.3 | 2.7 | 3 | 7.1 | - |
| 8.4 | 2.7 | 3.1 | 7.2 | - |
| 8.5 | 2.8 | 3.1 | 7.2 | - |
| 8.6 | 2.8 | 3.1 | 7.3 | - |
| 8.7 | 2.8 | 3.2 | 7.3 | - |
| 8.8 | 2.9 | 3.2 | 7.3 | - |
| 8.9 | 2.9 | 3.3 | 7.4 | - |
| 9 | 2.9 | 3.3 | 7.4 | - |
| 9.1 | 3 | 3.3 | 7.5 | 9.1 |
| 9.2 | 3 | 3.4 | 7.5 | 9.1 |
| 9.3 | 3.1 | 3.4 | 7.6 | 9.2 |
| 9.4 | 3.1 | 3.4 | 7.6 | 9.2 |
| 9.5 | 3.2 | 3.5 | 7.6 | 9.2 |
| 9.6 | 3.2 | 3.5 | 7.7 | 9.3 |
| 9.7 | 3.3 | 3.6 | 7.7 | 9.3 |
| 9.8 | 3.3 | 3.6 | 7.8 | 9.4 |
| 9.9 | 3.4 | 3.7 | 7.8 | 9.4 |
| 10 | 3.4 | 3.7 | 7.9 | 9.4 |
| 10.1 | 3.5 | 3.8 | 7.9 | 9.5 |
| 10.2 | 3.5 | 3.8 | 7.9 | 9.5 |
| 10.3 | 3.6 | 3.8 | 8 | 9.6 |
| 10.4 | 3.6 | 3.9 | 8 | 9.6 |
| 10.5 | 3.7 | 3.9 | 8.1 | 9.7 |
| 10.6 | 3.7 | 4 | 8.1 | 9.7 |
| 10.7 | 3.8 | 4.1 | 8.2 | 9.8 |
| 10.8 | 3.8 | 4.1 | 8.2 | 9.8 |
| 10.9 | 3.9 | 4.2 | 8.3 | 9.8 |
| 11 | 4 | 4.2 | 8.3 | 9.9 |
| *Grain info: age - 8.03 +/- 0.27 Ma; half-width - 66 (microns)* | | | | |
| 7 | 2.1 | 2.4 | 6.3 | - |
| 7.1 | 2.1 | 2.5 | 6.3 | - |
| 7.2 | 2.1 | 2.5 | 6.4 | - |
| 7.3 | 2.2 | 2.5 | 6.4 | - |
| 7.4 | 2.2 | 2.5 | 6.4 | - |
| 7.5 | 2.2 | 2.6 | 6.5 | - |
| 7.6 | 2.3 | 2.6 | 6.5 | - |
| 7.7 | 2.3 | 2.6 | 6.6 | - |
| 7.8 | 2.3 | 2.7 | 6.6 | - |
| 7.9 | 2.4 | 2.7 | 6.6 | - |
| 8 | 2.4 | 2.7 | 6.7 | - |
| 8.1 | 2.4 | 2.8 | 6.7 | 8.2 |
| 8.2 | 2.4 | 2.8 | 6.7 | 8.2 |
| 8.3 | 2.5 | 2.8 | 6.8 | 8.3 |
| 8.4 | 2.5 | 2.8 | 6.8 | 8.3 |
| 8.5 | 2.6 | 2.9 | 6.9 | 8.4 |
| 8.6 | 2.6 | 2.9 | 6.9 | 8.4 |
| 8.7 | 2.6 | 2.9 | 6.9 | 8.4 |

| | | | | |
|---|---|---|---|---|
| 8.8 | 2.7 | 3 | 7 | 8.5 |
| 8.9 | 2.7 | 3 | 7 | 8.5 |
| 9 | 2.7 | 3.1 | 7.1 | 8.6 |
| 9.1 | 2.8 | 3.1 | 7.1 | 8.6 |
| 9.2 | 2.8 | 3.1 | 7.2 | 8.6 |
| 9.3 | 2.9 | 3.2 | 7.2 | 8.7 |
| 9.4 | 2.9 | 3.2 | 7.2 | 8.7 |
| 9.5 | 3 | 3.3 | 7.3 | 8.8 |
| 9.6 | 3 | 3.3 | 7.3 | 8.8 |
| 9.7 | 3 | 3.3 | 7.4 | 8.8 |
| 9.8 | 3.1 | 3.4 | 7.4 | 8.9 |
| 9.9 | 3.1 | 3.4 | 7.5 | 8.9 |
| 10 | 3.2 | 3.5 | 7.5 | 9 |
| 10.1 | 3.2 | 3.5 | 7.5 | 9 |
| 10.2 | 3.3 | 3.6 | 7.6 | 9.1 |
| 10.3 | 3.3 | 3.6 | 7.6 | 9.1 |
| 10.4 | 3.4 | 3.7 | 7.7 | 9.1 |
| 10.5 | 3.5 | 3.7 | 7.7 | 9.2 |
| 10.6 | 3.5 | 3.8 | 7.8 | 9.2 |
| 10.7 | 3.6 | 3.8 | 7.8 | 9.3 |
| 10.8 | 3.6 | 3.9 | 7.9 | 9.3 |
| 10.9 | 3.7 | 3.9 | 7.9 | 9.4 |
| 11 | 3.7 | 4 | 8 | 9.4 |

*Grain info: age - 8.30 +/- 0.29 Ma; half-width - 62 (microns)*

| | | | | |
|---|---|---|---|---|
| 7 | 1.8 | 2.1 | 5.7 | - |
| 7.1 | 1.8 | 2.1 | 5.8 | - |
| 7.2 | 1.9 | 2.2 | 5.8 | 7.2 |
| 7.3 | 1.9 | 2.2 | 5.8 | 7.2 |
| 7.4 | 1.9 | 2.2 | 5.9 | 7.2 |
| 7.5 | 1.9 | 2.2 | 5.9 | 7.3 |
| 7.6 | 2 | 2.3 | 5.9 | 7.3 |
| 7.7 | 2 | 2.3 | 6 | 7.4 |
| 7.8 | 2 | 2.3 | 6 | 7.4 |
| 7.9 | 2 | 2.4 | 6.1 | 7.4 |
| 8 | 2.1 | 2.4 | 6.1 | 7.5 |
| 8.1 | 2.1 | 2.4 | 6.1 | 7.5 |
| 8.2 | 2.1 | 2.4 | 6.2 | 7.5 |
| 8.3 | 2.2 | 2.5 | 6.2 | 7.6 |
| 8.4 | 2.2 | 2.5 | 6.3 | 7.6 |
| 8.5 | 2.2 | 2.5 | 6.3 | 7.7 |
| 8.6 | 2.3 | 2.6 | 6.3 | 7.7 |
| 8.7 | 2.3 | 2.6 | 6.4 | 7.7 |
| 8.8 | 2.3 | 2.6 | 6.4 | 7.8 |
| 8.9 | 2.4 | 2.7 | 6.5 | 7.8 |
| 9 | 2.4 | 2.7 | 6.5 | 7.9 |
| 9.1 | 2.5 | 2.7 | 6.5 | 7.9 |
| 9.2 | 2.5 | 2.8 | 6.6 | 7.9 |
| 9.3 | 2.5 | 2.8 | 6.6 | 8 |
| 9.4 | 2.6 | 2.8 | 6.7 | 8 |
| 9.5 | 2.6 | 2.9 | 6.7 | 8.1 |
| 9.6 | 2.7 | 2.9 | 6.7 | 8.1 |
| 9.7 | 2.7 | 3 | 6.8 | 8.1 |
| 9.8 | 2.7 | 3 | 6.8 | 8.2 |
| 9.9 | 2.8 | 3 | 6.9 | 8.2 |
| 10 | 2.8 | 3.1 | 6.9 | 8.3 |
| 10.1 | 2.9 | 3.1 | 7 | 8.3 |
| 10.2 | 2.9 | 3.2 | 7 | 8.3 |
| 10.3 | 3 | 3.2 | 7 | 8.4 |
| 10.4 | 3 | 3.3 | 7.1 | 8.4 |
| 10.5 | 3.1 | 3.3 | 7.1 | 8.5 |
| 10.6 | 3.2 | 3.4 | 7.2 | 8.5 |
| 10.7 | 3.2 | 3.4 | 7.2 | 8.6 |
| 10.8 | 3.3 | 3.5 | 7.3 | 8.6 |
| 10.9 | 3.3 | 3.5 | 7.3 | 8.7 |
| 11 | 3.4 | 3.6 | 7.4 | 8.7 |

*Grain info: age - 8.30 +/- 0.26 Ma; half-width - 51 (microns)*

| | | | | |
|---|---|---|---|---|
| 7 | 1.6 | 1.3 | 4.7 | 5.7 |
| 7.1 | 1.6 | 1.4 | 4.7 | 5.8 |

| | | | | |
|---|---|---|---|---|
| 7.2 | 1.6 | 1.4 | 4.8 | 5.8 |
| 7.3 | 1.6 | 1.4 | 4.8 | 5.8 |
| 7.4 | 1.7 | 1.4 | 4.8 | 5.9 |
| 7.5 | 1.7 | 1.5 | 4.9 | 5.9 |
| 7.6 | 1.7 | 1.5 | 4.9 | 5.9 |
| 7.7 | 1.7 | 1.5 | 4.9 | 6 |
| 7.8 | 1.8 | 1.5 | 5 | 6 |
| 7.9 | 1.8 | 1.6 | 5 | 6.1 |
| 8 | 1.8 | 1.6 | 5 | 6.1 |
| 8.1 | 1.8 | 1.6 | 5.1 | 6.1 |
| 8.2 | 1.9 | 1.6 | 5.1 | 6.2 |
| 8.3 | 1.9 | 1.7 | 5.2 | 6.2 |
| 8.4 | 1.9 | 1.7 | 5.2 | 6.2 |
| 8.5 | 1.9 | 1.7 | 5.2 | 6.3 |
| 8.6 | 2 | 1.8 | 5.3 | 6.3 |
| 8.7 | 2 | 1.8 | 5.3 | 6.4 |
| 8.8 | 2 | 1.8 | 5.3 | 6.4 |
| 8.9 | 2.1 | 1.9 | 5.4 | 6.4 |
| 9 | 2.1 | 1.9 | 5.4 | 6.5 |
| 9.1 | 2.1 | 1.9 | 5.5 | 6.5 |
| 9.2 | 2.2 | 2 | 5.5 | 6.5 |
| 9.3 | 2.2 | 2 | 5.5 | 6.6 |
| 9.4 | 2.2 | 2.1 | 5.6 | 6.6 |
| 9.5 | 2.3 | 2.1 | 5.6 | 6.7 |
| 9.6 | 2.3 | 2.1 | 5.7 | 6.7 |
| 9.7 | 2.4 | 2.2 | 5.7 | 6.7 |
| 9.8 | 2.4 | 2.2 | 5.8 | 6.8 |
| 9.9 | 2.4 | 2.3 | 5.8 | 6.8 |
| 10 | 2.5 | 2.3 | 5.8 | 6.9 |
| 10.1 | 2.5 | 2.4 | 5.9 | 6.9 |
| 10.2 | 2.6 | 2.4 | 5.9 | 7 |
| 10.3 | 2.6 | 2.5 | 6 | 7 |
| 10.4 | 2.7 | 2.5 | 6 | 7 |
| 10.5 | 2.7 | 2.6 | 6.1 | 7.1 |
| 10.6 | 2.8 | 2.7 | 6.1 | 7.1 |
| 10.7 | 2.9 | 2.7 | 6.2 | 7.2 |
| 10.8 | 2.9 | 2.8 | 6.2 | 7.2 |
| 10.9 | 3 | 2.9 | 6.3 | 7.3 |
| 11 | 3 | 2.9 | 6.3 | 7.3 |

*Grain info: age - 8.42 +/- 0.13 Ma; half-width -35 (microns)*

| | | | | |
|---|---|---|---|---|
| 7 | 0.73 | 0.86 | 3 | 3.6 |
| 7.1 | 0.75 | 0.87 | 3 | 3.7 |
| 7.2 | 0.76 | 0.88 | 3.1 | 3.7 |
| 7.3 | 0.78 | 0.9 | 3.1 | 3.7 |
| 7.4 | 0.79 | 0.91 | 3.1 | 3.7 |
| 7.5 | 0.81 | 0.93 | 3.2 | 3.8 |
| 7.6 | 0.83 | 0.95 | 3.2 | 3.8 |
| 7.7 | 0.85 | 0.96 | 3.2 | 3.8 |
| 7.8 | 0.86 | 0.98 | 3.3 | 3.9 |
| 7.9 | 0.88 | 1 | 3.3 | 3.9 |
| 8 | 0.9 | 1 | 3.3 | 3.9 |
| 8.1 | 0.93 | 1 | 3.4 | 4 |
| 8.2 | 0.95 | 1.1 | 3.4 | 4 |
| 8.3 | 0.97 | 1.1 | 3.4 | 4 |
| 8.4 | 1 | 1.1 | 3.5 | 4.1 |
| 8.5 | 1 | 1.1 | 3.5 | 4.1 |
| 8.6 | 1.1 | 1.2 | 3.5 | 4.1 |
| 8.7 | 1.1 | 1.2 | 3.6 | 4.2 |
| 8.8 | 1.1 | 1.2 | 3.6 | 4.2 |
| 8.9 | 1.1 | 1.2 | 3.7 | 4.2 |
| 9 | 1.2 | 1.3 | 3.7 | 4.3 |
| 9.1 | 1.2 | 1.3 | 3.7 | 4.3 |
| 9.2 | 1.3 | 1.4 | 3.8 | 4.3 |
| 9.3 | 1.3 | 1.4 | 3.8 | 4.4 |
| 9.4 | 1.3 | 1.4 | 3.8 | 4.4 |
| 9.5 | 1.4 | 1.5 | 3.9 | 4.5 |
| 9.6 | 1.5 | 1.5 | 3.9 | 4.5 |
| 9.7 | 1.5 | 1.6 | 4 | 4.5 |
| 9.8 | 1.6 | 1.6 | 4 | 4.6 |

| | | | | |
|---|---|---|---|---|
| 9.9 | 1.6 | 1.7 | 4.1 | 4.6 |
| 10 | 1.7 | 1.8 | 4.1 | 4.7 |
| 10.1 | 1.8 | 1.8 | 4.1 | 4.7 |
| 10.2 | 1.8 | 1.9 | 4.2 | 4.7 |
| 10.3 | 1.9 | 2 | 4.2 | 4.8 |
| 10.4 | 2 | 2 | 4.3 | 4.8 |
| 10.5 | 2.1 | 2.1 | 4.3 | 4.9 |
| 10.6 | 2.2 | 2.2 | 4.4 | 4.9 |
| 10.7 | 2.3 | 2.3 | 4.4 | 5 |
| 10.8 | 2.4 | 2.4 | 4.5 | 5 |
| 10.9 | 2.5 | 2.5 | 4.5 | 5 |
| 11 | 2.5 | 2.6 | 4.6 | 5.1 |

*Grain info: age - 8.46 +/- 0.13 Ma; half-width -59 (microns)*

| | | | | |
|---|---|---|---|---|
| 7 | 1.6 | 1.9 | 5.4 | 6.7 |
| 7.1 | 1.7 | 2 | 5.4 | 6.7 |
| 7.2 | 1.7 | 2 | 5.5 | 6.8 |
| 7.3 | 1.7 | 2 | 5.5 | 6.8 |
| 7.4 | 1.7 | 2 | 5.5 | 6.8 |
| 7.5 | 1.8 | 2.1 | 5.6 | 6.9 |
| 7.6 | 1.8 | 2.1 | 5.6 | 6.9 |
| 7.7 | 1.8 | 2.1 | 5.6 | 6.9 |
| 7.8 | 1.8 | 2.1 | 5.7 | 7 |
| 7.9 | 1.9 | 2.2 | 5.7 | 7 |
| 8 | 1.9 | 2.2 | 5.8 | 7 |
| 8.1 | 1.9 | 2.2 | 5.8 | 7.1 |
| 8.2 | 2 | 2.2 | 5.8 | 7.1 |
| 8.3 | 2 | 2.3 | 5.9 | 7.2 |
| 8.4 | 2 | 2.3 | 5.9 | 7.2 |
| 8.5 | 2.1 | 2.3 | 5.9 | 7.2 |
| 8.6 | 2.1 | 2.4 | 6 | 7.3 |
| 8.7 | 2.1 | 2.4 | 6 | 7.3 |
| 8.8 | 2.2 | 2.4 | 6.1 | 7.3 |
| 8.9 | 2.2 | 2.5 | 6.1 | 7.4 |
| 9 | 2.2 | 2.5 | 6.1 | 7.4 |
| 9.1 | 2.3 | 2.5 | 6.2 | 7.5 |
| 9.2 | 2.3 | 2.6 | 6.2 | 7.5 |
| 9.3 | 2.3 | 2.6 | 6.3 | 7.5 |
| 9.4 | 2.4 | 2.6 | 6.3 | 7.6 |
| 9.5 | 2.4 | 2.7 | 6.3 | 7.6 |
| 9.6 | 2.5 | 2.7 | 6.4 | 7.7 |
| 9.7 | 2.5 | 2.7 | 6.4 | 7.7 |
| 9.8 | 2.5 | 2.8 | 6.5 | 7.7 |
| 9.9 | 2.6 | 2.8 | 6.5 | 7.8 |
| 10 | 2.6 | 2.9 | 6.6 | 7.8 |
| 10.1 | 2.7 | 2.9 | 6.6 | 7.9 |
| 10.2 | 2.7 | 3 | 6.7 | 7.9 |
| 10.3 | 2.8 | 3 | 6.7 | 8 |
| 10.4 | 2.8 | 3.1 | 6.7 | 8 |
| 10.5 | 2.9 | 3.1 | 6.8 | 8 |
| 10.6 | 2.9 | 3.2 | 6.8 | 8.1 |
| 10.7 | 3 | 3.2 | 6.9 | 8.1 |
| 10.8 | 3.1 | 3.3 | 6.9 | 8.2 |
| 10.9 | 3.1 | 3.3 | 7 | 8.2 |
| 11 | 3.2 | 3.4 | 7 | 8.3 |

# APPENDIX M

# CHAPTER 6 SUPPLEMENT:

# CONVENTIONAL (U-TH)/HE THERMOCHRONOLOGIC DATA

Table A6.1. Conventional (U-Th)/he age determinations for sample 07-AT-LB-B.

| Sample | [$^{4}$He] ncm$^{3}$ | [$^{238}$U] ng | [$^{232}$Th] ng | Raw Age (Ma) | Mean $F_T$ | $F_T$ corrected Age (Ma) | 2s (Ma) |
|---|---|---|---|---|---|---|---|
| LB-B z002 | 6.5462 | 1.6619 | 1.1101 | 27.92 | 0.816 | 34.2 | 1.0 |
| LB-B z003 | 15.6476 | 4.3005 | 3.2490 | 25.35 | 0.838 | 30.26 | 0.80 |
| LB-B z004 | 3.0624 | 1.1150 | 0.9482 | 18.79 | 0.771 | 24.38 | 0.78 |
| LB-B z005 | 2.3128 | 0.7292 | 0.6993 | 21.24 | 0.800 | 26.56 | 0.85 |
| LB-B z006 | 7.6114 | 2.2166 | 1.8646 | 23.52 | 0.809 | 29.07 | 0.86 |
| LB-B z007 | 3.2945 | 1.0351 | 0.7442 | 22.34 | 0.778 | 28.73 | 0.89 |
| LB-B z008 | 5.8606 | 1.5068 | 1.6713 | 25.31 | 0.836 | 30.29 | 0.92 |
| LB-B z009 | 5.1956 | 1.6534 | 1.3786 | 21.56 | 0.819 | 26.31 | 0.77 |
| LB-B z010 | 3.0118 | 1.1082 | 1.1448 | 17.95 | 0.790 | 22.72 | 0.69 |
| LB-B z011 | 6.8493 | 2.2532 | 1.6411 | 21.30 | 0.826 | 25.80 | 0.75 |
| LB-B z016 | 2.8399 | 0.8942 | 0.7226 | 21.90 | 0.750 | 29.19 | 0.85 |
| LB-B z018 | 1.4612 | 0.4415 | 0.4689 | 21.73 | 0.784 | 27.71 | 0.83 |
| LB-B z020 | 1.9950 | 0.6780 | 0.4121 | 21.13 | 0.733 | 28.81 | 0.95 |
| LB-B z022 | 4.5249 | 1.5495 | 1.4070 | 19.75 | 0.802 | 24.64 | 0.73 |
| LB-B z027 | 1.1441 | 0.3942 | 0.3814 | 19.41 | 0.723 | 26.83 | 0.87 |
| LB-B z029 | 4.0575 | 1.4362 | 0.9646 | 20.03 | 0.808 | 24.77 | 0.75 |
| LB-B z030 | 1.9407 | 0.4810 | 0.3244 | 28.56 | 0.786 | 36.3 | 1.2 |
| LB-B z031 | 4.0586 | 1.3090 | 1.0459 | 21.42 | 0.832 | 25.76 | 0.80 |
| LB-B z032 | 13.4032 | 5.4383 | 3.0072 | 17.91 | 0.850 | 21.06 | 0.65 |
| LB-B z033 | 12.9319 | 3.5466 | 2.8695 | 25.13 | 0.836 | 30.05 | 0.89 |
| LB-B z034 | 6.2263 | 1.8502 | 1.3530 | 23.56 | 0.821 | 28.69 | 0.88 |
| LB-B z035 | 1.6443 | 0.6454 | 0.4309 | 18.08 | 0.770 | 23.49 | 0.74 |
| LB-B z036 | 5.1238 | 1.6074 | 1.0261 | 22.74 | 0.812 | 28.00 | 0.83 |
| LB-B z037 | 3.8226 | 1.0983 | 0.7284 | 24.70 | 0.817 | 30.22 | 0.88 |
| LB-B z038 | 2.2594 | 0.7959 | 0.4154 | 20.75 | 0.751 | 27.64 | 0.86 |
| LB-B z039 | 1.1259 | 0.4644 | 0.4177 | 16.43 | 0.726 | 22.63 | 0.74 |
| LB-B z040 | 2.2056 | 0.7638 | 0.5841 | 20.09 | 0.818 | 24.55 | 0.76 |
| LB-B z041 | 1.6548 | 0.5366 | 0.5745 | 20.22 | 0.749 | 27.00 | 0.83 |
| LB-B z042 | 4.9833 | 1.3155 | 0.9744 | 26.46 | 0.768 | 34.5 | 1.0 |
| LB-B z043 | 2.9444 | 0.9415 | 0.8056 | 21.37 | 0.773 | 27.64 | 0.78 |
| LB-B z044 | 10.9717 | 3.2779 | 2.5998 | 23.15 | 0.829 | 27.93 | 0.77 |
| LB-B z045 | 5.5539 | 1.9671 | 2.0011 | 18.70 | 0.798 | 23.42 | 0.65 |
| LB-B z046 | 2.9054 | 1.1588 | 1.0186 | 17.06 | 0.780 | 21.88 | 0.62 |
| LB-B z047 | 2.7025 | 0.9344 | 0.5987 | 20.63 | 0.786 | 26.26 | 0.78 |
| LB-B z048 | 0.6568 | 0.2354 | 0.2114 | 18.91 | 0.758 | 24.94 | 0.80 |
| LB-B z049 | 1.8975 | 0.6293 | 0.4841 | 20.96 | 0.811 | 25.84 | 0.79 |

| | | | | | | | |
|---|---|---|---|---|---|---|---|
| LB-B z051 | 3.3776 | 1.0598 | 0.7567 | 22.39 | 0.773 | 28.96 | 0.83 |
| LB-B z052 | 1.5927 | 0.5936 | 0.6130 | 17.72 | 0.769 | 23.04 | 0.71 |
| LB-B z053 | 1.2168 | 0.4137 | 0.3896 | 19.76 | 0.738 | 26.79 | 0.78 |
| LB-B z054 | 1.1576 | 0.3827 | 0.3317 | 20.62 | 0.789 | 26.12 | 0.80 |
| LB-B z055 | 2.8591 | 0.9136 | 0.7253 | 21.64 | 0.809 | 26.74 | 0.74 |
| LB-B z056 | 5.8653 | 1.9090 | 1.3112 | 21.71 | 0.827 | 26.25 | 0.75 |
| LB-B z057 | 9.8043 | 2.7145 | 3.0343 | 23.47 | 0.820 | 28.63 | 0.81 |
| LB-B z058 | 1.5034 | 0.5213 | 0.4470 | 19.70 | 0.825 | 23.87 | 0.82 |
| LB-B z059 | 4.1734 | 1.3343 | 1.0069 | 21.80 | 0.768 | 28.38 | 0.83 |
| LB-B z060 | 2.6159 | 0.8572 | 0.8980 | 20.09 | 0.797 | 25.20 | 0.77 |
| LB-B z061 | 2.3250 | 0.7865 | 0.6408 | 20.36 | 0.799 | 25.49 | 0.80 |
| LB-B z062 | 0.4916 | 0.1759 | 0.1697 | 18.69 | 0.702 | 26.6 | 1.0 |
| LB-B z063 | 2.7070 | 0.9612 | 0.7142 | 19.68 | 0.780 | 25.22 | 0.79 |
| LB-B z064 | 3.2899 | 0.8897 | 0.6647 | 25.80 | 0.744 | 34.7 | 1.1 |
| LB-B z065 | 6.7278 | 2.1744 | 1.9324 | 21.00 | 0.818 | 25.67 | 0.80 |
| LB-B z066 | 5.4656 | 1.4703 | 1.6970 | 23.99 | 0.790 | 30.35 | 0.92 |
| LB-B z068 | 13.7157 | 0.6626 | 0.4395 | 18.73 | 0.807 | 23.22 | 0.74 |
| LB-B z069 | 1.7479 | 3.5309 | 3.1179 | 26.39 | 0.804 | 32.83 | 0.92 |
| LB-B z070 | 2.0569 | 0.7419 | 0.7526 | 18.37 | 0.798 | 23.02 | 0.71 |
| LB-B z071 | 4.7507 | 1.6332 | 1.4349 | 19.79 | 0.758 | 26.10 | 0.77 |
| LB-B z072 | 31.2480 | 4.9668 | 15.3668 | 29.86 | 0.848 | 35.21 | 0.92 |
| LB-B z073 | 1.1915 | 0.3825 | 0.2877 | 21.72 | 0.805 | 26.98 | 0.88 |
| LB-B z074 | 0.8903 | 0.3347 | 0.3137 | 17.89 | 0.800 | 22.37 | 0.69 |
| LB-B z075 | 1.1175 | 0.4057 | 0.3513 | 18.78 | 0.782 | 24.01 | 0.75 |
| LB-B z076 | 2.7132 | 1.1039 | 1.0790 | 16.41 | 0.829 | 19.78 | 0.60 |
| LB-B z077 | 1.4898 | 0.5069 | 0.3697 | 20.59 | 0.770 | 26.75 | 0.86 |
| LB-B z078 | 1.7019 | 0.4980 | 0.5698 | 22.10 | 0.708 | 31.23 | 0.92 |
| LB-B z079 | 0.6685 | 0.3093 | 0.2407 | 15.00 | 0.647 | 23.20 | 0.85 |
| LB-B z080 | 0.9695 | 0.3978 | 0.2758 | 17.20 | 0.683 | 25.18 | 0.87 |
| LB-B z081 | 1.4966 | 0.5027 | 0.4021 | 20.57 | 0.781 | 26.33 | 0.83 |
| LB-B z082 | 4.0231 | 1.0943 | 0.9291 | 25.14 | 0.779 | 32.29 | 0.90 |
| LB-B z083 | 1.4233 | 0.4374 | 0.4368 | 21.62 | 0.793 | 27.26 | 0.85 |
| LB-B z084 | 2.5810 | 0.8594 | 0.5643 | 21.35 | 0.782 | 27.31 | 0.78 |
| LB-B z085 | 2.4060 | 0.8776 | 0.7684 | 18.66 | 0.772 | 24.19 | 0.70 |
| LB-B z086 | 1.2631 | 0.3732 | 0.3328 | 22.95 | 0.722 | 31.81 | 0.98 |
| LB-B z087 | 0.6571 | 0.2073 | 0.2109 | 20.99 | 0.650 | 32.3 | 1.1 |
| LB-B z088 | 1.3432 | 0.4553 | 0.3877 | 20.17 | 0.794 | 25.41 | 0.82 |
| LB-B z089 | 2.4988 | 0.8879 | 0.8724 | 18.77 | 0.787 | 23.84 | 0.72 |
| LB-B z090 | 12.0736 | 2.7274 | 2.6511 | 29.55 | 0.739 | 40.0 | 1.2 |

| | | | | | | | |
|---|---|---|---|---|---|---|---|
| LB-B z091 | 1.8086 | 0.4968 | 0.3343 | 25.78 | 0.776 | 33.2 | 1.1 |
| LB-B z092 | 3.1969 | 0.4194 | 0.2790 | 24.79 | 0.755 | 32.8 | 1.1 |
| LB-B z094 | 3.3303 | 0.9181 | 1.2053 | 22.74 | 0.777 | 29.27 | 0.88 |
| LB-B z095 | 1.4652 | 1.2624 | 1.6054 | 16.00 | 0.765 | 20.93 | 0.71 |
| LB-B z096 | 2.8409 | 1.1678 | 1.0305 | 16.54 | 0.815 | 20.28 | 0.61 |
| LB-B z097 | 3.3008 | 1.3629 | 0.9825 | 17.00 | 0.773 | 21.99 | 0.69 |
| LB-B z098 | 21.8523 | 4.3716 | 7.4028 | 29.32 | 0.760 | 38.6 | 1.1 |
| LB-B z099 | 2.3430 | 0.9242 | 0.7792 | 17.37 | 0.833 | 20.86 | 0.66 |
| LB-B z100 | 1.3658 | 0.3960 | 0.6684 | 20.26 | 0.695 | 29.17 | 0.93 |
| LB-B z101 | 0.9039 | 0.3469 | 0.3058 | 17.72 | 0.775 | 22.85 | 0.87 |
| LB-B z102 | 1.0682 | 0.3874 | 0.2630 | 19.52 | 0.758 | 25.7 | 1.1 |
| LB-B z103 | 4.5613 | 1.0680 | 1.3362 | 27.07 | 0.767 | 35.3 | 1.3 |
| LB-B z104 | 1.0710 | 0.4027 | 0.2742 | 18.82 | 0.703 | 26.8 | 1.1 |
| LB-B z105 | 0.3492 | 0.1368 | 0.1047 | 17.76 | 0.744 | 23.9 | 1.0 |
| LB-B z106 | 0.7801 | 0.3063 | 0.2235 | 17.84 | 0.795 | 22.43 | 0.94 |
| LB-B z107 | 2.0725 | 0.7232 | 0.5497 | 19.95 | 0.812 | 24.58 | 0.97 |
| LB-B z108 | 4.3202 | 1.6718 | 0.9437 | 18.73 | 0.754 | 24.83 | 0.96 |
| LB-B z109 | 0.9781 | 0.3726 | 0.3408 | 17.73 | 0.744 | 23.82 | 0.96 |
| LB-B z110 | 4.7034 | 1.1590 | 1.0385 | 27.49 | 0.822 | 33.5 | 1.3 |
| LB-B z111 | 2.6667 | 1.0468 | 0.5912 | 18.46 | 0.803 | 22.98 | 0.90 |
| LB-B z112 | 3.4879 | 1.0065 | 0.9404 | 23.31 | 0.783 | 29.8 | 1.1 |
| LB-B z113 | 0.7199 | 0.2627 | 0.2147 | 18.87 | 0.767 | 24.60 | 0.95 |
| LB-B z114 | 4.7689 | 1.4434 | 1.3476 | 22.23 | 0.727 | 30.6 | 1.1 |
| LB-B z115 | 5.2182 | 2.0520 | 0.9954 | 18.74 | 0.833 | 22.50 | 0.88 |
| LB-B z116 | 1.4366 | 0.4292 | 0.5391 | 21.20 | 0.771 | 27.5 | 1.1 |
| LB-B z117 | 1.3725 | 0.4917 | 0.4286 | 19.01 | 0.727 | 26.16 | 0.89 |
| LB-B z118 | 2.0637 | 0.6497 | 0.4766 | 22.23 | 0.778 | 28.6 | 1.1 |
| LB-B z119 | 5.2140 | 1.6593 | 1.1928 | 22.06 | 0.769 | 28.7 | 1.1 |
| LB-B z121 | 2.0634 | 0.6005 | 0.6064 | 22.78 | 0.740 | 30.8 | 1.2 |
| LB-B z122 | 3.9112 | 1.1905 | 0.9487 | 22.70 | 0.828 | 27.4 | 1.0 |
| LB-B z123 | 1.0444 | 0.3722 | 0.2912 | 19.45 | 0.798 | 24.39 | 0.92 |
| LB-B z124 | 1.8210 | 0.7142 | 0.3006 | 19.05 | 0.742 | 25.7 | 1.0 |
| LB-B z126 | 1.6237 | 0.5362 | 0.5181 | 20.25 | 0.773 | 26.19 | 0.97 |
| LB-B z127 | 0.2980 | 0.1411 | 0.0981 | 14.91 | 0.659 | 22.61 | 0.96 |
| LB-B z129 | 4.0562 | 1.2959 | 1.5832 | 19.95 | 0.672 | 29.7 | 1.1 |
| LB-B z130 | 1.4816 | 0.7123 | 0.4331 | 14.94 | 0.647 | 23.10 | 0.86 |
| LB-B z131 | 1.7928 | 0.6610 | 0.5785 | 18.46 | 0.797 | 23.18 | 0.84 |
| LB-B z132 | 0.4706 | 0.1925 | 0.1465 | 17.02 | 0.752 | 22.62 | 0.88 |

# APPENDIX N

# CHAPTER 6 SUPPLEMENT:

# LASER MICROPROBE (U-TH)/HE THERMOCHRONOLOGIC DATA

Table A6.2. Laser microprobe age determinations for sample 07-AT-B-B.

| Sample | $^4$He (atoms) | Volume | [$^4$He] atoms/g | [U] ppm | [Th] ppm | Age (Ma) | Error (2s) |
|---|---|---|---|---|---|---|---|
| LBB ZR 030 | 4.78E+08 | 4.68E+03 | 2.197E+16 | 361.93 | 223.15 | 16.3 | 1.2 |
| LBB ZR 031 | 3.51E+08 | 2.54E+03 | 2.971E+16 | 221.50 | 179.46 | 34.6 | 2.5 |
| LBB ZR 032 | 1.00E+08 | 2.35E+03 | 9.182E+15 | 63.82 | 65.70 | 35.6 | 2.6 |
| LBB ZR 034 | 4.16E+08 | 1.46E+04 | 6.134E+15 | 62.85 | 60.72 | 24.4 | 1.8 |
| LBB ZR 035 | 3.12E+08 | 2.34E+03 | 2.869E+16 | 257.92 | 189.75 | 29.1 | 2.1 |
| LBB ZR 036 | 9.44E+07 | 4.23E+03 | 4.804E+15 | 63.87 | 36.93 | 20.4 | 1.5 |
| LBB ZR 038 | 1.21E+09 | 1.50E+04 | 1.733E+16 | 270.12 | 203.12 | 16.7 | 1.2 |
| LBB ZR 040 | 5.92E+08 | 1.38E+04 | 9.200E+15 | 84.72 | 94.70 | 26.4 | 1.9 |
| LBB ZR 041 | 5.67E+08 | 4.30E+03 | 2.837E+16 | 371.08 | 196.02 | 20.9 | 1.6 |
| LBB ZR 043 | 3.55E+08 | 3.97E+03 | 1.925E+16 | 187.07 | 101.97 | 28.? | 2.1 |
| LBB ZR 044 | 1.36E+09 | 1.33E+04 | 2.204E+16 | 197.61 | 240.11 | 26.6 | 2.0 |
| LBB ZR 045 | 6.95E+07 | 1.75E+03 | 8.527E+15 | 88.97 | 104.25 | 23.1 | 1.7 |
| LBB ZR 048 | 1.39E+08 | 3.24E+03 | 9.242E+15 | 124.52 | 80.88 | 19.8 | 1.5 |
| LBB ZR 049 | 2.13E+08 | 1.60E+03 | 2.848E+16 | 303.61 | 196.12 | 25.0 | 1.8 |
| LBB ZR 050 | 1.21E+08 | 1.66E+03 | 1.564E+16 | 209.06 | 161.74 | 19.4 | 1.4 |
| LBB ZR 051 | 3.08E+08 | 1.71E+03 | 3.870E+16 | 551.64 | 537.03 | 17.5 | 1.3 |
| LBB ZR 052 | 1.84E+08 | 1.66E+03 | 2.377E+16 | 173.02 | 143.63 | 35.3 | 2.6 |
| LBB ZR 054 | 7.90E+07 | 1.89E+03 | 8.968E+15 | 85.00 | 81.14 | 26.4 | 1.9 |
| LBB ZR 055 | 8.67E+07 | 1.85E+03 | 1.010E+16 | 123.52 | 94.36 | 21.3 | 1.6 |
| LBB ZR 057 | 1.98E+08 | 3.60E+03 | 1.182E+16 | 121.50 | 120.38 | 24.2 | 1.8 |
| LBB ZR 058 | 2.28E+08 | 3.80E+03 | 1.291E+16 | 181.58 | 149.85 | 18.3 | 1.3 |
| LBB ZR 060 | 1.57E+08 | 1.65E+03 | 2.052E+16 | 236.35 | 244.96 | 21.4 | 1.6 |
| LBB ZR 061 | 1.59E+08 | 3.13E+03 | 1.097E+16 | 115.93 | 92.97 | 24.5 | 1.8 |
| LBB ZR 063 | 1.09E+08 | 1.52E+03 | 1.544E+16 | 161.27 | 168.01 | 23.6 | 1.8 |
| LBB ZR 065 | 9.74E+07 | 1.42E+03 | 1.474E+16 | 92.85 | 96.31 | 39.1 | 3.1 |
| LBB ZR 066 | 1.44E+08 | 1.37E+03 | 2.260E+16 | 199.77 | 235.73 | 27.2 | 2.0 |
| LBB ZR 067 | 1.35E+08 | 1.43E+03 | 2.019E+16 | 266.67 | 191.08 | 19.9 | 1.5 |
| LBB ZR 010 | 4.99E+08 | 1.44E+04 | 7.483E+15 | 76.64 | 53.79 | 25.7 | 1.9 |
| LBB ZR 011B | 1.01E+09 | 1.49E+04 | 1.467E+16 | 141.79 | 91.47 | 27.7 | 2.0 |
| LBB ZR 012 | 2.29E+08 | 4.28E+03 | 1.151E+16 | 155.52 | 178.22 | 17.9 | 1.3 |
| LBB ZR 013B | 2.59E+08 | 3.97E+03 | 1.403E+16 | 110.93 | 82.87 | 32.9 | 2.5 |
| LBB ZR 014 | 2.89E+08 | 2.40E+03 | 2.592E+16 | 349.10 | 320.19 | 18.8 | 1.4 |
| LBB ZR 015 | 3.05E+08 | 2.10E+03 | 3.124E+16 | 283.24 | 224.60 | 28.5 | 2.1 |
| LBB ZR 016 | 7.35E+08 | 1.15E+04 | 1.376E+16 | 89.07 | 67.53 | 40.3 | 3.0 |
| LBB ZR 017 | 1.22E+08 | 2.09E+03 | 1.259E+16 | 122.36 | 81.89 | 27.4 | 2.3 |
| LBB ZR 018 | 1.19E+08 | 2.00E+03 | 1.279E+16 | 104.62 | 61.42 | 33.? | 2.8 |

| | | | | | | | |
|---|---|---|---|---|---|---|---|
| LBB ZR 019 | 4.01E+08 | 3.85E+03 | 2.243E+16 | 176.17 | 108.59 | 34.1 | 2.5 |
| LBB ZR 020 | 3.68E+08 | 3.81E+03 | 2.076E+16 | 124.82 | 70.57 | 45.1 | 3.3 |
| LBB ZR 021 | 6.89E+08 | 3.83E+03 | 3.871E+16 | 336.48 | 409.06 | 27.5 | 2.0 |
| LBB ZR 022 | 1.35E+08 | 1.81E+03 | 1.608E+16 | 170.08 | 91.40 | 25.8 | 1.9 |
| LBB ZR 023 | 1.28E+08 | 3.45E+03 | 8.005E+15 | 58.97 | 53.98 | 34.3 | 2.6 |
| LBB ZR 024 | 3.81E+08 | 3.52E+03 | 2.328E+16 | 145.09 | 154.61 | 39.4 | 2.9 |
| LBB ZR 025B | 1.92E+08 | 3.42E+03 | 1.210E+16 | 122.60 | 95.81 | 25.6 | 2.3 |
| LBB ZR 027 s2 | 2.20E+08 | 1.81E+03 | 2.610E+16 | 312.43 | 179.27 | 22.6 | 1.7 |

# APPENDIX O

## STATEMENT OF PERMISSION FROM CO-AUTHORS

Chapters 2-6 were prepared independently for publication with help from Kip Hodges (Chapters 2-6), Matthijs van Soest (Chapters 3, 5, 6), Talat Ahmad (Chapters 3, 4, 5), Jo-Anne Wartho (Chapters 2, 4), Christopher Edwards (Chapter 2), Frances Cooper (Chapter 2), Gwyneth Gordon (Chapter 4), Peter Clift (Chapter 4), and Brian Monteleone (Chapter 6). These co-authors have acknowledged and granted permission for the use of this work in the context of this dissertation.